UNIVERSITY OF CALIFORNIA,
IRVINE

Integration of Power and Cooling for Data Centers by Solid Oxide Fuel Cells and Absorption Chillers

DISSERTATION

submitted in partial satisfaction of the requirements
for the

DOCTOR OF PHILOSOPHY

In Mechanical Engineering

by

Alejandro Carlos Lavernia

Dissertation Committee:
Professor Jack Brouwer, Chair
Professor Scott Samuelsen
Professor Steve Davis

2022

Dedication

To my wife, Tessa, thank you for your unwavering love and support.

I could not have done this without you.

To my family, thank you for the encouragement and inspiration along the way.

Your faith in me got me through many hardships.

Table of Contents

List of Figures

List of Tables

Acknowledgements

I would like to thank Professor Jack Brouwer for his tireless commitment to his graduate students, research endeavors and the whole APEP family. His effort to take our science and help the world is inspirational and I hope to take his energy and carry it forward.

Many thanks to Professor Scott Samuelsen for his leadership and guidance. His unyielding professionalism provides a golden standard for all his students to aspire to.

The support Sean James, Mark Monroe, and the entire team at Microsoft has been crucial throughout my research. Thank you for direction, trust, and continued support in my effort to complete my PhD.

To my colleagues on the Microsoft Project: Luca Mastropasqua, Maryam Asghari, Melina Arrizon, Alexandra Huff; thank you for all your assistance, creativity, and comradery. The research we perform is vastly improved by your collective effort as is the fun had during it all.

I would also like to thank Max Venaas for his support and guidance during the construction of my experimental test stand. Our problem-solving brainstorming sessions solved many an issue and helped me keep my sanity.

Special thanks to my officemates Daniel Jaimes, Yan Zhao and Clinton Thai for all the times we got to escape our closet for lunch or ping-pong.

To the rest of the APEP family, thank you for your support both professionally and personally. The teamwork here at APEP creates an environment that helps us all perform research at higher levels.

VITA
Alejandro Carlos Lavernia

2013	**Mechanical Design Intern** UC Davis – BioMEMS Laboratory
2014	**Mechanical Design Intern** Sandia National Laboratories, Livermore, CA
2015	**Mechatronics Intern** Siemens Technik Akademie, Berlin, Germany
2015	**Teaching Assistant - Department of Computer Graphics Technology** Purdue University, West Lafayette, IN
2015 – 2016	**Undergraduate Researcher** Herrick Laboratories, Purdue University, West Lafayette, IN
2016	**B.S. in Mechanical Engineering** Purdue University, West Lafayette, IN
2016 – 2018	**Research Assistant** Herrick Laboratories, Purdue University, West Lafayette, IN
2018	**M.Sc. in Mechanical Engineering,** Advisor: Dr. Eckhard Groll Purdue University, West Lafayette, IN
2019	**Teaching Assistant – Department of Mechanical and Aerospace Engineering** University of California, Irvine
2021	**Fuel Cell Systems Engineer Consultant** Hydroplane Ltd., Thousand Oaks, CA
2021	**Thermal Systems Intern** Tri Alpha Energies, Foothill Ranch, CA
2018 – 2022	**Graduate Research Assistant** National Fuel Cell Research Center, University of California, Irvine
2022	**Ph.D. in Mechanical Engineering** Advisor: Dr. Jack Brouwer University of California, Irvine

Field of Study

Mechanical Engineering

Publications

Alejandro Carlos Lavernia, Tony Dover, Scott Samuelsen; “Operational and Economic Performance Analysis of a High-Temperature Fuel Cell Cogeneration Plant,” Journal of Power Sources, 520 (2022), 230798.

Alejandro Carlos Lavernia, Maryam Asghari, Luca Mastropasqua, Jack Brouwer, “Operational Optimization of a Thermally Integrated Solid Oxide Fuel Cell with Triple Effect Absorption Chiller for Data Centers,” Journal of the Electrochemical Society, in preparation.

Alejandro Carlos Lavernia, Maryam Asghari, Luca Mastropasqua, Jack Brouwer, “Absorption Cooling for Data Centers powered by Solid Oxide Fuel Cell Waste Heat,” International Refrigeration and Air Conditioning Conference. Paper 2220 (2020).

Alejandro Carlos Lavernia, Maryam Asghari, Luca Mastropasqua, Jack Brouwer, “Design Optimization of a Thermally Integrated Solid Oxide Fuel Cell with Triple Effect Absorption Chiller,” The Electrochemical Society (ECS) Transactions, Volume 103, Number 1, 2021 pp. 807-824.

Maryam Asghari, Alejandro Carlos Lavernia, Luca Mastropasqua, Jack Brouwer, “Degradation Analysis of a Commercial SOFC System,” The Electrochemical Society (ECS) Abstracts, Issue 1, pp. 65.

Alejandro Carlos Lavernia, Maryam Asghari, Jack Brouwer; “Absorption Cooling for Data Centers Powered by Solid Oxide Fuel Cell Waste Heat,” American Society of Heating Refrigeration Air Conditioning Engineers (ASHRAE) Transactions, Vol. 126, No. 1, 2020, pp. 204 - 211.

Maryam Asghari, Alejandro Carlos Lavernia, Alireza Saeedmanesh, Sean James, Jack Brouwer, “Integration of Solid Oxide Fuel Cell with Liquid Desiccant Cooling for Generation of Combined Cooling and Power for a Server,” The Electrochemical Society (ECS) Transactions, Volume 91, Number 1, 2019 pp. 167-177.

Davide Ziviani, Alejandro Carlos Lavernia, Xueyang Xu, Kunal Bansal, Bryce Shaffer, Eckhard A. Groll, “ High-Grade Waste Heat Recovery (WHR) from Residential Scale Gensets,” Book of Abstracts of the 5th Annual Engine ORC Consortium Workshop for the Automotive and Stationary Engine Industries, September 26-28, 2018.

Alejandro Carlos Lavernia; “Micro-scale Waste Heat Recovery from Stationary Internal Combustion Engines by Sub-critical Organic Rankine Cycle Utilizing Scroll Machinery,” ProQuest Dissertations & Theses Global (2018). (2054012322).

Alejandro Carlos Lavernia, Davide Ziviani, Kunal Bansal, Bryce Shaffer, Eckhard A. Groll, “Development of an ORC For High Temperature Waste Heat Recovery Utilizing Scroll Expanders,” International Refrigeration and Air Conditioning Conference. Paper 1995 (2018).

Alejandro Carlos Lavernia, Davide Ziviani, Nigora Gafur, Kunal Bansal, Bryce Shaffer, Eckhard Groll, “Testing of R245fa and R1233zd(E) in a High Temperature Waste Heat Recovery Application Utilizing a Scroll Expander,” 1st International Institute of Refrigeration Conference on the Application of Hydrofluoroolefin (HFO) Refrigerants, 2018.

Alejandro Carlos Lavernia, Davide Ziviani, Bryce Shaffer, Kunal Bansal, Eckhard A. Groll, “Optimization of an Organic Rankine Cycle as Bottoming Cycle of a 1 kWe GENSET for Residential Application,” Procedia Energy, Volume 129, September 2017, pp. 867–874.

Abstract of the Dissertation

Integration of Power and Cooling for Data Centers by Solid Oxide Fuel Cells and Absorption Chillers

By

Alejandro Carlos Lavernia

Doctor of Philosophy in Mechanical Engineering

University of California, Irvine, 2022

Professor Jack Brouwer, Chair

Data centers are the largest sectoral consumer of electricity in the United States and in order to reduce their carbon emissions the introduction of advanced power and cooling technologies is a necessity. Solid-oxide fuel cells (SOFCs) are a promising technology that can provide high-efficiency electricity to data centers while utilizing existing natural gas infrastructure for fuel. Additionally, SOFC cogeneration with absorption technology can provide free chilling while meeting the requirements of server computers. This dissertation explores how the successful integration between solid-oxide fuel cells and absorption refrigeration can meet the principal demands of data centers, reduce their carbon footprint, all while running on existing fuel infrastructure.

The feasibility of these systems' integration is explored numerically and experimentally. A server row-level model is constructed based on the experimental data collected from the lab-scale SOFC and absorption chiller setup. The operation of the SOFC and absorption chiller is then optimized to minimize carbon emission intensity, levelized cost of utility, and maximize primary energy savings (PES) ratio. The integrated system is able to operate with a carbon emission intensity of 0.38 kg/kWh compared to the grid's 0.44 kg/kWh, at a PES ratio of 25.8%, costing 75.7 $/MWh of utility production compared to the grid's 58.5 $/MWh.

Additionally, the integrated system can be further optimized to match the transient chilling requirement of the server computers. Adjusting the stack temperature and fuel utilization of the SOFC can control the

chilling capacity of the absorption chiller allowing the SOFC to operate more efficiently when chilling is not required but still meet peak chilling demand. Successful deployment of this active control can reduce the carbon emissions of a server row by 27.2%.

Additionally, the real-world feasibility is also explored in the case study of a 1.4 MW high-temperature fuel cell cogeneration plant on the UCI Medical Center. Operational and economic investigation of the system reveal that the primary driver of such an integrated system's success is the reliability of the power produced and consideration of stack degradation throughout its lifetime.

Finally, SOFC systems can incorporate blends of hydrogen or biogas to further reduce their carbon footprint and move towards a hydrogen economy. The production of green hydrogen can also come from solid-oxide technology at high efficiencies. This operation is explored experimentally with challenges such as delamination and electrode degradation analyzed.

Ultimately, the thermal integration solid-oxide technology presents a promising step towards decarbonizing the digital infrastructure industry.

Chapter 1 - Introduction

1.1 - Motivation

The current state of the world is that of a global climate crisis. Humanity's increased dependence and demand on electricity and transportation has increased the production of greenhouse gasses and other chemicals that adversely affect the planet's atmosphere. In the United States, energy usage between the months of January and May of the year 2016 surpasses 11.7 trillion kWh, in turn producing 6,511 trillion kilograms of carbon dioxide and its equivalents. Of this carbon dioxide emission, 28% is produced by the production of electricity. Electricity in the United States is used in anything from lighting a residence to powering an industrial plant. However, the largest consumer of electricity in the United States in the year 2014 was data centers consuming 32 billion kWh in servers, 7 billion kWh in data storage, 1.3 billion kWh in networking, and 35 billion kWh in supporting infrastructure (Andrae et al., 2015). Data centers are a relatively new commodity that serve to supply the internet connectivity that civilization has come to increasingly rely on. As shown in Figure 1.1, data center use between the years of 2000 and 2006 more than doubled. Figure 1.1 also shows the compound effect of technological improvements throughout time where the true demand increases as shown with a constant energy efficiency, in this case that of the year 2010.

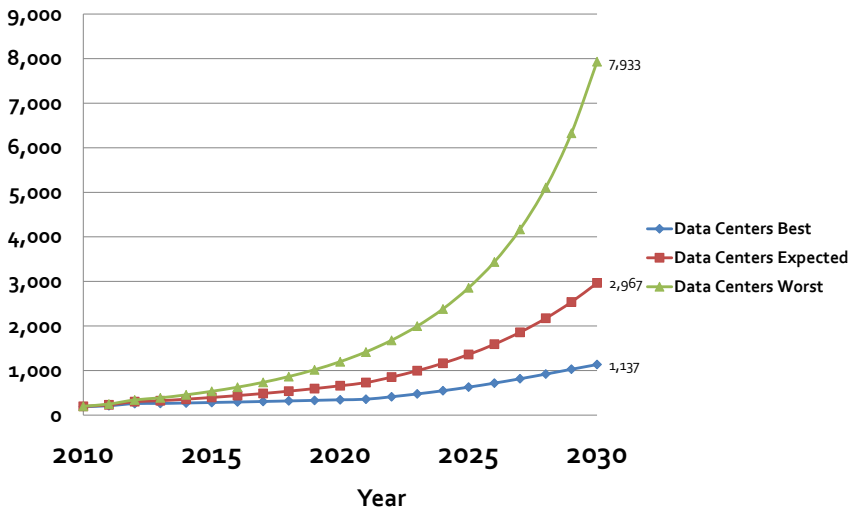

Figure 1.1 – Data Center Electricity Consumption (Andrae et al., 2015).

To meet the constantly increasing demand for computing power in data centers, new technologies are being investigated to improve the overall efficiencies of these enormous installations. Energy consumption in data centers can be broken into two sections: processing energy and supporting energy. Processing energy consists of electricity that is fed to the servers which enables them to perform the computations asked of them. Supporting energy consists mainly of the cooling required to maintain the servers' operation. Additionally, given that data centers have come to provide functions that have become integral to society; anything from email exchange to keeping hospitals operational, maintaining constant operation is an important consideration when designing these installations.

The importance of data centers will only increase in the future, and it will be important to continue to increase the efficiency and lower the emissions associated with these systems. By increasing the efficiency at which data centers get their power and cooling, it will be possible to reduce the carbon footprint of data centers. Then providing the electricity and cooling via zero emissions technology is required to eliminate emissions. Due to the critical nature or our environmental crisis, larger moves to solutions that more actively tackle the issues are necessary.

1.2 - Concept Background

To provide the foundation of understanding to build upon, it is important to have a good working knowledge of the systems involved in the theoretical improvement described above. Three system levels are selected to encompass the research for this application.

1.2.1 - Data Centers

The first level of understanding begins with the data centers themselves. Data centers are structures constructed to house large quantities of computer power which can provide a variety of services including data storage, computational power, cloud services, or networking services. There are many different types of data centers constructed at different scales for different applications. This research will focus on hyper-scale data centers favored by companies such as Microsoft. Hyper-scale data centers have various advantages: lower cost-per-square-foot, larger localized supporting systems, and negotiating power with utility companies due to the high demand. Traditionally, these centers are constructed in rural areas where land is inexpensive and close to power and internet connections for better connectivity.

Hyper-scale data centers primary advantage is the consolidation of supporting equipment. Shown in Figure 1.2 is a generic layout of server racks within a data center.

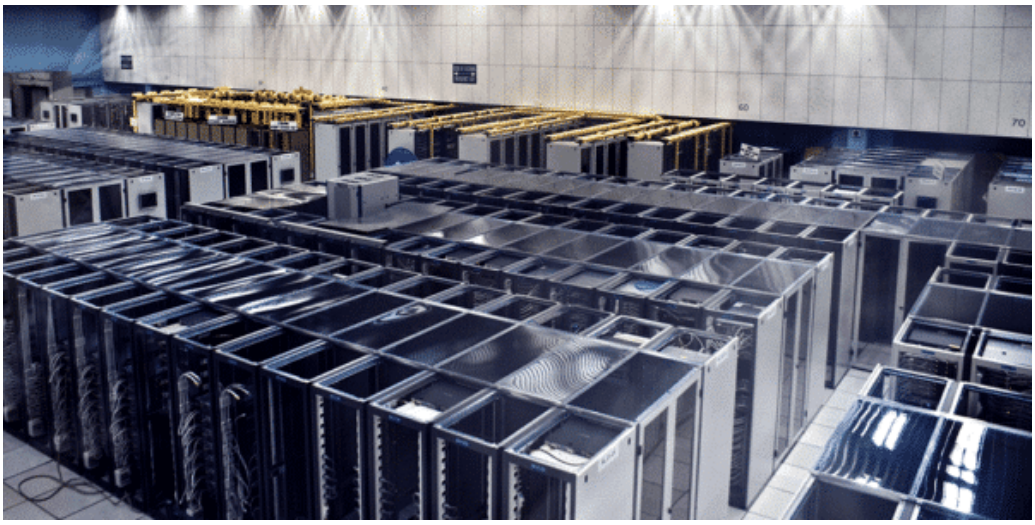

Figure 1.2 - Data Center Layout.

Besides electricity distribution, the most important supporting system for the server racks is the cooling. The servers require continuous air throughput to which they reject heat, protecting the silicon chips and boards which conduct operations. Several different cooling technologies are employed to cool the computers, but the principal technologies are direct, evaporative, and mechanical cooling. Direct cooling allows the ambient air to flow through the data center, cooling the servers, before being exhausted to the environment. This strategy is good for data centers in locations where the ambient air is rarely too hot to provide adequate cooling. Evaporative cooling allows cooling using the psychrometric properties of air to induce cooling by adding water to it. This approach is very simple and efficient but can be infeasible when the ambient air becomes too humid, or water is too expensive. Mechanical cooling has the advantage of working in almost any ambient condition but requires significantly more electricity to operate. In most instances, a data center is configured with direct-air cooling as the primary cooling methodology with backup mechanical systems for days when the ambient temperature is too high. This redundancy is required for hyper-scale data centers because maintaining a constant uptime is crucial.

Given the knowledge about the application, any novel cooling technology must provide the following: sufficient cooling at any ambient condition, consideration of the geographic resources, substantial reliability, and redundancy to maintain operation.

1.2.2 - Fuel Cells

The next level of understanding to be built upon is the power production for data centers. Traditionally, most power produced in the United States is produced by combined cycle natural gas power plants. These plants run gas turbines using the combustion of natural gas as the primary power production. A bottoming steam cycle helps to boost production efficiencies. This power is delivered to data centers either by a direct connection or via the existing grid infrastructure. The electricity is then conditioned and managed before being delivered to the computers within the data center. In the case of a grid fault or disconnection, backup generators are installed on site which can produce electricity for up to 48 hours. These generators are traditionally diesel combustion systems which produce large amounts of harmful emissions.

These power systems present a unique opportunity for improvement. The implementation of fuel cells to produce electricity for data centers could decrease the carbon emissions of data centers significantly. Fuel cell systems are electricity producing machines that operate using a fuel input and an oxidizer input similar to traditional combustion systems. However, fuel cells utilize electrochemistry to separate the two halves of the combustion reaction and allow for transference of electrons from one electrode to another to complete the loop. The reactions are shown in Figure 1.3. below.

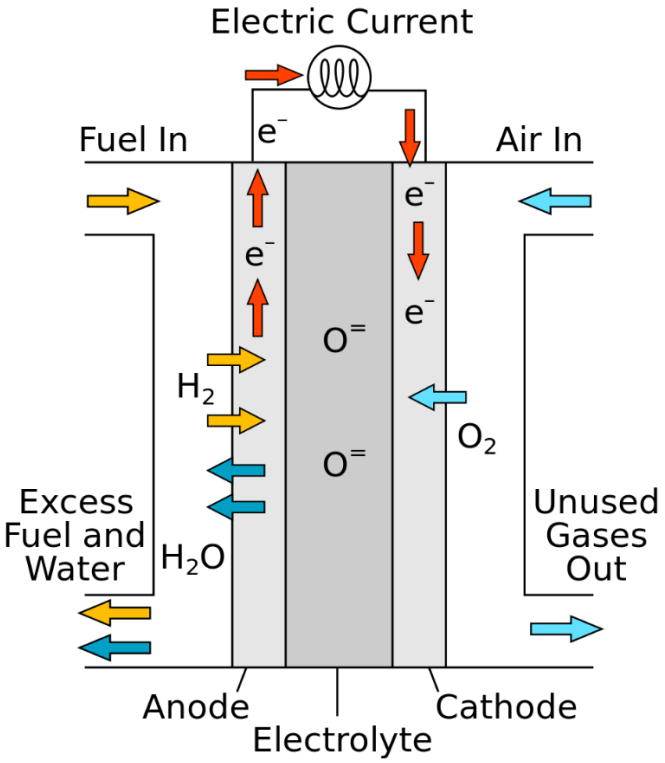

Figure 1.3 – Basic Fuel Cell Reactions.

Due to the ordered nature of the half reactions and the more direct conversion of energy, fuel cell systems can reach thermal efficiencies of over 60%. The electrical output of fuel cells is direct current due to the nature of the reactions and can either be rectified into alternating current to integrate into the existing grid infrastructure or can be directly wired to the computers within the data centers. This direct connection has significant efficiency implications and is discussed in the literature review.

There are several types of fuel cell machines that all operate on similar principles but with different specific chemistry. The most common fuel cell currently is a proton-exchange membrane (PEM) fuel cell. PEM fuel cells run on hydrogen gaseous fuel and facilitate the half reactions by transferring hydrogen ions (or protons) across the electrolyte. PEM fuel cells have the singular drawback of lack of fuel supply. Most hydrogen gas is produced from steam reformation of methane and is therefore carbon intensive. However, there is another type of fuel cell that does not have this issue. High temperature fuel cells are named as such due to the high temperatures at which the stack is kept while operating. These high temperatures allow for

internal and external reformation within the stack or balance of plant. This reformation process allows high temperature fuel cells to run on fuels other than gaseous hydrogen.

Solid oxide fuel cells (SOFC) are a specific type of high-temperature fuel cell which are named so due to the solid metal oxide (ceramic) electrolyte used to facilitate the transport of oxygen ions. SOFC systems can run on natural gas thanks to the reformation that occurs within the fuel cell. SOFC systems are the primary focus of the research in this dissertation since they present the unique opportunity of allowing a transition step from traditional grid supplied electricity to a completely carbon-neutral renewable hydrogen data center.

Natural gas is currently readily available in a piped grid system that covers most of the United States. The abundance of this fuel and its compatibility with SOFC systems could allow for on-site power generation at data centers. Additionally, in the future as natural gas is phased out the SOFC systems can operate on biogas or even pure hydrogen which future proofs the principal investment to install the SOFCs in the first place.

The implementation of SOFC systems has the added advantage of increased redundancy and robustness for the data center application. By installing an SOFC array at a data center, instead of using diesel backup generators, it is simply a case of installing n+1 fuel cell systems to provide power while keeping enough on-site natural gas storage for a 48 hour supply shortage. In this manner the reliability of power can be achieved without installing a full secondary power production system.

1.2.3 - Absorption Chillers

Assuming a successful implementation of SOFC systems at a data center for power production, a unique opportunity is created. The two primary needs of a server are power and cooling. To provide the cooling for data centers and considering the novel SOFC generators, a heat driven cooling system needs to be considered.

SOFC system operate at very high temperatures and therefore have a relatively large amount of waste heat which can still be valuable. To capture this otherwise wasted heat, waste heat recovery technologies

can be employed. Some of the options include bottoming heat engines like organic Rankine cycles or steam cycles. However, given the electrical and thermal requirements of the servers, a bottoming cycle which produces chilling is considered more applicable.

Absorption technology uses a thermodynamic cycle to produce chilling from heat. The thermodynamic cycle is shown in Figure 1.4 below.

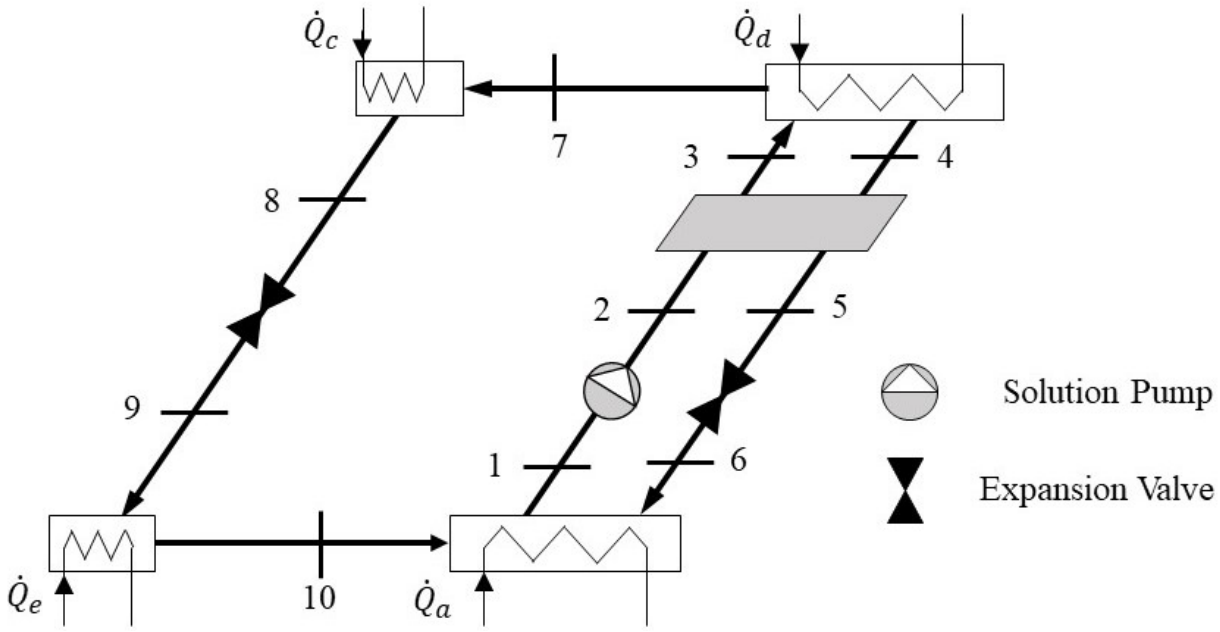

Figure 1.4 –Absorption Cycle.

The absorption cycle can be broken into two sections. As shown in Figure 1.4 on the left consisting of the condenser, expansion valve and the evaporator is the refrigerant section. On the right consisting of the absorber, pump, solution heat exchanger desorber and solution expansion valve is the solution section.

The refrigerant section mimics the traditional four component refrigeration cycle minus the compressor. The solution section acts as the thermodynamic compression process for the refrigerant which then provides cooling in the refrigerant section. The refrigerant is absorbed into a solution within the absorber from which it is pumped to a higher pressure in a liquid state. The high pressure liquid solution is then heated by the solution heat exchanger and the desorber. As the solution heats up, the refrigerant then evaporates out of

the solution and is released as a gas to the condenser, thus beginning the refrigerant section. The remaining solution is then cooled and returned to the lower pressure where it is then ready to re-absorb the refrigerant.

This cycle requires four thermal inputs/outputs to function. First, the heat source is used in the desorber, the highest temperature component, to evaporate the refrigerant. Second, a heat rejection medium is required to take heat from the condenser and the absorber which allow for the condensation of the refrigerant and the re-absorption of the refrigerant in the absorber. Lastly, heat is absorbed from the chilling medium into the evaporator and provides cooling to the chilling medium. All of these heat transfers are shown in Figure 1.4 as $\dot{Q}_a, \dot{Q}_c, \dot{Q}_d, \dot{Q}_e$.

By using waste heat to produce cooling, the integrated SOFC and absorption chiller system may provide the primary requirements of the servers an efficiency that without this synergistic integration would be impossible.

1.3 - Dissertation Organization

The unique synergistic combination of high-efficiency electricity and cooling produced by a thermally integrated SOFC, and absorption chiller has the potential to drastically reduce the carbon footprint of data centers around the world. This dissertation explores four different pillars to provide a wholistic perspective on the operation and feasibility of such a system as shown in Figure 1.5.

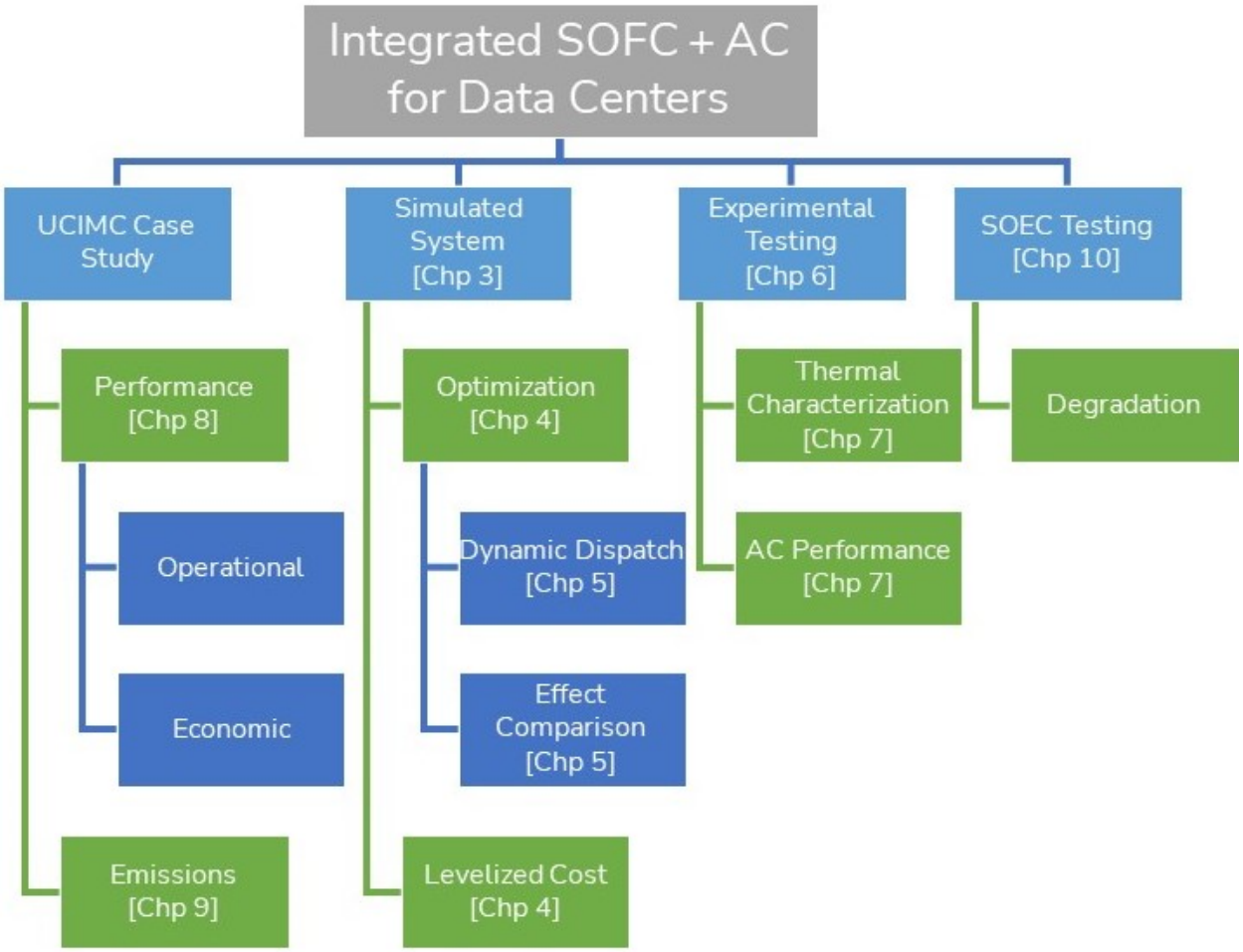

Figure 1.5 – Dissertation Organization.

To that end, this dissertation has been organized into the following chapters:

Chapter 2 performs a comprehensive literature review on integrated fuel cell systems with waste-heat-recovery systems and absorption chillers. The motivation for this research is also described

Chapter 3 outlines the modeling performed in the pursuit of designing and simulating a thermally integrated chilling system.

Chapter 4 explores the thermal optimization of the integrated SOFC and absorption chiller to minimize CO_2 and evaluate the economic performance in terms of LCOE and LCOU.

Chapter 5 applies the optimized thermally integrated SOFC and absorption chiller to a data center chilling demand profile to understand the transient operation of the system. Additionally, a dynamic

dispatch control strategy is proposed and evaluated for minimizing carbon output of an example data center. Lastly, three different chilling configurations are explored and compared for carbon reductions.

Chapter 6 outlines the experimental setup as it was constructed, the specifications of the core and supporting components, and the sizing of those components.

Chapter 7 examines the results of experimental testing done on the integrated test stand. Outlining the data collection and reduction systems as well as deciphering the takeaways from the absorption chiller's performance.

Chapter 8 describes a performance and economic analysis performed on an existing high-temperature fuel cell and absorption chiller system which is installed at UCIMC.

Chapter 9 continues the investigation of the UCIMC case study, outlining further analysis of the system's degradation. Additionally, it describes the emissions sampling equipment constructed and utilized for evaluating the carbon emissions of the cogeneration plant.

Chapter 10 describes a project which aims to utilize solid oxide technology for electrolysis. A test stand is constructed to perform experiments on SOEC button cells and study their degradation.

Chapter 11 wraps up discussion of the work performed.

Chapter 12 presents recommended continuation work that would further explore the concepts outlined in this dissertation.

Chapter 2 - Literature Review

2.1 - Thermally Integrated Fuel Cell Literature

The concept of an integrated fuel cell with a thermodynamic cycle is not unexplored in previous research, but that research does not include the specific scale or application of use in data centers. Despite this, it is useful to explore the prior art and learn from previous researchers' efforts. However, given the complexity of an integrated fuel cell with chiller and this system's interaction with the server racks, the breadth of a literature review must encompass several topics: integrated systems, small-scale (per-rack) fuel cells, and server dynamics. An understanding of these areas will provide serious support in moving the concept towards fruition.

Arguably the more important topic of investigation is that of the integrated system and looking at how systems have been constructed in the past, their benefits, drawbacks, and any other insightful information the research can provide. A study performed by Sevencan et al. (Sevencan et al., 2016) provides the most applicable background investigation: a study of combined cooling heat and power (CCHP) for a data center. The research presents a model of a molten carbonate fuel cell (MCFC) and a lithium bromide absorption chiller powering and cooling a data center.

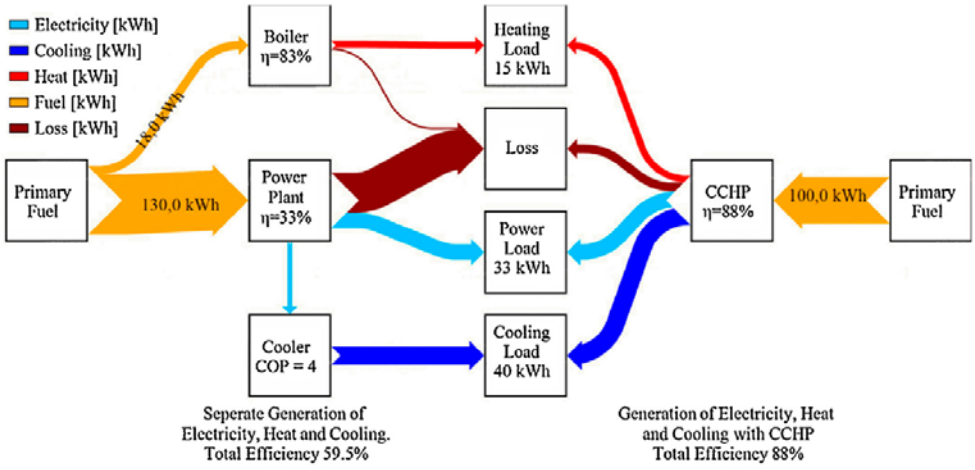

Figure 2.1 – Energy Distribution for Combined Cooling Heating and Power (CCHP). (Sevencan et al., 2016)

The analysis presents the benefits of localized power production in DC format, along with a standard Li-Br absorption cycle rejecting heat to a useful location, building heat. The study presents an overall efficiency of 88% for the CCHP system considering that all of the outputs from the system are utilized effectively, as shown in Figure 2.1. This improvement in efficiency allows for a €815,000 per year savings in operational cost. However, the study then continues on to indicate that the capital investment required for installing such a system is too large for significant payoff considering the lifetime of such a system, which is stated to be limited by the short stack lifetime of a MCFC. These lifetime issues present a serious challenge to MCFC technology, but the stack lifetime of a solid oxide fuel cell (SOFC) can be significantly longer than an MCFC which can allow for investment payoff in a reasonable amount of time. Given this, SOFC technology warrants more investigation for this application.

A similar study by Zhao et al. (Zhao et al., 2016) validates the concept of localized power generation for data centers by investigating a proton-exchange membrane fuel cell (PEMFC) installed within the frame of the server rack. This 10 kW fuel cell was experimentally shown to significantly improve the efficiency of the energy production for the server rack, as shown in Figure 2.2. Additionally, the investigation proved that the PEMFC had the ability to load follow effectively and maintain server operation even in erratic power draw patterns. This dynamic capability is shown in Figure 2.3 in a stair-stepping power output.

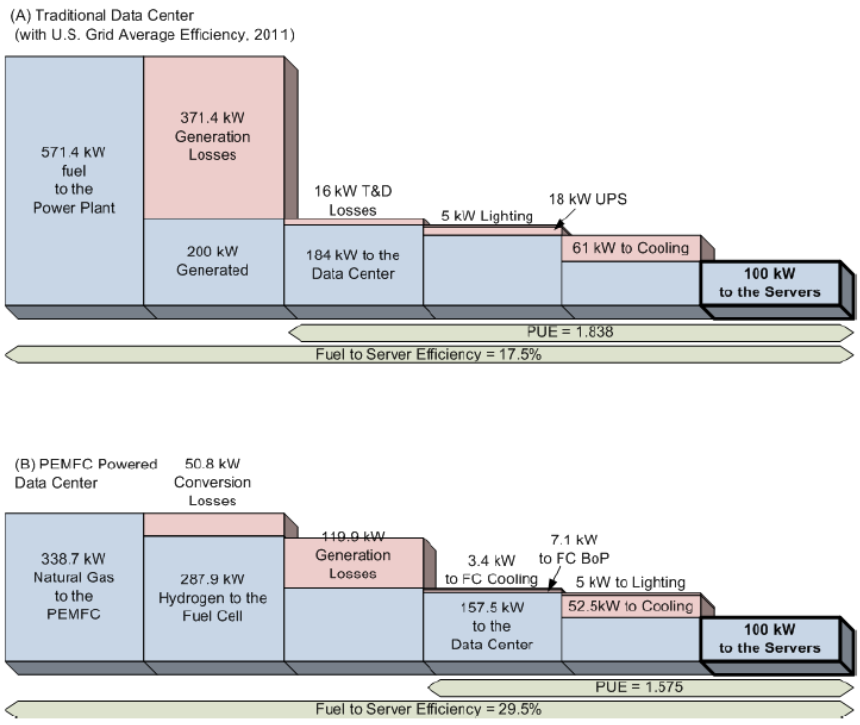

Figure 2.2 – In-Rack Fuel Cell Power Production Efficiency. (Zhao et al., 2016)

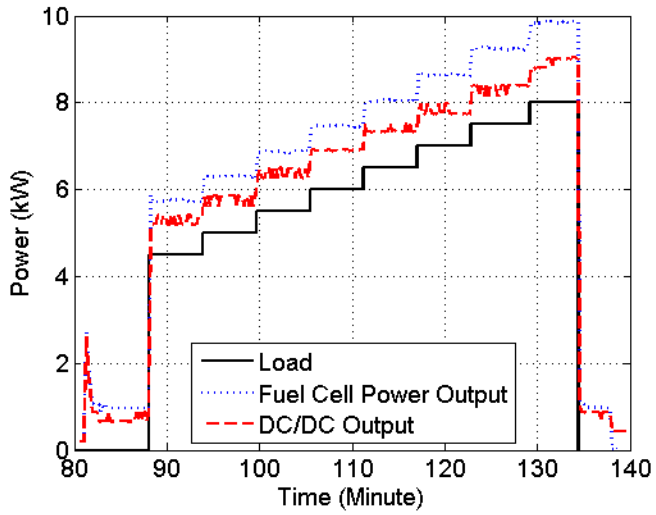

Figure 2.3 – Dynamic Capability of a PEMFC to Load Follow. (Zhao et al., 2016)

This study finds that operational costs can be reduced to $243.12-255.75 per rack per month compared to the baseline of $313.43 per rack per month, a maximum of 22% reduction in cost. This improvement can be expanded upon by utilizing the waste heat produced by the fuel cell. A study performed by Guizzi et al.

(Guizzi & Manno, 2012) indicates that the successful utilization of the waste heat from the fuel cell can make the operation cost reduction 47%. The investigated system is illustrated in Figure 2.4 featuring an external natural gas reforming process as well as a waste heat recovery circuit used for building heat.

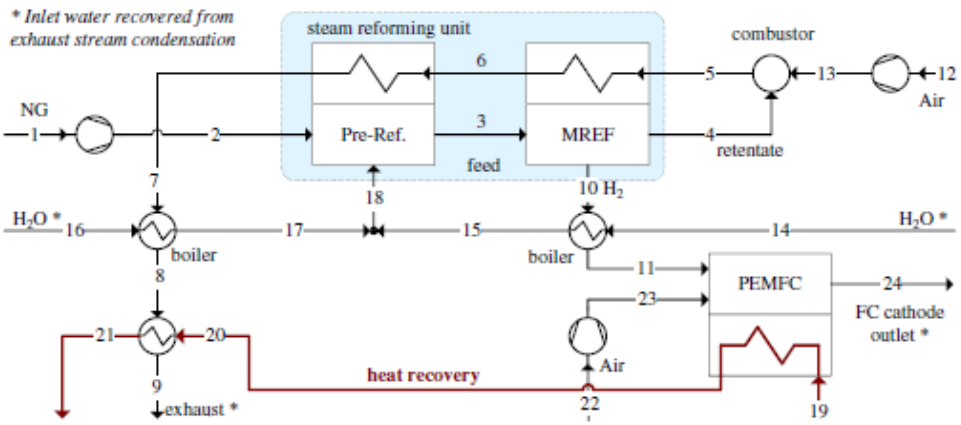

Figure 2.4 – System Schematic of PEMFC with Useful Waste Heat Recovery. (Guizzi & Manno, 2012).

This study similarly attributes much of the efficiency gain to the conversion and transmission losses that standard grid infrastructure encounter. The investigated configuration for use with a data center is presented in Figure 2.5.

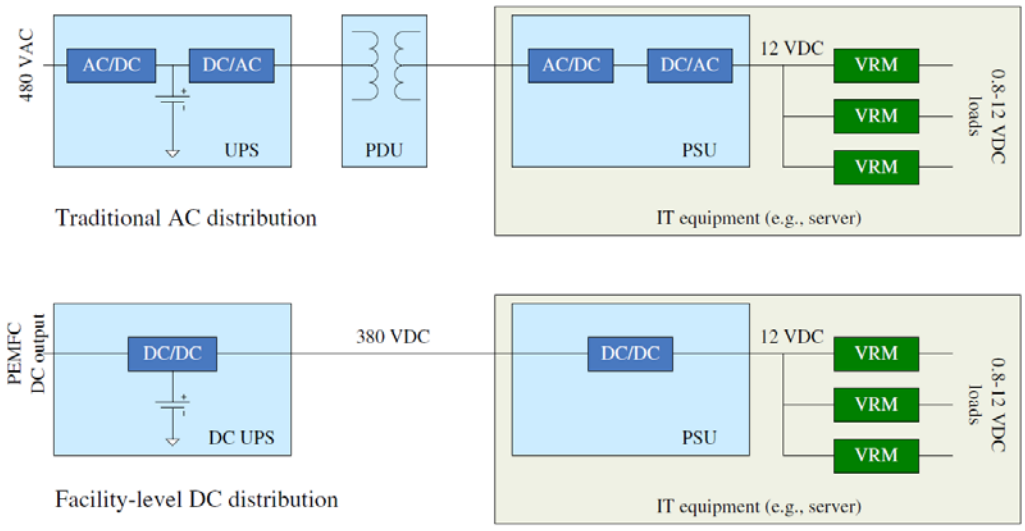

Figure 2.5 – Energy Conversion Comparison (Guizzi & Manno, 2012).

While the PEMFC is a promising option, the challenge of such a system is that it requires pure hydrogen to operate efficiently. Since there is not a hydrogen infrastructure in place yet, this study also suggests the use of an SOFC for this application since it can run off natural gas, which does have an existing infrastructure.

SOFC technology is also a widely investigated topic, with some research available on CCHP systems. A study performed by Choudhury et al. (Choudhury et al., 2013) presents a SOFC driven CCHP system, the system configuration is shown in Figure 2.6, which includes a direct product turbine, absorption chiller and bottoming turbine. This system corroborates the efficiency gains reported by Zhao et al., indicating that a CCHP system can achieve a 22% system improvement. The study also elaborates that the system can achieve 80% system efficiency at optimal conditions.

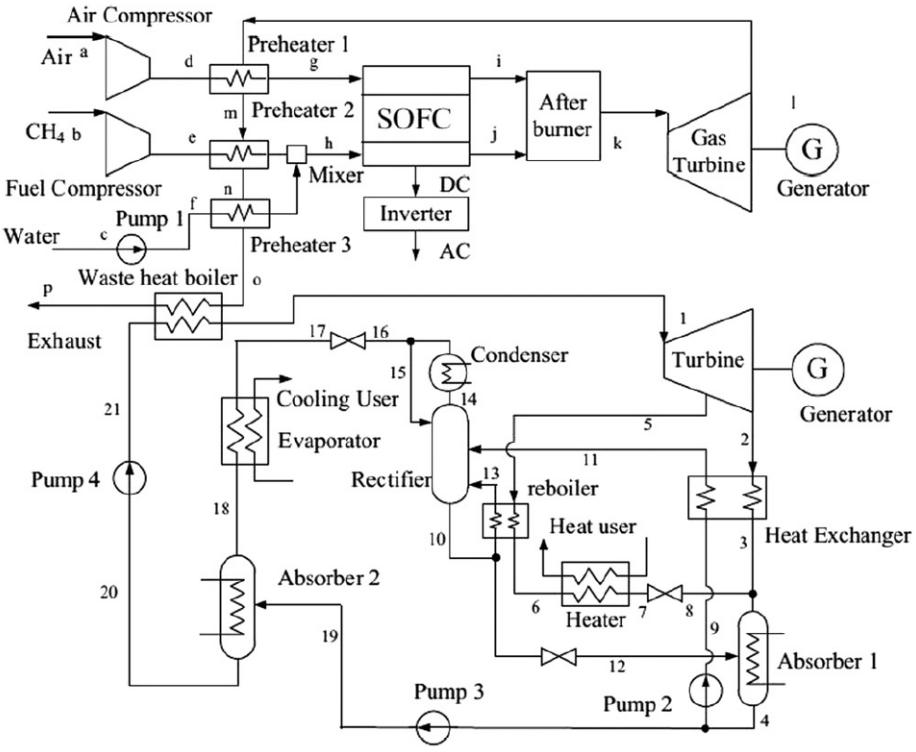

Figure 2.6 – Integrated SOFC with Waste Heat Recovery Systems. (Choudhury et al., 2013)

A similar system integration is studied by Tian et al. (Tian et al., 2018a) where a SOFC topping cycle is paired with two bottoming cycles, an organic Rankine cycle (ORC) and an absorption chiller (AC). The

system configuration is shown in Figure 2.7, and it should be noted that the ORC working fluid is Benzene, a medium temperature refrigerant.

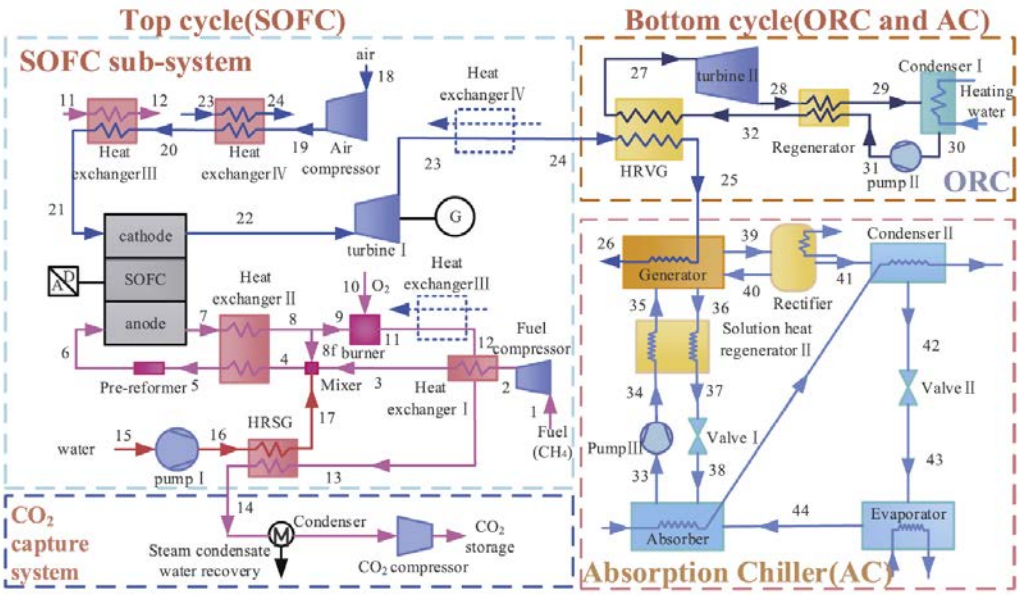

Figure 2.7 – Integrated SOFC with ORC and AC. (Tian et al., 2018a)

The integrated system is modeled with the following assumptions:

(1) The system reaches steady state.

(2) The air consists of 79% N_2 and 21% O_2.

(3) The fuel is CH_4, and it is ideal gas.

(4) The pressure and temperature of SOFC are uniform.

(5) The pressure and temperature of fuel and air at the exit of the SOFC channels are constant and equal to the SOFC operation pressure and temperature.

(6) Radiation heat transfer between gas channels and solid structure is negligible.

(7) Contact resistances are negligible.

(8) Heat losses towards the environment are negligible.

These are fair assumptions for a standard thermodynamic model, and the results produced are indicative of a steady state power plant. The system achieves a net electrical efficiency of 52.83%, an exergetic

efficiency of 59.95%, and a trigeneration efficiency of 74.28%. These efficiencies corroborate much of what has been previously described by fuel cells and their power production efficiencies. The study further investigates effects of changes to the inlet temperature and steam-to-carbon ratio on the stated efficiencies. Electrical efficiency is maximized at an inlet temperature of 550 degrees Celsius, while the exergetic efficiency is maximized at 635 degrees Celsius. These efficiency trends are indicated in Figure 2.8. In contrast, the authors note that the steam-to-carbon ration has little to no effect on system performance. It is important to understand the impact of these adjustments on operational efficiencies such that a new system is designed to achieve its maximum performance at the desired operational points.

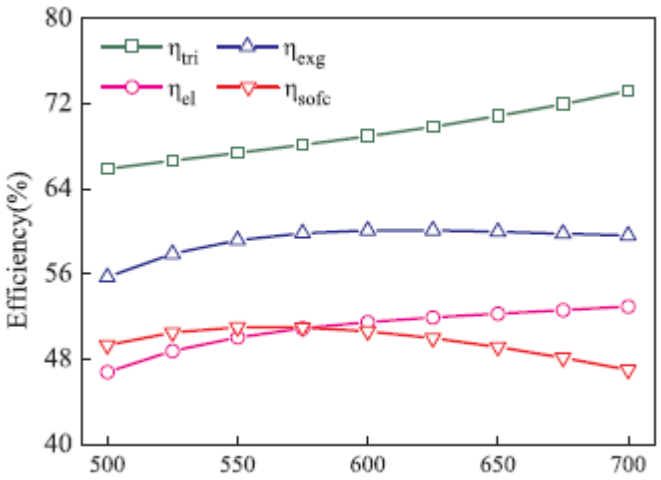

Figure 2.8 – Effect of Inlet Temperature on System Efficiencies. (Tian et al., 2018a)

The study also includes a breakdown of exergy destruction on a component basis. Understanding exergy destruction in each of the components can highlight the areas within a cycle where improvement would have the most effect. Tian et al. conclude that in the system modeled, the SOFC presents the largest exergy destruction at 24.42% relative exergy destruction. The complete component breakdown is shown in Figure 2.9.

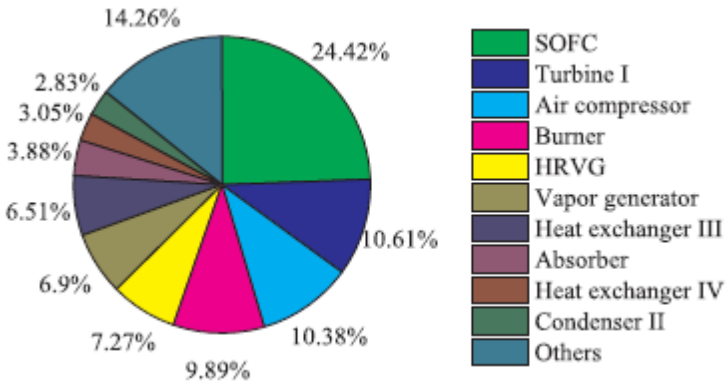

Figure 2.9 – Component Exergy Accounting. (Tian et al., 2018a)

A similar exergy accounting is performed in a study by Chitsaz et al. (Chitsaz et al., 2015), but there are some discrepancies between the reported accountings. While the two systems are admittedly not identical, Chitsaz et al. indicates that the primary waste heat recovery heat exchanger creates the largest relative exergy destruction: 32%. The accounting used here is presented in Figure 2.10.

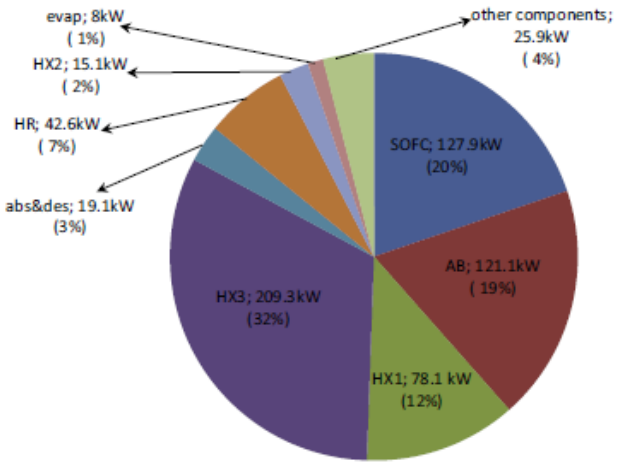

Figure 2.10 – Component Exergy Accounting. (Chitsaz et al., 2015)

The comparison creates two take-away points that should be reflected upon in the design of any integrated system. The first is that the fuel utilization efficiency of the SOFC has the largest impact on exergy destruction within an integrated system. Tian et al. report that their model predicts a fuel utilization of 65% while Chitsaz et al. assume a fuel utilization of 85%. This discrepancy helps to explain the change

in relative exergy destruction between the two studies. Secondly, the waste heat in the study by Chitsaz et al. is directly used in the desorber of an absorption cycle. This configuration has an inherent large temperature gradient across that heat exchanger. The second law of thermodynamics states that irreversibilities are proportional to temperature gradient, so the increased exergy destruction in the heat exchanger is not surprising. Tian et al. utilize a higher temperature heat exchanger prior to the ORC turbine to minimize the temperature gradient and the exergy destruction is reportedly reduced, 6.51% versus 32%. This architecture can be important to future integrated system designs. The layout of waste heat recovery should include the necessary architecture to minimize the exergy destruction within the cycle.

Given the significant research background into integrated systems, identifying a relevant gap in the knowledge base into which to contribute can be challenging. However, the lack of experimental investigation of combined systems integrated with data centers on a distributed level provides the primary motivation for this dissertation. It should also be noted that the continuous investigation of technologies that are being developed will be included in the research performed. The ultimate goal of this research is to develop a novel system that meets the power production and cooling requirements of a data center on a distributed level.

2.2 - Fuel Cell Economic Performance Literature

To curb the effects of climate change, the deployment of high-efficiency, distributed-generation power plants has become prevalent within the state of California. Large scale, megawatt-class fuel cells are one of the technologies selected for the on-site generation of power. Fuel cell systems are high-efficiency thermoelectric engines that operate on an array of fuels and can provide electricity at thermal efficiencies of up to 65%. These large fuel cells can also operate at high temperature with the opportunity to capture and use the waste heat to meet secondary energy demands.

Historically, fuel cells have faced challenges in adoption due to high capital investment costs (Kalina, 2016). To stimulate their adoption, several government-sponsored programs have been introduced financial incentives to drive volume and reduce the installed cost. Once deployed, a reduction in utility cost

associated with the high fuel-to-electricity efficiency combined with the opportunity to capture and use exhaust heat to displace other utility costs suggest that a fuel cell power plant may provide a positive financial return on investment over the period of operation (Alanne et al., 2006; Huang et al., 2011). The economic performance of such a fuel cell installation depends on the cost of the fuel to power the fuel cell and the competing cost of utility provided electricity. Generally, the deployment of fuel cells is most successful in areas of historically high utility electricity prices (Kalina, 2017). In California, over 300 MW have been deployed, more of which are operating on wheeled biogas (Curtin et al., 2017). Installations include a variety of customer sites (e.g., hotels, hospitals, research and university campuses, and data centers), all of which continue to demonstrate that on-site, base-load electrical power production of a stationary fuel cell can successfully displace more emission intensive grid electricity and provide other on-site value added attributes.

Cogeneration from high-temperature fuel cells is an especially attractive attribute to further increase the overall utilization of the fuel (Alcaide et al., 2006; Appleby, n.d.; Raj et al., 2011) and thereby improve the economic performance by producing, in addition to electricity, hot water, steam, or chilled water from the high-temperature heat available in the fuel cell exhaust (Alcaide et al., 2006).

The successful commercialization of fuel cells is directly related to the operational and economic performance of fuel cell installations (Penner et al., 1995). Several studies suggest that the principal factors in the economic performance are the capital investment and the fuel cost (Khani et al., 2016; Lipman et al., 2004; Mehmeti et al., 2018; Shamoushaki et al., 2017). While adjustments to the principal investment will change over time, the high sensitivity of economic performance to fuel cost can suggest operational strategies to minimize fuel usage. Other studies address fuel cell installations with CCHP applications. None, however, investigate the operational and economic performance from an existing commercial operation due to the challenges of (1) acquiring the detailed requisite data, and (2) unraveling the complex impacts of competing and convoluted utility electric rates and demand charges.

Using detailed fuel cell plant performance data from an operating system, and a detailed economic analysis from actual gas and electric utilities, this study addresses the operational and economic performance of an established HTFC paired with an absorption chiller.

2.3 - Dissertation Objectives

Following the review of solid oxide fuel cell thermal integration literature, the scope of research to be performed can be outlined. The objectives of this dissertation aim to fill the gap in the literature where no thermal integration has been applied to the data center requirements while fully exploiting the synergistic operation of a solid oxide fuel cell and absorption chiller.

1. Leverage existing research and knowledge about the systems toward developing a novel understanding of thermal integration.
2. Use thermophysical simulation to evaluate different thermal integration configurations to determine which can successfully provide the required power and cooling to a data center.
3. Optimize the operation of the thermally integrated SOFC and absorption chiller to minimize carbon emissions and levelized costs.
4. Understand how dynamic control of the optimized thermally integrated system can allow for dynamic dispatch to further reduce carbon emissions of data centers.
5. Develop an experimental platform to explore the operation of an integrated system.
6. Verify the thermophysical integrated model against experimental test results.
7. Evaluate an existing cogeneration case study for the thermodynamic and economic performance to further verify and support the presented thermophysical model.
8. Explore how solid-oxide technology can be utilized to produce hydrogen to further mitigate carbon emissions.

Chapter 3 - Modeling

3.1 - Server Level SOFC and Chiller

To evaluate the effectiveness of a thermally integrated AC with an SOFC for the application of distributed power and cooling in a data center, a mathematical model was developed in Engineering Equation Solver (EES) and MATLAB. The model consists of three sub models: a high-level thermodynamic model of an SOFC, a thermal loading and process airflow model for the servers, and a floating state point model of a Lithium Bromide (LiBr) AC. A full system schematic is shown for reference and model interactions in Figure 3.1. The SOFC model predicts exhaust stream temperature and flow rates based on server electrical demand and operating characteristics. The server model predicts the process airflow temperatures before and after the thermal load of the servers. The AC model predicts cycle performance given the heat source temperature and flow rate, the process air (to be chilled), and the heat sink temperature (often a cooling tower).

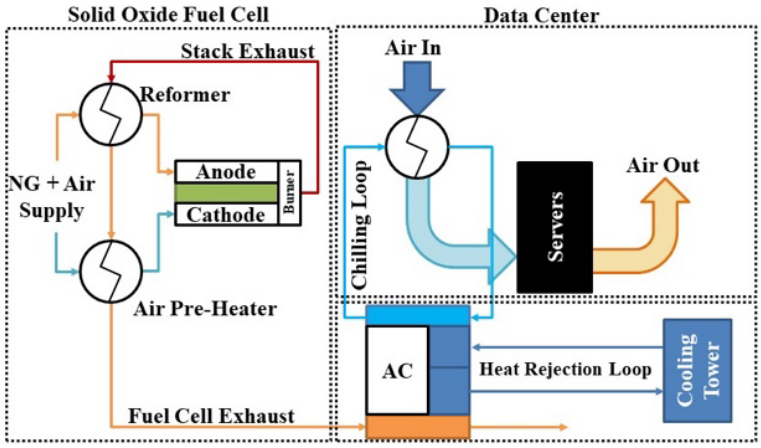

Figure 3.1 - SOFC, Data Center, and AC Model Configuration.

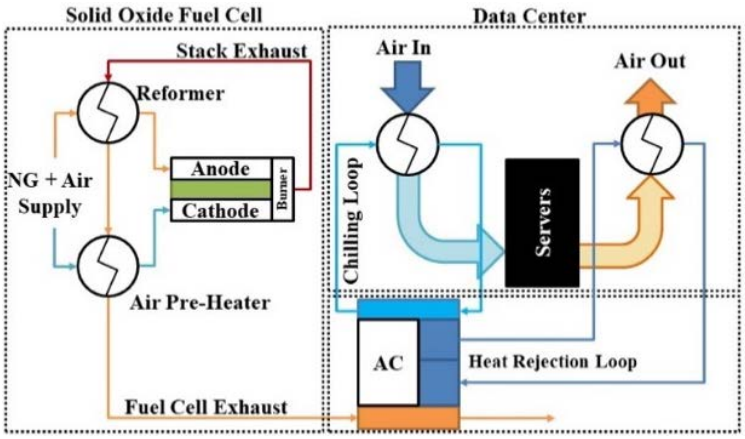

Figure 3.2 – Alternate Heat Rejection Configuration.

3.1.1 - Fuel Cell Model

The SOFC model consists of three components, the stack model, the reformer model, and the air pre-heater model. A fuel cell "stack" is comprised of a number of cells, each with an electrolyte and two electrodes, connected in electrical series by interconnects that serve as flow channels that make up the functional core of a fuel cell. Provision of fuel to the anode electrodes and oxidant to the cathode electrodes facilitates the electrochemical reactions, ion and electron transport that allow the fuel cell to produce electricity. The fuel cell is assumed to operate at steady state, which allows for direct determination of temperatures, pressures, and energy rates. While servers are highly dynamic machines, it should be noted that in a data center, with up to 21 servers per rack and twenty-two server racks in a row, the power and thermal loads are quite steady. The stack model is designed to be scalable, with no intrinsic physical properties to limit power output scale. This allows for several modeling simplifications when predicting the performance of the fuel cell. The fuel cell system is assumed to operate on natural gas and air, as expected for an SOFC installation at a data center. The SOFC model inputs are a fuel cell power output of 15 kW (14.25 BTU/s), a fuel utilization of 0.85 and an assumed cell voltage of 0.8 V. The power production is equivalent to a typical single server rack's maximum power draw. The fuel utilization is based on literature values. The cell voltage is assumed to be 0.8 V based upon existing system typical measurements. Note that the reformate inlet is assumed to be the product of complete reformation. The stack model uses the

inputs listed above to determine the necessary flow rates into the fuel cell to produce the desired amount of power. The current required to produce the desired power at the stack cell voltage is calculated, where P is the stack power, I is the stack current, and V is the cell voltage.

$$P_{fc} = I_{stack} * V_{cell} \tag{3-1}$$

Then, the current is used to determine the mole transport rate across the electrolyte. In this case, the number of electrons transported is four for every mole of oxygen reacted. This reaction is characteristic of SOFC and any other oxygen ion permeable fuel cell electrolytes. Note that F is the Faraday constant and n is the mols per second of oxygen reacted.

$$I_{stack} = 4 * F * \dot{n}_{O_2,react} \tag{3-2}$$

Now that the molar flow rate of oxygen is known, the molar flow rate of the incoming fuel can be determined. The fuel utilization input and the general reaction balance allows us to calculate the incoming reformate flow rate knowing the hydrogen and carbon dioxide concentrations at the inlet to the anode. Note that U is the utilization factor, n is the mols per second, and X is the concentration of the specied in the inlet flow.

$$U_f = \frac{\dot{n}_{H_2\,react}}{\dot{n}_{H_2\,in}} \; ; \; \dot{n}_{H_2\,in} = \frac{X_{H_2\,in}}{X_{CO_2}\,in} * \; \dot{n}_{CO_2\,in} \tag{3-3}$$

Given the reformate inlet flow rate and concentration, calculate the oxidizer inlet flow rate. Typically, SOFCs are run with an air-fuel ratio of around 10. The air inlet flow rate is controlled to maintain a constant stack temperature and thus protect the internals of the SOFC. Knowing the moles of oxygen and hydrogen reacted and applying the reaction stoichiometry, the inlets and outlet flow rates from the stack are calculated. These outputs are presented in Table 3.1.

Table 3.1– Calculated SOFC Flows.

Flow	*Molar Flow Rate [kmol/s]*	*Mass Flow Rate [kg/s] (lbm/s)*	*Concentration [-]*
Hydrogen In	1.143 e -4	2.305 e -4 (1.047 e -4)	0.15
Carbon Dioxide In	2.968 e -5	1.306 e -3 (0.594 e -3)	0.85
Oxygen In	1.008 e -4	3.226 e -3 (1.466 e -3)	0.21
Nitrogen In	4.335 e -4	1.214 e -2 (0.552 e -2)	0.79
Oxygen Reacted	4.858 e -5	-	-
Hydrogen Reacted	9.717 e -5	-	-
Hydrogen Out	1.715 e -5	3.457 e -5 (1.571 e -5)	0.0119
Carbon Dioxide Out	2.968 e -5	1.306 e -3 (0.594 e -3)	0.4227
Steam Out	9.717 e -5	1.714 e -3 (0.779 e -3)	0.5661
Oxygen Out	5.224 e -5	1.671 e -3 (0.759 e -3)	0.1211
Nitrogen Out	4.335 e -4	1.214 e -2 (0.552 e -2)	0.8789

Water formation in a fuel cell is exothermic and is the primary producer of thermal energy in the SOFC. For simplification, the heat produced inside the reacting cell is approximated using the lower heating value (LHV) of the incoming reformate. Note that P is the power produced by the cell, LHV is the lower heating value of the fuel, m is the mass flow rate, and h is the specific enthalpy in kJ/kg.

$$P_{fc} - LHV_{H_2}\dot{m}_{H_2} = \sum \dot{m}_{out}h_{out} - \sum \dot{m}_{in}h_{in} \tag{3-4}$$

Using Equation 3-4, it is possible to determine the outlet temperature of the exhaust gasses as they leave the stack. This outlet temperature includes post-stack combustion process to eliminate the remaining hydrogen from the exhaust. The reforming process is assumed to occur outside of the stack in an external reformer that is powered by the heat from the stack's exhaust stream which can be modeled as a heat exchanger with the reforming kinetics included. Two primary reformation reactions were considered: steam reformation and water-gas shift.

$$CH_4 + H_2O \rightarrow CO + 3\,H_2 \tag{3-5}$$

$$CO + H_2O \rightarrow CO_2 + H_2 \tag{3-6}$$

$$CH_4 + 2\,H_2O + 165\,\frac{kJ}{kmol} \rightarrow CO_2 + 4\,H_2 \tag{3-7}$$

Based upon the incoming fuel flow rates and the enthalpy of reaction listed, the heat consumed by the reforming reactions is calculated. An effectiveness heat exchanger model calculates the heat transfer between the stack exhaust and the incoming reformate. The reformation heat exchanger was assumed to

have 0.35 effectiveness based on existing systems. Following the reformer, the exhaust stream is used to preheat the incoming oxidant stream. The effectiveness of this heat exchanger is assumed to be 0.45 based on existing systems. The output values in Table 3.2 are utilized as the heat source for the AC and the power production is used by the server model. The power produced by the fuel cell relative to the energy available from the supplied fuel is calculated to be 0.654 which is typical, if not a bit optimistic, for such an SOFC system.

Table 3.2 – SOFC Plant Processes and Temperatures.

Process	*Heat Transfer Rate [kW] (BTU/s)*	*Temps In [°C] (°F)*	*Temps Out [°C] (°F)*
External Reformer	5.094 (4.83)	Exhaust – 897.9 (1648.2) Fuel – 25.0 (77.0)	Exhaust – 687.3 (1269.1) Fuel – 243.6 (470.48)
Air Preheater	4.235 (4.02)	Exhaust – 687.3 (1269.1) Air – 25.0 (77.0)	Exhaust – 472.0 (881.6) Air – 292.8 (559.0)

3.1.2 - Single Effect Absorption Chiller Model

For the purpose of evaluating the chilling capabilities of the distributed case, a small-scale single effect LiBr AC was selected for modeling. The single effect system is comprised of eight components: a solution pump, an internal heat exchanger (IHX), a desorber, a condenser, a refrigerant expansion valve, a solution expansion valve, an evaporator and an absorber. The single-effect AC is shown in Figure 3.3.

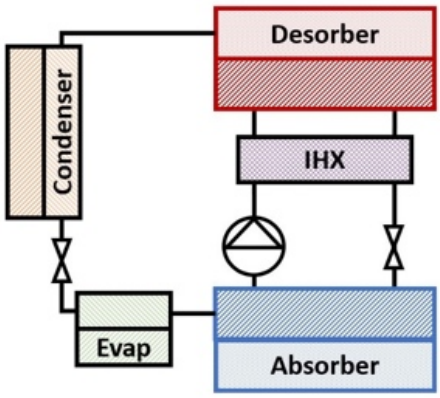

Figure 3.3 – Single-Effect Absorption Chiller Process Diagram.

Solution Pump

An incompressible pumping model was used to calculate the enthalpy of the solution at the outlet of the solution pump using a pump efficiency of 0.65 based on an assumed saturated liquid inlet state from the absorber, where h is the specific enthalpy, P is the pressure, V is the suction volume, and eta is the efficiency of the pump.

$$\Delta h_{sol} = \frac{\Delta P * V_{suc}}{\eta_{pump}} \quad (3\text{-}8)$$

Internal Heat Exchanger (IHX)

An assumed effectiveness analysis was used to simulate the heat transfer within the IHX. The pump outlet and the assumed saturated condition of the desorber, along with the assumed effectiveness of the heat exchanger allow the outlet states of the IHX to be determined.

Desorber

The AC desorber was modeled using an effectiveness analysis from a preset desorber operating pressure. The solution saturation temperature is calculated using an assumed concentration obtained from an existing small-scale AC specification. The desorber heat transfer rate, Q, is calculated using the effectiveness of the heat exchanger, epsilon, the mass flow rate of the exhaust, m, and the specific enthalpies of the exhaust, h, at various conditions.

$$Q_{des} = \epsilon_{des}\dot{m}_{exh}\left(h_{exh} - h_{exh}|_{T_{sat}}\right) \quad (3\text{-}9)$$

Using the desorber heat input from the exhaust gas and the enthalpy of vaporization of the incoming solution, the refrigerant state can be calculated. The mass flow rate of the boiled refrigerant is calculated via mass balance.

$$Q_{des} = \dot{m}_{sol,out}h_{sol,out} + \dot{m}_{ref}h_{ref} - \dot{m}_{sol,in}h_{sol,in} \quad (3\text{-}10)$$

Condenser

The refrigerant condenser uses the refrigerant outlet state from the desorber model and predicts the outlet state using an effectiveness analysis. The condenser is cooled using various sources and the condenser is either cooled in series with the absorber or in parallel. The configuration is determined by the medium with which is it used: parallel for water from cooling tower, series for server process air; discussed later.

Expansion Valves

The refrigerant expansion valve is simulated using a pure-fluid constant enthalpy process. The solution expansion valve is modeled using the Sorption Systems Consortium (SSC) flash routine which predicts temperature, quality, liquid and vapor enthalpies given the pressure drop.

Evaporator

The refrigerant evaporator is modeled using a pinch point analysis. The server rack's process airflow is considered to be supplied by ambient conditions and thus the evaporation pressure is determined by the ambient temperature. An assumed superheating amount for the refrigerant is introduced to calculate the outlet stat point.

Absorber

The absorber is modeled using the strong solution and evaporated refrigerant state points as well as the inlet to the pump.

$$Q_{abs} = \dot{m}_{sol,out} h_{sol,out} - \dot{m}_{ref} h_{ref} - \dot{m}_{sol,in} h_{sol,in} \quad (3\text{-}11)$$

Based on the convergence of the AC model, the performance of the cycle when paired with the fuel cell heat source can be evaluated. The performance characteristics are presented in Table 3.3. It is apparent that the cooling capacity of the AC system is normal but less than the expected cooling load.

Table 3.3– Calculated AC Model Performance.

Output	*Value(s)*
Heat Recovered	7.453 kW (7.08 BTU/s)
Heat Rejected	13.314 kW (12.68 BTU/s)
Cooling Achieved	5.089 kW (4.83 BTU/s)
Pump Power	0.0086 kW (.0081 BTU/s)
COP	0.773

3.1.3 - Server Heat Production Model

The server heat production model simulates the rise in temperature of the process airflow across the server rack. Airflow is assumed to be 254 m^3/hr (150 CFM) of air for every kilowatt of energy consumed by the servers. A server conversion efficiency of 0.98 was used to represent the complete conversion minus a small amount of heat losses due to conduction. Based on this heating load, the process air flow rate and cooling available from the AC, the temperature profile for the process air was simulated. The temperature rises and heat transfer rates are shown in Table 3.4.

Table 3.4 – Server Airflow Process.

Process	*Heat Transfer Rate*	*Temp Change [Δ°C]*	*Inlet Temp [°C]*	*Outlet Temp [°C]*
Chilling by AC	5.089 kW	4.54	25.0	20.46
Server Heating Load	14.70 kW	11.66	20.46	32.12

3.1.4 - Server Level Results

Evaluating the primary results from the integrated model, it is apparent that the small-scale single-effect AC system will not provide enough cooling to the servers to fully offset the heating load. The SOFC is operating at an efficiency of 0.654, which indicates that the power output of the fuel cell is roughly twice that of the thermal output. Since the exhaust stream leaves the fuel cell stack at 897 °C (1646 °F), the potential for heat recovery is significant. However, the reforming and air-heating processes lower this exhaust temperature to 472 °C (881 °F) and are required for the operation of the fuel cell. These processes limit the recoverable amount of energy from the exhaust to 7.4 kW (7.03 BTU/s).

Given the AC system's performance and the heating load expected of a single server rack, it is impossible to create a fully offset closed loop cooling system using the waste heat of an SOFC in this configuration. However, by assuming a fuel utilization factor of 0.85, the amount of fuel that is thermally oxidized following the stack is limited. A lower fuel utilization factor increases the available waste heat but can overheat the fuel cell and damage internal systems. To compensate, a higher air-fuel ratio would provide a higher flow through the fuel cell and a cooler stack temperature.

Figure 4a illustrates that with decreased fuel utilization, the available chilling from the AC increases. However, the electricity produced by the SOFC is a larger component of the system efficiency so decreasing the efficiency of electricity production lowers the overall system efficiency. Figure 3.5 shows that while the system efficiency changes less than the fuel cell efficiency due to the AC heat recovery shown in Figure 3.4. Steps should be taken in the future to optimize the fuel utilization of the SOFC to produce the desired AC cooling capacity, while maximizing SOFC efficiency.

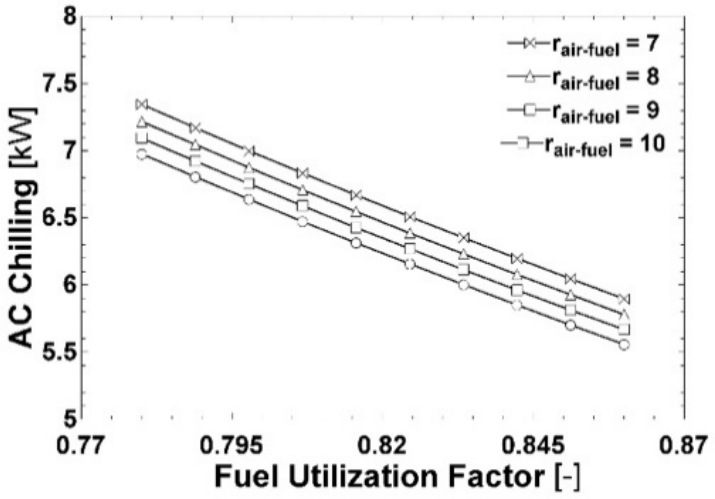

Figure 3.4 – Achievable AC Chilling with various Fuel Utilization Factors and Air-Fuel Ratios.

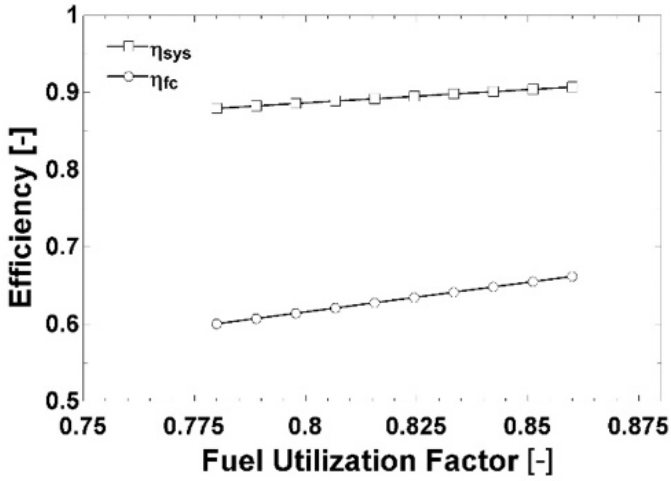

Figure 3.5 – Fuel Cell and System Efficiency with different Fuel Utilization Factors.

The second point of discussion from the analysis performed is regarding possible alternate configurations that could further improve the practically of such a system installation. The heat rejection temperature of the AC is above the server process return air. The large flow rate of the process server air presents the possibility of being a feasible heat rejection medium. Based on the configuration in Figure 3.2, it is possible to eliminate the cooling tower hardware, lowering system cost. The condensing temperature of 40.1 °C (104.2 °F) and the absorber saturation temperature of 45.4 °C (113.7 °F) can be rejected to the

return process air from the servers. The temperatures are listed in Table 3.5. The integration of an AC with an SOFC and the server air stream can produce a system efficiency of up to 0.89.

Table 3.5 – Alternate Heat Rejection Processes.

Heat Source	*Heat Transfer Rate [kW] (BTU/s)*	*Temp Change [Δ°C] (Δ°F)*	*Inlet Temp [°C] (°F)*	*Outlet Temp [°C] (°F)*
Condenser	6.025 (5.72)	4.77 (8.5)	32.12 (89.7)	36.89 (98.2)
Absorber	7.289 (6.92)	5.78 (10.4)	36.89 (98.2)	42.67 (108.6)

3.2 - Double Effect Absorption Chiller Model

In reviewing the performance of the single-effect rack scale absorption chiller system detailed above, it is evident that such a system does not accomplish the goal of providing adequate chilling to offset the thermal load of the servers. However, absorption technology is able to scale up its performance by adding increased levels of desorption in a second effect stage. The double-effect parallel flow absorption cycle is shown in Figure 3.6.

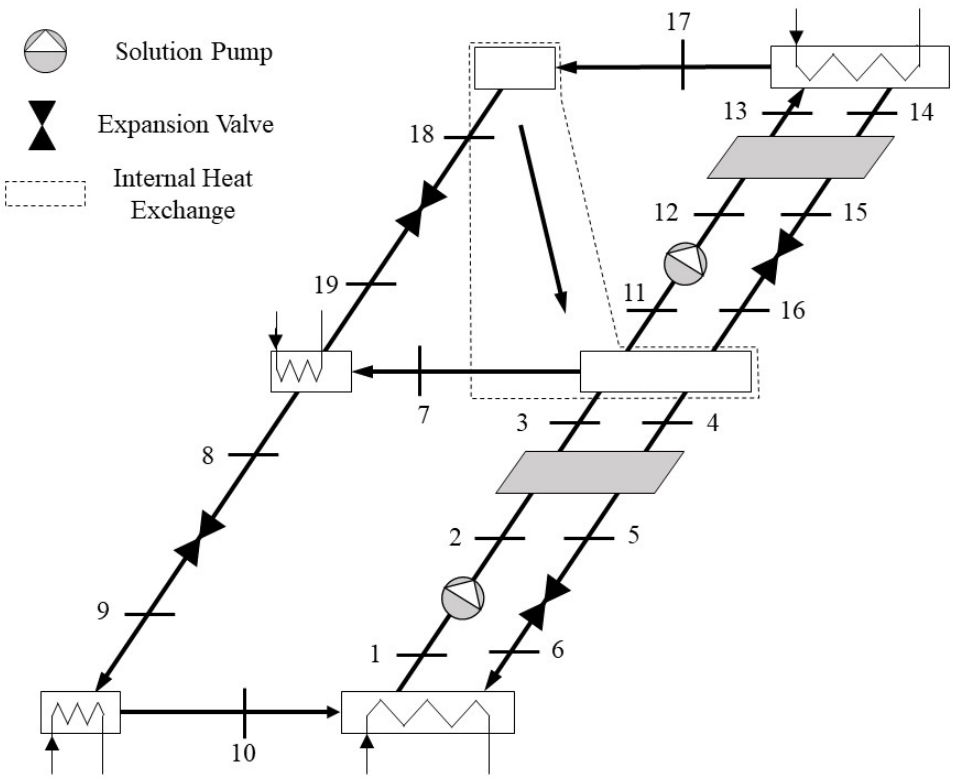

Figure 3.6 – Double Effect Parallel Flow Absorption Cycle.

Notice how the original single-effect cycle is shown in the lower half of the schematic, but a second tier of desorption is added on top. This second effect facilitates more evaporation of the refrigerant from solution in the second desorber. By doing so, there is more refrigerant mass flow at state point 9 entering the evaporator which allows for more chilling capacity. The increase in efficiency stems from the internal heat transfer depicted between the second condenser and the first desorber. This internal staging is accomplished by having the second desorber at a higher temperature and pressure, allowing the second condenser to pass heat down to the lower temperature desorber.

Double-effect absorption machines typically operate at a COP of around 1.1-1.2 compared to the 0.7 of a single-effect machine. This section will detail the model constructed to predict the performance of a double-effect absorption chiller when integrated with a fuel cell system.

3.2.1 - Li-Br vs. Ammonia

When considering double effect absorption technology, there are two primary working fluid options: aqueous Lithium Bromide (Li-Br) or water and ammonia. Each working fluid option has certain advantages and disadvantages in their operation but maintain similar performance characteristics.

Water ammonia systems use water as the solution base and ammonia as the working refrigerant. This means that ammonia is evaporated in the desorber and expanded which enables chilling at temperatures below freezing. However, since both ammonia and water are independently liquid, evaporation within the desorber often contains some fraction of water, which could freeze and damage the system. To protect against this, an additional component, a rectifier, is added after each desorber which further separates the ammonia and water. The main drawback to operating a system on water and ammonia is the toxicity of the ammonia within the system.

Aqueous Li-Br absorption chillers operate with water as the working refrigerant and Li-Br salts as the solution base. Li-Br systems do not require rectification since it is impossible for Li-Br to evaporate at the temperatures experience by the system. However, since water is the working refrigerant, chilling is limited to temperatures above 0 °C (32 °F). The other drawback to Li-Br systems is that at certain temperatures and concentrations the Li-Br in aqueous solution can come out of solution and crystalize. This crystallization can damage the internal components of the chiller so operational protection is important.

For the purpose of providing chilling to servers, since sub-zero chilling temperatures are not necessary, and the challenges associated with ammonia's toxicity make Li-Br systems the principal choice.

Property Characterization

The thermodynamic properties of aqueous Lithium Bromide (Li-Br) are well documented and are available in lookup table format in internal processes of Engineering Equation Solver (EES). However, to meet the goal of integrating a thermodynamic chiller model with the fuel cell model, it was important to make these thermodynamic values available in MATLAB. To meet this demand, a comprehensive set of

lookup tables was created for referencing. The properties indexed included: specific enthalpy, specific entropy, saturation temperature/pressures, crystallization concentrations, specific heats, density, dynamic viscosity, and thermal conductivity.

These lookup tables allowed for state point lookup by any MATLAB models using either two or three-dimensional interpolation. However, when implementing this solution into iterative models, the speed of the interpolation caused computational time to increase by a factor of 10. The double effect model has up to 25 state points that must be iteratively solved for and while this may have been sustainable for initial modeling, any parametric exercises were impractical. Thus, it was important to create a faster method for determining state point properties.

The solution was found in the article by Zhe Yan et al. in the form of Multiproperty Free Energy Correlations for thermodynamic properties. These algebraic properties can predict the thermodynamic properties of aqueous lithium bromide using up to second order polynomials.

To calibrate these polynomials, the lookup tables that were previously developed were used and MATLAB's polynomial fitting functions were utilized. The polynomials for enthalpy, entropy and specific heat capacity which depend on temperature, pressure and concentration were of the form shown below.

$$\begin{aligned} Prop(\boldsymbol{T},\boldsymbol{X},\boldsymbol{P}) \; = \; & [(C_1\boldsymbol{X}^2 + C_2\boldsymbol{X} + C_3)\boldsymbol{P} + (C_4\boldsymbol{X}^2 + C_5\boldsymbol{X} + C_6)]\boldsymbol{T}^2 \ldots \\ & +[(C_7\boldsymbol{X}^2 + C_8\boldsymbol{X} + C_9)\boldsymbol{P} + (C_{10}\boldsymbol{X}^2 + C_{11}\boldsymbol{X} + C_{12})]\boldsymbol{T} \ldots \\ & +[(C_{13}\boldsymbol{X}^2 + C_{14}\boldsymbol{X} + C_{15})\boldsymbol{P} + (C_{16}\boldsymbol{X}^2 + C_{17}\boldsymbol{X} + C_{18})] \end{aligned} \tag{3-12}$$

Using this form, the polynomials were tuned using the lookup tables for enthalpy, entropy, and specific heat capacity. The constants determined within these forms are shown in Table 3.6.

Table 3.6 – Enthalpy and Entropy Polynomial Constants.

Constant #	*Enthalpy [kJ/kg]*	*Entropy [kJ/kg-K]*	*Specific Heat [kJ/kg-K]*
1	1.590860498E-09	-2.274499234E-10	1.590860498E-09
2	4.456255816E-09	2.713920544E-10	4.456255816E-09
3	-3.135236591E-09	-7.956336676E-11	-3.135236591E-09
4	-4.268725591E-03	-1.275815184E-05	-4.268725591E-03
5	4.193084581E-03	2.126724250E-05	4.193084581E-03
6	-7.176659315E-04	-1.332738783E-05	-7.176659315E-04
7	-4.179683958E-08	4.321154379E-08	-4.179683958E-08
8	2.599040729E-06	-4.274575445E-08	2.599040729E-06
9	-1.565577052E-06	1.000835196E-08	-1.565577052E-06
10	1.475008824E+00	4.568623262E-03	1.475008824E+00
11	-4.355972893E+00	-1.416628951E-02	-4.355972893E+00
12	3.980058625E+00	1.318300688E-02	3.980058625E+00
13	-2.410874923E-04	-1.963920927E-06	-2.410874923E-04
14	-5.320673827E-04	1.991475276E-06	-5.320673827E-04
15	9.242691691E-04	-7.101581013E-07	9.242691691E-04
16	1.827477977E+03	1.459497276E+00	1.827477977E+03
17	-1.539072865E+03	-1.807994898E+00	-1.539072865E+03
18	3.094651770E+02	5.465256523E-01	3.094651770E+02

Using these coefficients and polynomials, it was useful to quantify the error each of these polynomials would produce over the full range of the lookup tables. Therefore, the error was plotted for each and is shown in Figure 3.7 - Figure 3.9 for enthalpy entropy and specific heat capacity, respectively.

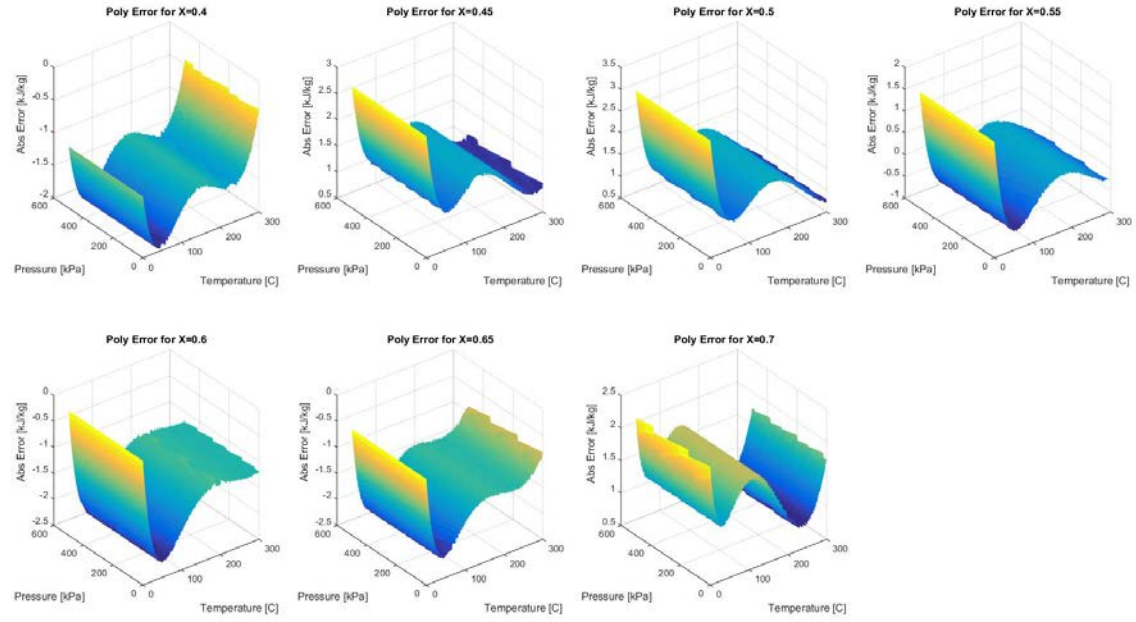

Figure 3.7 – Absolute Error from Enthalpy Polynomial.

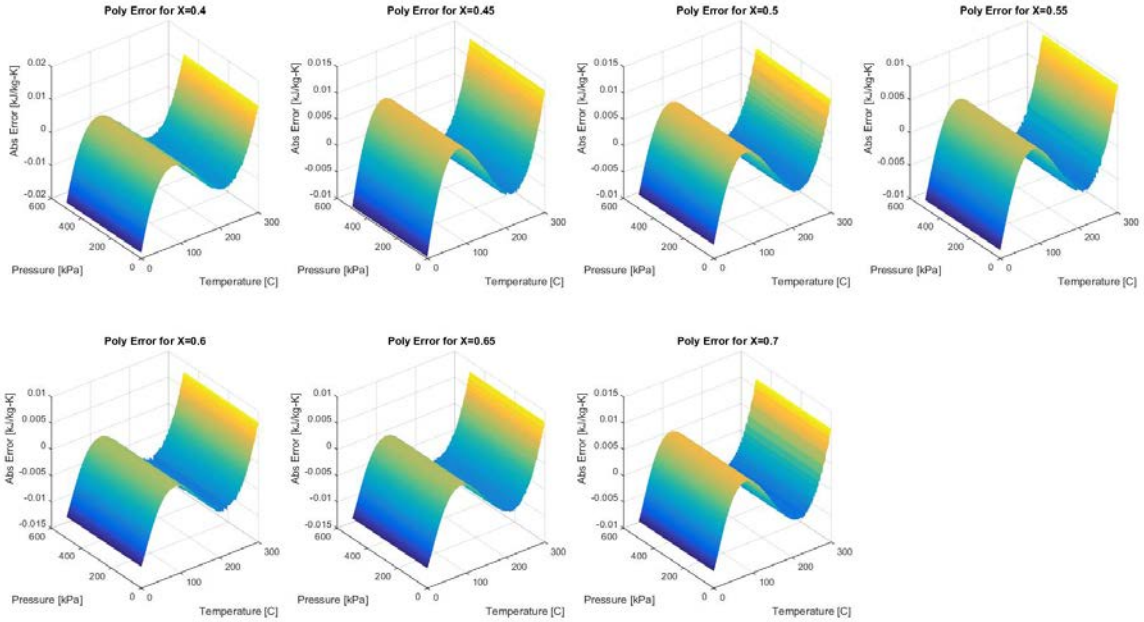

Figure 3.8 – Absolute Error from Entropy Polynomial.

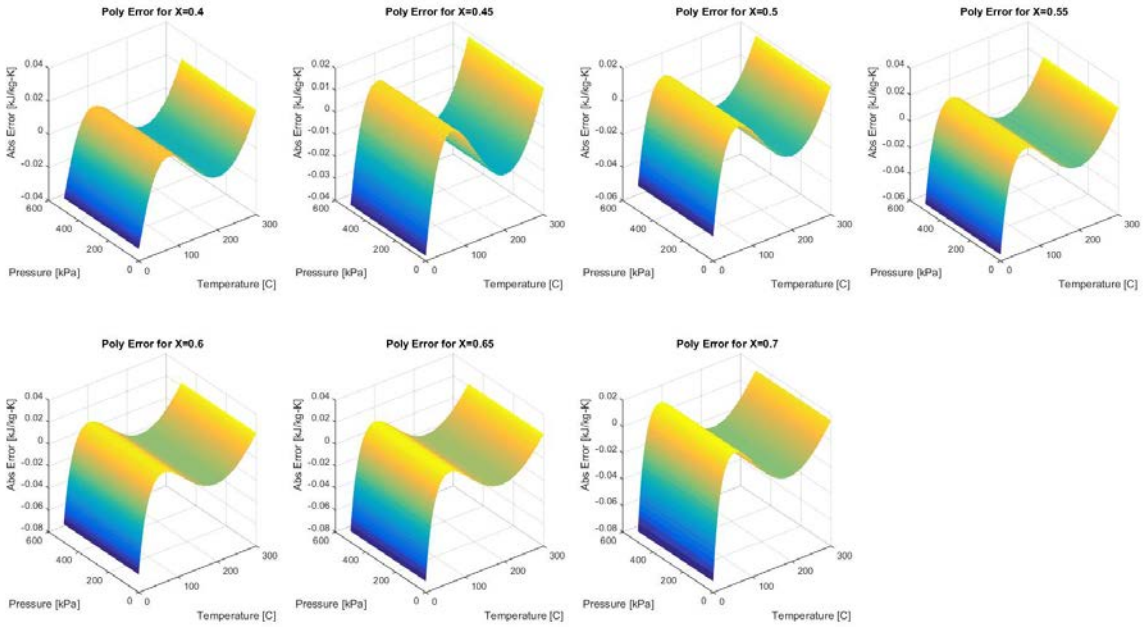

Figure 3.9 – Absolute Error from Heat Capacity Polynomial.

Notice that the maximum absolute specific enthalpy error is less than 3 kJ/kg, the specific entropy error is less than 0.02 kJ/kg-K, and the heat capacity error is less than 0.08 kJ/kg-K. While further tuning could further improve this error, the accuracy of this system and the speed with which the MATLAB model could calculated the state point properties made it sufficient for this effort.

Next, all properties that are determined independently of pressure were calibrated to the polynomial of the form shown below.

$$Prop(\boldsymbol{T}, \boldsymbol{X}) = [(C_1\boldsymbol{X}^2 + C_2\boldsymbol{X} + C_3)]\boldsymbol{T}^2 + [(C_4\boldsymbol{X}^2 + C_5\boldsymbol{X} + C_6)]\boldsymbol{T} \ldots$$
$$+[(C_7\boldsymbol{X}^2 + C_8\boldsymbol{X} + C_9)] \quad (3\text{-}13)$$

These properties include specific volume (density), thermal conductivity, saturated heat capacity, saturated enthalpy, saturated entropy, and dynamic viscosity. The coefficients for each are shown in Table 3.7 and Table 3.8.

Table 3.7 – Pressure Independent Polynomial Coefficients.

Constant #	*Spec. Volume [m^3/kg]*	*Thermal Cond. [W/m-K]*	*Sat. Spec. Heat [kJ/kg-K]*
1	3.850306395E-11	1.811549878E-07	9.955699653E-05
2	-5.169282719E-09	5.680965559E-06	-1.084797769E-04
3	3.068050583E-09	-6.204848502E-06	2.726735622E-05
4	5.662776372E-07	-6.451841356E-05	-3.889084300E-02
5	-2.483707269E-07	-1.087210008E-03	4.157660866E-02
6	1.694090030E-07	1.723219051E-03	-9.734560910E-03
7	-9.452562345E-06	4.784600450E-03	3.326308266E+00
8	-6.932217151E-04	-3.157273848E-01	-6.387940416E+00
9	9.962687651E-04	5.747310744E-01	4.483139427E+00

Table 3.8 – Pressure Independent Polynomial Coefficients cont.

Constant #	*Sat. Enthalpy [kJ/kg]*	*Sat. Entropy [kJ/kg-K]*	*Dynamic Viscosity [cP]*
1	-0.004103237	-1.268577077E-05	0.005726126
2	0.003945821	2.154406024E-05	-0.004911583
3	-0.000600488	-1.352766221E-05	0.001124211
4	1.412403977	4.394390039E-03	-2.357670373
5	-4.283573845	-1.405374860E-02	2.020696886
6	3.953959348	1.317920034E-02	-0.462682133
7	1833.200286919	1.479182001E+00	237.820026596
8	-1545.059198830	-1.825965957E+00	-203.083347126
9	311.162176887	5.502349746E-01	4.483139427E+00

Similar to the pressure dependent properties, the error was calculated for each thermodynamic property and shown in Figure 3.10 through Figure 3.15.

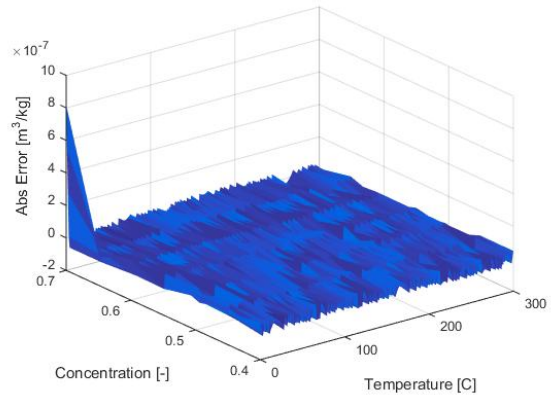

Figure 3.10 – Specific Volume Polynomial Error.

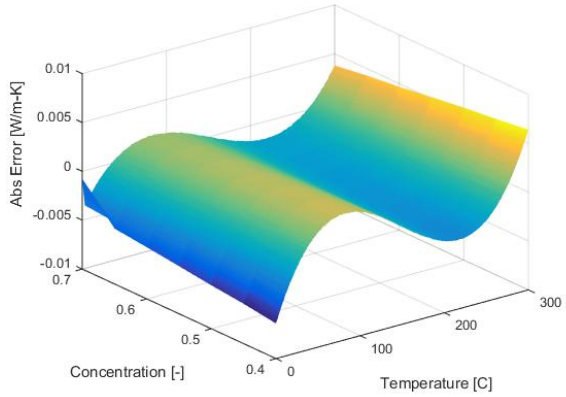

Figure 3.11 – Thermal Conductivity Polynomial Error.

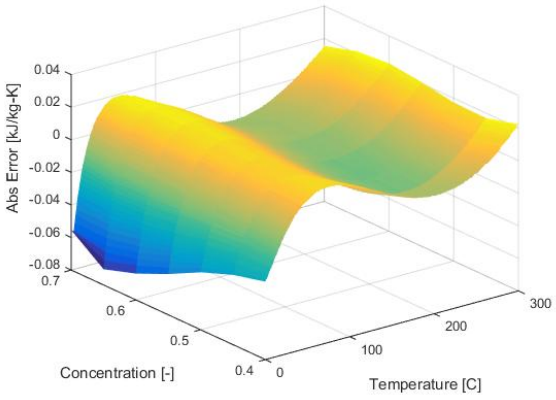

Figure 3.12 – Saturated Heat Capacity Polynomial Error.

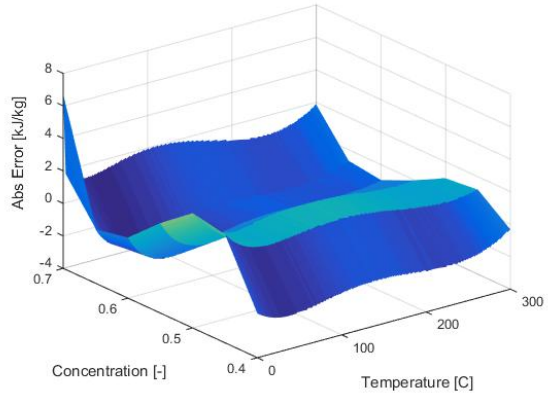

Figure 3.13 – Saturated Enthalpy Polynomial Error.

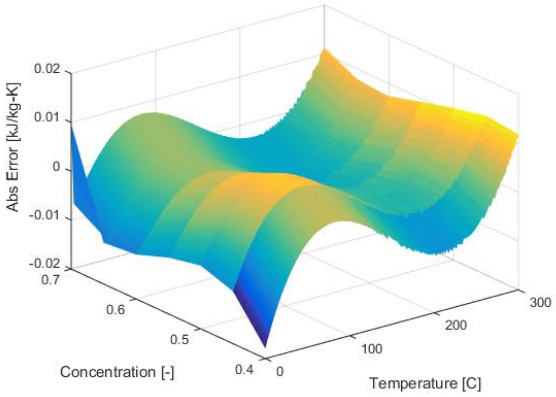

Figure 3.14 – Saturated Entropy Polynomial Error.

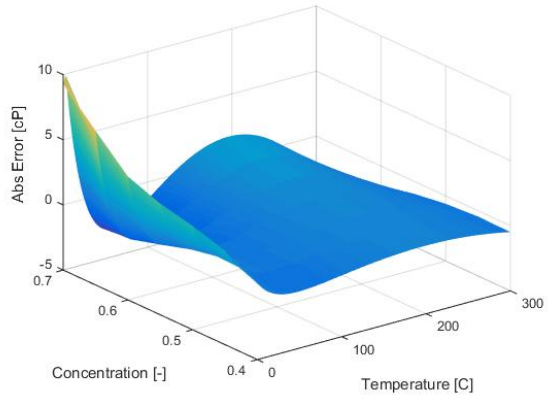

Figure 3.15 – Dynamic Viscosity Polynomial Error.

All of the polynomial results for the thermodynamic properties except for the dynamic viscosity show acceptable error across the entire range of the lookup tables. The dynamic viscosity error at low temperatures and high concentrations generates a larger amount of error but should not overly affect the modeling since this is outside of the operational window for the model. However, this error has been monitored during exercising the model for impacts on any of the thermophysical models.

3.2.2 - Modeling Methodology

When designing the model to predict performance of a double effect absorption chiller, it is important to consider the recursive nature of the state point loops. Notice that in Figure 3.16 there are two primary loops that must be considered, the solution pump and the refrigerant loop. Additionally, there are multiple interdependencies that must also be accounted for including the internal heat exchangers and the condenser/desorber. To model such a complicated cycle, an iterative approach with guess values is taken. Normally, such a system would be created in a software like EES with iterative solving core to its functionality, but in order to integrate with the existing fuel cell model, it was necessary to construct the iterative solver in MATLAB. The solver works by solving each component linearly and updating a guess array of thermodynamic properties for the future iteration. The logic of the solver and the interdependencies are shown in Figure 3.16.

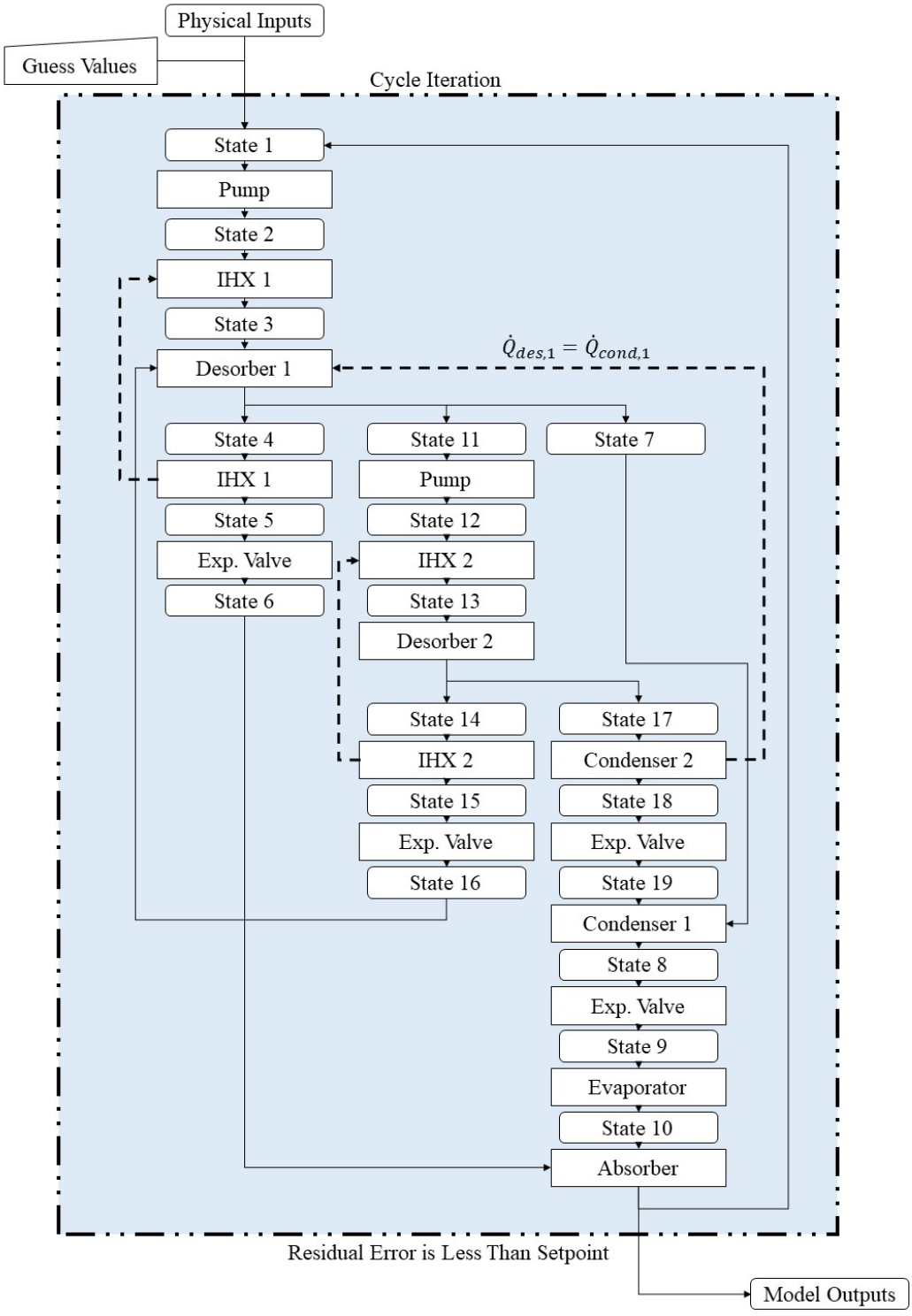

Figure 3.16 – Double-Effect Model Iterative Solver Logic.

Notice that several components have multiple inputs and outputs with dependencies on state points earlier or later in the loop. To accomplish this, a full array of guess values is created and updated each loop to allow for convergence. The model is considered converged when the residual error between the state point array of the current iteration and the past iteration is less than a specified value.

3.2.3 - Component Models

To implement the model methodology selected for the double effect absorption chiller, several different component models were developed to simulate the thermophysical performance. When developing the models, it was important to maintain scalability within the models since the system could be applied to either a rack, row, or larger scale in the data center.

The double effect absorption chiller model relies on a few state assumptions as shown in Table 3.9. Note that all state points correlate with Figure 3.6.

Table 3.9 – Thermodynamic State Point Summary.

Point	*State*	*Note*
1	Saturated Liquid Solution	Vapor quality set to 0 as assumption.
2	Subcooled Liquid Solution	State calculated from pump model.
3	Subcooled Liquid Solution	State calculated from solution HX model.
4	Saturated Liquid Solution	Vapor quality set to 0 as assumption.
5	Subcooled Liquid Solution	State calculated from solution HX model.
6	Vapor-Liquid Solution	Flash from Expansion Valve.
7	Superheated Water Vapor	Assumed to be pure water.
8	Saturated Liquid Water	Vapor quality set to 0 as assumption.
9	Vapor-Liquid Water	Flash from Expansion Valve
10	Saturated Water Vapor	Vapor quality set to 1 as assumption.
11	Saturated Liquid Solution	Vapor quality set to 0 as assumption.
12	Subcooled Liquid Solution	State calculated from pump model.
13	Subcooled Liquid Solution	State calculated from solution HX model.
14	Saturated Liquid Solution	Vapor quality set to 0 as assumption.
15	Subcooled Liquid Solution	State calculated from solution HX model.
16	Vapor-Liquid Solution	Flash from Expansion Valve.
17	Superheated Water Vapor	Assumed to be pure water.
18	Saturated Liquid Water	Vapor quality set to 0 as assumption.
19	Vapor-Liquid Water	Flash from Expansion Valve

Desorber

To model the desorption process with the required scalability, a heat transfer coefficient times surface area and log-meant temperature difference (UA-LMTD) method was determined to be the best solution. While a more mechanistic model could better indicate the thermodynamic performance, at the time of this modeling, no physical parameters were known about the theoretical chiller.

The UA values for the theoretical chiller were obtained from previous literature and implemented in the model shown below, where Q is the heat transfer rate in the desorber, UA is the effective heat transfer coefficient and area, and delta T is the log mean temperature difference.

$$Q_{des} = UA_{des}\,\Delta T_{lmtd} \tag{3-14}$$

The UA-LMTD model accounts for heat exchanger sizing within the chiller while also allowing the absorption cycle state points to adjust their pressures to match the temperature profile of the incoming heat source.

Absorber

Similar to the desorber model, the absorption process is modeled using a UA-LMTD method in combination with mass and energy balances. Since the absorber is the culmination of the absorption chiller cycle, the final check on value matching is done between the mass and energy output of State Point 1 and the guessed value from the previous iteration.

Condenser and Evaporator

The condenser and evaporator were modeled using an overall UA-LMTD method to determine the overall heat transfer characteristics based on the assumed state points. However, a separate process produced a one-dimensional model of the heat exchangers, incrementing both streams by steps of enthalpy to check the temperature profile. This method allowed for a separate check on thermal cross-over and was used to maintain a minimum pinch point.

Internal Heat Exchangers

The internal heat exchangers were modeled using a constant effectiveness model to simplify calculations. The effectiveness calculations used are shown below where Q is the heat transfer rate, epsilon is the effectiveness, C is the heat capacity, and T is the temperature.

$$\dot{Q}_{IHX} = \varepsilon_{IHX}\, C_{min}\left(T_{h,in} - T_{c,in}\right) \tag{3-15}$$

$$C_{min} = min\left(C_p\dot{m}|_h, C_p\dot{m}|_c\right) \tag{3-16}$$

Pump

For the solution pumps within the system, the liquid is considered incompressible and pumped to the set pressure of the next state point. The equation for enthalpy change across a defined pressure change for an incompressible fluid is shown in Equation 3.2.6 below, where dh is the change in specific enthalpy, cp is the specific heat capacity, dT is the temperature delta, v is the specific volume, and dP is the pressure change.

$$dh = c_P\, dT - v\, dP \tag{3-17}$$

This equation holds true for any pure fluid and while the solution in the double effect absorption chiller is not a pure fluid, it is assumed the difference is negligible.

Expansion Valve

Two methods are required to simulate the vapor flash within expansion valves. The first is for the pure water as it expands from state point 18 to 19 and 8 to 9. An isenthalpic process is assumed, and the quality is determined from the pressure and enthalpy of the resultant state.

However, when expanding solution, the flash is calculated by evaluating the solution at its incoming concentration at the lower pressure it will be expanded to. The saturation temperature of the solution at the incoming concentration is assumed to be the outlet temperature and the quality of vapor is then calculated from the energy balance across the expansion valve.

3.2.4 - Double Effect Results

The double effect chiller model was exercised in two directions. The first direction was to understand the impact of increasing the heat source temperature. This change simulates different exhaust characteristics from different operating points of a fuel cell. By running a fuel cell hotter, the fuel cell itself is less efficient, but more waste heat is available in the exhaust stream. The second direction was adjusting the chiller outlet temperature. Since data center applications do not require actual refrigeration and simply must return the

server exhaust air to an acceptable ambient temperature the temperature can be varied to understand how the operation of a chiller at different outlet temperatures can affect the performance. It should be noted that this study does not take into effect the process air heat exchanger that would be required to implement this heat transfer into the process air. The colder the chiller outlet temperature, the smaller that heat exchanger needs to be, but the more entropy generation that will occur.

The efficiency results from the double effect chiller are presented in Figure 3.17 below.

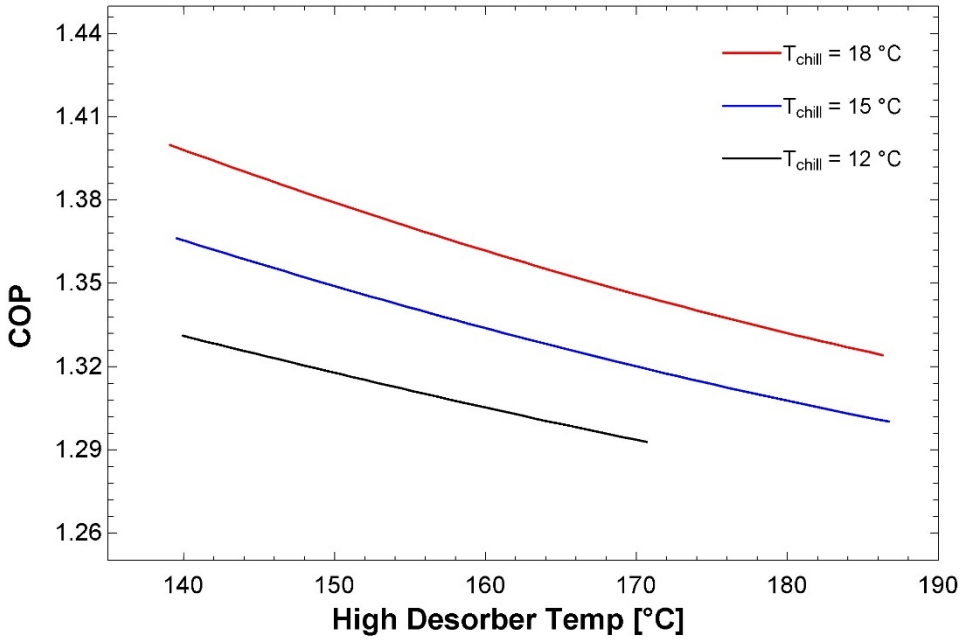

Figure 3.17 – Double-effect Chiller Coefficient of Performance Results.

What is interesting about these results is the fact that chiller performance decreases as the desorber temperature is allowed to increase. This desorber temperature increase is associated with hotter and hotter heat medium inlet temperatures. The decreased efficiency is indicative of the higher temperature delta over which the chiller is operating. For comparison, this is similar to how a standard four component HVAC system operates when the high side pressure is increased. It is important to recognize that the negative effects of a higher high side pressure associated with the heat pump are not overcome by the positive effects of higher temperature inlet for the heat engine. What is impressive however is the fact that the chiller can

produce at COPs of up to 1.4. By allowing the chiller to operate at higher chiller output temperatures, which are still acceptable in the data center application, the chiller can operate outside of its standard window.

While the efficiency results of the double effect system are relatively positive, the chilling capacity results tell a different story and are shown in Figure 3.18.

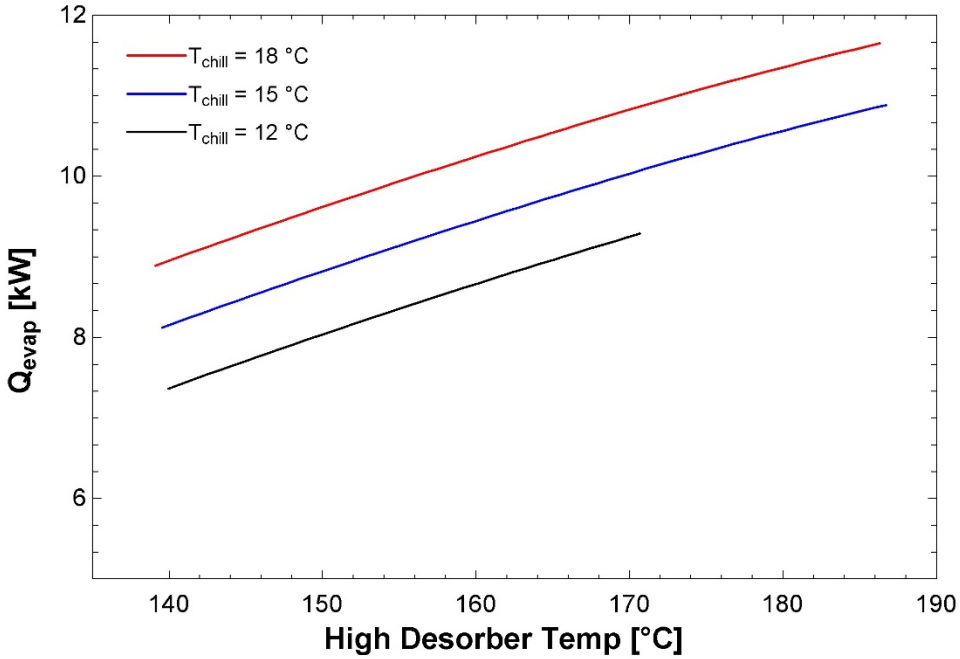

Figure 3.18 – Double-effect Chiller Capacity Results.

In reviewing the chilling capacity of the double effect machine, it is immediately apparent that despite the improved efficiency, the chiller is still not capable of producing enough chilling to fully offset the electrical load of a 15 kW server rack. However, there are still important takeaways from the results shown. First, the increasing exhaust temperature allows for higher chilling capacity, but when analyzing the results in conjunction with the COP results above, it is immediately apparent that in order to achieve these higher chilling capacities, more heat must be absorber from the fuel cell exhaust. This increased heat capacity from the fuel cell exhaust would require a subsequent reduction in electrical production efficiency and may damage the overall system efficiency. Second, the higher chiller outlet temperatures allow for more chilling

to be produced, this matches the results shown in the COP analysis and the increased capacity can be directly attributed to higher efficiency.

Considering the double-effect absorption chiller's inability to produce the chilling required to fully offset the electrical load produced by the server rack, two lessons were learned that would guide research moving forward. The high dependency of the chiller's performance on the temperature and heat capacity of the exhaust flow requires a better understanding of this heat source. To produce better operational windows for the chiller models, it will be important to have a good source of temperature and flow information. Thus, a fuel cell system model was constructed and will be discussed next.

Additionally, the lack of chilling capacity produced by the double effect chiller suggests that further increases in the chiller efficiency are required. The next iteration of absorption chiller systems is the triple-effect machine. These systems are highly complex and can only be produced at a minimum size of 100 kW which is more suitable to a row-level approach to server cooling. The investigation of such a system is discussed later.

3.3 - Triple Effect Absorption Chiller Model

Based on the results from the SOFC system model and the double-effect absorption chiller model, the investigation of a triple-effect row-level absorption chiller was required. The triple effect absorption chiller cycle is shown below in Figure 3.19.

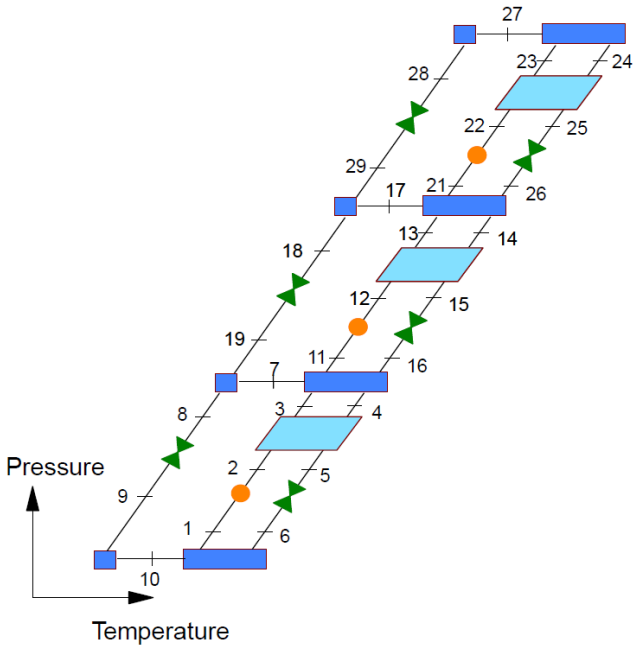

Figure 3.19 – Triple Effect Absorption Cycle.

The triple effect absorption cycle is very similar to the double effect configuration but includes a third level of the solution pump. The high desorber performs the waste heat recovery at even higher temperatures and pressures allowing for even more refrigerant to be evaporated out of the solution. The additional refrigerant allows the efficiency of the chiller to be augmented to a maximum of 1.8. The triple effect absorption cycle is modeled using the same component models from the double effect system. However, the internal heat transfer models are assisted by state point quality assumptions which define the saturation of different state points. The triple-effect absorption model was developed to explore how its performance changes at different heat characteristic inputs from a solid oxide fuel cell. The principle changes that the absorption cycle would see are adjustments to the high desorber's pressure and therefore its saturation temperature. Understanding how the triple effect machine operates at various temperature inlets will allow for the ultimate optimization of the integrated system. To this end, the triple effect cycle model was exercised with preliminary results of the model shown in Figure 3.19.

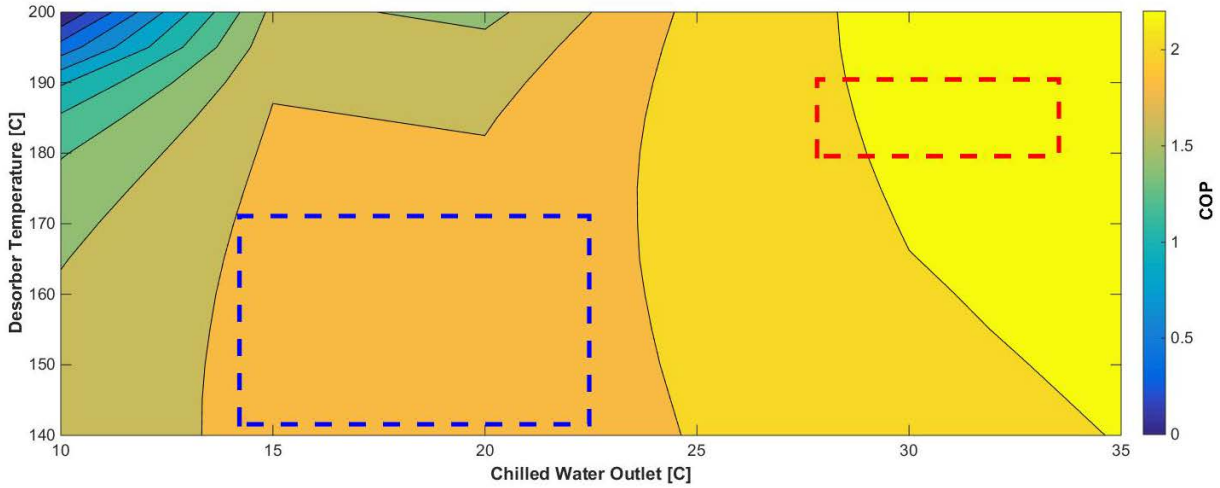

Figure 3.20 – Triple Effect Chiller Preliminary Results.

Analyzing the results from the simplified triple-effect chiller model, it is immediately apparent that the triple effect chiller performs consistently at COPs above 1.6. Briefly considering this result with an assumed exhaust capacity of ~120 kW, the assumed chilling capacity of such a system could theoretically offset the majority of the thermal load of 200 kW of servers in the traditional sense. However, it is possible to further increase the efficiency of the system by cooling at higher temperatures. The two overlaid rectangles on Figure 3.19 indicate traditional air cooling region in blue and the potential for water cooled servers in the red region. The water cooling of servers allows the cooling medium to operate at a higher temperature, up to 35 °C, and achieve a COP of up to 2.2. This boost in performance coupled with the exhaust heat present a system that could theoretically produce 200 kW of electricity from the SOFC while completely offsetting the thermal load of the servers by cooling using a triple effect absorption chiller. Note that the discontinuities in the contours shown in Figure 3.19 are results from manual and discrete adjustments to the intermediate pressures within the triple-effect cycle.

Given the initial performance characteristics of the triple-effect system, it is now important to accurately predict the exhaust conditions of the SOFC. The next section will explore the effort to mathematically model the exhaust characteristics of a commercial SOFC plant.

3.4 - SOFC System Model

To better understand the thermodynamic heat source and the different operational strategies and their impact on exhaust temperature, flow and heat capacity, a comprehensive SOFC system model was constructed. Following the logic that such systems are better implemented at row level, a 200 kW existing SOFC system made by Bloom Energy was selected as the basis for this model.

3.4.1 - Model Overview

The Bloom Power Server Solid Oxide Fuel Cell (SOFC) is a 200-kW generation system designed for steady state base loads similar to that of a data center. The SOFC runs on natural gas and air from the ambient and can achieve thermal efficiencies of around 55%. The layout of the Bloom SOFC balance of plant is detailed in Figure 3.21. Note that there are four primary mass flow inlets: natural gas, fuel cell air, combustor air, and makeup water. The rest of the system is comprised of a heat exchanger network that includes an anode recuperator, an external steam reformer, an anode cooler, a cathode recuperator and a steam generator. Additionally, a post-anode reactor, anode recirculation valve, and a liquid condenser are present.

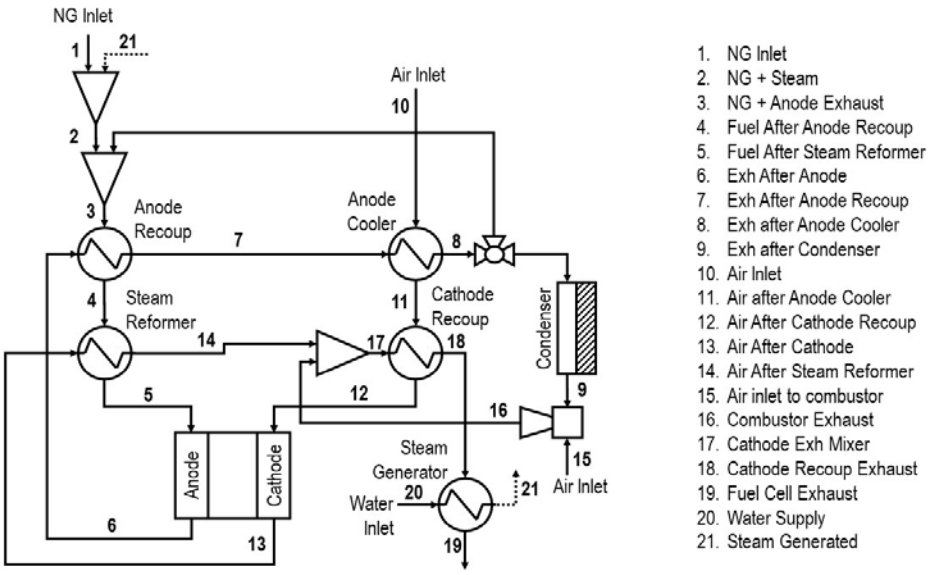

Figure 3.21 - Bloom Power Server Balance of Plant Schematic.

The Bloom Power Server model is coded in MATLAB and utilizes an iterative averaging solution to converge the twenty-one state points. Each state point contains a temperature, pressure, concentration, mass flow rate, and heat capacity.

The model begins with a set of guess values for all the state points placed within an initialization matrix. These guess values can be updated while running the model through a parametric study. Temperature, pressure and mass flow guess values are set deterministically, while composition and heat capacity are determined using mass balances and polynomial heat capacity curves based on temperature.

Each of the following component models will be detailed in the following section.

3.4.2 - Component Models

Component models determine their outlet states mechanistically based on the inlet states and given specifications about their operation. The solved for outlet state is placed in the state point array of the next iteration.

Mixing Chambers

The updated output state of a mixing chamber is calculated by using a mass balance and an energy balance. In this way, the outlet state's temperature, concentration, mass flow, and heat capacity can be calculated. For simplicity, we assume that all mixing chambers are adiabatic, as shown in the equations below where m is the mass flow rate and h is the specific enthalpy of the incoming and outgoing flows.

$$\sum_{in} \dot{m}_i = \sum_{out} \dot{m}_i \tag{3-18}$$

$$\sum_{in} \dot{m}_i h_i = \sum_{out} \dot{m}_i h_i \tag{3-19}$$

Anode Recirculation Valve

The recirculation valve is given input that determines the percentage of mass flow that is recirculated into State 3. This constant can be used as a control mechanism to adjust the steam to carbon ratio. The two outlets of the recirculation valve are calculated using a mass balance.

Heat Exchangers

The four basic heat exchangers utilized in the system are modeled mechanistically using a constant heat exchanger effectiveness, provided as an input to the model. The heat exchange capacity is determined below where Q is the heat transfer rate, epsilon is the heat exchanger effectiveness, m is the mass flow rate, and h is the specific enthalpy.

$$\dot{Q}_{HX} = \epsilon \, min\left(\dot{m}_c\left(h_c|_{T_h} - h_c\right), \dot{m}_h\left(h_h - h_h|_{T_c}\right)\right) \tag{3-20}$$

The heat exchanger is discretized to produce the temperature profiles of the hot and cold streams. Then, the heat exchanger pinch point and average effective convective heat transfer coefficient can be determined. It should be noted that all the heat exchangers were modeled in a counter flow configuration to maximize performance.

$$T_{pinch} = min\left(T_{h_i} - T_{c_i}\right) \tag{3-21}$$

Steam Generator

The steam generator is modeled similarly to the basic heat exchangers, but the pinch point is checked at the saturated liquid condition of the inlet water stream. Additionally, the outlet mass flow is assumed to only consist of water vapor, so the mass flow rate will not increase without the required heat input.

Condenser

The water drop-out condenser is modeled similarly to the basic heat exchangers, but additionally utilizes a drop-out efficiency which compares the exit state of the condenser to the saturation condition of the incoming stream. Note that C is the concentration of water, and eta is the efficiency of the condenser as set by the model.

$$C_{H2O,out} = \eta_{dropout} * C_{H2O,sat}|_{in} \tag{3-22}$$

Combustor

The post-anode combustor is treated as an ideal reacting combustor in which all of the combustible fuels are reacted completely. Their reacting equations are shown below where Q is calculated from the lower heating values (LHV) of the fuels. Note that incomplete combustion can be modelled in case of a shortage of oxidizer.

$$CH_4 + 3\ O_2 \rightarrow CO_2 + 4\ H_2O_{(g)} + Q_{comb} \tag{3-23}$$

$$H_2 + \frac{1}{2}\ O_2 \rightarrow H_2O_{(g)} + Q_{comb} \tag{3-24}$$

The temperature of the outlet stream is calculated using an energy balance shown below assuming the combustor is not a work producing or consuming component.

$$\sum_{in} \dot{m}_i h_i + Q_{comb} = \sum_{out} \dot{m}_i h_i \tag{3-25}$$

External Steam Reformer

The external steam reformer is modeled using a given methane conversion input, which determines the fraction of moles which are reacted. The external reformer functions as a heat exchanger while some of the heat transfer is utilized in the endothermic reactions of the steam-methane reformation and water gas shift. The reformer is considered to have a mechanistic heat exchange effectiveness which determines the heat transfer capacity based on the two inlet streams as shown previously. Then the amount of heat transfer required for the reformation is calculated in below.

$$CH_4 + H_2O + 206\frac{kJ}{kmol} \rightarrow CO + 3H_2 \tag{3-26}$$

$$CO + H_2O \rightarrow CO_2 + H_2 + 41\frac{kJ}{kmol} \tag{3-27}$$

$$\dot{Q}_{reform} = 165\frac{kJ}{kmol}\,\dot{n}_{CH_4}\eta_{reform} \tag{3-28}$$

The final outlet states of the reformer are calculated by subtracting the heat transfer capacity of the heat exchanger and the required reformation heat.

Fuel Cell Stack Model

To simulate the performance of a solid oxide fuel cell (SOFC) stack, a one-dimensional model was constructed in Engineering Equation Solver (EES). The purpose of the model is to evaluate the SOFC's cell voltage at varying current densities and temperatures.

Several phenomena that affect cell voltage were considered in the model. First, the thermodynamic voltage was calculated using Nernst equation as shown below, where E is the voltage, R is the gas constant, T is the cell temperature, n is the number of ions per mole of fuel, F is Faraday's constant, a is the chemical activity, and nu is the stoichiometric number. Note that all constants and values will be detailed in Table 3.10.

$$E = E_t - \frac{RT_{fc}}{nF} ln\left(\frac{\prod a_{prod}^{v_i}}{\prod a_{react}^{v_i}}\right) \tag{3-29}$$

Where the thermodynamic voltage when accounting for non-standard temperature is calculated as shown below.

$$E_t = E^0 + \frac{\hat{\Delta s}}{nF}\left(T_{fc} - T_0\right) \tag{3-30}$$

In this way, the thermodynamic voltage accounts for pressure, concentrations, and temperature effects. The next step is to account for the ohmic and cathodic overpotentials within the cell. The assumption that the anode overpotential is negligible is a relatively good assumption in most SOFC cell models. The ohmic overpotential can be calculated below.

$$\eta_{ohmic} = j(ASR_{ohmic}) = j\frac{t^M T_{fc}}{A_{SOFC}\, e^{-\frac{\Delta G_{act}}{RT}}} \tag{3-31}$$

Similarly, we can calculate the cathodic overpotential as shown below. Note the inclusion of the stoichiometric number to account for gas depletion effects.

$$\eta_{cathode} = \frac{RT_{fc}}{4\alpha F} ln\left(\frac{j}{j_0 P^C\left\{\frac{\lambda_{O_2} - 1}{(1+\omega)\lambda_{O_2} - 1} - t^c \frac{jRT_{fc}}{4Fp^C D_{eff}^{cat}}\right\}}\right) \tag{3-32}$$

Finally, the overall cell voltage can be determined and accounts for thermal, pressure, concentration, ohmic, cathodic, and gas depletion effects in the cell.

$$V_{FC} = E - \eta_{ohmic} - \eta_{cathode} \tag{3-33}$$

By discretizing through potential current densities as well as cell temperatures for the cell, it is possible to generate the voltage for all the possible operating. The last step was to calculate the power output of a stack that operated based on the characteristics of this model.

$$P_{FC} = V_{FC} * j * A_{FC} \tag{3-34}$$

The values used in simulating this fuel cell are listed here in Table 3.10.

Table 3.10 – Stack Modeling Parameters.

Parameter	*Symbol*	*Value*	*Unit*
Reversible Voltage	E^0	1.23	V
Fuel Cell Temperature	T_{fc}	1023 – 1223	K
Standard Temperature	T_0	298	K
Cathode Pressure	P^C	101325	Pa
Anode Pressure	P^a	101325	Pa
Effective Cathode Diffusivity	D_{eff}^{cat}	2e-5	m^2/s
Transfer Coefficient	α	0.5	-
Reference Current Density	j_0	0.1	A/cm^2
Electrolyte Constant	A_{SOFC}	9e7	K/ohm-m
Electrolyte Activation Energy	ΔG_{act}	100e3	J/mol
Electrolyte Thickness	t^M	20e-6	m
Cathode Thickness	t^c	800e-6	m
Stoichiometric Number	λ_{O_2}	15	-
Oxygen Molar Ratio	ω	3.76	-
Mole Fractions	X_{CH_4}	0.155	-
	X_{O_2}	0.21	-
	X_{H_2O}	0.471	-

Fuel Cell Stack Exercise and Results

The cell model was exercised parametrically from a current density of 0.05 to 2 A/cm2 to create a polarization curve which is shown in Figure 3.22. Additionally, the model was worked from a stack temperature of 750 to 950 °C to observe the impacts of temperature on the voltage.

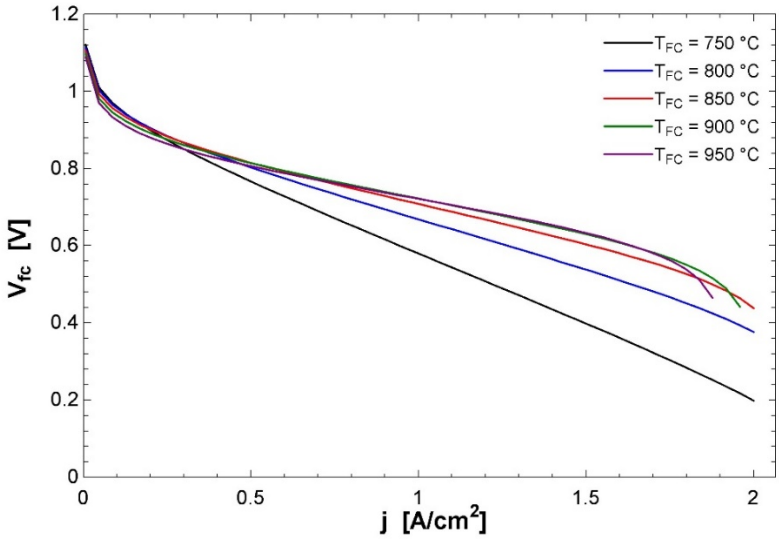

Figure 3.22 – Polarization Curve Temperature Results.

Similarly, the model output of stack power was exercised similarly to the polarization curves to produce Figure 3.23.

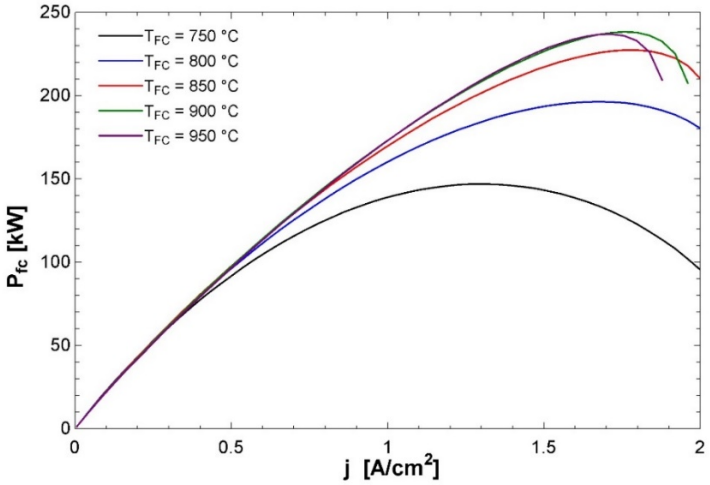

Figure 3.23 – Stack Power Output.

Then, the model was exercised with varying pressures with a constant stack temperature of 900 °C at the inlet of the stack to observe the impact of higher pressures on the voltage of the cell. The results are plotted in Figure 3.24.

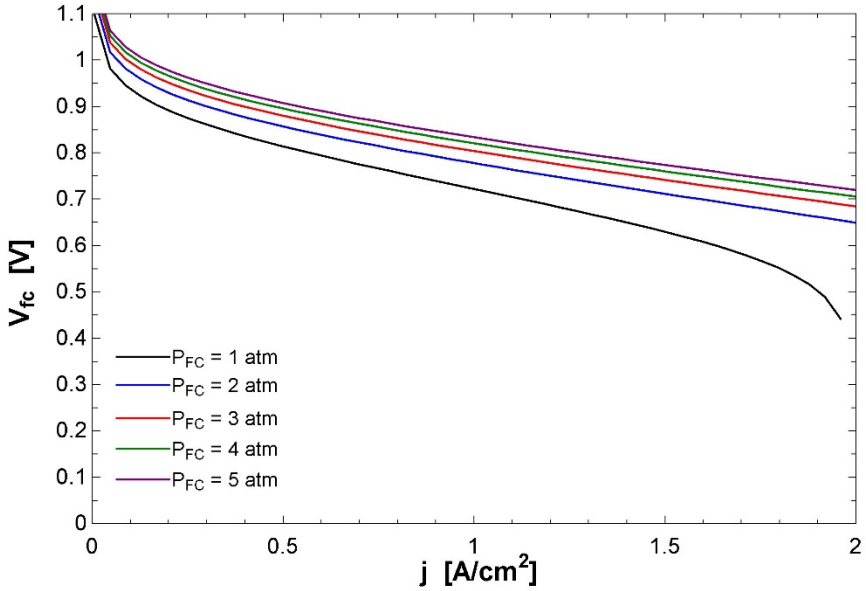

Figure 3.24 – Polarization Curves Pressure Results.

Reviewing the performance trends of the SOFC cell, there are several important take-aways regarding the operation of the cell. First, in Figure 3.22, it is apparent that in order to maximize the cell voltage that a higher cell temperature should be utilized. However, by increasing the stack temperature, the cathodic overpotential is exacerbated and causes a limitation on the current density. Additionally, the marginal increase of voltage is minor when stepping from 900 to 950 °C so any increase in temperature further than 900°C is disadvantageous. Similarly, when analyzing the power output of the stack, it is apparent that by increasing the stack temperature to 950 °C the maximum power output actually decreases. This would again suggest that the optimal operating condition lies closer to 900 °C.

The second exercise of the model investigates increasing the pressures at the inlet of the fuel cell. Typically, this is done with a compressor or blower to facilitate more mass flow through the cell channels. In Figure 3.24, notice that by increasing the inlet pressures the cathodic overpotential is minimized and allows for a higher current density. Once again, the marginal cell voltage increases when moving to pressures higher than 3 atm demonstrate diminishing returns. Finally, it should be noted that operating high temperature stacks at higher pressure leads to issues with sealing and structural resistance to cracking and

warping. These factors, while not investigated in this study, should be considered when choosing a nominal operating pressure for the fuel cell.

3.4.3 - Model Convergence

After each component model provides the new outlet state points, the model computes an iteration average between the new state point array and the past state point array. The function of this step is to minimize convergence overshoot and converge on a solution faster. This iteration average can be weighted to allow for faster more reliable solution.

Additionally, after each iteration state point heat capacities are calculated using a fitted polynomial function that is mapped for each gaseous component.

This system model is constructed using the physical input flows, physical characteristics of heat exchangers and the thermal matrix to calculate the state points. In order to facilitate certain state points or operational constants such as steam to carbon ratio, a separate script was written to adjust the flowrates resulting in a “goal” value for operational values such as power, steam to carbon ratio, etc. This script was utilized to ensure that all parametric sweep adhered to realistic operational values.

The SOFC system model will be explored further, but now that it is possible to characterize the performance of the stack and balance of plant, it is possible to attempt an optimization of the integrated system. The optimization of the integrated SOFC and triple effect absorption chiller is investigated in the next chapter in an effort to minimize the carbon emissions, primary energy savings ratio, and levelized costs.

Chapter 4 - Operational Optimization of a Thermally Integrated Solid Oxide Fuel Cell with Triple Effect Absorption Chiller for Data Centers

The objective of this study is to perform an operational optimization of the SOFC and triple effect absorption chiller configuration.

4.1 - Optimization Methodology

This study focuses on the application of an integrated SOFC and AC system at a data center for providing power and cooling for the servers. The principal demands of servers being electricity and cooling suggest that such an integrated system could have enormous utility if implemented. This integrated concept is illustrated in Figure 4.1.

Hyper-scale data centers are the focus of this study because their operators can most easily implement such a novel integrated system into their infrastructure. Data center computers are usually organized into racks, which host up to twenty computers for a total power consumption of approximately 15 kW/rack. Rows of these racks are then grouped for thermal management, creating a hot or cold aisle where air is passed through the server computers and into the air handling unit (AHU). The number of servers in a row varies but is generally around 10-15 server racks (comprising a total electrical load of around 200 kW). A hyper-scale data center is typically characterized by having over 5,000 servers for a total electric power demand of greater than 50 MW.

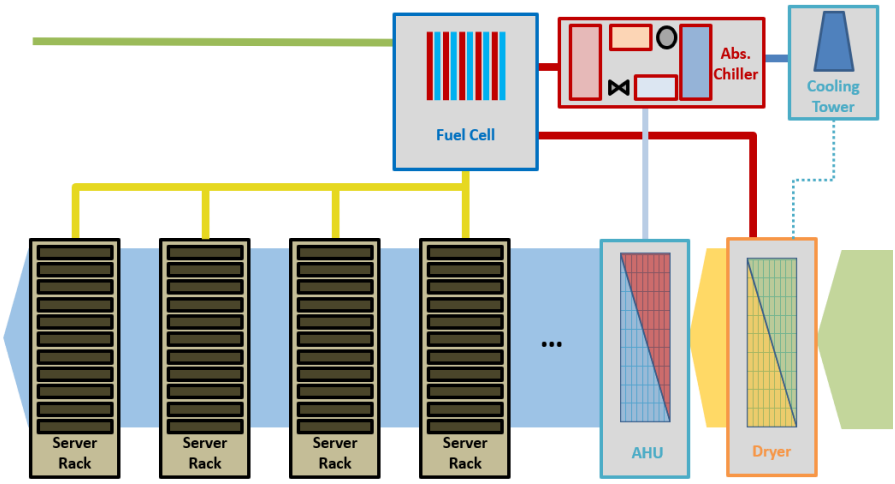

Figure 4.1 – SOFC and AC Integrated Concept for Data Centers.

When considering the implementation at data centers, there are a few constraints that govern the commissioning of such an integrated system. First, data centers require incredibly high reliability of electric power supply (Sverdlik, 2016), therefore a single SOFC power system would not be very feasible due to reliability that is less than required for the data center, which would certainly require a backup power supply. But SOFC systems are inherently modular, which would allow implementation at the row level, which single point of failure requires a smaller backup power system. At some level of modularity, for example, the implementation of SOFC systems at rack level as proposed by Zhao et al., (Zhao et al., 2016), can increase the robustness of the power supply, perhaps sufficient to eliminate the need for backup power, but such a concept increases operation and maintenance costs. Additionally, commercial absorption chilling systems are more typically produced at row level capacities (~200 kW). Thus, a row-level configuration is selected for the current analysis of an integrated SOFC and AC system. The analysis at the row level can also be applicable to smaller data centers that may utilize similar groups of servers. The integrated system is therefore investigated to optimize its ability produce electricity and chilling for the servers within a data center row.

To optimize the dispatch of a thermally integrated AC with an SOFC for the application of power and cooling in a data center, a mathematical model is developed in MATLAB and paired with property data

from Engineering Equation Solver (EES). The integrated system consists of three models: a thermodynamic model of an SOFC, a floating state point model of a Lithium Bromide (LiBr) AC, and an economic model for the installation and operation of the system.

4.1.1 - Solid Oxide Fuel Cell Model

To better understand the SOFC and how different dispatch strategies affect efficiency, exhaust temperature, flow, and heat capacity, we develop a thermodynamic SOFC system model. A 200 kW SOFC system meets the row-level configuration electricity demand requirements, exists commercially, and has been previously installed at data centers to supply steady state base load and backup power (Bulletin, 2012). The specified SOFC runs on natural gas and the layout of the balance of plant is detailed in Figure 4.2.

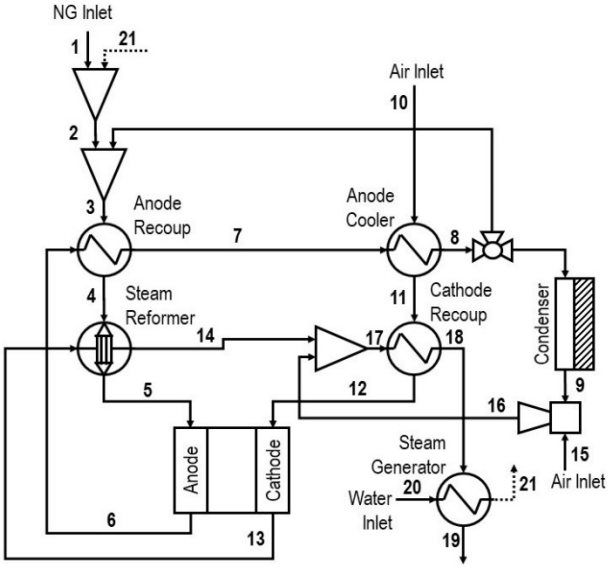

Figure 4.2 – SOFC Balance of Plant Schematic.

The SOFC system model is coded in MATLAB and utilizes an iterative solution to converge the twenty-one state points shown above in Figure 3. Each state point contains a temperature, pressure, concentration array, mass flow rate, and heat capacity. Component models determine their outlet states mechanistically based upon the inlet states and the respective physical, chemical, and electrochemical phenomena involved in their operation. The solution of each outlet state is placed in the state point array of the next iteration.

The power output is set at 210 kW (AC) and the steam-to-carbon ratio is set at 2.5 at the inlet of the external steam reformer. These values are achieved by controlling the inlet natural gas and water flows into the system. The full set of modeling assumptions is presented in Table 4.1. The following component models are utilized within the balance of plant.

The output state of a mixing chamber is calculated by using a mass balance and an energy balance assuming adiabatic mixing. In this way, the outlet state temperature, concentration, mass flow, and heat capacity can be calculated. It is assumed that no reactions occur in mixing. Note that m is the mass flow rate and h is the specific enthalpy.

$$\sum_{in} \dot{m}_i = \sum_{out} \dot{m}_i \tag{4-1}$$

$$\sum_{in} \dot{m}_i h_i = \sum_{out} \dot{m}_i h_i \tag{4-2}$$

The recirculation valve is a given input that determines the percentage of mass flow that is recirculated into State 3. The two outlet mass flow rates of the recirculation valve are calculated using a mass balance.

The four basic heat exchangers utilized in the system are modeled using a constant heat exchanger effectiveness, provided as an input to the model. This methodology allows the model to scale easily. The heat exchange capacity is determined below, where Q is the heat transfer rate and epsilon is the effectiveness. Pressure and thermal losses are assumed for each component and can also be found in Table 4.1.

$$\dot{Q}_{HX} = \epsilon \, min\left(\dot{m}_c\left(h_c|_{T_h} - h_c\right), \dot{m}_h\left(h_h - h_h|_{T_c}\right)\right) \tag{4-3}$$

Each heat exchanger is then discretized to produce the temperature profiles of the hot and cold streams. The heat exchanger pinch point and average effective heat transfer area can then be determined. It should be noted that all the heat exchangers were modeled in a counter flow configuration to maximize performance. Note that UA is the heat transfer coefficient and area for heat transfer.

$$\dot{Q}_{HX} = UA_{HX}\left(\frac{\Delta T_h - \Delta T_c}{\ln\left(\frac{\Delta T_h}{\Delta T_c}\right)}\right) \tag{4-4}$$

The post-anode combustor is treated as an ideal reacting combustor in which all the combustible fuels are reacted completely. The exothermic heat transfer is calculated from the lower heating values (LHV) of the fuels. Note that incomplete combustion can be modelled in case of a shortage of oxidizer.

$$\sum_{in} \dot{m}_i h_i + Q_{comb} = \sum_{out} \dot{m}_i h_i \tag{4-5}$$

The external steam reformer is modeled assuming a partially complete reaction to an equilibrium set by the outlet temperature of the reformer. The equilibrium concentration, K, at the outlet of the reformer is calculated using the equilibrium constant (Franchi et al., 2020). The external reformer is a diabatic reactor, as external heat is supplied to the endothermic reaction of steam-methane reformation.

$$K_{ref} = 1.0132^2 * \exp\left(-\frac{45203 - 52.54 * T}{1.987 * T}\right) \tag{4-6}$$

A bulk fuel cell stack model was created to predict the effects of temperature and species concentrations on cell voltage within the fuel cell stack. The model was based on the SOFC stack model provided in O'Hayre et al. and is presented in equations above (O'Hayre et al. 2009). Overpotentials from ohmic losses within the cell and cathodic losses due to both activation polarization and mass transport losses are considered.

$$\mathrm{V_{FC}} = E_{thermo} - \eta_{ohm} - \eta_{cat} \tag{4-7}$$

$$\eta_{\mathrm{ohm}} = \frac{t_M T}{A_{SOFC} \exp\left(-\frac{\Delta G_{act}}{RT}\right)} \tag{4-8}$$

$$\eta_{\mathrm{cat}} = \frac{RT}{4\alpha F} \ln\left[\frac{j}{j_0 P_c \left\{x_{O_2} - \frac{t_c j RT}{4F P_C D^{eff}_{O_2,N_2}}\right\}}\right] \tag{4-9}$$

Complete conversion of methane via internal reforming is assumed to occur along the length of the anode compartment producing four hydrogen molecules for every methane molecule that enters the compartment. Thus, hydrogen is assumed to be the only electrochemically active species. The cell model energy balance accounts for the endothermic internal reforming and the exothermic oxidation of hydrogen

which allows the model to calculate the species concentrations and enthalpy at the outlets of both the anode and the cathode.

Table 4.1 – SOFC Model Assumptions and Inputs.

Component	Assumption	Value
Mixing Chambers	Adiabatic Mixing	-
Anode Recirc Valve	Fixed Percentage Recirc	0.4
Anode Recoup HX	Constant Effectiveness	0.75
Anode Cooler HX	Constant Effectiveness	0.8
Cathode Recoup HX	Constant Effectiveness	0.85
Anode Condenser HX	Constant Effectiveness	0.45
External Reformer HX	Constant Effectiveness	0.85
External Reforming	Fraction of Equilibrium Concentration	0.7
Heat Exchanger Pressure Loss	Constant Pressure Drop	0.75 kPa
Heat Exchanger Thermal Loss	Proportional Transfer Loss	10%

Since the goal of the analysis is the thermal integration between the SOFC and an AC, the dispatch conditions that determine the outputs of the SOFC model are focused upon the thermodynamic characterization of the exhaust, but also include overall efficiency and carbon emissions implications of the dispatch. The net electrical efficiency of the SOFC system is calculated using the LHV of the fuel input as shown below, where eta is the efficiency, E is the energy production rate, m is the fuel mass flow, and LHV is the lower heating value of the fuel.

$$\eta_{\mathrm{SOFC,elec}} = \frac{\dot{E}_{FC}}{\dot{m}_{fuel}\, LHV_{NG}} \tag{4-10}$$

Adjustments to input variables such as anode recirculation and heat exchanger effectiveness were made to ensure that solutions match acceptable operating values.

The recursive nature of the interactions between the different state points requires the development of an iterative solver to converge a solution. The SOFC model is a physical parameter-based model, and therefore solves the heat transfer rates, electricity production, electrochemical and chemical, and reactions based upon the specified inputs of inlet flows, component effectiveness, and other thermodynamic assumptions. To achieve a specific power output, steam-to-carbon ratio, and stack temperature an algorithm is developed to adjust the input natural gas, air, and water flows. The power output is solved by adjusting

the natural gas flow and corrected as the steam-to-carbon ratio is solved by adjusting the inlet water flow. Once the power and steam-to-carbon ratio are converged, the algorithm adjusts the air flow into the system to meet the stack temperature target. The power is solved to an accuracy of 100 W, the steam-to-carbon ratio is solved to an accuracy of 0.1.

The two nested iterative algorithms are exercised by one supervisory algorithm, which steps the system model through a specified domain of stack temperatures and fuel utilizations. This exploration of the temperature and utilization domain produces the result figures shown below. The second convergence algorithm converges the stack temperature to within 0.01 °C. The inaccuracy of the converged temperature causes slight non-linearities in the results, but further increasing the converged accuracy exponentially increases computing time.

4.1.2 - Absorption Chiller Model

A triple effect absorption chiller is selected for its higher coefficient of performance (COP) and temperature compatibility to capture heat from the exhaust of the SOFC. Aqueous Lithium-Bromide is selected as the working fluid due to its availability in commercial systems and the lack of producing chilling below freezing temperatures. A floating-point model using saturation data for aqueous Lithium Bromide is created to simulate the cycle's performance in conjunction with the SOFC heat source. The interface heat exchangers (i.e., desorbers, absorbers and condensers) are all modeled using a log-mean-temperature approach, while internal heat exchangers are modeled using a constant effectiveness approach. Additionally, vapor quality assumptions are made to certain state points to reflect the saturated state of different fluid points. These assumptions are listed in Table 4.2.

Table 4.2 – Absorption Cycle Model Assumptions.

#	State Point	State	Comment
1	*Abs Sol Outlet*	Saturated Liquid Solution	Vapor quality set to 0 as assumption.
2,12,22	*Pump Outlet*	Subcooled Liquid Solution	State calculated from pump model.
4,14,24	*Strong Sol Outlet*	Saturated Liquid Solution	Vapor quality set to 0 as assumption.
9,19,29	*Exp Valve Outlet*	Vapor-Liquid Solution	Flash from Expansion Valve.
7,17,27	*Des Ref Outlet*	Superheated Water Vapor	Assumed to be pure water.
8,18,28	*Cond Outlet*	Saturated Liquid Water	Vapor quality set to 0 as assumption.
10	*Abs Ref Inlet*	Saturated Water Vapor	Vapor quality set to 1 as assumption.
11,21	*Des Weak Sol Outlet*	Saturated Liquid Solution	Vapor quality set to 0 as assumption.

The modelled parallel effect triple effect absorption chiller system is shown schematically in Figure 4.3. Heat capture from the exhaust of the SOFC occurs in the third desorber between state points 23, 24, and 27, and is shown as $\dot{Q}_{des}$. Chilling is produced in the evaporator between states 9 and 10 and is shown as $\dot{Q}_{evap}$. External heat rejection occurs from the third condenser between state points 19, 7, and 8 and is shown as $\dot{Q}_{cond}$. Finally, heat is also rejected from the absorber between state points 1, 6, and 10 and is shown as $\dot{Q}_{abs}$.

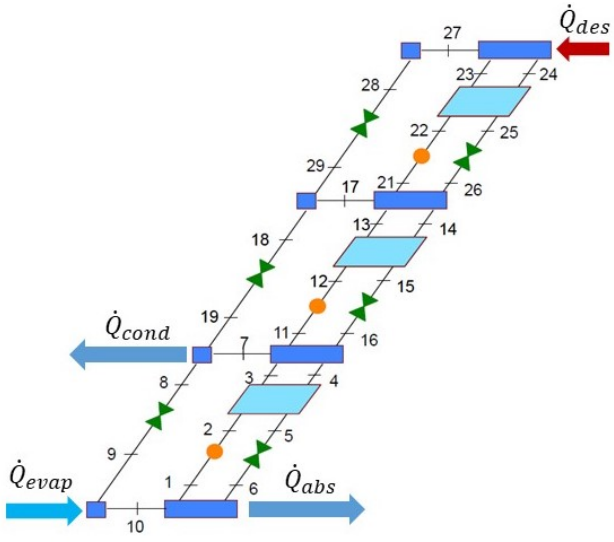

Figure 4.3 – Triple Effect Absorption Chiller System Schematic.

The absorption model predicts the cycle's performance for various desorber temperatures and evaporator temperatures. The objective is to find an optimal temperature at which to capture heat from the

SOFC exhaust to maximize the COP. The COP of the triple-effect absorption chiller is defined below, where COP is the coefficient of performance and Q is the heat transfer rate in either the evaporator or desorber. The output from the AC model is shown in Figure 4.9. Note that for this analysis pump work is neglected in the absorption cycle.

$$\mathrm{COP_{AC}} = \frac{\dot{Q}_{evap}}{\dot{Q}_{des}} \tag{4-11}$$

To maximize the chilling COP, a higher desorber temperature should be used, however increasing the desorber temperature decreases the amount of maximum heat recovery from the exhaust. To calculate the heat capacity of the SOFC exhaust and therefore the heat into the desorber is used. Note that Q is the heat transfer rate, m is the mass flow rate, cp is the specific heat transfer rate, and T is the temperature.

$$\dot{\mathrm{Q}}_{exh} = \dot{m}_{exh} C_p (T_{exh} - T_{des}) \tag{4-12}$$

4.1.3 - Economic Model

The integrated model is completed with an economic simulation that predicts the economic performance of the integrated SOFC, absorption chiller, and cooling tower. The economic model first calculates the capital investment to install each subsystem. For the purposes of this analysis, a dry cooling tower is considered to minimize the impact of water consumption in hot climates, where mechanical chilling for data centers is typically needed.

The economics of the SOFC plant are broken down into three categories: capital investment, operation/maintenance, and cost of fuel. The capital investment of installation is shown in Table 3. The capital cost of the SOFC power system is referenced to a modeled scenario in Scataglini et al. with 250 kWe units produced at 50,000 units a year (Scataglini et al., 2015). This large manufacturing size is assumed to match the assumption that such production would be necessary to mega-scale data center power demands. The installation of SOFC systems in data centers could represent an untapped opportunity to boost the manufacturing capacity of the SOFC industry. We believe that the technological learning associated with the supply of SOFC systems for this market will justify a sharp cost reduction in the future. The operation

and maintenance costs are sourced based on existing installations and include the cost of restacking during its lifetime. Lastly, the fuel costs are based on bulk wholesale natural gas prices in southern California.

The economics of the absorption chiller and the cooling tower are each broken down into two categories: capital investment and operation/maintenance. The capital investment for the absorption chiller is determined for a triple effect large-scale chilling per kW. The operation and maintenance costs are also taken from an existing plant (Flores, 2016). Finally, the AC plant is oversized by a factor of 1.5 since commercial plants perform at their maximum COP when producing 70% of their full capacity. The cooling tower is similarly oversized by a factor of 1.25 to ensure its ability to meet the heat rejection needs of the AC plant. The values for all these costs are shown in Table 4.3.

Table 4.3 – Economic Model Inputs. (Flores, 2016; Tian et al., 2018b; Scataglini et al., 2015)

Parameter	Value	Unit
SOFC: Capital Investment	499	$ kW^{-1}
SOFC: Operation & Maintenance	6	$(MWh)^{-1}$
SOFC: Fuel Cost	0.159	tm^{-3}
AC: Capital Investment	4200	kW^{-1}
AC: Operation & Maintenance	14	$(MWh)^{-1}$
CT (Dry): Capital Investment	224	kW^{-1}
CT (Dry): Operation & Maintenance	7.2	$(MWh)^{-1}$
Operational Lifetime	20	years

Using these inputs, the economic model calculates the levelized cost of electricity (LCOE) and chilling (LCOC) as follows. Note that I is the initial capital investment, M is the operational and maintenance costs, F is the fuel costs, E is the energy produced (electricity or chilling), P is the electrical power, Q is the chilling capacity, and r is the discount rate.

$$\mathrm{LCOE, LCOC} = \frac{\sum_{t=1}^{n} \frac{I_t + M_t + F_t}{(1+r)^t}}{\sum_{t=1}^{n} \frac{E_t}{(1+r)^t}} : E_t|_{LCOE} = P_{SOFC}, \qquad E_t|_{LCOC} = \dot{Q}_{chill} \tag{4-13}$$

The economic model results are calculated following the thermodynamic model of both the SOFC and the absorption chiller and are discussed in the following section. The calculation of LCOE and LCOC at different nominal design condition will be used to identify the most cost effective operating point.

4.1.4 - Optimization algorithm

To perform the dispatch optimization of the integrated system, two independent operational parameters are identified as controllable: stack temperature and fuel utilization. We exercise the integrated model to explore a wide map of operating conditions across a range of stack temperatures (830-875°C) and single-pass fuel utilizations (0.4-0.6), useful to best match the operating conditions of the SOFC and AC, while meeting the server row electricity and cooling load requirements. An initial converged condition is obtained using the physical inputs into the model and then a spiral search pattern is used to explore the temperature and utilization domain. This strategy is adopted to minimize the step distance between dispatch condition points and thus improves the stability and speed of the iterative model. The objective of the optimization is to determine where the integrated system operates with the maximum primary energy savings, discussed later, and where it operates with the lowest levelized cost of energy.

4.2 - Results and Discussion

4.2.1 - SOFC Model Results

The SOFC model operates with the fuel utilization and stack temperatures as independent input variables, so it is important to verify the cell voltage model which predicts the cell's voltage at various conditions. Figure 4.4 illustrates the SOFC voltage model which accounts for the electrochemical impacts of temperature, pressure, species concentrations. The dashed lines shown in Figure 4.4 illustrate the predicted voltages at various current densities at different stack temperatures. The operating points shown illustrate the simulated conditions at which the SOFC is operating in the following figures. The linear relationship between cell voltage and current density at the varying stack temperatures can be attributed to the constant power output from the stack.

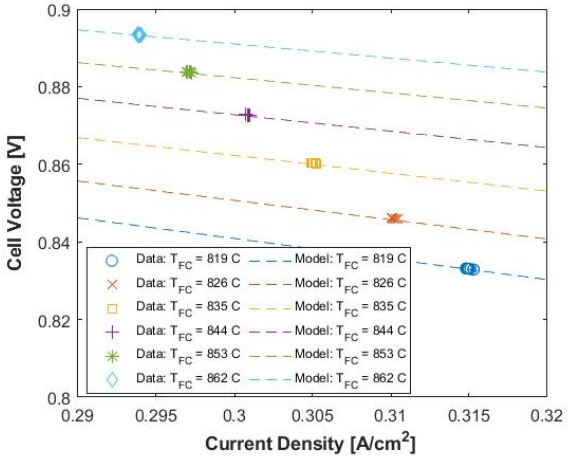

Figure 4.4 – SOFC Cell Voltage Model Polarization Results.

To demonstrate how the operation of the SOFC is adjusted across the results domain, the fuel and air inlet mass flow rates are charted in Figure 4.5. Note that the values of the fuel and air flow rates are produced by an algorithm to meet the specified power, steam to carbon ratio and stack temperature. Additionally, recall that the slight non-linearities are caused by the iterative convergence of temperature and are minimized with higher resolution convergence but at the cost of computational time. The results presented indicate varying fuel utilization and stack temperature but maintain the 210 kW electrical output and a steam-to-carbon ratio of 2.5 prior to the reformer.

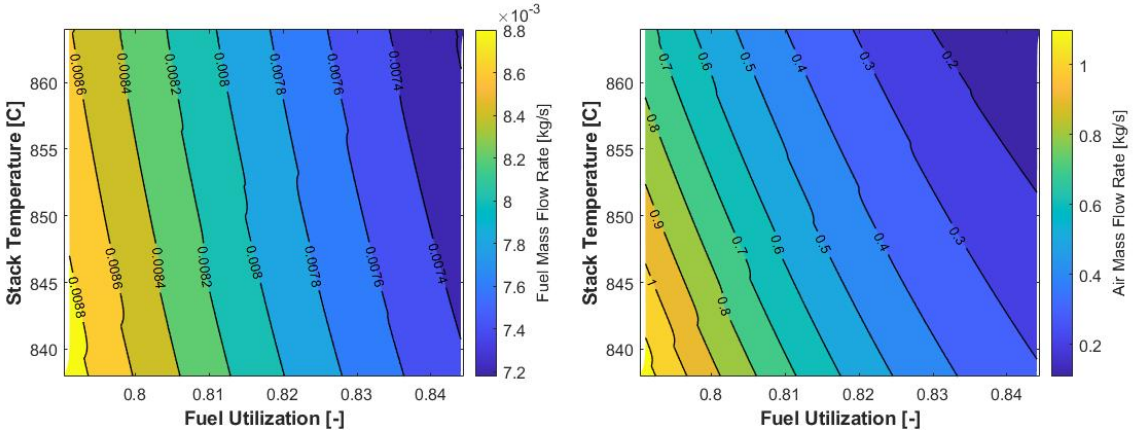

(a) (b)

Figure 4.5 – Mass flow rate of (a) fuel and (b) air into the SOFC system to produce a constant electric power of 200 kW.

The fuel flow rates shown in Figure 4.5a reflect that as the fuel utilization decreases, more fuel is required to produce the 210 kW output of electricity. Also, the lower the stack temperature the lower the cell voltage, which requires more fuel to maintain power output. Similarly, the air flow rates shown in Figure 4.5b reflect how the cathode inlet air stream is used to control the stack temperature. To consider the fuel utilization and the stack temperature as independent variables, it is necessary to implement an active control of the incoming air which is used to regulate the stack temperature. To achieve a lower the stack temperature more air flow is needed to remove the heat from the stack.

The oxidizer temperature ranges between 950 – 1250°C and is dependent primarily on fuel utilization due to its direct impact on the fuel-to-air ratio in the post-anode combustor. The SOFC system model calculates that the oxidizer temperatures are relatively independent of stack temperature but linearly dependent on the fuel utilization.

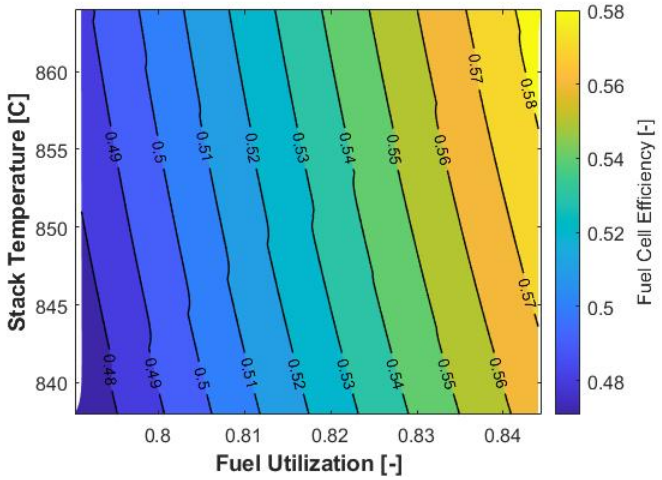

Figure 4.6 – SOFC system efficiency over operational domain.

The SOFC system efficiency is a critical output from the integrated model and is calculated using the LHV for the natural gas fuel inlet. The system efficiency is shown in Figure 4.6 and as expected the fuel utilization has the largest impact on the system efficiency. The dependence on stack temperature can be explained by the increased cell voltage at higher temperatures resulting in better efficiencies. The range of efficiencies from 0.48 to 0.58 indicate that the system can compete with much larger advanced combined cycle natural gas plants on a much smaller scale.

The final output from the SOFC system model is the carbon emissions produced by making electricity from natural gas. The output of CO_2 from the system is shown in Figure 4.7.

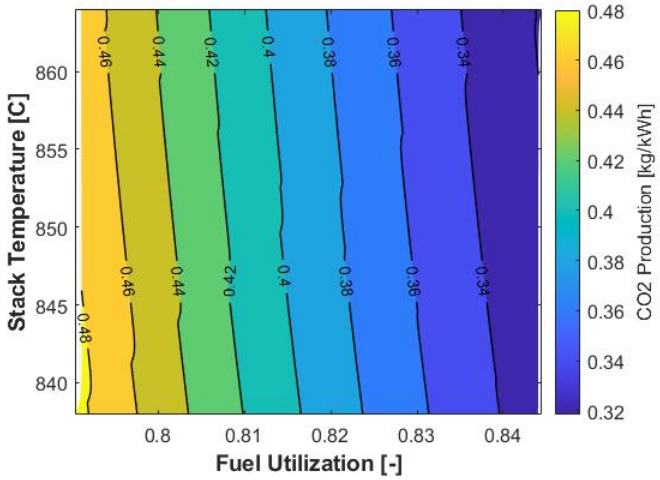

Figure 4.7 – Carbon dioxide emission intensities from SOFC system.

As expected, the carbon emission intensities are very closely tied to the fuel utilization because at lower fuel utilization more fuel is burned in the post-anode oxidizer. It should be noted that at CO_2 productions above 0.44 kg/kWh, the SOFC is producing more CO_2/kWh than the existing natural gas grid and these operating conditions should be avoided (Spath et al., 2000).

4.2.2 - Integrated Model Results

Now that the operation of the SOFC has been explored and the impacts of stack temperature and fuel utilization on the SOFC are understood, the model can characterize the exhaust of the SOFC and its utility to an absorption chiller. The temperature and mass flow rate of the SOFC system's exhaust are shown in Figure 4.8.

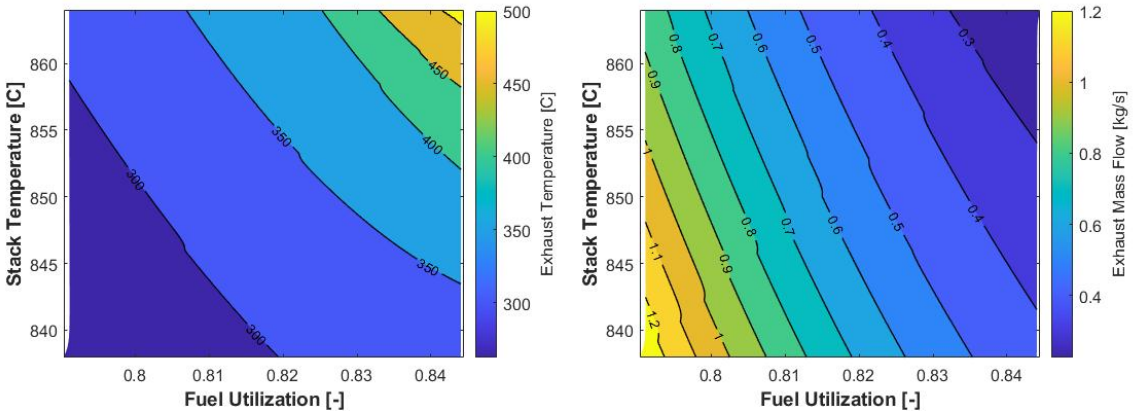

(a) (b)

Figure 4.8 – SOFC system exhaust (a) temperature and (b) mass flow rate.

Figure 4.8a shows that the SOFC system exhaust temperature is predominantly influenced by the stack temperature. This is caused in part because at higher stack temperatures there is less airflow through the system, causing the exhaust to carry the same heat in a smaller mass flow. Similarly, independently increasing the fuel utilization also increases the exhaust temperature. This indicates that the heat generated within the stack is more dominant than the heat generated in the post-anode oxidizer.

In contrast, the exhaust mass flow, shown in Figure 4.8b, is mostly influenced by the fuel utilization since the lower the utilization the more fuel and air that flows through the system. Similarly, the more cooling air flow rate the cooler the stack temperature.

Combining the temperature, mass flow, specific composition, and specific heat of the exhaust from the SOFC system, it is possible to calculate the useful thermal energy available in the exhaust. The range of desorber temperatures within the triple-effect model are shown in Figure 4.9 and the desorber temperature is chosen to maximize the amount of heat capacity available in the exhaust to be used by the AC system. When the heat capacity of the exhaust is explored in the SOFC operational domain, the SOFC system's useful exhaust heat capacity is primarily corelated to the fuel utilization. Lower fuel utilizations allow for more thermal energy in the exhaust, given that more fuel is flowing into the system and is ultimately converted to heat in either the stack or the oxidizer.

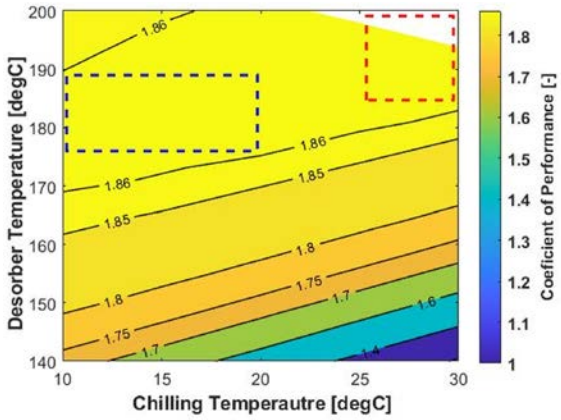

Figure 4.9 – Absorption Chiller Coefficient of Performance at varying temperature constraints.

Dashed blue and dashed red regions identify the feasible operating points for air cooling and liquid cooling, respectively. Utilizing the useful heat and exhaust characterization within the triple-effect absorption chiller, it is possible to calculate the available chilling from the integrated system. The results from the absorption chiller model are shown below in Figure 4.10.

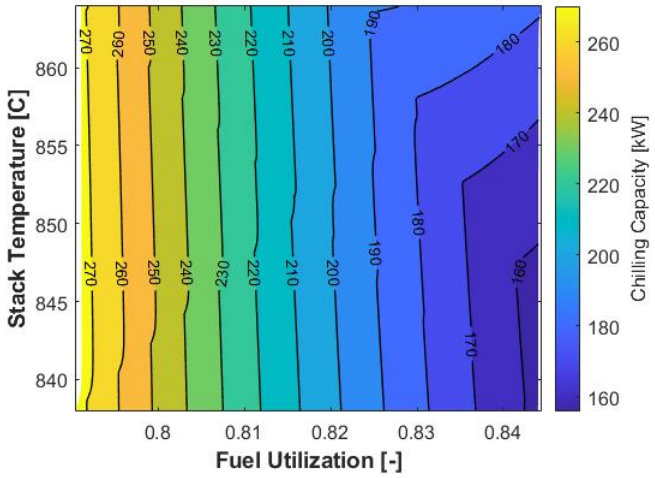

Figure 4.10 – Triple-effect absorption chiller chilling capacity from SOFC exhaust heat.

The chilling capacity is very closely tied to the heat capacity within the SOFC system exhaust, and with COPs ranging from 1.60 to 1.82, the maximum chilling capacity is 272 kW. Based on these results it is possible to produce the needed 200 kW of chilling to fully offset the server's thermal requirement while operating the SOFC at a fuel utilization around 0.82. Note that the increased chilling capacity at high stack

temperatures and higher fuel utilizations is a result of increased AC performance due to higher desorber temperatures, as shown in Figure 4.9.

It is promising to show that an integration between an SOFC system and an absorption chiller could produce the necessary power and chilling for a row of servers within a data center. In this synergic configuration, the SOFC system produces most of the power and thermal load and allows a reduction in primary energy usage through cogeneration. To compare the cogeneration of this integrated system with the more classical approach of grid provided electricity with industrial chilling units, we utilize the primary energy savings ratio metric (PES) calculated below, where E is the energy either in fuel or electricity, eta is the efficiency of either the electricity production or the chilling production, and Q is the chilling capacity.

$$PES = 1 - \frac{E_f}{\frac{E_{el}}{\eta_{el,ref}\ p} + \frac{Q_{th}}{\eta_{th,ref}}} \tag{4-14}$$

For this calculation, we assumed a reference electrical production efficiency of 52.5%, a reference grid efficiency of 89.2%, and a reference COP for chilling of 5. The PES is then computed within the operational domain to show the effects of adjusting the fuel utilization and stack temperature on primary energy savings.

Figure 12 summarizes the achievable PES range across the spanned operating conditions, showing the ability to save between 18 and 30% of primary energy input. The highest PES can be achieved operating the SOFC unit at higher fuel utilization and high stack temperature. However, considering the previously discussed operational constraints to meet the chilling demand, the carbon emissions maximum target, and temperature rises in the cathode and anode, a new operational envelope is found and overlaid in Figure 4.11.

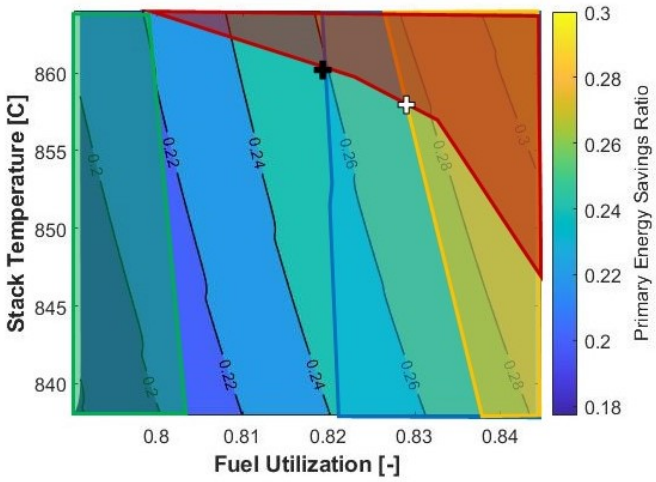

Figure 4.11 – Operational envelope superimposed on primary energy savings ratio.

The overlays on Figure 12 are as follows: the red region represents conditions where the temperature rise across the anode is greater than 80 °C, the orange region represents conditions where the temperature rise across the cathode is greater than 85 °C, the green region represents conditions where carbon dioxide emissions are above 0.44 kg/kWh, and the blue region represents conditions where less than 200 kW of chilling is available. The thermal gradients within the cell were chosen to limit temperature rise to less than 15 °C/cm (Rosner et al., 2020). Considering these constraints and maximizing primary energy savings, the best operating condition is shown in Figure 4.11 as the black cross with operational parameters of 0.819 for fuel utilization and a stack temperature of 861°C, which results in a PES of 25.8% and a CO_2 emission of 0.38 kg/kWh.

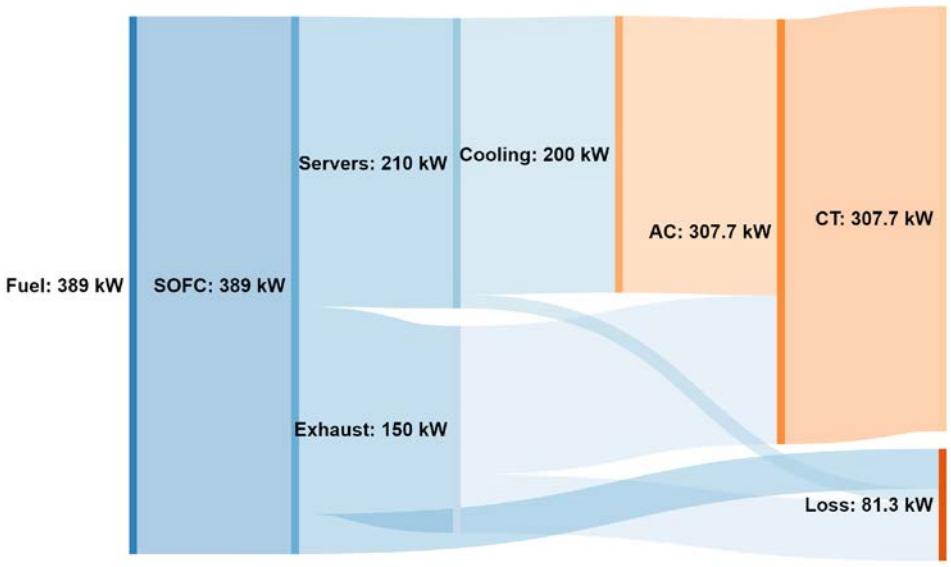

Figure 4.12 – Optimized Energy Flow Diagram.

In the optimized condition for maximum PES, the energy flow through the integrated system is shown in Figure 4.12. The nominal fuel input is 389 kW, based on the LHV, which is then consumed by the SOFC at an efficiency of 53.9%, resulting in 210 kW of electricity. The servers then consume 200 kW of power for processing, converting it to heat, which is absorbed by the AC. The AC also receives 107.7 kW of thermal energy from the SOFC exhaust and rejects the cumulative heat to a cooling tower.

However, when considering this maximized PES solution, it is also prudent to consider the transient nature of the servers cooling requirement. For example, should the ambient air temperature allow some induction of outside air to assist in cooling, the demand for cooling capacity can be decreased. In these instances, the imposed constraint of 200 kW of chilling can be lowered or removed. This allows for an alternative maximized PES solution which is shown as the white cross in Figure 4.11. In this condition, the SOFC can operate more efficiently at a fuel utilization of 0.827 and a stack temperature of 859°C while the chiller operates at partial capacity. Referencing Figure 4.10, we can see that even at the secondary maximized point, the chilling capacity is 184kW. Using this active control with feedback from ambient conditions, the primary energy savings can be maximized, and carbon emissions can be minimized.

4.2.3 - Economic Model Results

The integrated model is used to understand the effect that the adjustments to the operational parameters, fuel utilization and stack temperature, have on the economics of a theoretical installation. Using the cost inputs described in Table 3 and Equation 10, it is possible to calculate the levelized cost of electricity and the levelized cost of chilling. Exploring these values in the same operational domain, the levelized costs of electricity and chilling are shown below in Figure 4.13.

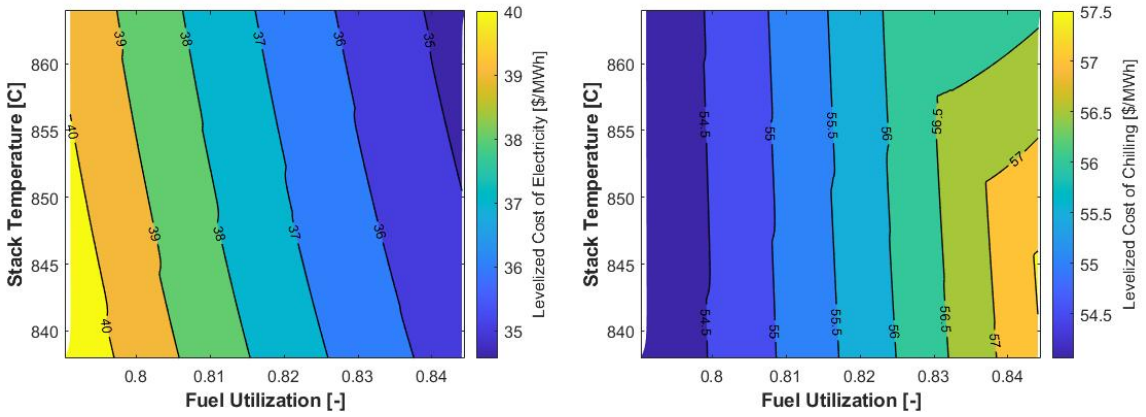

(a) (b)

Figure 4.13 – Levelized costs of (a) electricity and (b) chilling for the integrated system.

Figure 4.13a shows the levelized cost of electricity within the selected operating range of fuel utilization factors and stack temperatures. LCOE results ranging from $35/MWh - $42/MWh, hence comparable with current natural gas combined cycle plant electricity production cost which ranges from 30 – 40 $/MWh (USEIA, 2021). Capital cost expenditures – specifically for the emerging SOFC system cost – are the primary drivers to reduce LCOE. On the other hand, Figure 4.13b depicts the variation of the cost of chilling ranging from 54 to 57 $/MWh. Compared to comparable state-of-the-art mechanical chilling solutions which can operate at a LCOC of $30.4 (Thakar et al., 2021), the absorption chilling requires a larger capital investment due to the complexity of triple-effect absorption chiller costs (52% of the lifetime cost). In contrast, the capital cost of traditional mechanical chilling systems only occupies ~3% of the lifetime cost,

but the AC considers the intake of thermal energy to be “free” compared to the cost of electricity. Additionally, the cost of chilling scales with the chilling capacity because it is assumed that the chiller will be sized to match the thermal output of the fuel cell.

When considering the combined integrated system, it is possible to assess the levelized cost of utility (LCOU), where utility is the sum of the electric power and chilling power. To account for the thermodynamic value of thermal energy (chilling) compared to work (electricity) the chilling energy is valued at 0.2 kWh/kWh of electricity production due to a traditional mechanical chiller’s typical COP of 5. The levelized cost of utility is shown below in Figure 4.14.

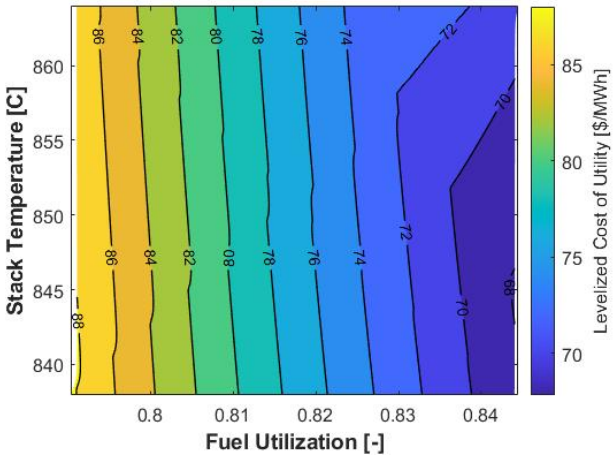

Figure 4.14 – Levelized cost of utility (electricity & chilling) from the integrated SOFC and absorption chiller.

Note in Figure 4.14 that LCOU is primarily corelated inversely to fuel utilization, which indicates that the impact of LCOE is more important on LCOU than LCOC, which is to be expected due to the higher weighting of electricity production. When attempting to optimize the operation of the integrated system based on minimizing the LCOU, it is apparent that a higher fuel utilization and a higher stack temperature, up to a maximum fuel utilization of 0.83, return the best economic performance of 75.72 $/MWh. This result matches the optimization performed upon the maximization of PES, showing that an integrated system comprised of an SOFC and AC will have the highest rate of economic return in conjunction with its most efficient operation.

The overall costs of utility of $70-$88/MWh are still high compared to traditional electricity and chilling plants which, using the reference values of $40/MWh for LCOE and $30.4/MWh for LCOC of a traditional plant, stand at LCOU of $58.5/MWh (EIA, 2021). However, when considering conventional production is remote from the data center, the cost of transmission and distribution must also be considered. The Energy Information Administration (EIA) estimates that traditional grid electricity incurs a cost of $43/MWh in 2020 (Aniti, 2021). The ultimate delivery of the electricity to data centers raises the LCOU to 94.5 $/MWh. Additionally, the greenhouse gas and criteria pollutant emissions benefits and the future potential of such a system further boost the value of the integrated SOFC and AC system. The integrated SOFC system is able to provide its maximum LCOU of $75.72/MWh with a CO_2 emission intensity of 0.380 kg/kWh. Compared to the combined cycle's CO_2 emission intensity of 0.44 kg/kWh (0.46 kg/kWh with transmission losses) (Spath, 2000), the integrated SOFC and AC system is able to compete economically while reducing the carbon footprint of data centers.

Based upon these findings, advanced power systems such as an integrated SOFC system and absorption chiller are efficiently synergistic, can reduce the carbon footprint of data centers while running on existing natural gas infrastructure, and can compete economically with conventional power and cooling technologies. Additionally, further reduction of carbon emission intensity by the injection of hydrogen may increase the viability of such integrated systems for the powering and cooling of data centers.

4.3 - Summary and Conclusions

The objective of this research effort is to evaluate the feasibility of thermal integration between an SOFC system and an absorption chiller for data center applications. To investigate this thermal integration, an integrated model was developed to explore the impact of adjustments to the operational parameters of fuel utilization and stack temperature on the electrical and chilling production. By adjusting the stack temperature and fuel utilization, it is possible to control the heat output from the SOFC system. Useful heat within the exhaust ranges from 90-140 kW and can utilized by a triple-effect Lithium Bromide absorption chiller to produce chilling for the computers. Capturing heat from the exhaust at desorber temperatures

between 150 and 190 °C, the chiller can achieve a maximum COP of 1.82. Paired with the thermal output from the SOFC, the absorption chiller can make between 160 and 260 kW of chilling for the servers. This capability indicates that by selecting the correct operational values for the fuel utilization and stack temperature, it is possible to both power and cool a row of servers using this integrated setup. The tradeoff between fuel utilization, stack temperature, and both SOFC and AC performance is studied.

Additionally, the primary energy savings from the integrated setup is explored and found to be between 18 and 30%. By defining the constraints of chilling, carbon emissions, and temperature rises in the cathode and anode, an operational envelope can be created within the resultant domain. A fuel utilization of 0.819 and a stack temperature of 861°C maximizes the PES ratio within the envelop and allows for 25.8% primary energy savings. This represents a large overall efficiency increase using an integrated system compared to traditional power and cooling strategies. Using these results and by implementing an active control strategy, it could be possible to further maximize the energy savings by allowing for diminished chilling capacity when it is not required.

Lastly, an economic model investigates the impact of the operational parameters on the levelized costs of electricity, chilling, and utility. The levelized costs of electricity are calculated to be between 35 and 42 $/MWh, which is optimistic but could be attainable at larger scale data center installations where cost at scale can be considered. The levelized cost of electricity tracks very closely with the SOFC system efficiency and is therefore higher at lower fuel utilizations. The levelized cost for chilling is calculated to be between 54 and 57 $/MWh and is mostly affected by the chiller capital cost which scales with chilling capacity. This high cost is due to the high complexity of the triple-effect absorption chiller and the included cost of a dry cooling tower. Interestingly, while higher fuel utilizations lead to a lower LCOE, the diminished chilling production increases the LCOC. These competing economic performances must therefore be reconciled. To do so, the costs for the electricity and chilling can then are combined and weighted to create a levelized cost of utility. Optimizing to minimize LCOU, it is apparent that the optimal operating condition for economic performance is the same as the optimal condition for maximizing primary energy savings. The synergy between the operational and economic performance presents the strengths of

such an integrated system. The optimized operating condition produces an LCOU 75.72 $/MWh that is economically competitive with conventional delivery, and the integrated system is even more competitive thanks to its lower emission intensity, high operating efficiency, future use of renewable hydrogen, and the distributed power's ability to eliminate backup power systems.

Chapter 5 - Dynamic Dispatch Control of Integrated SOFC and AC for Powering and Cooling Data Centers

Following the operational optimization of the integrated SOFC and triple-effect absorption chiller, the possibility of utilizing the optimized operational envelope to produce a dynamic dispatch control for the absorption chiller using the SOFC's operating parameters became apparent.

The objective of this study is to compare several integrated chilling configurations across a transient chilling profile to determine what architecture minimizes the carbon emissions of a data center the most.

5.1 - Methodology

This study focuses on the dynamic application of an integrated SOFC and AC system at a data center for providing power and cooling for the servers. It is possible to meet transient cooling loads of a hyper-scale data center by using the thermal integration between SOFC and AC. By changing the operating conditions of the SOFC, it is possible to modulate the thermal characteristics of the exhaust, thereby adjusting the performance of the absorption chiller. To investigate the possibility of an active dispatch control, two models were created: a data center thermal model and an integrated SOFC and AC system model. The system models were then combined and optimized to create an active dispatch control strategy.

5.1.1 - Data Center Model

In order to calculate the amount of cooling required for data center a MATLAB code has been developed. Inputs of the model are weather data associated with data center location including temperature, pressure, and relative humidity. The weather data are obtained from TMY from 2006 to 2016. In order to calculate the load, the acceptable weather condition for data center is required. Table 5.1 shows the boundaries that define the ASHRAE recommended and allowable environmental envelopes (ASHRAE, 2016).

Table 5.1 – ASHRAE 2016 Thermal Guidelines.

Parameter	Recommended Envelope	Allowable Envelope
Max Dry Bulb	27℃	32℃
Dew Point	5.5-15℃	5.5-18℃
Relative Humidity	60%	80%

Based on outside weather data, cooling zones for data center is defined in 4 regions (Economizer, Economizer+ Evaporative Cooling, Evaporative cooler, and Mechanical Cooling) based on ASHRAE recommendations (Metzger, 2011). Weather conditions with wet bulb temperature higher than 18.7℃ or dew point higher than 18℃ fall under mechanical cooling zone. The model calculates the number of hours that the system needs mechanical cooling for each of the location using the weather data.

5.1.2 - Integrated System

The integrated SOFC and AC system model is scaled at 200 kW electrical power output to match a row-level configuration for the servers. The SOFC runs on natural gas and its configuration is based on existing commercial SOFC systems. The SOFC produces electricity that runs the servers and thermal energy, some of which is lost, but primary exits through the exhaust. The exhaust is then connected to an AC system which captures thermal energy from the exhaust stream. The AC system utilized the captured heat to boil refrigerant out of solution and produce chilling. Lower grade heat from the AC is then rejected to a cooling tower.

The SOFC model is a balance of plant (BOP) model that simulates all of the heat exchange, external reforming, internal reforming, condensation, combustion, and mixing of the SOFC system. The external reformation is approximated as a fixed percentage of chemical equilibrium. Electrochemical cell potentials are calculated based on cell temperature, fuel concentrations, losses in the electrolyte, and losses due to mass transfer.

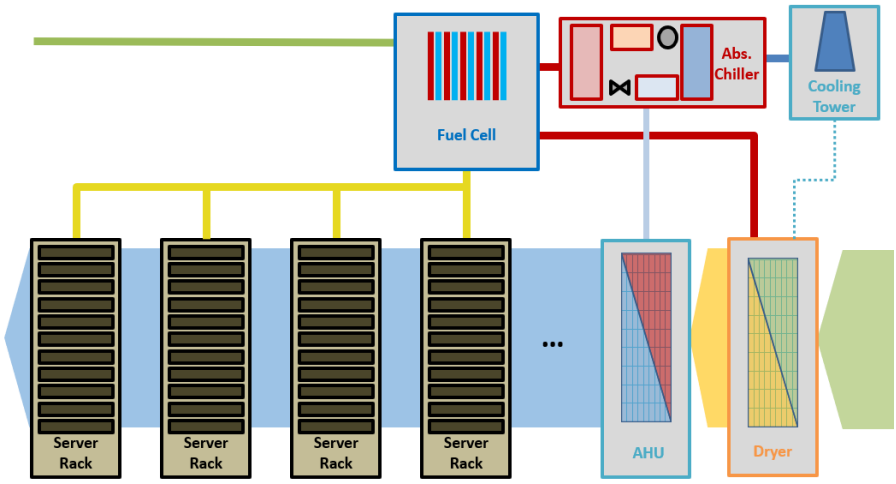

Figure 5.1 – SOFC and AC Integrated Concept for Data Centers

When considering the implementation at data centers, there are a few constraints that govern the commissioning of such an integrated system. First, data centers require incredibly high reliability of electric power supply, therefore a single SOFC power system would not be very feasible due to long restart times (24 hours) and a required backup power supply. The implementation of SOFC systems at rack level, like the concept proposed by Zhao et al., can increase the robustness of the power supply, but radically increases operation and maintenance costs. Additionally, commercial absorption systems are more typically produced at row level capacities (200 kW). Due to these challenges, a row-level configuration was selected as the most relevant for and integrated SOFC and AC system. The analysis at the row level can be applicable to smaller data centers that may utilize similar groups of servers. The integrated system is therefore investigated to optimize its ability produce electricity and chilling for the servers within a row.

To optimize a thermally integrated AC with an SOFC for the application of power and cooling in a data center, a mathematical model is developed in MATLAB and paired with property data from Engineering Equation Solver (EES). The integrated system consists of three models: a thermodynamic model of an SOFC, a floating state point model of a Lithium Bromide (LiBr) AC, and an economic model for the installation and operation of the system.

5.1.3 - Waste Heat Recovery Optimization

When operating the integrated SOFC and AC systems, the goal is to operate at the maximum possible system efficiency to lower CO2 production. However, in certain cases, maximizing the individual component efficiency will sometime lead to poorer overall system performance. For example, the waste heat from the SOFC exhaust must be captured by refrigerant solution in the desorber of the absorption chiller. In a physical system, the temperature at which the desorber captures heat from the exhaust would depend mostly on the physical layout, heat transfer surface area, and high side pressure in the desorber. When simulating this physical interaction, we have the flexibility to adjust the temperature at which the desorber captures heat by assuming that the physical configuration can be constructed to match the optimized solution.

When selecting the temperature of the high side desorber, the initial approach was to maximize the efficiency of the absorption chiller. This strategy resulted in selecting higher desorber temperatures, at which the absorption chiller would operate more efficiently with a higher COP. However, when considering the overall system, this strategy does not produce the most effective result. By increasing the desorber temperature to maximize the AC efficiency, the capacity of waste heat that can be utilized is reduced. Capturing waste heat at lower desorber temperatures allows more of the waste heat to be captured and increases the AC chilling capacity correspondingly. Since the deliverable of the AC system is ultimately the chilling capacity, an alternative strategy of selecting a desorber temperature that maximizes chilling capacity is adopted. For each operating point within the exhaust's domain, an optimal desorber temperature is calculated that maximizes the chilling capacity. These optimal desorber temperatures for a triple-effect AC are shown below in Figure 5.2.

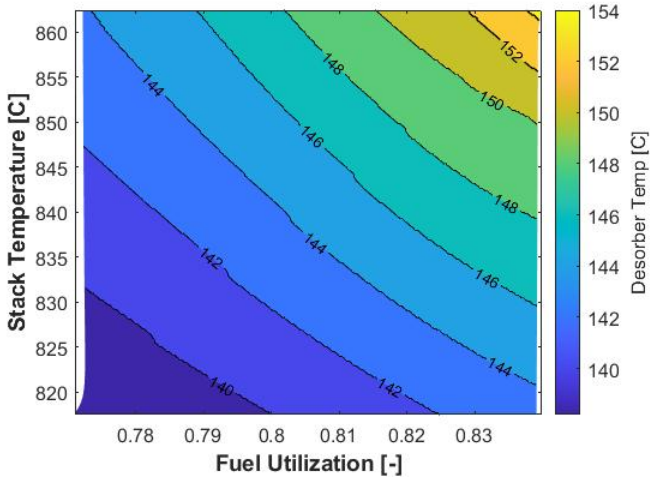

Figure 5.2 – Triple-Effect Absorption Optimized Desorber Temperatures.

Note how in Figure 5.2 the desorber temperature increases with stack temperature and fuel utilization. These trends are mirrored in the double and single effect optimizations but are at lower temperatures: 90-110 °C for double effect and 57-67 °C for single effect. The desorber temperature trends follow the exhaust temperature of the SOFC, with higher temperature exhaust allowing for higher desorber temperatures.

Utilizing the optimized desorber temperature to calculate the waste heat recovery capacity, the absorption chiller model then calculates the chilling capacity for each configuration. The chilling capacity for the triple, double, and single effect absorption chillers are shown in Figure 5.3.

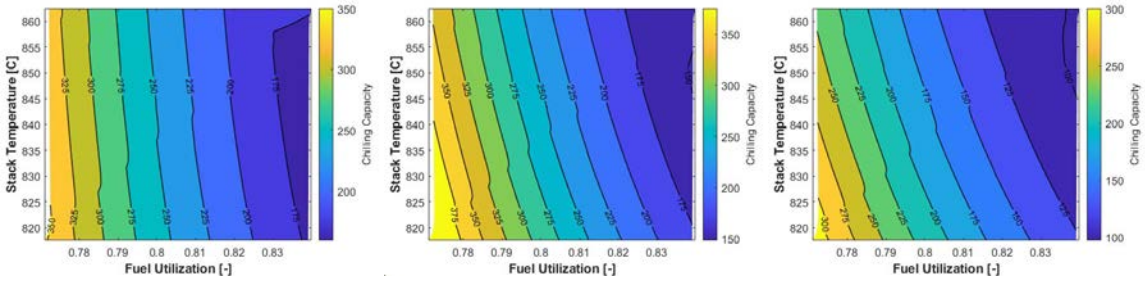

(a) Triple Effect (b) Double Effect (c) Single Effect

Figure 5.3 – Optimized Absorption Chilling Capacities.

The optimized chilling capacities for each level of absorption, shown in Figure 5.3, illustrate that as the SOFC fuel utilization decreases, the amount of available chilling increases. This increasing effect makes sense because the utilization is also heavily tied to the SOFC electrical efficiency. Additionally, there is an inverse correlation between stack temperature and chilling capacity showing that the hotter the stack, the less chilling is available. This phenomenon is due to the heavy sensitivity the exhaust heat capacity to its mass flow, which is primarily made up of air. The lower stack temperatures require higher airflow to maintain the cooler temperature and therefore have higher mass flow out of the exhaust. Note however that the triple effect configuration is much less sensitive to this effect compared to the double effect and single effect. The single effect is more susceptible to capacity decrease due to higher stack temperature because the low desorber temperature means a more consistent temperature delta between the exhaust gasses and the waste heat recovery.

5.1.4 - Integrated System Optimization

Now that the system performance of both the SOFC and the AC is optimized for every point in the operational domain, the question becomes where in the domain should the system operate to minimize the carbon emissions of the data center?

First, there are several boundary conditions that need to be imposed on the operation of the integrated system including: temperature rise in the anode, temperature rise in the cathode, maximum stack temperature, maximum fuel utilization, and maximum CO_2 emission intensity. These boundary conditions are listed in Table 5.2.

Table 5.2 - Integrated System Boundary Conditions.

Boundary Condition	Value	Unit
Maximum Temperature Rise: Anode	70	Δ°C
Maximum Temperature Rise: Cathode	80	Δ°C
Maximum Stack Temperature	865	°C
Minimum Stack Temperature	815	°C
Maximum Fuel Utilization	0.84	-
Maximum CO_2 Emission Intensity	0.449	kg/kWh

Once the SOFC operating boundary conditions are implemented, an operational envelope can be produced in which the integrated system can operate. The integrated system's operational envelop is shown in Figure 5.4 with the system's emission intensity indexed.

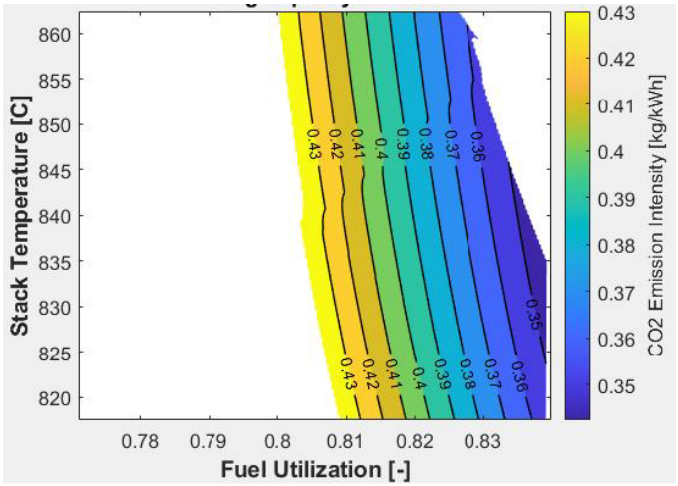

Figure 5.4 – Integrated System Operational Envelope.

Reviewing the operational envelope in Figure 5.4 and looking to minimize the CO_2 emission intensity, it is apparent that the integrated system should run at the maximum fuel utilization with a stack temperature of 834.3 °C. However, recall from Figure 5.3 that while the SOFC may be minimizing its carbon output, the chilling capacity available might not be enough to cover the cooling demands of the server row. To make a determination for the optimal operating condition, the CO2 production from the SOFC must be considered in conjunction with the electrical and thermal demands of the data center. Additionally, consider that based on the transient data center model that the cooling needs of a server row vary greatly over the course of a year. To better understand how the chilling requirement affects the SOFC performance, an additional boundary condition is added: chilling demand.

When applying the chilling demand boundary condition, the quantity of chilling is incremented from the minimum capacity within the initial operating envelop to the maximum capacity. By doing so, it is possible to gain an understanding how the integrated system should be run to minimize CO_2 emissions

while meeting whatever chilling demand is required. The incremented approach for the chilling boundary condition is shown in Figure 5.5 and Figure 5.6.

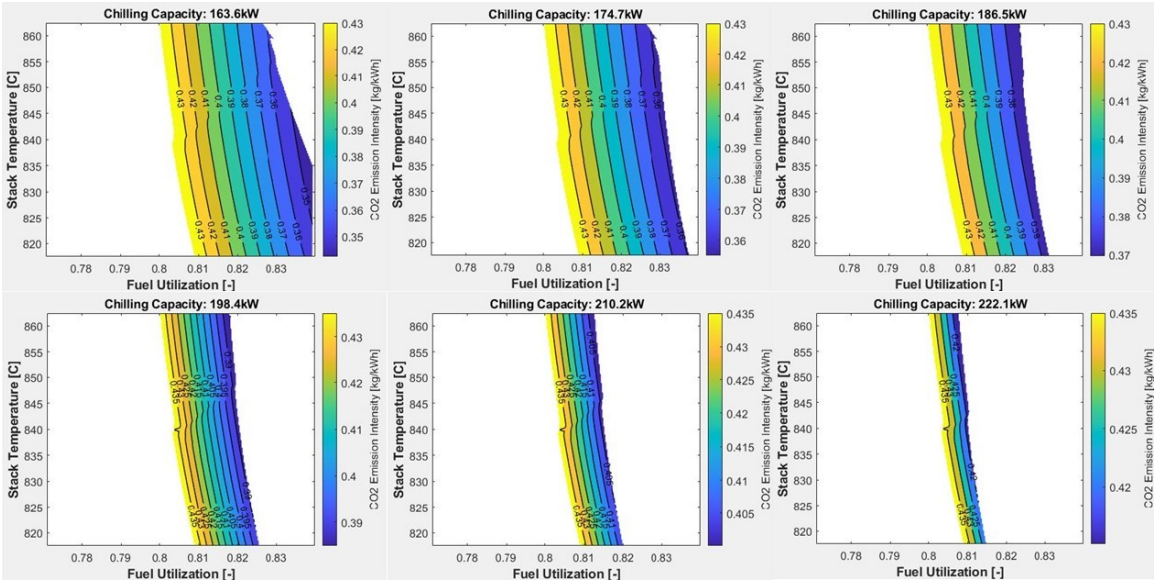

Figure 5.5 – Incremented Operational Envelope for Triple Effect Absorption Chiller

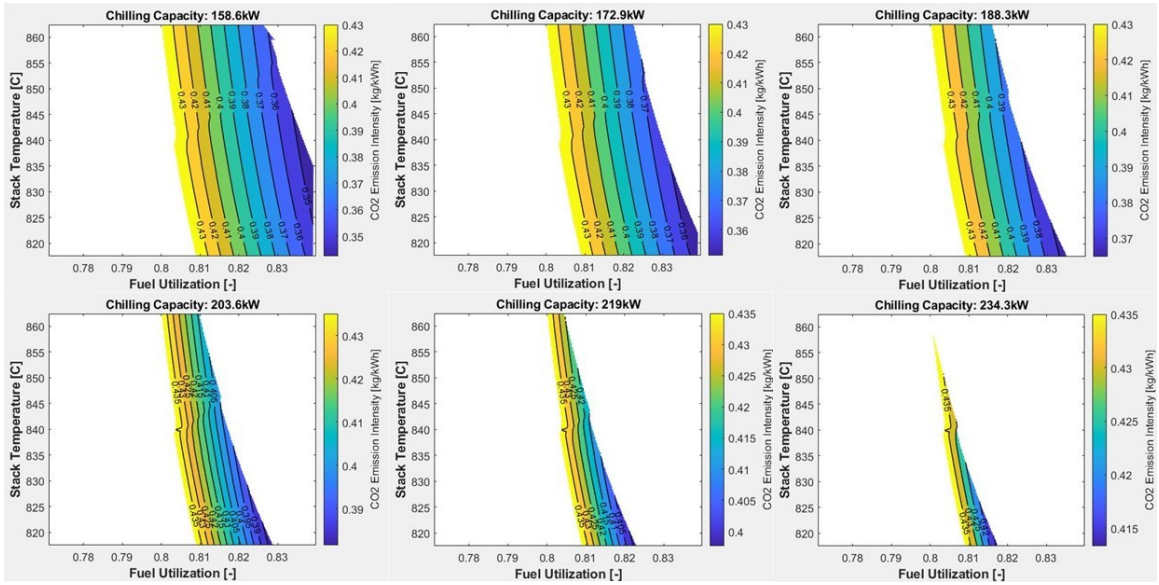

Figure 5.6 – Incremented Operational Envelope for Double Effect Absorption Chiller.

In Figure 5.5, notice how the chilling boundary condition is incremented from 163.6 kW to 222.1 kW. As the chilling boundary condition increases, the operating point with the minimum CO_2 emission intensity increases its stack temperature and lowers its fuel utilization. The relatively low sensitivity of the triple-effect absorption chiller's capacity to the stack temperature forces the optimal point of operation towards the maximum stack temperature.

However, in Figure 5.6, notice that as the chilling boundary condition is incremented from 158.6 kW to 234.3 kW, the operating point with the minimum CO_2 emission intensity instead follows the maximum fuel utilization boundary until it hits the minimum stack temperature boundary. This alternative behavior is a result of the increased sensitivity of the double-effect absorption chiller to the stack temperature. While one would assume that both AC architectures would follow similar optimal routes, this study shows that the dependence on stack temperature ultimately affects how the optimization unfolds. It should be noted that the single-effect absorption chiller's operational envelope development follows a very similar pattern to the double-effect's and is therefore not shown.

Beginning with the data center cooling requirements outlined by the data center thermal model and applying the optimized SOFC and AC system, it is possible to see how the integrated system can be exercised to minimize the carbon footprint of the data center.

5.1.5 - Thermal Storage Model

To complement the thermally integrated SOFC and absorption chiller, a thermal storage model was developed to assist during the transient simulation in the case that the integrated chiller cannot meet the needed chilling requirement for the data center. The thermal storage is assumed to be bulk energy storage to which the absorption chiller can absorb heat at its full capacity regardless of the state of charge. Additionally, it is assumed that the thermal storage is able to supply cold water to supplement the absorption chiller's capacity regardless of its operating temperature. To ensure the validity of these assumptions, the thermal storage is modeled as cold water storage which operates between the temperatures of 10 and 28 °C.

Keeping the thermal storage within this range helps ensure that the assumptions hold true during transient operation.

When considering thermal storage, it is also important to consider the thermal losses accrued over the operating period. The thermal loss is calculated assuming a constant thermal resistance between the storage and the ambient. The thermal loss is calculated using the Equation below.

$$\dot{Q}_{loss} = \frac{T_{amb} - T_{storage}}{R_{ins}} \tag{5-1}$$

During transient operation, the thermal storage contributes additional chilling capacity at any point where the chilling available is less than chilling requirement from the data center model. Additionally, the thermal loss rate is multiplied by the time step to calculate the heat loss and applied during every time step. It is assumed that when no chilling is required and the thermal storage is full, the chiller is not operating and the only heat transfer from the storage is the thermal loss. However, when the thermal storage is not full, or at its lowest temperature, the absorption chiller recharges the storage by running at its minimum capacity. While there are conditions where having the chiller operate at its maximum capacity to increase the recharge rate, it was found that this strategy is not necessary to successfully operate the thermal storage over the course of a year.

The thermal storage capacity is set at the beginning of the year at its “full” state. The transient profile then applied to the integrated system and storage model to see if the storage is ever depleted past its minimum, or if it is not recharged before the end of the year. The storage size is then converted from energy units to kilograms of the storage medium, water, by assuming that the temperature operating range is between 10 and 28 °C.

It should be noted that the only chilling configuration that requires thermal storage is the single-effect configuration because its maximum chilling capacity is ~190 kW and can therefore not meet the maximum chilling requirement of 200 kW.

5.2 - Results

5.2.1 - Integrated System Optimization Results

Utilizing the methodology outlined for obtaining the optimal operating point for different chilling requirements, the controls required to operate the SOFC and AC system can be illustrated. Figure 5.7 illustrates how the SOFC electrical efficiency changes the stack temperature and fuel utilization are changed to meet the required chilling.

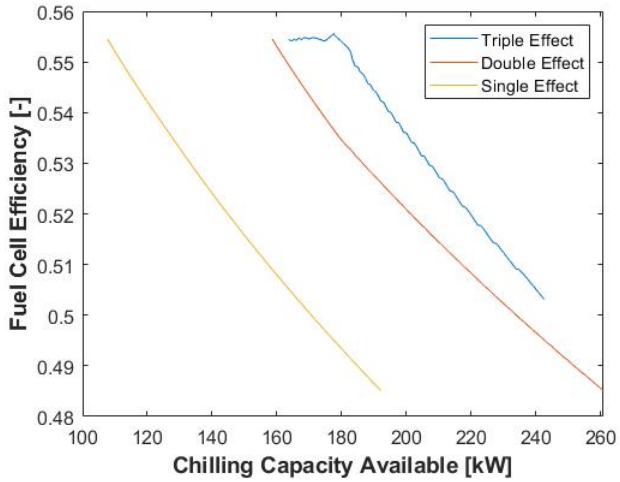

Figure 5.7 – SOFC Electrical Efficiency at Varying Chilling Requirements.

Looking at Figure 5.7, each of the absorption chiller architectures begin at the same starting efficiency when their chilling capacity is at its minimum. It is promising that each of these chillers can produce 108, 158, and 163 kW respectively at their minimum capacity when the SOFC is operating at its most efficient. However, considering that a data center can require chilling equivalent to the electrical consumption of the server computers, each system architecture will require the SOFC to operate at a lower efficiency to meet the 200 kW demand of a server row. The triple effect chiller can produce the 200 kW of chilling with the SOFC operating at the highest efficiency when compared to the double or single effect chiller.

To achieve the variable chilling output, the two operational controls over the SOFC system must be modulated to achieve the results shown in Figure 8. Following the trends shown in Figure 5.5 and Figure

5.6, we understand that the stack temperature and fuel utilization paths for the triple, double, and single effect absorption machines is varied. This effect is shown in Figure 5.8.

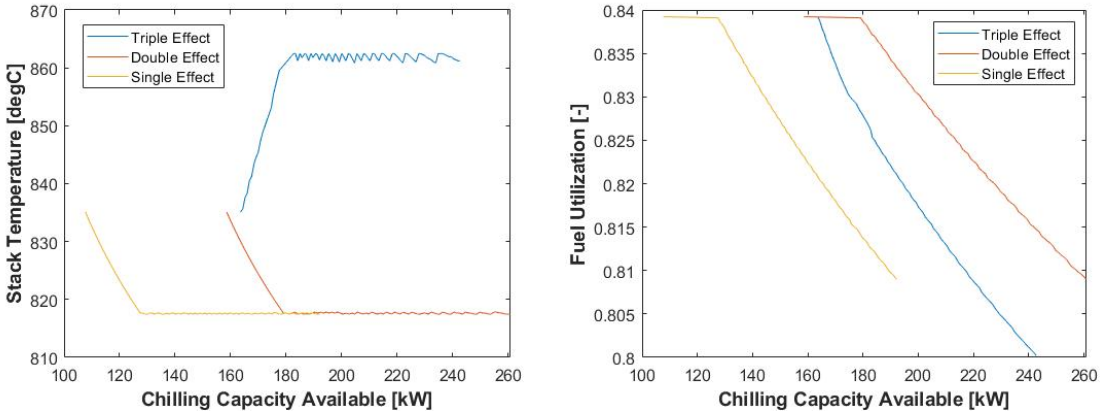

(a) Stack Temperature (b) Fuel Utilization

Figure 5.8 – SOFC Operating Parameters for Variable Chilling.

Looking at Figure 5.8a, the stack temperature at which the integrated system produces the chilling requirement at the minimum CO_2 emissions intensity follows two different paths. For the triple effect chiller, the stack temperature increases until it reaches the upper temperature boundary condition. Note that the non-linearities in this trend are due to the discretization's reduced resolution when iterating through the optimized operational envelope. However, for the double and single effect absorption chillers the stack temperature decreases immediately, reaching the minimum stack temperature and staying there until the maximum chilling is achieved. This behavior is due to the increased sensitivity of the lower effect systems on the exhaust mass flow rate as explained previously.

In contrast, Figure 5.8b shows that the fuel utilization trends for all three architectures are relatively similar. Each begins at the maximum fuel utilization of 0.84 and decreases as the chilling requirement increases. However, notice that the triple-effect chiller configuration requires the fuel utilization to decrease immediately. This is because as the chilling requirement increases the operational envelope follows the temperature rise boundary conditions for the cathode and anode until it reaches the maximum stack temperature. Therefore, fuel utilization cannot stay at the maximum for the triple-effect architecture unlike

the double and single effect systems which do not run into any boundary conditions and are therefore allowed to stay at the maximum fuel utilization until they reach the minimum stack temperature. Finally, note that the fuel utilization at which the triple-effect system achieves its maximum chilling capacity is lower than the double or single effect systems at 0.8.

Finally, it is critical to understand how the CO_2 emission intensity changes through these operational adjustments. Figure 5.9 illustrates how the system emission intensity changes at varying levels of chilling requirement.

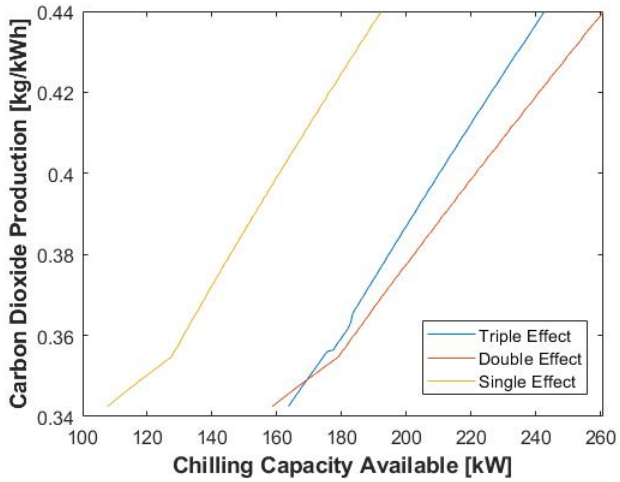

Figure 5.9 – System Emission Intensity at Varying Chilling Requirements.

Reviewing Figure 5.9, the carbon emission intensity of the integrated system begins at the same level for all three chilling architectures. For the single and double effect systems the rate at which the CO_2 emission intensity increases is defined by the boundary condition which the operation is following. As the fuel utilization stays constant and the stack temperature decreases the increase in emission intensity per unit chilling is relatively low. However, as the fuel utilization changes and the stack temperature stays constant the emission intensity increases more drastically per unit chilling capacity.

In contrast, for the triple-effect absorption chiller the emission intensity increase per unit chilling capacity changes several times throughout the progression. First, the system follows the cathode temperature rise boundary condition as the stack temperature increases and the fuel utilization decreases.

The next boundary condition it tracks is the anode temperature rise, which follows a similar rate of increase but has a slightly lower emission intensity overall. Finally, the triple effect architecture follows the upper stack temperature boundary condition until it reaches its maximum chilling capacity. Note that the rate of emission intensity increase per unit chilling capacity is higher at the highest stack temperature versus the lower stack temperatures of the double or single effect systems. While the triple effect is expected to operate more efficiently, at the same capacity the double effect chiller produces less carbon emission intensity at capacities greater than 172 kW.

5.2.2 - Data Center Transient Demand Results

Given the performance of the integrated system at varying chilling requirements, it is now possible to see how the system performs when subject to a transient demand profile. Utilizing the thermal model for a data center, a representative year-long chilling requirement profile is generated. The location selected for the representative profile is San Antonio, Texas. This location is selected due to its high level of chilling required thanks to the hot and humid ambient conditions seen during the summer. Using the geographic data and the data center thermal model, the chilling demand profile for a data in San Antonio is simulated and is shown in Figure 5.10.

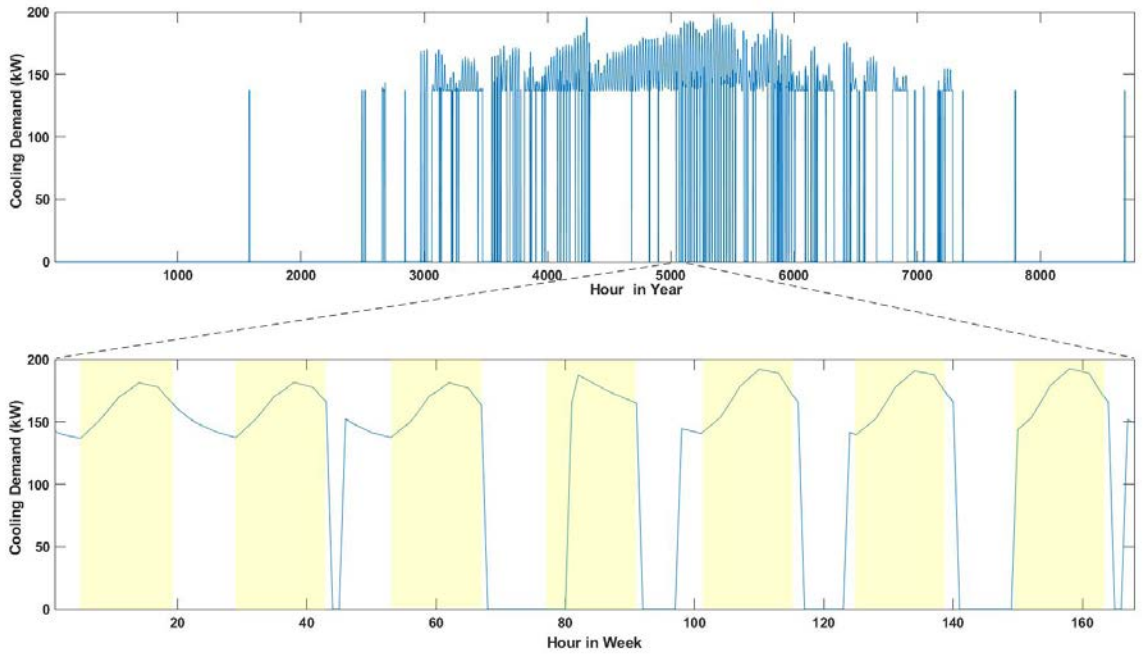

Figure 5.10 – Chilling Demand Profile for San Antonio, Texas.

Note that for the purposes of this study, the demand profile is scaled to match the server row level that has been under analysis thus far at a maximum of 200 kW. Looking at Figure 5.10 it is apparent that at different seasons, the chilling demand varies greatly. During the colder winter spring months, it is possible to utilize direct cooling, or the induction of ambient air into the data center, to cool the computers. However as ambient temperatures rise during the summer, more mechanical chilling is required. The transient profile for the chilling demand reaches its maximum in the late summer, but it should be noted that even during the summer there is a clear day and night thermal cycle. The inset of Figure 5.10 illustrates an example week during this period where the mechanical chilling is required during the day, highlighted in yellow, but is not required during the night so the demand falls to zero.

This simulated chilling demand profile is then used to exercise the integrated thermal model. Note that the hourly resolution of the chilling demand profile allows the integrated model to be assumed at a pseudo-steady-state operation.

Note however that the maximum chilling demand of the yearly profile exceeds the maximum chilling capacity of the integrated single-effect absorption chiller. To meet the transient chilling demand, it is

assumed that the single effect chiller can be paired with a thermal storage system to overcome the periods when the chiller's capacity is unable to meet the demand. Utilizing the thermal storage model, the single effect chiller is exercised through the yearly chilling requirement profile. The storage utilization of the integrated SOFC and single effect absorption chiller are shown in Figure 5.11.

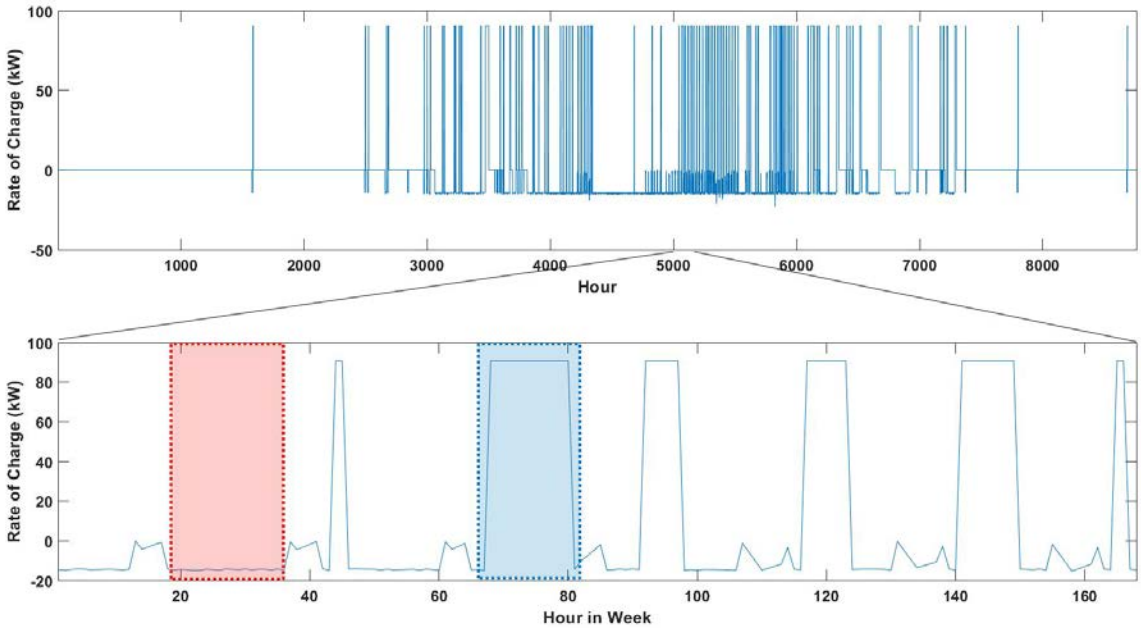

Figure 5.11 – Storage Utilization by Integrated Single-Effect Chiller.

Looking at Figure 5.11, it is apparent that the thermal storage system is only utilized during the hotter summer months when the chilling requirement exceeds the capacity of the single-effect chiller. Within Figure 5.11s inset, the red highlighted area demonstrates that when the chilling requirement exceeds the absorption chiller's capacity cold water is drawn from the storage to supplement and meet the demand. Conversely, the blue highlighted area shows that during the night or at points where chilling is not required the single-effect chiller is able to recharge the thermal storage by cooling the storage medium. What is promising is that the chiller is able to recharge the storage during these periods even when operating at its minimum capacity, which in turn minimizes the system's carbon emissions. Integrating across the storage utilization, it is possible to predict the required storage capacity and its state of charge throughout the simulated year. Figure 5.12 illustrates the thermal storage state of charge throughout the year.

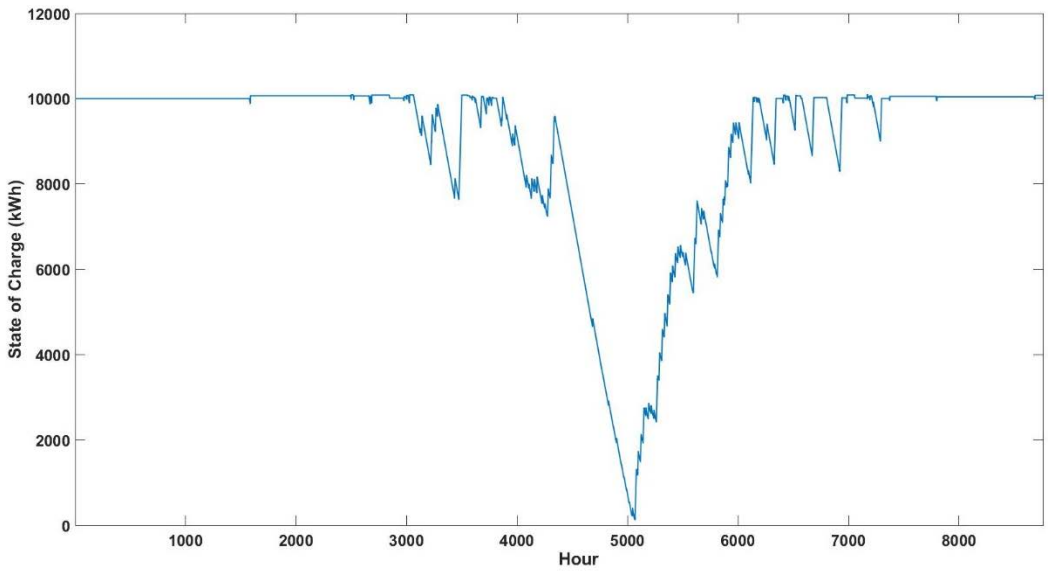

Figure 5.12 – Thermal Storage State of Charge.

Notice in Figure 5.12 that the thermal storage goes relatively unused for the winter and spring months but is highly required during the hotter summer months. Additionally, it is critical that the single-effect absorption chiller is able to return the thermal storage to its "full" state by the end of the year to ensure successful continuous operation. Finally, the capacity of the thermal storage is estimated to be roughly 10,000 kWh, which when considering a liquid water, single-phase, thermal storage system equates to a liquid volume of roughly 473 m^3 (~125,000 gallons) for storage.

5.2.3 - Dynamic Dispatch Control Results

Now that all three absorption configurations can achieve the chilling capacity requirements of the simulated year, it is important to understand how each operates throughout the simulated transients. To meet the chilling demands, a dynamic dispatch control system is proposed that is capable of adjusting the SOFC operating conditions to actively allow the thermally integrated absorption chiller to produce the necessary chilling.

Since the carbon emission intensity has been selected as the objective function, one of the most important performance indicator for the integrated system is the electrical efficiency of the SOFC. Figure

5.13 illustrates how the SOFC electrical efficiency changes as the integrated system responds to the chilling demand requirements.

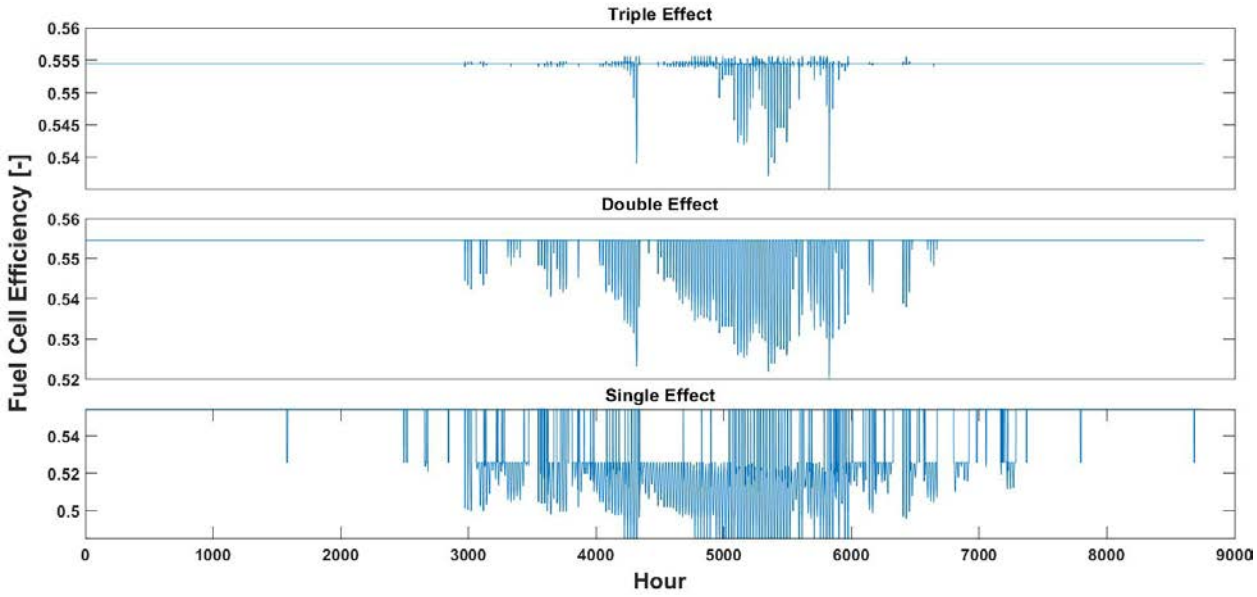

Figure 5.13 – SOFC Electrical Efficiency over Simulated Year.

Analyzing Figure 5.13, notice that the triple effect absorption chiller configuration is able to maintain higher SOFC electrical efficiencies throughout the year than either of the other two configurations. Conversely, the single effect absorption architecture requires the SOFC to remain at its lowest efficiency in order to maximize the available chilling capacity even when paired with the thermal storage. Overall, notice in Figure 5.13 that for each of the integrated systems with the dispatch control, the SOFC can operate at a higher efficiency for most of the year when there is no chilling requirement. This allows the yearly average of the SOFC efficiency to be much higher than if the system had simply been specified to meet 200 kW of chilling continuously. Similarly, it is possible to calculate the integrated system's carbon emission intensity as the SOFC is operated dynamically throughout the year. The resulting CO_2 emission intensity throughout the year is shown in Figure 5.14.

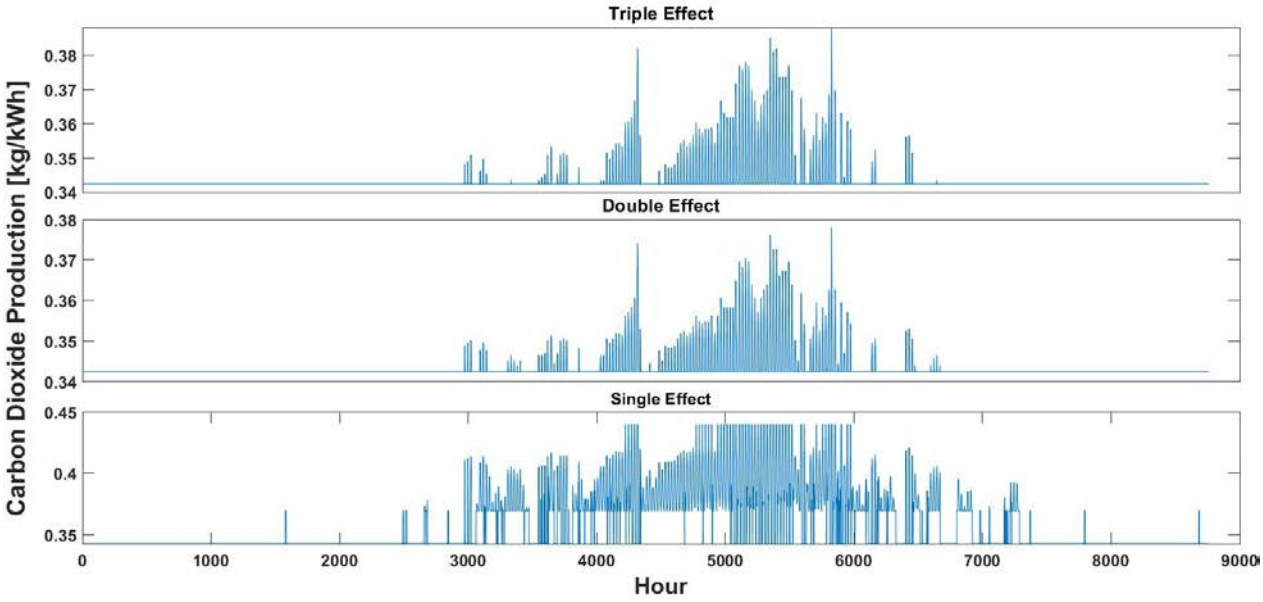

Figure 5.14 – Integrated System CO_2 Emission Intensity over Simulated Year.

Notice in Figure 5.14 that the CO_2 emissions track relatively inverse to the SOFC electrical efficiency shown in Figure 5.13. However, there are some discrepancies when comparing the triple and double effect configurations. Note that the maximum CO_2 emission intensity for the triple effect case is 0.387 kg/kWh while the double effect configuration's maximum is 0.377 kg/kWh. This increased production of CO_2 from the triple effect chiller is a result of the optimization shown in Figure 5.5. The optimized path of the triple effect configuration towards the maximum stack temperature creates a higher sensitivity of emission intensity to the chilling required, as shown in Figure 5.9. Ultimately this sensitivity produces more CO_2 while the triple effect system is operating at the higher chilling capacities. As expected, the single effect configuration operates at the highest emission intensity because the SOFC is required to operate at lower efficiencies throughout the year to maintain chilling capacity.

To assess the performance of the three different chilling configurations across the simulated yearly chilling demand profile, the cumulative CO_2 production is considered as the final output of the system. Table 5.3 lists the CO_2 emission intensity and carbon production for the simulated year with and without utilizing the dispatch control. The "continuous operation" case is created by assuming that the thermally integrated system is set up to produce the full 200 kW of chilling year-round and operated at steady state.

The total electricity production for a 210 kW SOFC over the course of the year is 1,838.7 MWh and combined with the emission intensity gives the CO_2 production in a year. To compare the performance of the novel thermally integrated system, a conventional delivery case was created. The conventional delivery assumes that all electricity is delivered by the electric grid at the average emission intensity of the Texas grid. Additionally, the chilling for the conventional case is assumed to be created by a mechanical refrigeration chiller at a COP of 5.

Table 5.3 - Configurations CO_2 Production.

Configuration	**Mean CO_2 Emission Intensity**	**Total CO_2 Production**
Triple Effect w/ Dispatch Control	0.3434 kg/kWh	631.7 tons
Double Effect w/ Dispatch Control	0.3433 kg/kWh	631.5 tons
Single Effect w/ Dispatch Control	0.3589 kg/kWh	660.0 tons
Triple Effect Cont. Operation	0.3869 kg/kWh	711.4 tons
Double Effect Cont. Operation	0.3780 kg/kWh	695.0 tons
Conventional Case	0.449 kg/kWh	868.34 tons

Reviewing the total year results presented in Table 5.3, it is apparent that the best configuration is the double-effect absorption chiller with the dynamic dispatch control. The double-effect configuration is only marginally better than the triple effect, producing 631.5 tons of CO_2 compared to the triple effect's 631.7 tons. Additionally, the single effect with dispatch control performs the worst of the three dynamic control cases, but still produces less CO_2 than both the triple and double configurations in continuous operation cases.

Comparing the dynamic dispatch control, continuous operation, and conventional cases it is apparent that implementation of the integrated system is beneficial when considering CO_2 production. The best performing chilling configuration is the double-effect absorption chiller in both the dispatch control and continuous operation cases. The double-effect configuration has a 19.9% and 27.2% reduction in total CO_2 for the continuous operation and dispatch control cases respectively.

Economic Effects of Chiller Capacity Factor

The introduction of actively controlling the absorption chiller to meet a transient demand profile, while dramatically reducing the carbon emissions of a data center, presents the challenge of a reduced capacity factor throughout the year. Instead of running the absorption chillers at their maximum capacity of 200 kW continuously, as was assessed in Chapter 4, the dynamic operation produces a significant reduction in the amount of chilling that is required to be performed over the course of the year. Compared to the steady-state operation, the capacity factor for the operation of a triple-effect absorption chiller for the Texas case as presented above is 0.271; meaning that the chiller is only operated at about one quarter of the time throughout the year. Due to this diminished operating time and output, but that which still requires the full 200 kW capacity at certain times, the levelized cost of chilling increases significantly. Considering the reduced capacity of both the chiller and the cooling tower, the LCOC for the triple effect configuration in the presented year increases from the optimized steady state value of 55.8 $/MWh to 145.6 $/MWh in the actively controlled case. This makes the absorption chilling configuration quite expensive compared to the conventional delivery case presented of chilling through a mechanical chiller. However, it should be noted that a designated mechanical chiller at a data center would suffer the exact same capacity factor if it is controlled to the same accuracy as the absorption chiller. Note that the LCOC of the mechanical chiller would not increase as much because while the chilling capacity across the year is lower, the electricity usage is also lower, which will lower the overall cost of operating the system.

The economic impact of the transient operation of the SOFC are much less pronounced. Since the SOFC is still most typically running near the design conditions of 200 kW power output, the only additional costs incurred are from additional fuel when operating at a slightly lower efficiency during the dynamic dispatch case. This cost increase can be factored into the LCOE of the SOFC system, which increases from 36.7 $/MWh in the optimized steady-state case, to 39.0 $/MWh in the actively controlled triple effect configuration.

Combining the effects of the reduced capacity factors of both chilling and electricity, the LCOU for the integrated system is similarly affected. Considering the triple effect configuration and calculating for the total utility provided in the active control scenario, the LCOU rises from 75.72 $/MWh, in the optimized steady-state case, to 193.0 $/MWh in the actively controlled case.

While the effects of a reduced capacity factor would be very similar between the triple and double effect configurations, the introduction of thermal storage for the single effect system changes the operation of the absorption chiller, requiring the chiller to offset both the chilling required by the data center and the thermal losses of the storage. This additional load, and the lower maximum capacity of the single effect chiller, translate to a much higher capacity factor of 0.637. This higher capacity factor would indicate that the increase in LCOC for the single effect system would not be as highly effected, however, it should be noted that in order for the single effect to operate in this manner, the installation of a thermal energy storage would drive the capital and operational costs higher.

Given that the feasibility of such a system is based both upon the operation and the economic competitiveness, the effects of this reduced capacity factor significantly change how feasible such a system could be. However, considering the directives of the companies which operate data centers, a certain value added for the removal of CO_2 should be considered. The ability to reduce the CO_2 production within a year by 27.2% presents a significant benefit to data center operations, but the value of these emissions reductions must be weighed against the significant increase in LCOC and by extension LCOU. Additionally, it can be assumed that the successful integration of absorption technology into primary chilling for data centers would also present an increased market size, therefore the capital price of the absorption chiller units should reduce if adopted at scale.

Lastly, when considering the different chilling configurations, assessing how the capacity factor and maximum chilling capacity installed affects the levelized costs for the integrated system could shed light on which chilling configuration would present the best economic viability.

5.3 - Discussion

The novel control strategy adopted for the operation of a thermally integrated SOFC and absorption chiller represents a significant opportunity to minimize the carbon emissions of data centers by exploiting the operational controls of the integrated system. The control of the SOFC is achieved by adjusting the fuel utilization and the stack temperatures: these adjustments are achieved by modulating the fuel, air, and water flow into the SOFC. Changing the SOFC's fuel utilization and stack temperature ultimately change how the BOP performs thermally and results in varying temperatures and flows of the exhaust. The adjustable characteristic of the exhaust offers the opportunity to control the chilling capacity of an absorption chiller which runs on the thermal energy from the exhaust gasses. Absorption chillers, like most thermally driven thermodynamic cycles, exhibit efficiency and capacity changes when the thermal source is altered. This downstream capacity control is then utilized to match the chilling demand requirements of a data center. For the purposes of this study a row-level server configuration was investigated since it corresponds well to the commercially available 200 kW SOFC units. Three chilling configurations were considered for comparison: triple-effect, double-effect, and single-effect absorption cycles.

Exercising the SOFC, absorption chiller, and data center models, the proposed active dispatch control strategy is developed. The first level of optimization is between the SOFC and the absorption chiller. The temperature at which the absorption chiller's high temperature desorber is operated, the capacity of waste heat that is recoverable is adjusted. While lower desorber temperatures offer greater opportunity for waste heat recovery, the efficiency of the absorption cycle decreases with lower desorber temperatures. To manage these contrasting effects, an optimization is written to maximize the chiller's chilling capacity. Interestingly the result of this optimization does not follow the maximum chiller's efficiency. Instead, it balances the increased capacity with the decreases in efficiency to pick an optimal desorber temperature shown in Figure 5.2. This optimized chilling capacity is characterized for each of the chiller configurations and is shown in Figure 5.3. When comparing the triple and double effect chiller's capacity it is interesting that the double effect system can produce more chilling than the triple. This phenomenon is a result of the

optimization mentioned because the double effect can operate closer to its maximum COP with lower desorber temperatures.

Additionally, it is noted that the double and single effect configurations are more sensitive to the mass flow of the exhaust and therefore the stack temperature. This is because when calculating the recoverable waste heat, the capacity is a function of the mass flow and the temperature difference between the exhaust and the desorber. Since the temperature delta is relatively large, small changes in the exhaust temperature affect the capacity relatively little, while the mass flow affects the capacity much more significantly. This increased sensitivity is important because when investigating the operational envelope of the integrated system in Figure 5.5 and Figure 5.6, the chilling capacity is introduced as a boundary condition. The slope of the chilling boundary condition forces the optimal operating point, when minimizing emission intensity, either towards the maximum stack temperature in the case of the triple effect configuration, or towards the minimum stack temperature in the case of the double and single effect configurations.

This deviating behavior ultimately defines how the optimized operating point for each configuration trends as the chilling requirement is adjusted. Figure 5.8 shows that a significantly different operating strategy is used when achieving the optimal operating point for the double and single effect configurations. While the triple effect configuration operates with the lowest emission intensity initially, the different operational path forces it to have higher emission intensity at higher chilling capacities. Interestingly, the triple effect configuration would represent the best case if the chilling requirement was less than 172 kW. However, because data center computers utilize their input electricity and turn it into heat, the application requirement of 200 kW of chilling would initially indicate that the double-effect configuration should perform better.

To further investigate the transient performance of the integrated system, a yearly chilling requirement profile is produced for a data center in San Antonio, Texas, USA. This geographic location was chosen because it is an example of a data center that exists in a climate where mechanical chilling is required. Certain geographic locations require no mechanical chilling because the ambient conditions remain cool enough during the year for direct air cooling or are dry enough for evaporative cooling during hotter days.

However, in hot and humid climate conditions, like those in Texas, mechanical chilling is required to offset the server thermal load often.

The data center model predicts that for a typical year mechanical chilling is required during late spring, summer, and early fall. This behavior is expected for the northern hemisphere and the chilling capacity rises and falls in both the annual pattern and on a day/night cycle illustrated in Figure 5.10. Figure 5.10 also illustrates an issue with the single-effect chilling configuration which is that the maximum required chilling capacity of 200 kW exceeds the maximum chilling available from the single-effect system. To resolve this issue and provide the extra capacity during the hotter summer months, a thermal storage solution is introduced for the single-effect configuration case.

The thermal storage model allows the single-effect chiller to produce more than its maximum capacity at times when required. However, the thermal storage requires recharging during times when not in use. Optimistically, the single-effect system is able to achieve the recharging while the integrated system is operating at is lowest emission intensity. The size of the thermal storage is then determined to be 473 m^3 (125,000 gallons). In comparison, this thermal storage size would require the equivalent of a single Olympic pool's water for 5 server rows. While thermal storage solutions have been built at this scale, it is important to consider the cost of constructing and maintaining such a thermal system could make the single-effect configuration impractical.

Applying the three different chilling configurations to the yearly chilling requirement, the efficiency of the dispatch control is exercised to operate the integrated system at the optimal point to minimize the carbon emissions. The advantage of the dispatch control is that the integrated system is able to operate at its maximum electrical efficiency when chilling is not required, but the SOFC can adjust its operation when chilling is required. The emission intensity of the integrated system follows a similar trend as the electrical efficiency, with periods when no chilling is required allowing for lower carbon operation. However, the higher sensitivity of the triple effect chiller means that at peak capacity conditions, this configuration produces higher emission intensity than the double-effect configuration as shown in Figure 5.14. Ultimately, this effect is seen in the cumulative carbon emissions for the integrated system across the year.

Table 2 demonstrates that the proposed dispatch control cases have the lowest carbon emissions for a year of operation. The double and triple effect chiller configurations with the dispatch control have the lowest carbon emissions and are relatively similar. Considering this result, the double effect case is the most effective solution for minimizing carbon production. Additionally, the double-effect absorption cycle is simpler than the triple-effect and commercial units are cheaper.

Also, when comparing the active control cases to the continuous operation cases, the effectiveness of the dynamic control is apparent. The single-effect configuration with dispatch control is able to outperform both the triple and double effect chillers in continuous operation. Additionally, the system performance in comparison to the conventional case demonstrates the significant improvement that an integrated SOFC and absorption chiller system has in producing the primary power and chilling for data centers.

Finally, investment into such integrated systems plays well to the existing natural gas infrastructure. However, as emission regulations develop and constrain further, injection of green hydrogen into the natural gas supply for the SOFC systems can further reduce the emission intensity of the integrated system. This immediate feasibility with longer term robustness is promising for the adoption of such systems for this application.

5.4 - Conclusions

In order to combat climate change and reduce pollutant emissions, the data center industrial sector is striving to mitigate its carbon, and criteria pollutant emissions. The movement towards clean, robust energy conversion has introduced solid oxide fuel cells (SOFC) as promising power generation platforms for primary electricity production. SOFC system's ability to run on the existing natural gas infrastructure and the ability to shift towards green hydrogen promotes their feasibility. An additional benefit is the opportunity for cogeneration from their high quality waste heat. This study investigates the possibility of integrating an SOFC with an absorption chiller to produce primary electric and chilling for data centers.

A mathematical model of the integrated SOFC and absorption chiller was created and optimized to compare three different integration configurations: triple-effect absorption, double-effect absorption, and

single-effect absorption chilling. The operation of the SOFC can be controlled by adjusting the stack temperature and the fuel utilization. These adjustments change the electrical and thermal outputs of the SOFC and allow for control over the operation of the absorption chiller. Utilizing this ability to control the chilling capacity by altering the SOFC operation, a dynamic dispatch control strategy is proposed.

Chapter 6 - Experimental Setup

The proposed thermally integration between an SOFC and absorption chiller can be shown through the modeling presented previously to be advantageous in mitigating the carbon emissions of data centers. However, in parallel to the modelling effort an experimental test stand was constructed to verify the simulated findings, explore real world challenges of the thermal integration, and present a laboratory scale demonstration of the concept.

6.1 - Concept

To explore the real-world feasibility of an integrated SOFC and absorption chiller system for providing power and cooling for a server rack, an experimental test stand was constructed. The objective of the test stand is to produce electricity using SOFCs for a server rack while also producing cold air to cool the servers using an absorption chiller that runs on the waste heat in the fuel cell exhaust. The first step towards the experimental setup was the creation of a process and instrumentation diagram (P&ID). The diagram that was utilized to begin the layout of the laboratory experiment is shown below in Figure 6.1 below.

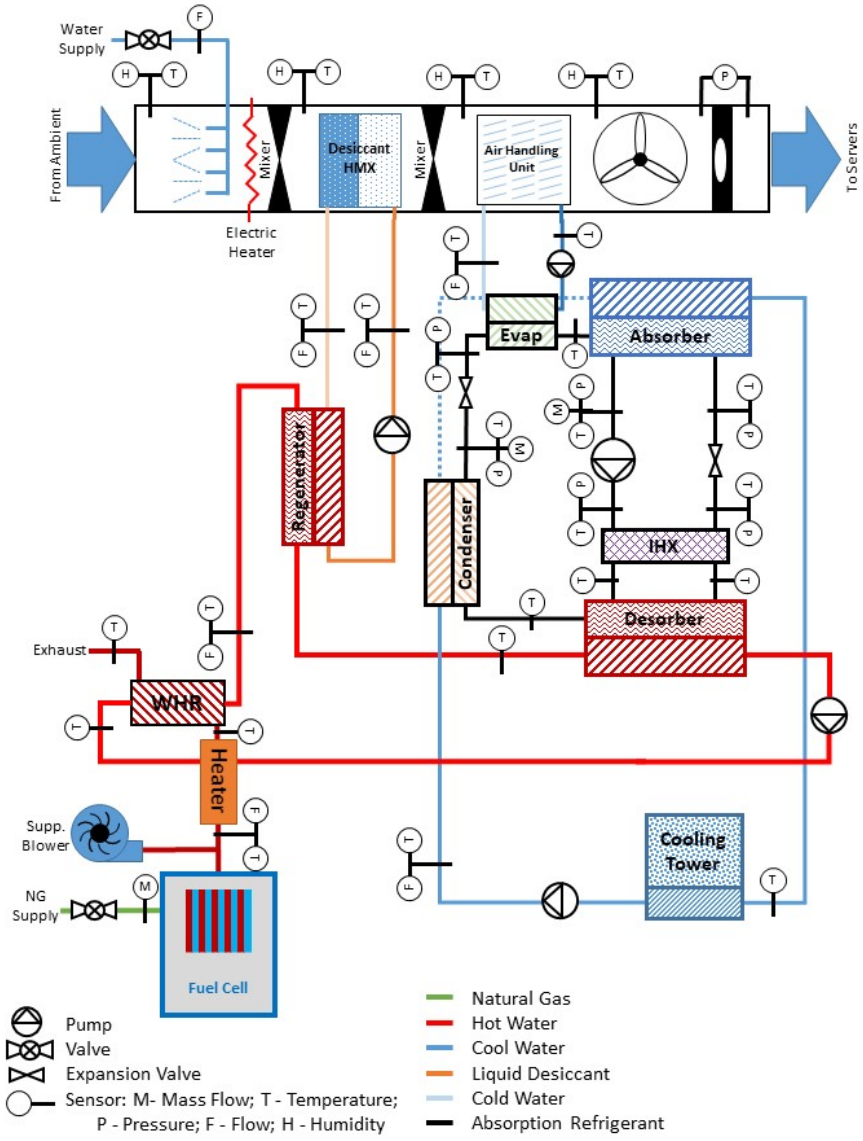

Figure 6.1 – Initial Experimental P&ID.

A laboratory scale experimental setup was constructed with full control and instrumentation to assist in operation and optimization of an integrated SOFC absorption chilling system. The final laboratory setup is shown in Figure 6.2.

Figure 6.2 – Experimental Setup.

6.1.1 - CAD Layout

In designing the laboratory scale experiment, a dedicated laboratory space was selected in the Engineering Laboratory Facility. The laboratory space was then measured and drawn up in Solidworks including doors, access points and other immovable fixtures. Additionally, an overhead structure was designed to carry electrical conduit, signal cables and water lines without interfering with the rest of the setup. The CAD layout can be found in Figure 6.3 and Figure 6.4 with both the top and perspective view shown.

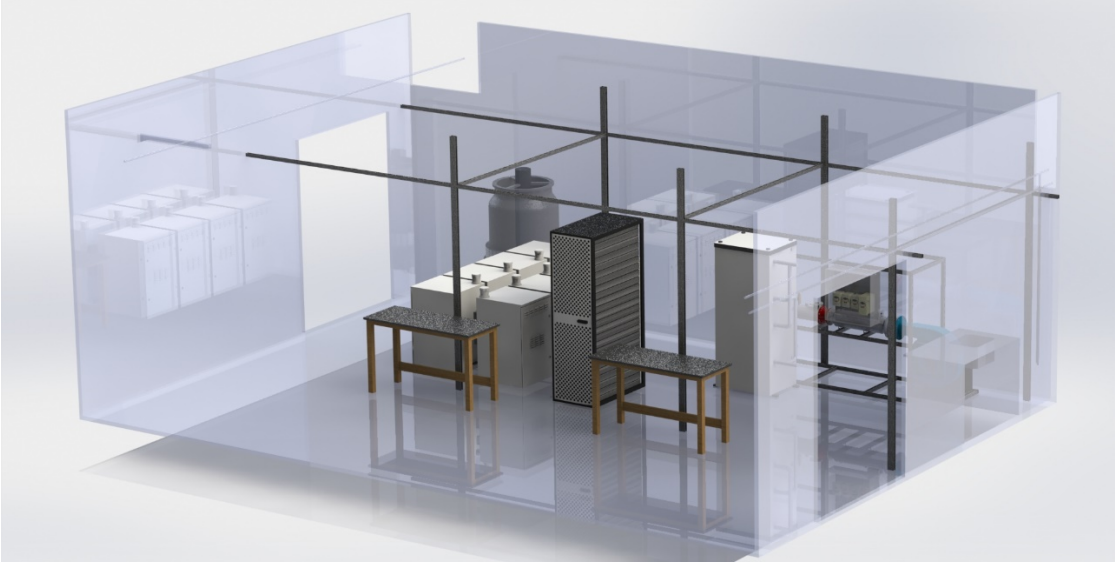

Figure 6.3 – Perspective View of Laboratory Layout.

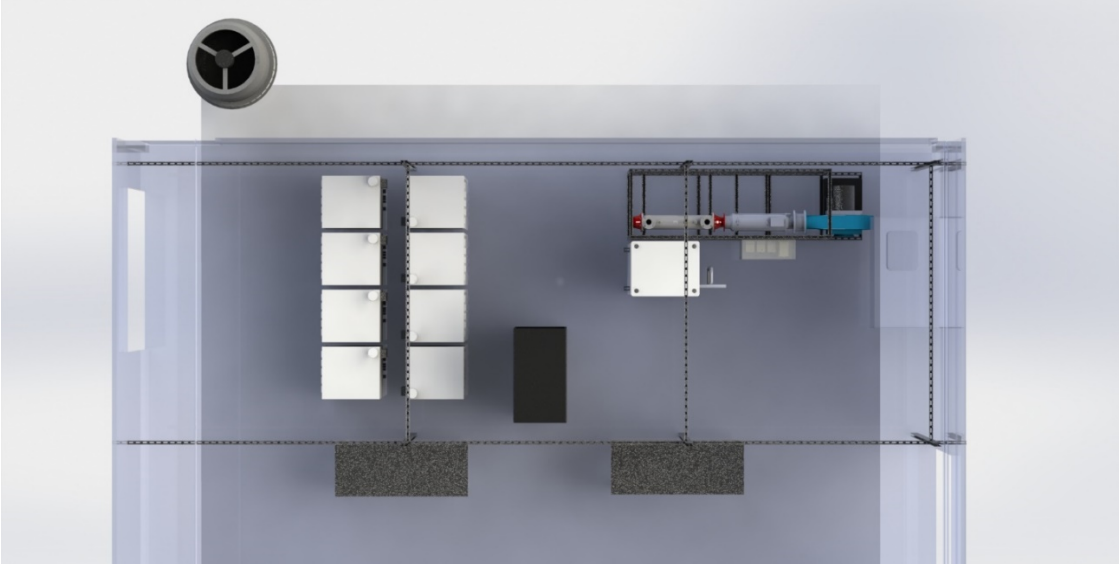

Figure 6.4 – Top View of Laboratory Layout.

The CAD layout had to consider positioning of the eight fuel cells (left in Figure 6.4) in such a manner that they could all be powered and connected easily. Additionally, access to the servers for software operation and maintenance was also considered while creating the most streamlined process air stream possible. The absorption chiller test stand (upper right in Figure 6.4) was designed to be modular and

movable as one unit should the need arise. By designing the lab space layout in CAD, it was possible to streamline the connections and operation of the test stand.

6.2 - Solid Oxide Fuel Cell Systems

To achieve the objectives of the experiment it is necessary to operate a solid oxide fuel cell system which provides power to the server rack. To simplify the experimental work, a commercially available SOFC package was selected which allowed out-of-box operation. Additionally, the SOFC's power output must match the laboratory scale of a single server which consumes ~15 kW nominally.

6.2.1 - BlueGEN SOFC Systems

The SOFC system that was selected was the BlueGEN SOFC cogeneration system from Solid Power. Each BlueGEN system produces 1.5 kW of electricity and runs on natural gas. These systems are designed as residential appliances and are roughly 1m x 0.6m x 0.6m. The system container is shown in Figure 6.5.

Figure 6.5 – BlueGEN System.

The BlueGEN systems operate at a nominal thermal efficiency of 62% with the potential for further utility in an optional hot water supply loop that can provide hot water to a residence.

To meet the single server rack scale selected for the laboratory setup, an array of eight BlueGEN systems was obtained to provide a total of 12 kW to offset the electrical consumption of the servers. All eight BlueGEN systems are connected to a common electrical source which then provides the power to the

server rack. The system is supported by the electrical grid of the laboratory because the internal inverters in the BlueGEN systems require a valid grid connection to operate and constructing an electrical island with proper load balancing is outside of the scope of this experiment.

6.2.2 - Operation

The BlueGEN SOFC systems are semi-autonomous systems operated remotely by the manufacturer, Solid Power. Each BlueGEN system has independent operational controls built in to maintain the desired fuel utilization and power output. These controls are not accessible for adjustment within this experiment, so all testing where manipulation of these parameters is necessary require contact with the manufacturer.

The only controllable parameter for these systems is the power output level of the BlueGEN systems which is adjustable in an online portal where the power output profile is adjustable as a constant or based on a schedule. Using this interface, the BlueGEN systems were exercised through a set power profile designed to explore the full range of power outputs and indirectly the fuel utilization. The results of this exercise are discussed later in the results chapter.

Additional control of the BlueGEN systems require the remote control by Solid Power. By communicating with the commissioning engineer, a variety of fuel utilizations and stack temperatures can be controlled for.

6.2.3 - Installation

The BlueGEN systems each require six points of connection to operate: electrical, fuel, exhaust, water, drain, and internet. Each of these subsystems and the designs created to serve the array of fuel cells will be detailed here.

BlueGEN Electrical Connections

The BlueGEN systems require an electrical connection for two reasons, to successfully operate during startup and to export the electricity produced during normal operation. Additionally, as mentioned earlier

the internal inverters in the BlueGEN systems require a valid grid connection to export electricity properly. To facilitate the electrical export and make it compatible with the laboratory's electrical connections, the following electrical configuration was designed and is shown in Figure 6.6.

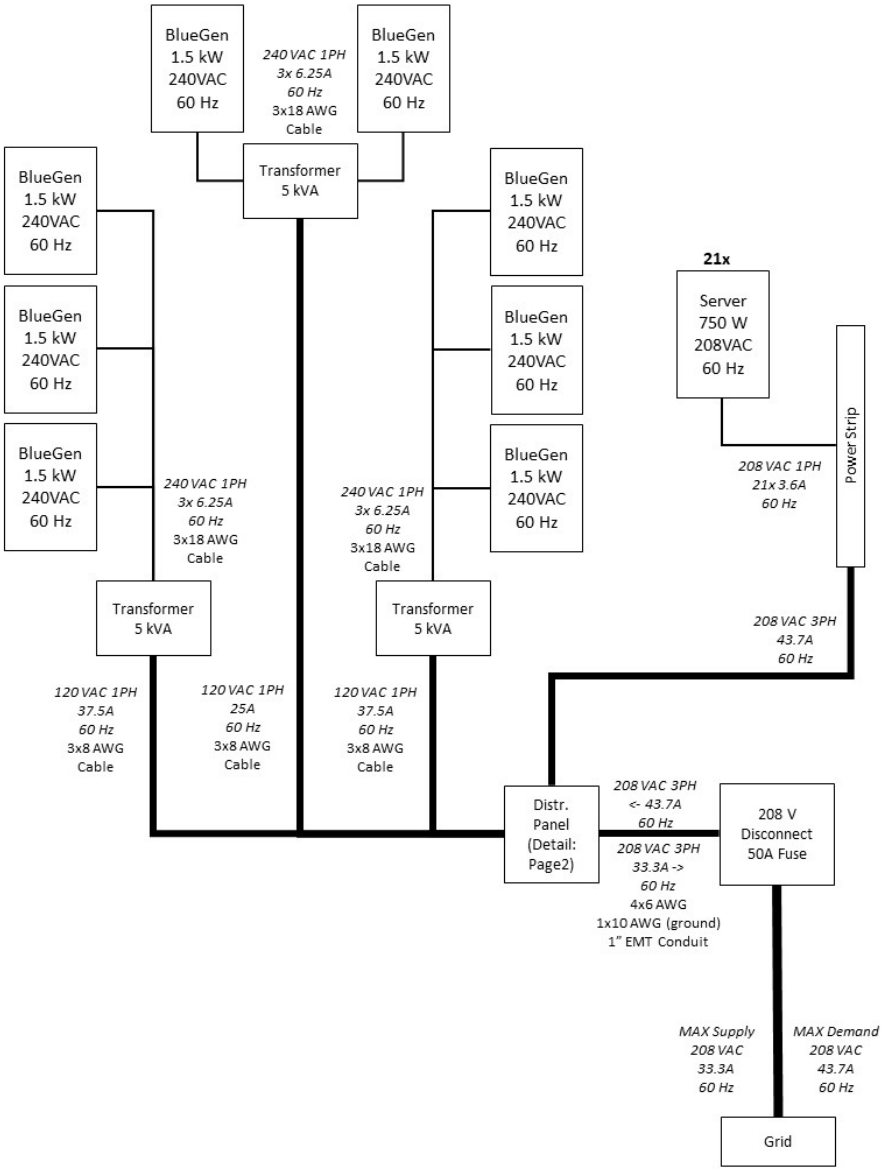

Figure 6.6 – BlueGEN System Electrical Connection Design.

First, the eight BlueGEN systems were split into three banks to match the three-phase connection available in the laboratory. Two banks of three and one bank of two were adopted to help balance the load

across the three phases and took into consideration the installation of a ninth BlueGEN system which is a part of a different experiment.

The BlueGEN systems produce electricity at 240 VAC at a frequency of 60 Hz after the appropriate configuration of the internal inverter. The 240 V is transformed to 120 V using a general-purpose transformer rated for 5 kVA. The neutral line downstream of the transformers is constructed using a grounded neutral. One transformer per bank of BlueGEN systems connected in parallel is used to distribute the load. The three banks of 120 V electricity are connected to the three phases of the 208 VAC grid connection as shown in Figure 6.7.

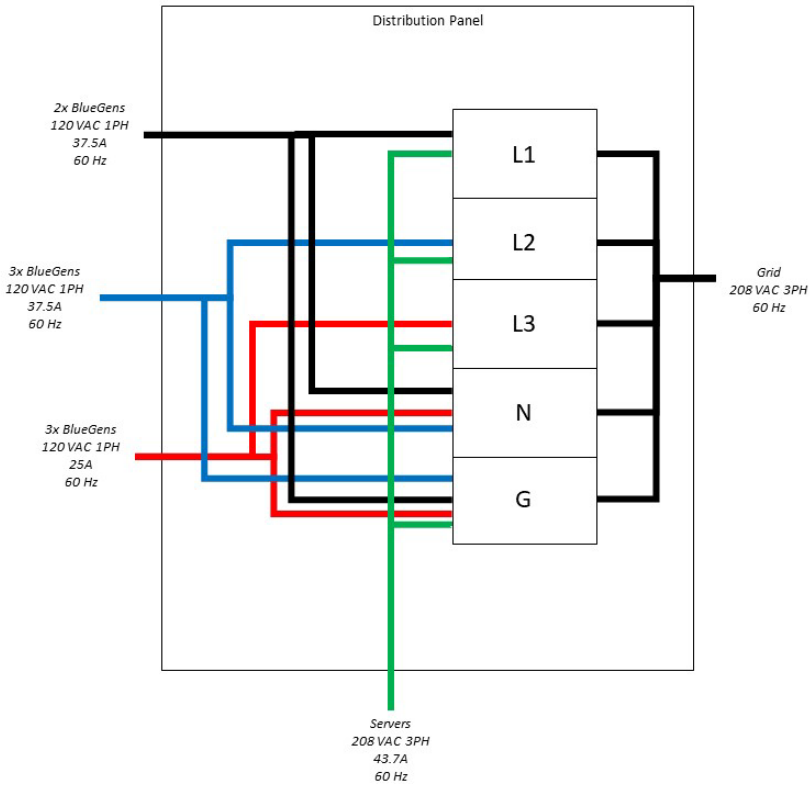

Figure 6.7 – Electrical Distribution to BlueGEN Banks.

Note that the server rack connection is detailed in Figure 6.6 and Figure 6.7, this connection will be discussed in detail later but is compatible in its 208 V three phase configuration.

It should also be noted that the entire electrical configuration is connected to the grid through a fused disconnect box for emergency shutoff. The fusing within the disconnect is rated at 50 amps to accommodate

the full electrical draw of the servers which is 43.7 A but can also accommodate the full generation of the BlueGEN systems. The supply and sink functionality of the grid connection allows for much more flexibility in the operation of the servers in conjunction with the fuel cells.

BlueGEN Fuel Connections

The BlueGEN systems run on natural gas as their fuel source which is commonly available in residences at ~18 mbar. To regulate the incoming pressure of the natural gas, each BlueGEN unit is installed with an external pressure regulator. To install the eight BlueGEN systems in the laboratory, there are two possible connection points available: standard low-pressure natural gas (24 mbar) and district high-pressure natural gas (2.7 bar). Additionally, the lab facility has the ability to pressurize the district natural gas for separate experiments up to pressures of ~7 bar. Due to the flow required for the eight BlueGEN systems, the low-pressure standard supply of natural gas would have been insufficient. Therefore, the high-pressure district natural gas source was selected to supply the BlueGEN array. The natural gas is then regulated from its high pressure to an intermediate pressure (100 mbar) using an adjustable natural gas pressure regulator shown in Figure 6.8.

Figure 6.8 – High Pressure Natural Gas Regulator.

The regulator was selected to be adjustable with no porting for purge to minimize leakage into the lab space. The intermediate pressure natural gas enters a manifold which distributes it to the eight BlueGEN regulators mentioned earlier. The manifold pressure is instrumented to a pressure gauge which allows for fine tuning of the adjustable regulator. Finally, the BlueGEN systems are connected to their external regulators using a flexible hose which allows for the units to by slid forward or back to facilitate servicing. The final manifold setup is shown in Figure 6.9.

Figure 6.9 – BlueGEN Systems NG Connection Manifold.

One additional note about the operation of the natural gas manifold regarding the interaction between the high-pressure regulator and low-pressure individual regulators is necessary. The high-pressure regulator is incapable of maintaining the intermediate pressure within the manifold when there is no flow through it. This is likely due to damage to the sealing surface in the regulator, and the large pressure difference across it. This creates operational challenges when starting up the fuel cell array since the low-pressure regulators have a lock-out system which shuts them off if they experience upstream pressure which is too high. Therefore, it is necessary to have constant flow through the high-pressure regulator to maintain the intermediate pressure for the low-pressure regulators while the fuel cells are starting up. This effect was

achieved by venting some of the flow from a single low-pressure regulator into the exhaust system while starting up the first system.

BlueGEN Exhaust Connection

The BlueGEN systems also require an exhaust system to vent unwanted gasses out of the laboratory. The exhaust connections are made on the top of the BlueGEN systems and are connected via double-walled 4 inch ducting. The laboratory facility runs a dedicated exhaust port available in the lab space which maintains a constant negative pressure, ensuring continuous flow. To interface the array of eight BlueGEN systems with the available exhaust port, an exhaust duct manifold was constructed and is shown in Figure 6.10.

Figure 6.10 – BlueGEN Exhaust Manifold.

The BlueGEN exhaust manifold was then modified to reroute exhaust from the BlueGEN systems into the absorption chiller test stand. In order to do so, the exhaust manifold was lowered and reversed such that the outlet of the exhaust collection would be injected prior to the waste heat recovery heat exchanger, discussed later. Additionally, the exhaust was insulated using mineral wool ducting insulation to minimize the thermal losses that the exhaust incurred between the BlueGEN systems and the absorption chiller test

stand. The modified exhaust manifold is shown below in Figure 6.11. Note that the exhaust is ducted into the absorption chiller test stand but is still routed to the exhaust vent for the building.

Figure 6.11 – Modified BlueGEN Exhaust Manifold.

The communal exhaust duct is introduced to the waste heat process stream upstream of the supplemental heater. A custom box adapter was created to merge the supplemental blower and the exhaust manifold. The adapter is shown in Figure 6.12. The supplemental heater can then be used to modulate the temperature of the exhaust before it enters the waste heat recovery heat exchanger. A thermocouple connected directly to the outlet of a BlueGEN system can be used to meter what temperature the exhaust is produced at and then allow for heating to overcome the losses incurred within the ducting.

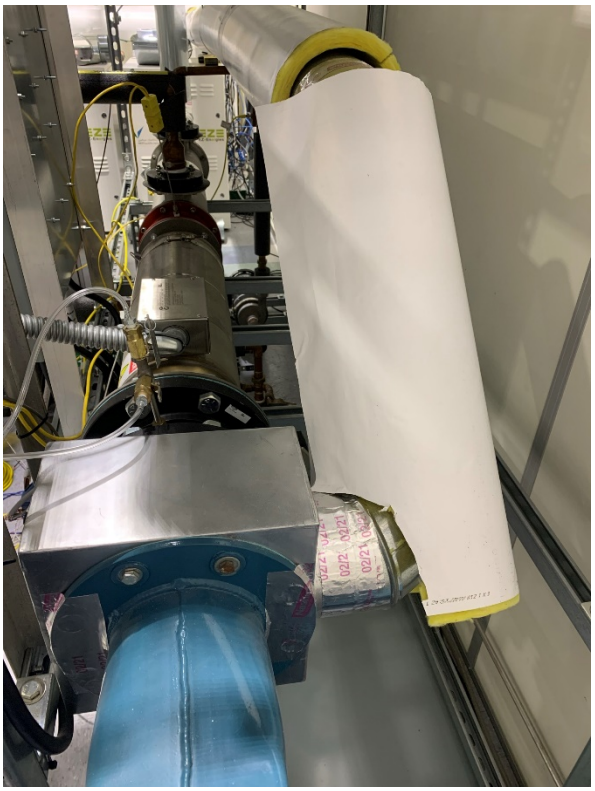

Figure 6.12 – Exhaust Connection to WHR Process Stream.

BlueGEN Water Connection

The BlueGEN systems require a water supply system to provide water for reformation within the BlueGEN system's balance of plant. The BlueGEN systems are connected to the industrial water supply available in the lab via an aluminum header and valving system. The header distributes the flow to each of the fuel cells and allows for individual shutoff in the case of disconnection or service. The header system is shown in Figure 6.13.

Figure 6.13 – BlueGEN Water Manifold and Distribution System.

BlueGEN Drain Connections

The BlueGEN systems also require a drainage system to discharge water accumulated during operation. The water is accumulated due to the thermal interaction between the exhaust the exhaust heat exchanger, which is utilized to preheat the incoming air, heat, and partially reform the incoming natural gas, and finally heat the optional hot water loop. The exhaust is cooled to the point of condensation and the condensate is accumulated in a drainage tray which can then be pumped into the drainage system. The drainage system is designed for very low pressure drop and immediate access to a floor-level drain and therefore cannot overcome the distance required to operate within the lab. To facilitate the flow from the fuel cells to the laboratory drain, a sump pump with water reservoir is used to achieve the required pump head to reach the drain. The sump pump with drainage manifold is shown in Figure 6.14.

Figure 6.14 – BlueGEN Drainage Sump Pump.

It should be noted that the sump pump operates intermittently using a water level switch to actuate its operation autonomously. The system runs for roughly 20 seconds every five minutes at an acceptable duty for the pump.

BlueGEN Internet Connection

The final point of connection for the BlueGEN systems is an internet access via an ethernet connection. Since the BlueGEN systems are operated remotely by Solid Power, a continuous internet connection is required. To facilitate this connection, a micro network was setup within the laboratory which includes all the eight BlueGEN systems as well as the servers within the server rack. The network is connected behind a Sonic Wall which provides the connectivity and the protection for the systems and will be discussed in detail in the server rack setup section.

6.2.4 - Commissioning

The BlueGEN systems were commissioned by an engineer from Solid Power. The commissioning consisted of opening the BlueGEN casing which arrived without the stack installed. The stack was then removed from its separate packaging and prepped for the installation. Special ceramic sealant is used on the bottom of the stack before it is placed on within the insulating case. A BlueGEN undergoing this process is shown in Figure 6.15.

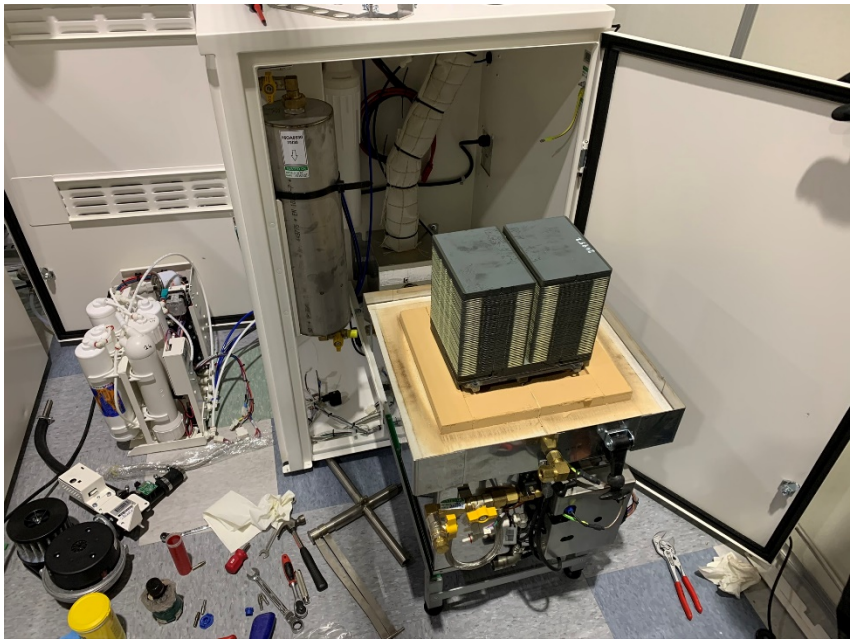

Figure 6.15 – BlueGEN Undergoing Commissioning.

The final steps of the commissioning included properly connecting all the electrical and gas lines to the stack. The BlueGEN unit was then started up in a slow warm up process.

6.3 - Absorption Chiller System

To test the integration of SOFC systems with absorption technology experimentally, it was necessary to design and construct a laboratory scale absorption chilling system. The absorption chiller test stand should allow for operation of an absorption chiller off the exhaust or simulated exhaust gasses of an SOFC. Additionally, the test stand must allow for incremental control of all operating parameters, allowing for

experimental control and exploration. Lastly, the test stand should be constructed in such a way as to allow for integration with multiple fuel cell systems for future testing.

6.3.1 - Absorption Chiller

The key component of the absorption chiller test stand is indeed the absorption chiller itself. A commercially produced absorption chiller was selected since the technology is already readily available and to expedite the construction of the test stand. Therefore, significant effort went into selecting an appropriate system which could deliver the necessary cooling capacity for one server rack, 15 kW, as well as run on the SOFC exhaust gasses.

Currently, there are two popular types of absorption chillers differentiated by the working fluid they employ to achieve cooling. The first is a Lithium Bromide (LiBr) absorption chiller which operates using aqueous LiBr and can only achieve chilling above freezing since water is the refrigeration working fluid. The second type is a water-ammonia absorption chiller where the ammonia acts as refrigerant working fluid and can therefore achieve chilling below freezing. However, water-ammonia systems require additional steps such as rectification after desorbing to operate and pose the risk of toxic exposure in the event of a leak. Due to these challenges along with the fact that sub-freezing chilling is not necessary for server cooling, a LiBr absorption chiller was selected for this experiment.

The absorption chiller selected for this experiment is a Yazaki WFC-SC5 LiBr chiller. The WFC-SC5 is a 5 refrigeration-ton chiller (~18 kW) and is the smallest commercially available LiBr absorption chiller on the market. The WFC indication refers to the “water fired chiller” meaning that the heat input is in the form of hot water delivered to the chiller. This allows for the design and customization of the exhaust heat exchanger, which will be discussed later. Additionally, the implementation of water loops to carry the thermal inputs and outputs of the test stand are relatively simple and inexpensive to construct. The chiller is shown in Figure 6.16. Note the ports for water loop inputs, but no connections at the time of the photo.

Figure 6.16 – Yazaki WFC-SC5 LiBr Absorption Chiller.

6.3.2 - Hot Water Loop

The hot water loop is the first of three water loops that facilitate the thermal inputs and outputs of the absorption chiller. The hot water loop captures heat from the exhaust gasses and delivers it to the desorber of the absorption chiller. The specified flow and temperature rating for the absorption chiller are 72 L/min (19 GPM) and 70-95 ℃ (158-203 ℉). The loop is constructed from 1” copper pipe for a maximum flow velocity of 2.36 m/s (7.74 ft/s) to minimize pressure loss. The piping is joined using silver solder and all components are connected using unions to facilitate maintenance, changes or moving of the test stand. The piping is also wrapped in one-inch foam insulation to minimize heat loss to ambient. The hot water loop is pictured in Figure 6.17 along with the exhaust heat exchanger and heater to which it is connected.

Figure 6.17 – Hot Water Loop with Exhaust Heat Exchanger.

Exhaust Heat Exchanger

The principal component of the hot water loop is the exhaust heat exchanger which enables waste heat recovery from the SOFC exhaust or the simulated exhaust. To select the exhaust heat exchanger, it was necessary to ensure that the selected component would provide ample heat transfer to the water while minimizing the pressure losses within the exhaust. To meet the second criteria and due to the large commercial availability, a shell and tube heat exchanger with no baffles in the exhaust pathway was selected.

The primary supplier of exhaust heat exchangers that meet both the heat transfer and size criteria for this experiment is EJ Bowman who offer a variety of products that match our description. To fully specify the exhaust heat exchanger before ordering, a mechanistic thermodynamic model was constructed to size the heat exchanger. First, the operating parameters of the heat exchanger were outlined and are shown in Table 6.1.

Table 6.1 – Exhaust Heat Exchanger Model Parameters.

Parameter	*Value(s)*	*Unit*
Exhaust Flow Rate	849 (500)	m^3/hr (CFM)
Exhaust Temperature	300 (572)	℃ (℉)
Water Flow Rate	72 (19)	L/min (GPM)
Water Temperature Range	70-95 (158-203)	℃ (℉)
Goal Heat Transfer Rate	25	kW

Using the parameters listed above, a mechanistic model was developed to estimate the heat transfer performance from several of the EJ Bowman products. The technical specifications of the components were sourced from the producer to ensure accuracy. The technical specification of the range of heat exchangers are listed in Table 6.2 below.

Table 6.2 – Example EJ Bowman Technical Specifications.

Parameter	*Value(s)*	*Unit*
Heat Exchanger Length	1 (3.28)	m (ft)
Tubes Diameter	1.27 (0.5)	cm (in)
Shell Diameter	20.32 (8)	cm (in)
Number of Tubes	48	-

The model was constructed using the effectiveness-NTU method for shell and tube heat exchangers. First, the overall heat transfer coefficient is calculated within the heat exchanger as shown in below, where U is the overall heat transfer coefficient and h is the convective heat transfer coefficient.

$$U = \frac{1}{\frac{1}{h_i} + \frac{1}{h_o}} \tag{6-1}$$

Where hi denotes the convective heat transfer internal to the tubes and ho denotes the convective heat transfer outside the tubes in the shell. To determine the internal heat transfer, an internal flow correlation was used to calculate the Reynolds number (Re). Note that m is the mass flow rate, D is the flow diameter, and mu is the dynamic viscosity of the fluid.

$$Re_D = \frac{4\dot{m}}{\pi D \mu} \tag{6-2}$$

Assuming that the airflow through the tubes was evenly distributed across the 48 tubes, the corresponding Reynolds number was found to be 10,122 indicating a turbulent flow. Therefore, using the convective flow relation for turbulent flow it is possible to calculate the Nusselt number. Note that Pr is the Prandtl number.

$$Nu_D = 0.2023\, Re_D^{\frac{4}{5}}\, Pr^{0.4} \tag{6-3}$$

Using the Reynolds number calculated and assuming the Prandtl number for air is 0.71, the Nusselt number was found to be 282.3. It is now possible to calculate the internal convective heat transfer coefficient where k is the thermal conductivity of the fluid and D is the diameter.

$$h_i = Nu_D \frac{k}{D} \tag{6-4}$$

The internal convective heat transfer coefficient was found to be 987.23 W/m2-K. The external heat transfer coefficient was calculated using the Zukauskas correlation for cross flow over a bank of tubes shown below.

$$\overline{Nu}_D = C_1\, Re_{D,max}^m\, Pr^{0.36} \left(\frac{Pr}{Pr_s}\right)^{\frac{1}{4}} \tag{6-5}$$

Where C1 and m are determined based on the Reynolds number and the alignment of the tubes within the bank. To determine the maximum Reynolds number within the bank of tubes, the maximum velocity is determined where ST and SL indicate the center to center distances between the tubes.

$$V_{max} = \frac{S_T}{S_T - D}\, V_{bulk} \tag{6-6}$$

In this case, it is necessary to assume a rectangular profile of the tube bank even though within the shell, it is more accurately a circular profile. That being said, the bulk cross velocity is calculated assuming a cross sectional area as found by the conversion factor shown below.

$$A_{rec} = A_{cir} \frac{2}{\pi r} \tag{6-7}$$

Using these conversions, the bulk velocity was 0.5 m/s and the maximum velocity was found to be 3.12 m/s. Then we can determine the Reynolds number where nu is the kinematic viscocity.

$$Re_D = \frac{V_{max} D}{\nu} \tag{6-8}$$

The Reynolds number for the water flow through the shell was found to be 803 indicating a laminar flow across the tubes. Then, using the assigned coefficients of C1 = 0.9 and m = 0.4, it is possible to determine the Nusselt number for the flow across the bank of tubes. Assuming the Prandtl number for the water was 2 the Nusselt number was found to be 16.98. The convective heat transfer coefficient was found to be 878.26 W/m2-K. Combining the internal and external heat transfer coefficients, the average heat transfer coefficient for the shell and tube heat exchanger was found to be 464.65 W/m2-K.

This overall heat transfer rate can then be used to calculate the overall heat transfer rate of the heat exchanger by adding up the heat transfer surface area, per the specs of the heat exchanger and dividing by the minimum heat capacity as shown below.

$$NTU \stackrel{\text{def}}{=} \frac{UA}{C_{min}} \tag{6-9}$$

The number of transfer units (NTU) was calculated for each heat exchanger option per the manufacturer's specifications and the heat exchanger effectiveness was then calculated. Note that C is the specific heat capacity.

$$\varepsilon = \frac{1 - exp[-NTU(1 - C_r)]}{1 - C_r\, exp[-NTU(1 - C_r)]} \tag{6-10}$$

Thus, the overall heat transfer of the shell and tube heat exchanger was calculated as shown below.

$$q = \varepsilon C_{min}\left(T_{h,i} - T_{c,i}\right) \tag{6-11}$$

Using this methodology, the different options for heat exchanger from the manufacturer were evaluated. The final selection was the model 6-32-3741-5 which produced 24.49 kW of heat transfer from the exhaust to the water stream at maximum thermal input.

Hot Water Pump

The hot water pump provides the flow for the hot water loop, pushing water through the exhaust heat exchanger and then through the absorption chiller's desorber to power the chiller. The pump was selected using two criteria: ability to meet the flowrate required and the ability to operate with water at temperatures up to 100 ℃ (212 ℉). To estimate the flow capacity of the pump, it was necessary to estimate the pressure drop within the hot water loop. Based on the technical specifications provided by EJ Bowman based on the selected 3741-5 heat exchanger, the pressure drop across the shell side is 0.4 kPa (0.058 psi). Additionally, the WFC-SC5 chiller lists the pressure drop in the desorber as 69 kPa (10.01 psi). Using these values combined with an estimated tubing length of 3.5m and 6 elbow connections, it is possible to calculate the pressure drop using the Darcy-Weisbach equation as shown below, where delta p is the change in pressure, L is the length, f is the friction factor, rho is the fluid density, v is the fluid velocity, and D is the diameter.

$$\frac{\Delta p}{L} = f_D \frac{\rho}{2} \frac{\langle v \rangle^2}{D} \tag{6-12}$$

Similarly, the pressure drop across 90 degree elbows is calculated using the equivalent length method where the equivalent length for the elbows sourced to construct the hot water loop have a length to diameter ratio of 20. Thus, the overall estimated pressure drop through hot water loop is found to be ~ 150 kPa (21 psi). The pump must therefore be able to deliver 72 L/min (19 GPM) at a pressure of at least 150 kPa (21 psi).

To meet the pressure drop requirement and temperature requirements stated, a stainless steel pump for chemicals was specified and is shown in Figure 6.18. The full technical specifications can be found in Appendix A.

Figure 6.18 – Hot Water Loop Pump.

The hot water pump also needed to be compatible with a variable frequency drive (VFD) to remotely control the speed. The VFD selected was an Automation Direct GS2-22P0, capable of running up to a 2 HP three-phase motor. The VFD allows for remote enabling and speed control for fine tuning of the system from the test stand monitor. The VFDs and their controls will be discussed in detail later.

Hot Water Loop Supporting Systems

To ensure proper and safe operation of the hot water loop, several other components were installed in the hot water loop. The first is an air-pressure-balanced expansion tank which allows for thermal expansion of the working fluid and can be adjusted to meet the internal pressures experienced by the hot water loop. The second is a pressure relief valve which protects the loop and the desorber internal structure from excessive pressure by venting the water should an over pressure occur. These two systems help protect the operation of the system and are specified by the pluming diagrams included in the absorption chiller manual.

Additionally, a software “boil protection” safety loop was designed to monitor the thermocouples installed in the hot loop and shuts down the supplemental heater if the loop comes too close to boiling.

6.3.3 - Cold Water Loop

The cold water loop is the second thermal input to the absorption chiller. Similar to the hot water loop, it captures heat from the process air and then delivers that heat to the evaporator in the absorption chiller. The specified flow and temperature outlet for the cold water loop are: 45.8 L/min (12.1 GPM) and 7 ℃ (44.6 ℉). The loop is constructed from 1” copper pipe for a maximum flow velocity of 1.5 m/s (4.9 ft/s) to minimize pressure loss. The piping is joined using silver solder and all components are connected using unions to facilitate maintenance, changes or moving of the test stand. The piping is also wrapped in one-inch foam insulation to minimize heat loss to ambient. The cold water loop is pictured in Figure 6.19 along with the exhaust heat exchanger and heater to which it is connected.

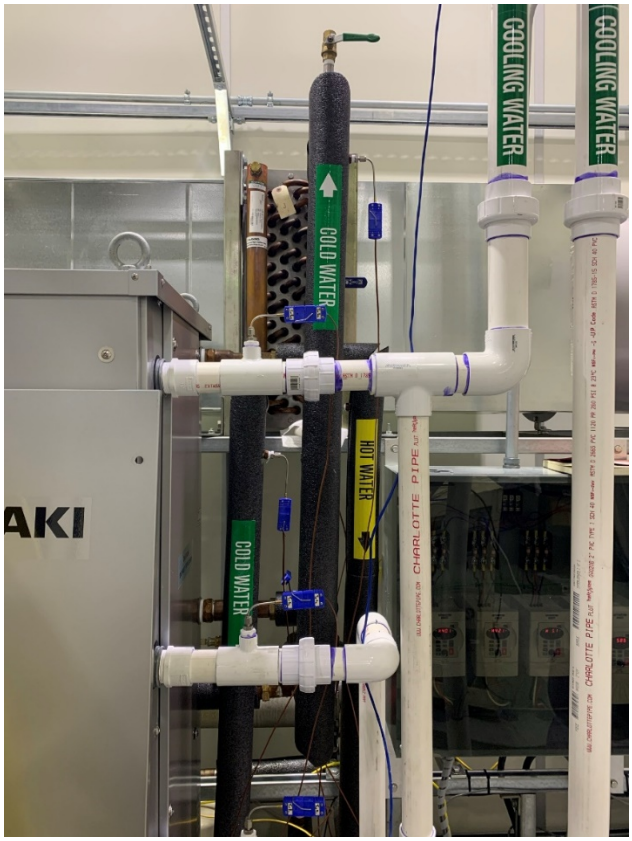

Figure 6.19 – Cold Water Loop and Duct Heat Exchanger.

Process Air Heat Exchanger

The principal component of the cold water loop is the process air heat exchanger which captures heat from air within the process air duct and transfers it to the evaporator within the absorption chiller. The process air heat exchanger was selected in the tube and fin design due to its effectiveness in water to air heat transfer and its availability. The ducting sizing was determined based on the process airflow requirements and is discussed later. For the purposes of sizing the process air heat exchanger, the duct was assumed to be a square duct with dimensions of 0.6 x 0.6 m (2 x 2 ft) with an airflow rate of 3565 m^3/hr (2100 CFM). Additionally, the cold water flow from the absorption chiller was assumed based on the technical specifications of the chiller at 45.8 L/min (12.1 GPM) and 7 ℃ (44.6 ℉).

Using the constraints listed above, there were a few other considerations that could be taken into account when modeling the process air heat exchanger. First, based on the cold water flow rate and assuming that the water is distributed via a header to a bank of copper tubes of a defined diameter per the manufacturers specification the number of tubes in a cross section could be determined. The specifications are listed in Table 6.3 below.

Table 6.3 – Process Air Heat Exchanger Parameters.

Parameter	*Value(s)*	*Unit*
Process Air Flowrate	3565 (2100)	m^3/hr (CFM)
Process Air Inlet Temperature	25 (77)	℃ (℉)
Process Air Duct Dimensions	0.6 x 0.6 (2 x 2)	m (ft)
Cold Water Flowrate	45.8 (12.1)	L/min (GPM)
Cold Water Inlet Temperature	7 (44.6)	℃ (℉)
Copper Tube Diameter	1.58 (0.625)	cm (in)
Copper Tube Spacing	3.81 (1.5)	cm (in)
Aluminum Fin Spacing	0.3175 (0.125)	cm (in)

Knowing the spacing of the copper tubes and the ducting, and therefore the heat exchangers, height, there are 16 copper tubes running across the surface opening of the process air heat exchanger. Additionally,

we know that there are perpendicular aluminum fins configured with a spacing of 0.3175 cm (0.125 in) and assume that the fin extends half the copper tube spacing in all directions. Based on these dimensions, we can calculate the heat transfer surface area by assuming a fin surface area effectiveness of 0.8. The final surface area for the first bank of tubes is calculated using Equation 4.3.13 and is found to be 0.679 m^2 (7.3 ft2).

$$SA_{eff} = SA_{tubes} + \epsilon SA_{fins} \tag{6-13}$$

Knowing the effective surface area of a bank of tubes in the process air heat exchanger and assuming a convective heat transfer coefficient of 13.1 kW/m^2-K (2.3 Btu/(ft2-hr-F)) it is possible to determine the heat transfer rate of the first bank of tubes.

$$Q_{bank} = U_{eff}\, A_{bank}\, LMTD \tag{6-14}$$

The heat transfer of the first bank was found to be 3.82 kW (13,034 Btu/hr). Utilizing this heat transfer rate, the outlet temperatures of the cold water and the process air were calculated and the next bank was solved with a new LMTD value. Iterating upon this procedure, the calculations per bank were continued until the cumulative heat transfer rate exceeded the goal heat transfer rate of 17.6 kW (60,000 Btu/hr). The required number of banks was found to be five banks. This number was corroborated by the manufacturer and a custom fin and tube heat exchanger was designed and produced. The final process air heat exchanger is shown in Figure 6.20 with five banks of tubes resulting in a width of 10 inches.

Figure 6.20 – Process Air Heat Exchanger.

The process air heat exchanger was then installed within the process air ducting on top of the absorption chiller test stand. The layout of this setup will be discussed later in the server rack ducting section of this chapter.

Cold Water Pump

Similar to the hot water loop pump, the cold water pump was specified to meet the requirements of achieving the necessary flow rate through the process air heat exchanger, chiller evaporator, and the plumbing. The temperature requirement for the cold water pump also corresponded to the lower temperature range with temperatures as low as 7 °C (44.6 °F).

The pressure drop through the cold water loop was calculated similarly to the hot water loop using Equation 4.3.12 and accounting for the measured pressure drop through the process air heat exchanger of 5.95 kPa (0.86 psi) and the measured pressure drop through the chiller evaporator of 52.6 kPa (7.6 psi).

The total pressure drop across the cold water loop was calculated to be ~125 kPa (18.12 psi), so a ¾ horsepower water circulation pump that could achieve the necessary 45.8 L/min (12.1 GPM) at the estimated pressure drop was selected. The cold water pump is shown in Figure 6.21 and the full technical specifications can be found in Appendix A.

Figure 6.21 – Cold Water Pump.

The cold water pump also needed to be compatible with a VFD to remotely control the speed. The VFD selected was an Automation Direct GS2-21P0, capable of running up to a 1 HP three-phase motor. The VFD allows for remote enabling and speed control for fine tuning of the system from the test stand monitor. The VFDs and their controls will be discussed in detail later.

Cold Water Loop Supporting Systems

To ensure proper and safe operation of the cold water loop, several other components were installed in the cold water loop. The first is an air-pressure-balanced expansion tank which allows for thermal contraction of the working fluid and can be adjusted to meet the internal pressures experienced by the cold water loop. The second is a pressure relief valve which protects the loop and the desorber internal structure from excessive pressure by venting the water should an over pressure occur. These two systems help protect the operation of the system and are specified by the pluming diagrams included in the absorption chiller manual.

Additionally, a software “freeze protection” safety loop was designed to monitor the thermocouples installed in the cold loop and shuts down the supplemental chiller if the loop comes too close to freezing.

6.3.4 - Cooling Water Loop

The final thermal connection to the absorption chiller is the cooling water loop which absorbs heat from the absorption chiller’s absorber and condenser and then rejects it to the ambient. The cooling loop is the largest of the three water loops since it must carry the summation of both the cold water and hot water thermal inputs out to the ambient.

The specified flow and temperatures for the cooling water loop are: 156 L/min (44.2 GPM), 31 °C (87.8 °F) at the inlet and 35 °C (95 °F) at the outlet of the chiller. The loop is constructed from 2” PVC pipe for a maximum flow velocity of 1.37 m/s (4.49 ft/s) to minimize pressure loss. The piping is joined using PVC cement and all components are connected using unions to facilitate maintenance, changes or moving of the test stand. The cooling water loop passes through two walls to reach the exterior of the laboratory facility.

No insulation is installed on the cooling water loop because any heat loss to ambient will benefit the cooling capacity of the cooling tower and temperature measurements are made close enough to the chiller to minimize error. Part of the cooling water loop is pictured in Figure 6.22 along with the cooling tower and pump while the PVC connections to the absorption chiller are shown previously in Figure 6.19.

Figure 6.22 – Exterior Cooling Water Loop with Cooling Tower.

Cooling Tower

To facilitate the heat rejection to ambient, an evaporative cooling water tower was selected as the most conventional and cost effective method. Additionally, the chiller was specified to match a standard size of evaporative cooling tower which simplifies the design.

The cooling tower rejects heat to the ambient air using evaporation of the water within the cooling water loop. The internal structure of the cooling tower is shown in Figure 6.23.

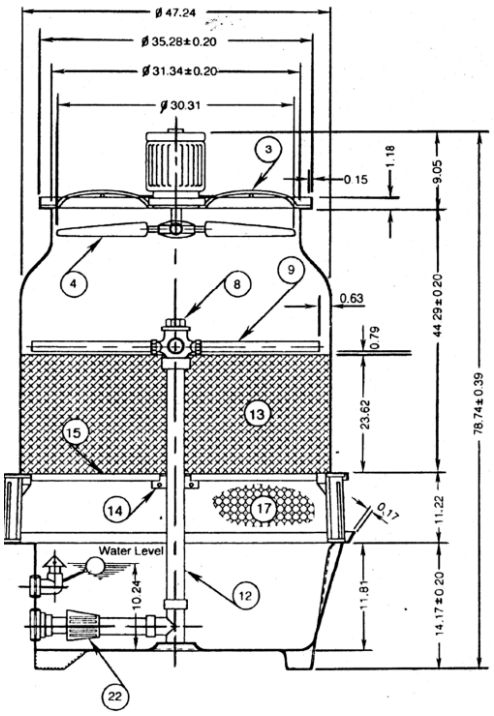

Figure 6.23 – Cooling Tower Internal Structure Schematic.

The outlet of the cooling tower is indicated by number 22 and is in the middle of the bottom reservoir to minimize debris entrance to the cooling tower loop. An additional filter is placed over the outlet to further protect the components from debris. The inlet of the cooling tower is located next to the outlet, but the water is pumped up central shaft, number 8, to the rotors, number 9, where the water is sprayed over the cooling matrix, number 13, which allows the water to fall slowly in opposite flow to the air which is being pulled up the tower by the fan, number 4. The dry air enters through a grating, number 17, and absorbs evaporating water as it falls down the matrix facilitating the cooling of the water.

Using the methodology stated above, the cooling tower is able to achieve a maximum heat rejection of 65.9 kW (225,000 Btu/hr) at the specified flow rate and inlet temperature of 156 L/min (44.2 GPM), 31 °C (87.8 °F).

Cooling Tower Pump

The cooling tower pump was selected to achieve the required flow rate for the cooling water loop. The first cooling tower pump specified was selected in conjunction with the cooling tower and rated for the continuous flow rate required by the system and is shown in Figure 6.24 next to the cooling tower.

Figure 6.24 – First Cooling Tower Pump.

The cooling water pump was based on a 1.5 horsepower motor configured for 1 phase connections to 120 VAC or 230 VAC. During the initial operation of the test stand this pump was connected to a standard 120 VAC outlet which was protected by a 20 A circuit breaker. However, during multi-hour tests, the pump would trip the circuit breaker, causing a fault to the chiller system. To remedy the issue, the pump was then configured to a 208 VAC disconnect. When running the pump on 208 VAC the pump was expected to pull 6.7 A maximum and was therefore fused at 10 A using two time delay fuses. This setup allowed the pump to operate for only two minutes before the fuses were blown. Upon further inspection, it was determined

that the motor windings had been either delivered damaged or damaged during testing since the internal resistance of two of the windings were significantly lower than the third indicating a motor short.

A replacement cooling water pump was specified to replace the faulty pump. During the prior testing, it was possible to measure the pressure drop within the cooling water loop using the pressure gauge placed at the outlet of the cooling water pump, shown in Figure 4.3.9. This allowed the new pump to be specified to meet the necessary flowrate of 156 L/min (44.2 GPM) at a pressure drop of 172 kPa (25 psi). The selected cooling water pump was a three-phase pump to operate off the 208 VAC three phase available while minimizing the current draw. Additionally, the new pump's electrical configuration allowed for a VFD to be installed to control the flowrate of the cooling water loop. The new pump and VFD are shown in Figure 6.25 next to the cooling tower.

Figure 6.25 – New Cooling Water Pump with VFD.

Note that a secondary port was place downstream of the pump to allow priming of the system to minimize the chance of damage to the water pump.

The VFD selected for the cooling water pump was an Automation Direct GS2-22P0, capable of running up to a 2 HP three-phase motor. While the VFD does allow for remote control, this VFD was configured to be manually operated due to its location outside the laboratory facility.

Cooling Tower Supporting Systems

Since the cooling water loop is technically an open loop system, no expansion tanks or pressure relief valves are necessary to safely operate the cooling tower. However, as the cooling tower operates, the water evaporated into the air will reduce the amount of water within the reservoir over time. To counter this effect, a make-up water line is connected to the cooling tower and is controlled by a level float switch. Additionally, a water over-flow valve is installed to protect the cooling tower from overfill.

The cooling tower fan is powered by a connection to a 120VAC outlet nearby the cooling tower and facilitates a soft startup using a capacitor in the power lines.

6.4 - Simulated Exhaust System

To completely explore the operation of the absorption chiller, a simulated exhaust system was designed to provide exhaust gasses at alternative temperatures and flow rates. The addition of this system allows the absorption chiller test stand to simulate the exhaust heat of fuel cell systems other than the attached BlueGEN system array and at operating conditions that are wider than those that could be produced by the BlueGEN system array.

The simulated exhaust system consists of two primary components, a centrifugal blower which provides controllable flow of air, and an electrical heater which allows for temperature control over the simulated exhaust stream.

6.4.1 - Electrical Air Heater

The principal requirement for the electrical heater was the ability to produce hot air at temperatures which simulate the exhaust of a fuel cell system. The temperature and flowrate of the simulated exhaust gasses were calculated for the BlueGEN system bank as well as the minimum input to fully operate the absorption heater. Based on the heat transfer characteristics of the exhaust heat exchanger mentioned above, a simulated exhaust stream would need a maximum capacity of 300 °C (572 °F) at 849 m^3/hr (500 CFM). To create a simulated exhaust stream at this temperature and flowrate from the ambient air, a 75 kW electrical heater is required considering a 1.2 capacity factor.

The Flow Torch 800

The electrical heater selected is a Tutco-Farnam Flow Torch 800 and is shown in Figure 6.26.

Figure 6.26 – Electrical Heater: Flow Torch 800.

The Flow Torch operates as a resistive heater, inducing electrical current in a spiral-wound dual element heater and operates at 480 VAC in a three phase configuration. The Flow Torch heater was configured with two reducing fittings to match the diameters of the blower and the exhaust heat exchanger. Custom flanges were then water jetted to match the bolt hole patterns of each flange and the inner diameter of the heater. Note it was necessary to use custom flanges since the exhaust heat exchanger is configured in metric units while the blower is configured to ANSI specifications. The heater with its modified flanges is shown in Figure 6.27 with the markings for flange phasing showing prior to welding.

Figure 6.27 – Electric Heater with Custom Flanges.

To seal the flanged faces, a standard Buna-N gasket was used upstream of the heater and a high temperature fiberglass gasket was used downstream where temperatures would be higher.

Heater Controller

To operate the Flow Torch 800, a heater controller was also ordered from Tutco-Farnam which was rated for the specified 75 kW heater. The heater controller would allow for steady-state setpoint operation of the heater using downstream thermocouples while also introducing levels of safety. The heater controller is shown in Figure 6.28.

Figure 6.28 – Heater Controller.

The heater controller has a front facing user interface that allows the operator to set various values including set point, high temperature, and different alarm values. The controller also introduces safety features such as a flow switch shutoff, redundant thermocouple sensor, and a thermal snap switch. These safety features are connected to the rest of the test stand using the data acquisition and control system. The wiring block diagram for the heater and heater controller are shown in Figure 6.29.

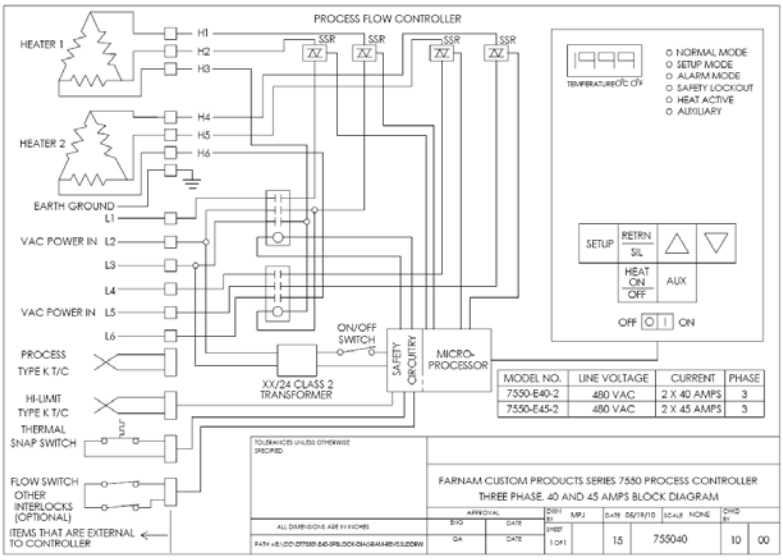

Figure 6.29 – Electric Heater Block Diagram.

Notice the sensors and safety relay switches mentioned before in the bottom left of the block diagram. Additionally, notice that the heater and controller operate on two separate three phase 480 VAC inputs. The solid state relays (SSR) are shown at the top of the wiring diagram and the heat sinks that dissipate the heat produced are shown in black on the sides of the controller in Figure 6.28.

Wiring and Supporting Infrastructure

To power the heater, two 480 VAC three phase connections with a capacity of 45 amps are necessary. To further protect the system, a set of quick action fuses are required upstream of the heater controller. The wiring diagram designed for the electrical connection is shown in Figure 6.30.

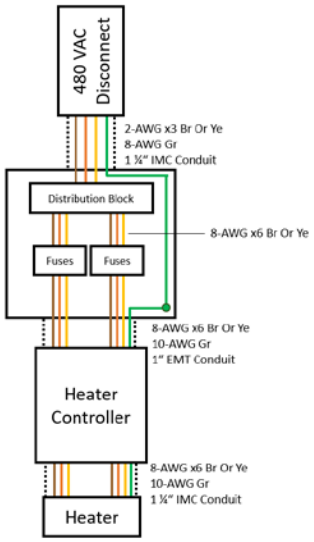

Figure 6.30 – Heater Grid Connection Wiring Diagram.

The laboratory has a 480 VAC disconnect with 100 A fuses installed and it is from this point of connection that the rest of the wiring was configured. The 100 A lines from the disconnect are broken into two 50 A lines using a distribution block. This facilitates the two connections required by the heater controller and heater. The two three phase lines are then run through a block of 50 A quick-blow fuses. The distribution block and fuses are all located within an electrical enclosure and are shown in Figure 6.31.

Figure 6.31 – 480 V Disconnect, Distribution Block, and Fuse Blocks.

The distributed and fused wiring is then routed into 1” EMT conduit to protect the wiring as it is connected across the laboratory space. The conduit was sized to maintain a packing factor of no more than 0.5.

Electrical Failure

Following the completion of the test stand, the experiment was operated for eight consecutive hours, providing steady state data at 27 operating points. However, during this testing the electrical infrastructure for the heater suffered severe damage due to overheating inside the electrical enclosure that houses the distribution block and fuses. No damage to the facility or harm to the operator was sustained outside the enclosure. The enclosure is shown with the sustained damage in Figure 6.32.

Figure 6.32 – Electrical Failure in Heater Fuse Enclosure.

The failure stemmed from thermal overloading of the conductors as they were connected to the fuse blocks. It is presumed that the lugs connecting the conductors to the studs were improperly crimped and therefore produced substantial resistance and therefore heat generation. This problem was compounded by the connection to the fuse block which was affixed using the structural integrity of the plastic block base. The initial heat of the crimp connection softened the fuse block base material which allowed the lug to slightly disconnect from the stud creating a smaller contact patch for the electricity to flow through. This reduced contact patch between the lug and the stud created even more heat which ultimately damaged the insulation of the conductor and caused shorting between the lines.

This electrical fault occurred within the time of the authoring of this material so the solution to this issue is currently lacking. However, moving forward all design decisions and construction will be verified and inspected to ensure that this fault does not occur again.

Fuse Enclosure Renovation

Following the electrical failure within the fuse enclosure, several changes were implemented to ensure safe operation in the future. The first change was an increase of the enclosure size to limit thermal build-up

during operation. Secondly, the conductors between the fuses and the heater controller were upgraded from 8AWG to 6AWG to meet the continuous duty rating. Additionally, crimped connections were directly made between the conductors and the fuse leads minimizing electrical current through the fuse holder studs. Lastly, the layout of the distribution wires was reformatted to minimize crossover and thermal influence. The final design is shown in Figure 6.33 with all of these changes implemented.

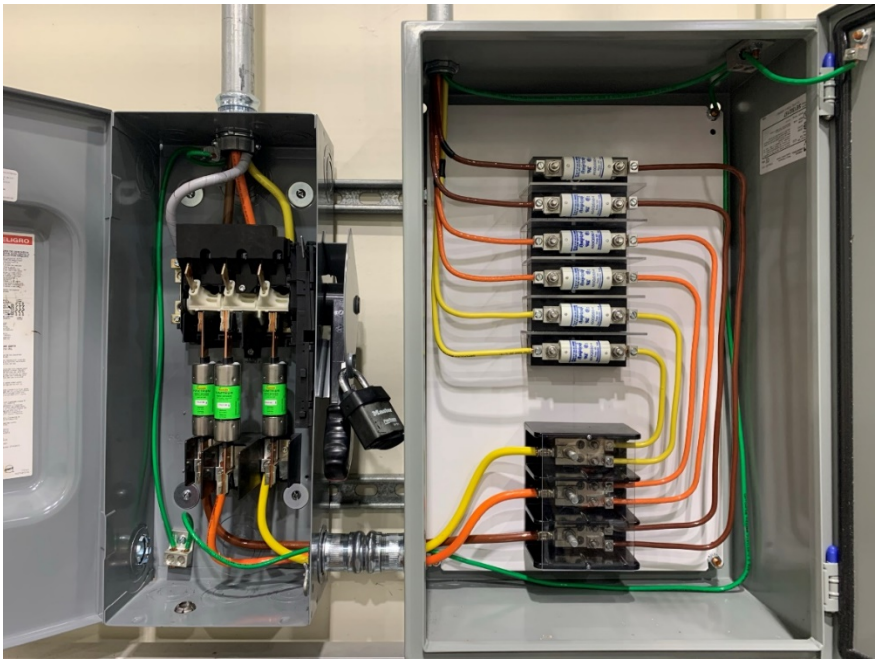

Figure 6.33 – Renovated Fuse Enclosure Layout.

Following the renovation of the fuse box enclosure, the test stand was operated continuously, and no further failures were incurred.

6.4.2 - Blower

The second component of the simulated exhaust system is the blower which provides the airflow through the heater at a rate which simulates the exhaust flow of the SOFC systems. Based on the initial BlueGEN model, the minimum exhaust flow rate is required to be ~84.9 m^3/hr (50 CFM). Additionally, the blower must be able to provide up to 849 m^3/hr (500 CFM) as specified by the exhaust heat exchanger model to achieve full chilling capacity within the absorption chiller.

Knowing the pressure drops through the exhaust heat exchanger and the electric heater provided the total pressure drop through the simulated exhaust system since they are directly connected in series. The pressure drop of each is listed in Table 6.4 below.

Table 6.4 – Simulated Exhaust Pressure Drops.

Parameter	*Value(s)*	*Unit*
Simulated Exhaust Max Flow	849 (500)	m^3/hr (CFM)
Entry Region Pressure Drop	2.09 (8.426)	kPa (in.wc.)
Electric Heater Pressure Drop	0.57 (2.3)	kPa (in.wc.)
Exhaust Heat Exchanger Pressure Drop	0.7 (2.81)	kPa (in.wc.)
Connections Pressure Drop	1.02 (4.129)	kPa (in.wc.)

Given the pressure drops of each component, it is possible to estimate the overall pressure drop through the simulated exhaust system. Using the values from Table 6.4 the overall pressure drop is 4.39 kPa (17.6 in.wc.). Based on this information and the required flowrate, a custom blower company, Twin City Blowers, was contacted to consult on the design of an appropriately sized blower. The fan curve provided by them to match the characteristics of our flow requirements is shown in Figure 6.34 with both static pressure and power draw.

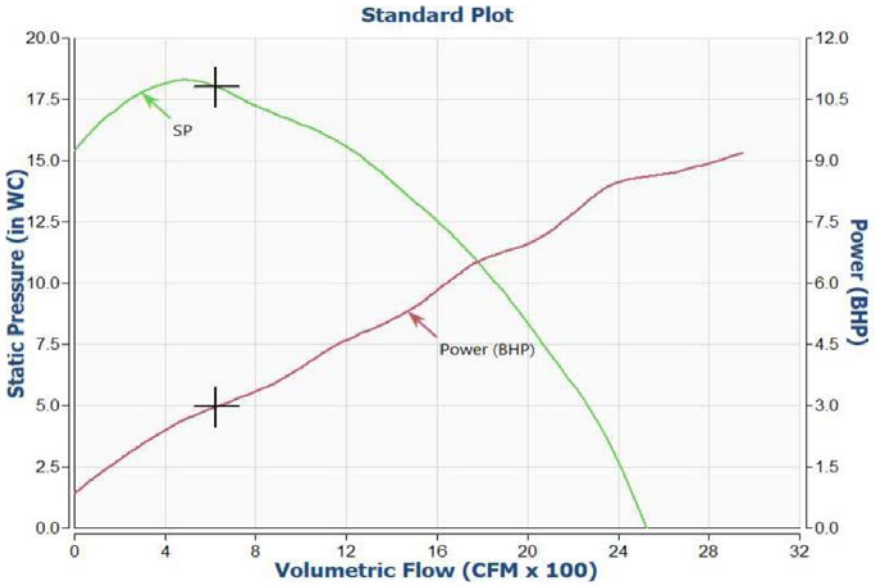

Figure 6.34 – Blower Fan Curve.

The blower was specified for 849 m^3/hr (500 CFM) at 4.39 kPa (17.6 in.wc.) static pressure and the resulting motor power draw is 2.3 kW (3 hp). The blower itself is shown in Figure 6.35.

Figure 6.35 – Simulated Exhaust Blower.

The blower is a centrifugal blower that can produce 500 CFM of flow across the simulated exhaust system. Note the flanged connection between the blower and the heater which houses the pitot tube used for measuring the flowrate of the simulated exhaust. Discussion of the pitot tube sensor will be done later.

Additionally, the motor driving the blower is connected to a VFD to control the speed, so an AEGIS ring was installed which grounds the blower impeller from the motor and protects the blower from shorts to the casing or other components on the test stand.

6.5 - Server Rack

The recipient of both the power and cooling produced by the BlueGEN systems and the absorption chiller test stand is a single server rack operated in the laboratory. The server rack and computers were donated by Microsoft to investigate the feasibility of powering and cooling the servers using fuel cell technology.

The server rack is a standard 42 slot server rack with dimensions of 0.55 x 1.87 x 1.16 m (22 x 74 x46 in). The server rack allows for servers to be mounted within it using adjustable rails. These rails also allow the servers to be partially slid out for internal maintenance. The server rack with computers installed is shown in Figure 6.36.

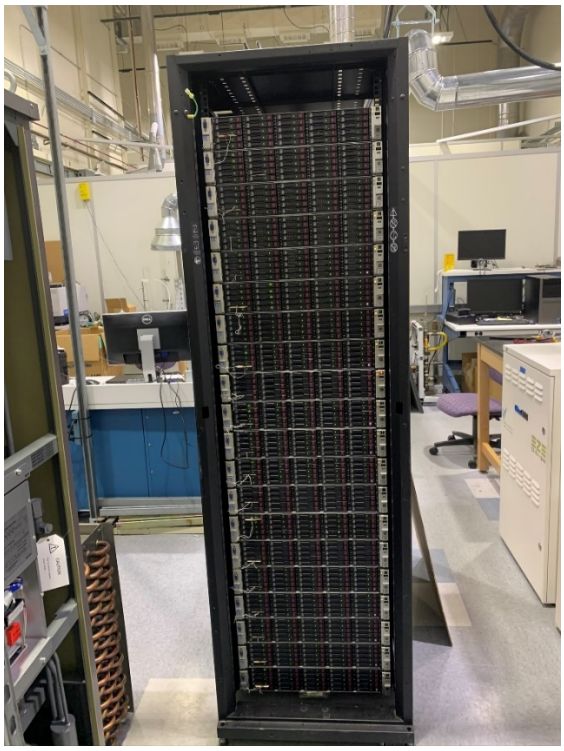

Figure 6.36 – Server Rack with Installed Computers.

Twenty-one HP 380E server computers were also donated to be installed within the server rack. These computers are decommissioned from Microsoft data centers but are still fully operational. Each computer has an 8-core CPU, 100 GB RAM, and 25 600 GB SATA disk drives for storage.

Additionally, a 32 port network switch is installed within the server rack to connect all the computers to the laboratory network and allow for localized benchmarking. To further assist with the operation of the computers, a mobile workstation was constructed and attached to the server rack. An external monitor, keyboard and mouse can then be connected to each computer in the rack to setup and operate each individually. The workstation is shown in Figure 6.37 below.

The software run on each of the computers was Prime95. This benchmarking software allows for the computers to be operated at their maximum thermal output, running both the CPU and onboard memory at maximum.

Figure 6.37 – Server Rack Computer Workstation.

6.5.1 - Electrical Configuration

The servers are powered by a 208 VAC server configured power strip. The power strip has three banks of seven computer power ports which connect to one of the two power supplies in each computer. The power strip is plugged into a non-NEMA 50A style C outlet which is rated for the electrical input of up to 43.7 A. This disconnect allows for moving the server rack and modularity in the future. The outlet is connected to the three phase distribution panel to which the BlueGEN systems are also connected. See Figure 6.6 for details.

6.5.2 - Software Setup

To operate the servers in a manner that simulates real world operation, it is necessary to run a benchmarking software on the servers. The benchmarking software artificially exercises the internal systems to determine their performance. For the purposes of this experiment, the exercise allows for full thermal loading of the servers simulating full load. Additionally, the software will allow for all the servers to be exercised and controlled remotely as a cluster simplifying the user operation.

6.5.3 - Ducting and Airflow

To operate the servers at full load, they must receive sufficient airflow through them to maintain an acceptable temperature gradient. The maximum temperature gradient allowed across the servers is 25 °C (45 °F) with a maximum outlet temperature of 45°C (113 °F). To prevent this, an airflow rate of 3567 m^3/hr (2100 CFM) through the server rack is required. This airflow is produced within the process air stream by an in-duct fan.

To connect the server rack to the absorption chiller test stand, a custom square duct was designed in AutoCAD. The mounting points for the blower, cold air heat exchanger and server rack were predetermined, and the ducting shape was designed to minimize pressure loss through it. The finalized design is shown Figure 6.38.

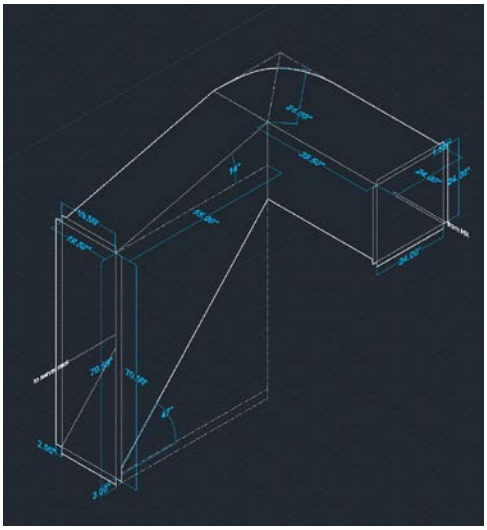

Figure 6.38 – Custom Process Air Ducting.

The custom ducting does contain a hard ninety degree turn, but it is impossible to soften this turn due to the placement of the chiller within that slot. In the future, it may prove advantageous to install guiding vanes to better direct the air through this turn. The flanges on both sides facilitate the connection to the cold water heat exchanger and the server rack. The ducting was then fabricated in 24 gauge sheet steel since the

internal pressures are quite low. The ducting was then installed on the test stand and can be seen in Figure 6.39.

Figure 6.39 – Process Air Ducting Installed on Absorption Chiller Test Stand.

To achieve the required airflow through the server rack as mentioned above, a duct fan was selected. The duct fan was sized to be able to achieve the necessary airflow through the sized ducting considering the pressure drop across the cold water heat exchanger. The duct fan runs on a 0.55 kW (0.75 hp) electrical motor which is also controlled by an independent VFD. The duct fan is shown in the top right of Figure 6.39 and during its installation in Figure 6.40.

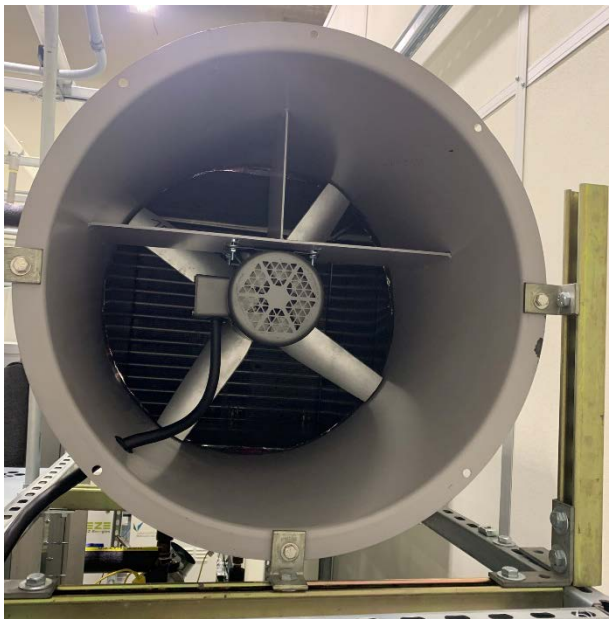

Figure 6.40 – Process Air Duct Fan.

To measure flow and temperature profiles within the ducting, a hot wire anemometer thermocouple probe is utilized at specific points. The points are predetermined based on the ducting size and shape.

6.6 - Supporting Infrastructure

All the systems described relied on certain supporting infrastructure supplied by the laboratory. Four electrical disconnects were utilized with appropriate fusing for each. Additionally, the exhaust stacks within the laboratory are used to vent the exhaust from the SOFC systems. Lastly, the supporting structure is mounted to the floor of the laboratory space for earthquake protection.

Chapter 7 - Experimental Results

7.1 - Instrumentation

To monitor and operate the SOFC BlueGEN systems, the absorption chiller test stand and the server rack computers, an independent lab computer is installed. The computer monitors the performance of the BlueGEN systems by an online portal where it is possible to control the power production and weekly power profile. The operators of the BlueGEN systems also report data into a dedicated email via excel sheets that summarize each day for all eight units. To monitor the absorption chiller test stand, a comprehensive sensor array is installed and measured by the computer terminal.

7.1.1 - Data Acquisition System and Virtual Interface

The interface selected for monitoring, collecting, and analyzing data is National Instruments LabVIEW. Within LabVIEW a virtual interface (VI) is constructed to operate and monitor the data coming from the sensor array while logging the data for further analysis. The VI designed contains a user interface that mirrors the test stand setup for clarity and is shown in Figure 7.1.

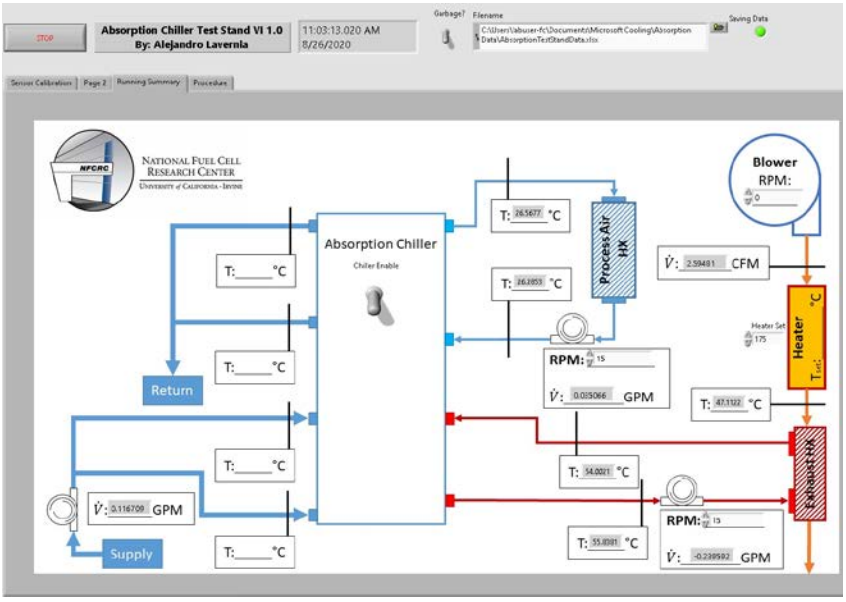

Figure 7.1 – LabVIEW Virtual Interface for the Absorption Chiller Test Stand.

The VI allows for a live display of temperatures and flowrates collected by the data acquisition system; a National Instruments Compact DAQ with an 8 slot chassis. The DAQ operates using independent sensor cards which define select channels for thermocouple, voltage, current inputs and SSR and voltage outputs. Using these dedicated channels, the VI is able to monitor, log and control the different components of the test stand.

The DAQ system operates several different levels of control for various components on the test stand including the VFDs, the chiller relays, and the heater relays. The DAQ system is able to remotely enable each VFD independently using a SSR and control the frequency output of the VFD by analog voltage 0-10 VDC. Similarly, the DAQ system operates as the safety system for both the chiller and heater by closing their safety relays remotely via user input. Additionally, the VI is programmed to enact autonomous safety shutdowns if certain conditions are met. The safety fault conditions are listed int Table 7.1.

Table 7.1 – VI Safety Shutdown Conditions.

Condition Name	*Argument*	*Action*
Freeze Protection	$T_c < 2$ ℃	Deactivate Chiller
Boiling Protection	$T_h > 95$ ℃	Deactivate Heater
Simulated Exhaust Flow Fault	$V_{exh} < 25$ CFM	Deactivate Heater
Simulated Exhaust Overtemp	$T_{exh} > 350$ ℃	Deactivate Heater
Emergency Stop	User Initiated	Shut Down All VFDs, Chiller, Heater

The control wiring for the DAQ is contained within a small electrical enclosure with terminal connections for faster diagnosis and repair. The electrical enclosure is shown in Figure 7.2.

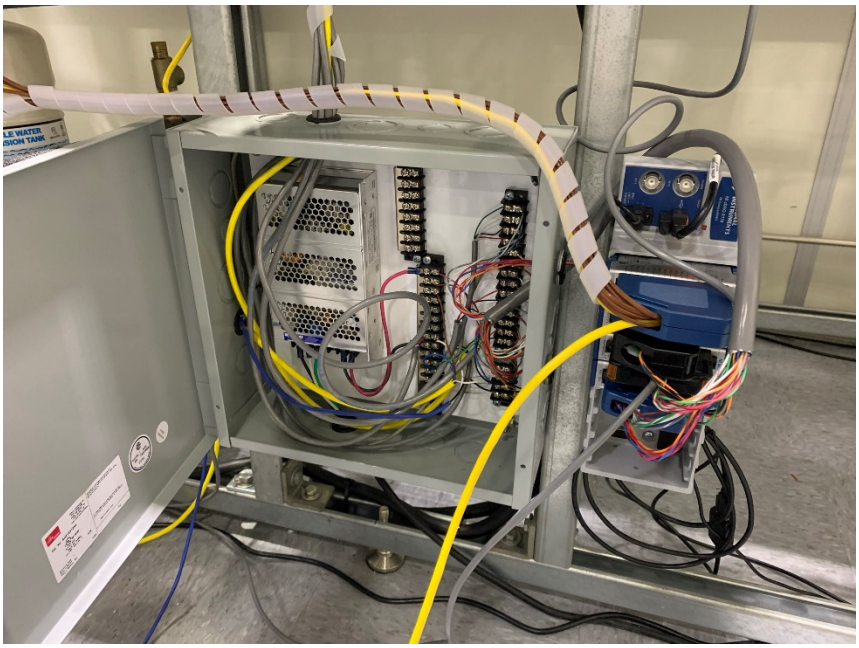

Figure 7.2 – Low Voltage Control Box with DAQ.

An additional 24 VDC power supply is built into the control box to power the various sensors. The complete wiring diagram for the control box is shown in Figure 7.3. Notice the three banks of inputs and outputs at the bottom being the DAQ system, the two banks of inputs at the top being the absorption chiller and the VFDS indicated on the left. The R1 and R1C connections on the VFD are normally open relays that activate upon enabling of the drive. The right blocks show the inputs and outputs of all the analog sensors place on the test stand.

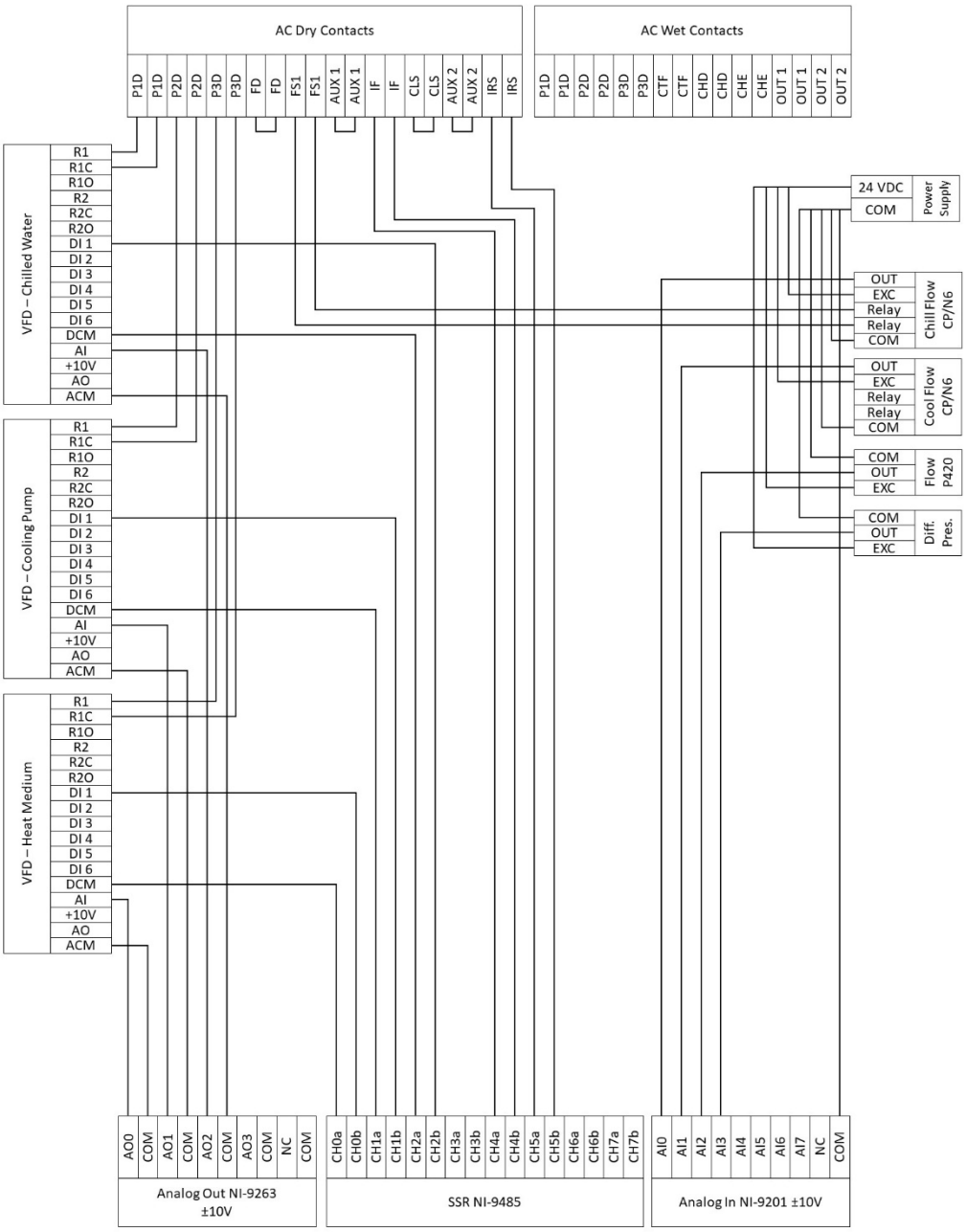

Figure 7.3 – Low Voltage Control Wiring Diagram.

7.1.2 - Sensor Array

To accurately monitor the test stand, several types of sensors were designed into the systems. The first and most common are thermocouple sensors which measure temperature using an electrical potential

difference across two different metals that scales with temperature. The test stand employs two types of thermocouples: Type T and Type K. Type T thermocouples are installed in the hot, cold, and cooling water loops since they provide more accurate readings within the narrower temperature window of liquid water. Type K thermocouples are installed are installed within the simulated exhaust system to measure the higher temperatures experienced.

The second type of sensors are vortex-shedding flow meters for measuring the volumetric flow rate of the water loops on the chiller test stand. Vortex-shedding flow meters operate off the principle that vortices produced by flowing liquid increase their frequency at higher flow rates. By introducing an obstruction to the flow, the vortices are produced at a precise location and measured using a piezoelectric sensor as shown in Figure 7.4. Vortex shedding flow meters are advantageous due to their robustness, simplicity, and low cost.

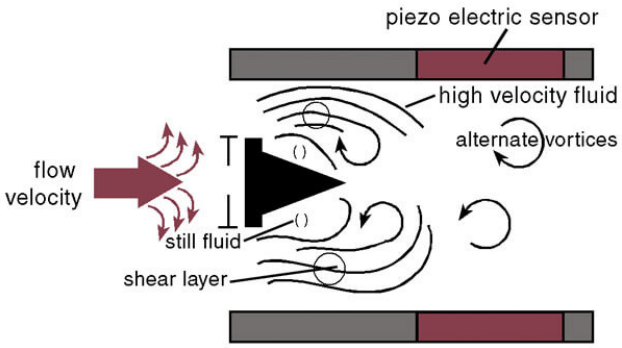

Figure 7.4 – Vortex Shedding Flow Schematic.

The flow meters selected for the test stand were specified for their specific flows, temperatures, and line sizes. Three flow meters were selected, one for each water loop with the flow capacities of up to 132 L/min (35 GPM), 190 L/min (50 GPM), and 454 L/min (120 GPM). The hot and cold water flow meters are made using a brass body with a visual indicator on the front as shown in Figure 7.5. These sensors operate on 24 VDC and output an analog current of 4-20 mA. The cooling water flow meter is made of PVC and outputs 4-20 mA to the DAQ system.

Figure 7.5 – Hot Water Flow Meter.

It should be noted that these flow meters are highly sensitive to having air within the water lines, often trapping air bubbles within their measuring mechanism. If the operator notices sever oscillation of flow measurements, it is recommended to check the charge of the system.

The third type of sensor on the chiller test stand is a differential pressure transducer which measures the pressure differential across the pitot tube installed in the simulated exhaust system. The difference between the static and stagnation pressures indicate the velocity of the flow using Bernoulli's equation shown below, where v is the fluid velocity, delta P is the difference between static and stagnant pressure, and rho is the density.

$$v^2 = \sqrt{\frac{2\Delta P}{\rho_{air}}} \tag{7-1}$$

The pitot tube installed in the flow is an averaging pitot tube with two openings for both static and stagnant pressure. Thus, we are able to calculate the flowrate through the exhaust simulation system assuming a uniform flow distribution, which is likely based on the Reynolds number. The differential pressure transducer operates on 24 VDC and outputs a voltage between 0.2 and 5.2 V. The pressure

transducer is shown with its connections to the pitot tube as installed in Figure 7.6. It is assumed that the pressure drop within the pitot tube and connecting lines is negligible.

Figure 7.6 – Differential Pressure Transducer with Pitot Tube.

Process Air Sensor Calibration

To calibrate the flow rate measurements from the differential pressure transducer and to calculate the process air flow through the server rack, a hot wire anemometer was utilized to measure spot air velocities. Using a ASHRAE standard seven-point flow measurement pattern, the air flow through the server rack is approximated. Since there is no flow instrument within the process air for the server rack, flow through the duct is assumed to be directly correlated to the process air fan speed. The flow through the process air duct is shown below in Table 7.2. Note that for this calculation, it is assumed that all the flow through the process air duct can be specially averaged, and that the flowrate does not change substantially with temperature variations from 12-25 °C.

Table 7.2 – Process Airflow Calibration Data.

Process Air Fan Speed (Hz)	*Average Velocity (m/s)*	*Process Flowrate*
30	1.175	2378.6
40	1.609	3255.4
50	1.973	3992.4
60	2.646	5353.7

7.1.3 - Data Analysis

The data collected by the DAQ system are logged once every 3 seconds and is saved to an Excel file with indicated time stamps for reference. Following any experiment, the data is then saved to the cloud to ensure its safety. To analyze the data, post processing is performed to calculate heat transfer rates, energy balances and overall performance. The data are categorized as “critical” and “non-critical” depending on what type of situation is being investigated. For example, when investigating steady state performance, the user is able to visually ascertain steady state and indicate that to the DAQ via a switch in the VI. Within the post processing, the critical data are then evaluated to see if steady state was indeed achieved and then the state point is considered as a test condition. The same process could be used for investigation of transient operation.

Data Reduction

The data recorded by the DAQ system and saved to an Excel file are then broken down for post-processing to analyze the operation of the test stand. The data consist of the streams listed in Table 7.3.

Table 7.3 – Data Streams.

Channel	*Number of Streams*	*Unit*
Time	1	Timestamp
Type T Thermocouples	8	°C (°F)
Type K Thermocouples	2	°C (°F)
VFD Frequency Outputs	4	Hz
Flow Meter Voltage Outputs	4	V
Binary Control Outputs	8	-
Flow Meter Flow Rate Outputs	4	L/min (GPM)
Critical Data Binary	1	-

Using the data available, it is possible to calculate the coefficient of performance (COP) of the chiller and the chilling capacity using the following steps. First, the volumetric flow rates are converted to mass flow rates by determining the density of each stream. The density of the water streams is determined based on their average temperature and a polyfit function which outputs the density in kg/m^3.

$$\rho_w = 1000.5 - 0.0661\,\bar{T} - 0.0036\,\bar{T}^2 \tag{7-2}$$

The mass flow rate of each of the water streams is then calculated, where V is the volumetric flow rate.

$$\dot{m}_w = \dot{V}_w\,\rho_w \tag{7-3}$$

Then the heat transfer across each of the processes is calculated using the temperature of the water streams and an assumed water pressure to determine enthalpy from a lookup table. The enthalpy state points combined with the mass flow rates give the heat transfer rate as shown below.

$$\dot{Q} = \dot{m}_w \left(h_{w,in} - h_{w,out}\right) \tag{7-4}$$

The heat transfer rates are calculated for the hot water loop, the cold water loop, and the two components of the cooling water loop that go through the absorber and condenser, respectively. A net system energy balance is performed to determine the accuracy of the heat transfer calculations along with any heat losses sustained within the system.

To calculate the coefficient of performance (COP) for the chiller, the heat transfer rates from the hot water loop and the cold water loop are considered as shown below.

$$COP = \frac{\dot{Q}_{cold}}{\dot{Q}_{hot}} \tag{7-5}$$

These equations are the fundamentals of the data reduction performed on the first set of experimental results, but in the future, more in depth analysis of each component is possible by delving into the data further.

Uncertainty

When calculating the performance of the absorption chiller using the equations presented previously, it is important to understand how the error in each of the sensors propagates into the calculated performance metrics. To calculate the uncertainty in each calculated value, the following equation is used where U is the uncertainty for a measurement.

$$U_y = \sqrt{\sum \left(\frac{\delta y}{\delta x_i}\right)^2 {U_x}^2} \tag{7-6}$$

Utilizing the rated accuracy for each of the sensors listed, it is possible to calculate the relative uncertainty in each of the calculated performance metrics: COP and chilling capacity. The absolute and relative errors are presented below for an example data point in

Table 7.4 – Calculated Uncertainty in Chiller Performance Metrics.

Name	*Value(s)*	*Abs. Uncertainty*	*Rel. Uncertainty*	*dY/dX*	*Unit*
COP	**0.7382**	**±0.042**	**5.68%**	**-**	**-**
Cold Loop Temps	10.5, 6.9	0.1	-	±0.209	℃
Hot Loop Temps	58.4, 63.2	0.1	-	±0.1516	℃
Cold Loop Flowrate	12.14	-	2%	0.0608	gpm
Hot Loop Flowrate	11.92	-	2%	-0.0619	gpm
Chilling Capacity	**11.37**	**±0.5093**	**4.47%**	**-**	**kW**
Cold Loop Temps	10.5, 6.9	0.1	-	±3.22	℃

Cold Loop Flowrate	12.14	-	2%	±0.9369	gpm

7.2 - Experimental Step Transients

Following the completion of the experimental test stand, several tests were run to ensure the successful operation of each component individually. Following these tests, it was possible to exercise the test stand to obtain some preliminary data. The first data point was constructed somewhat arbitrarily with flow rates at roughly 60% of maximum to ensure flow but not overload the system. With a successful operation of the full system, a operational sweep was determined to exercise the system and explore the performance of the chiller across a range of operating points.

The first sweep was built around the chillers response to varying exhaust temperature inputs to the system. The sweep parameters are listed in Table 7.5.

Table 7.5 – Initial Sweep Parameters

Parameter	*Value(s)*	*Unit*
Chiller Setpoint	7 (44.6)	℃ (℉)
Cooling Water Loop Flowrate	168.5 (44.5)	L/min (GPM)
Cold Water Loop Flowrate	45.8 (12.1)	L/min (GPM)
Hot Water Loop Flowrate	34.0 (9.0)	L/min (GPM)
Simulated Exhaust Flow Rate	229.4 (135)	m^3/hr (CFM)
Exhaust Temperature Range	150-300 (302-572)	℃ (℉)
Exhaust Temperature Step	25 (45)	℃ (℉)

The test stand was brought to steady state operation at the first state point, 150 ℃ (302 ℉), and the data was recorded over a three minute window where steady state was achieved. The exhaust temperature was then stepped up by manipulating the electrical heater setpoint. The heat controller then brought up the exhaust temperature to the next set point. The thermal step is shown in Figure 7.7 through Figure 7.10 below for the hot, cold, cooling and exhaust streams.

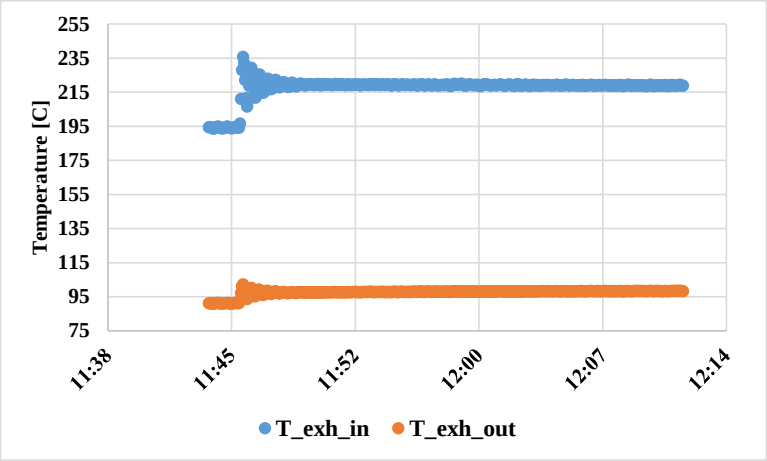

Figure 7.7 – Exhaust Temperature Transient Step.

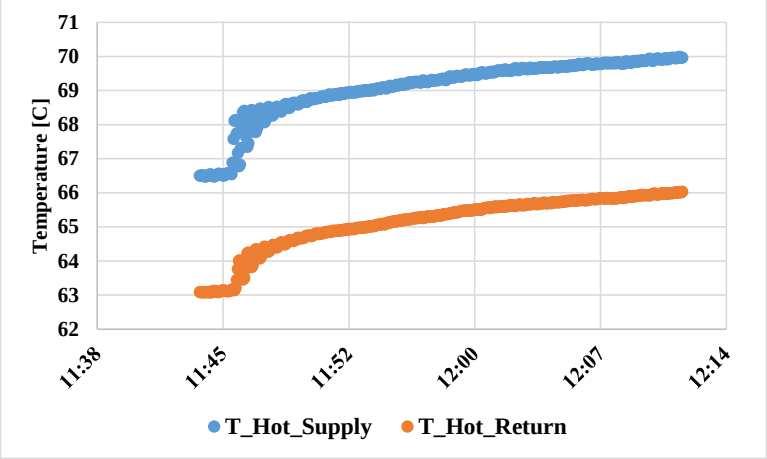

Figure 7.8 – Hot Water Loop Temperature Transient Response.

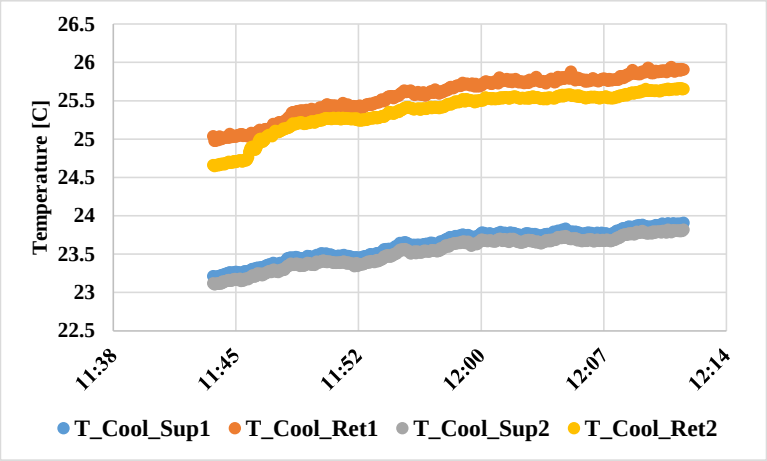

Figure 7.9 – Cooling Water Loop Temperature Transient Response.

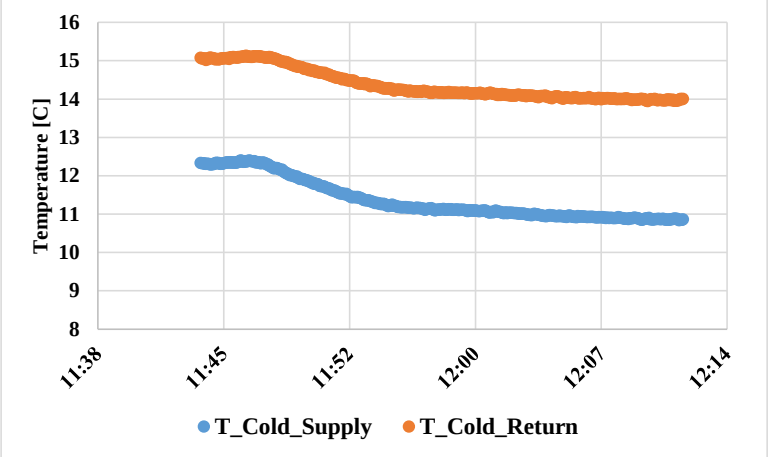

Figure 7.10 – Cold Water Loop Temperature Transient Response.

Looking at Figure 7.7, the controller brings the exhaust stream to temperature relatively quickly with some overshoot but is otherwise very stable as it reaches steady state. Figure 7.8 shows that the hot water loop follows the step increase with an expected thermal lag but eventually reaches steady state. Similarly, Figure 7.10 shows that the chiller is able to lower the cold water supply temperature due to the higher thermal input from the hot water loop. Notice that the chiller is operating at part capacity and is not able to reach its desired cold water setpoint due to the lack of hot water thermal input. Lastly, the cooling water temperature increases with accordance to the exhaust temperature but never truly reaches steady state, this

can be attributed to the continuous warming of the ambient outside air during the day. Still, the change in temperature is relatively small so a quasi-steady state is assumed.

7.3 - Experimental Results

Utilizing the stepping methodology illustrated, the integrated absorption chiller can then be exercised through several parametric sweeps to gain a better understanding of its operational performance.

The first array of experimental results that we are interested in is the performance of the absorption chiller at varying levels of exhaust temperature. To explore this, the exhaust temperature that was induced into the WHR heat exchanger was modulated across an operating range from 150 up to 350 °C. The results of the chiller performance, as defined by its coefficient of performance (COP), as calculated by Equation 7.5, is shown below in Figure 7.11.

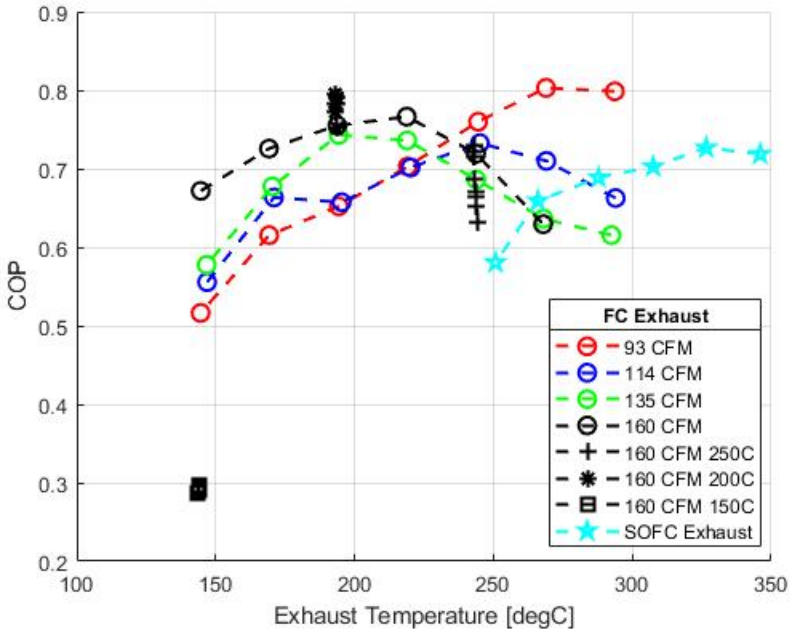

Figure 7.11 – Chiller Efficiency at Varying Exhaust Temperatures.

Reviewing Figure 7.11, it is apparent that in general the efficiency of the chiller follows a general parabolic shape, with an optimal efficiency at a specific exhaust temperature, but loses efficiency higher or lower than that optimal condition. The different trends displayed in Figure 7.11 explore the operation of the

chiller in several different methods. The first set of data presented in the series: “93 CFM, 114 CFM, 135 CFM, and 160 CFM” explore the operation by modulating only the exhaust temperature while keeping the exhaust flowrate at the specified value. Reviewing these series, each has a slightly different shape, but in general follow the described parabolic trend. The lowest exhaust flowrate peaks at the highest temperature of 268 °C, and its shape is more of the “front end” of the parabola, increasing over the majority of the range. This characteristic can be explained that at the lower exhaust flowrate, the chiller was operating at lower efficiencies because there was not enough heat entering the desorber, causing the evaporated refrigerant mass flow to decrease, thus decreasing the overall efficiency of the thermal pump. What is curious however, is that the system is performing at a COP above 0.8 at the higher exhaust temperatures, which is above the rated maximum performance of 0.7 suggesting that the chiller can exceed its ratings at lower flowrate and higher exhaust temperatures. In contrast, at higher flowrates, like the series “135 CFM,” the COP maximizes at a lower exhaust temperature of 193 °C. This maximum at lower temperatures indicates that exhaust temperatures above 193 °C push enough heat into the desorber that the desorber pressure rises, causing the COP of the chiller to decrease because the thermal pump must overcome a higher pressure differential.

The second set of series plotted in Figure 7.11 explore the chiller operation at set exhaust temperatures and flowrates but adjust the WHR hot water flowrate. The specifics of this trend are explored later, but it is interesting to superimpose these results on the performance to understand that the effect of moving more or less heat into the desorber can significantly change the chiller’s performance. For example, in Figure 7.11, notice that the trend “160 CFM, 250C” shows that even at a given exhaust temperature and flowrate, the COP can be lowered from 0.72 to 0.63 if the WHR hot water flowrate delivers too much or too little heat into the desorber. It should also be noted that the data of series “160 CFM 150C” has extremely poor performance compared to its corresponding data point in the series “160 CFM.” This lowered performance is a result of cooling water temperatures and will be discussed later.

The final trend illustrated in Figure 7.11 is labeled “SOFC Exhaust.” This series was created following the retrofit of the SOFC exhaust ducting into the WHR heat exchanger. This trend uses the real life flowrate

of the BlueGEN SOFCs installed in the lab to produce chilling which is roughly equivalent to 54 CFM. The temperature is then modulated from 250 to 350 °C using the supplemental heater. This series has the lowest flow of the set and therefore requires the highest exhaust temperatures, following a similar trend to "93 CFM." This suggests that the flowrate of the SOFC system is insufficient to fully power the chiller unless at significantly higher temperatures. This conclusion is expected because the capacity rating of the chiller is 18 kW with a hot side heat capacity of 25 kW, while the SOFC array can only output 12 kW of electricity at 60% efficient, leaving a maximum of 8 kW in the exhaust. This discrepancy was foreseen and resolved using the supplemental heater and blower described in the Experimental Setup chapter.

The next important performance indicator of the absorption chiller is the chilling capacity available at the different exhaust temperatures. These results are shown below in Figure 7.12 for all the trends mentioned previously.

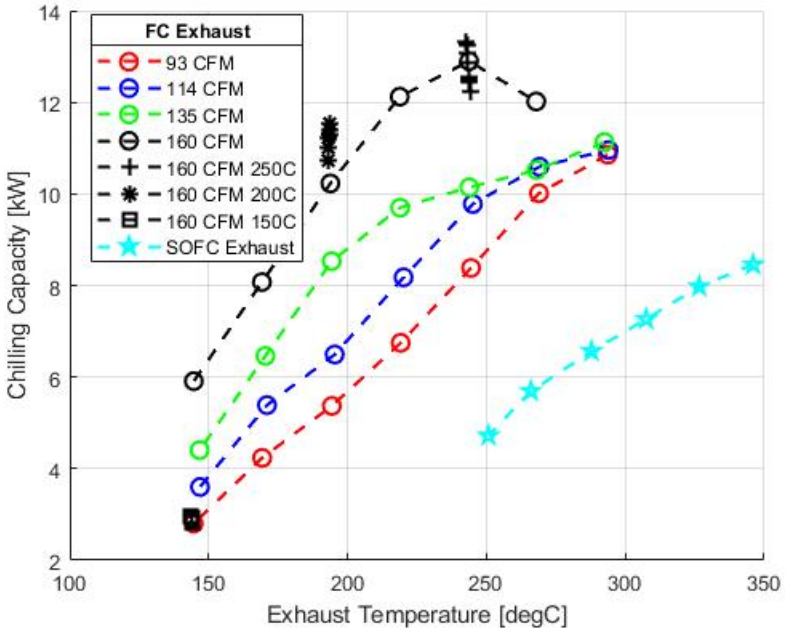

Figure 7.12 – Chiller Capacity at Varying Exhaust Temperatures.

Figure 7.12 tells the second half of the story regarding the performance of the absorption chiller. The chilling capacity available for the first set of constant exhaust flow series "93 CFM and 114 CFM" follow

a more linear correlation between the capacity and the exhaust temperature. These trends would indicate that the heat transfer taken into the desorber is correlated by the difference between the exhaust temperature and the desorber temperature. However, when considering the results from Figure 7.11, it can be assumed that the desorber pressure, and therefore its temperature, increases throughout the series. This effect is more visibly seen in the series “135 CFM” where the chilling capacity initially follows the linearity of the first two trends, but falls off as the exhaust temperature passes 220 °C. This diminishing return is due to the desorber pressure rising over the trend and decreasing the amount of heat transfer captured because the delta from the exhaust to the desorber changes.

The final constant-flow trend, “160 CFM” also initially follows the linear correlation between the capacity and the exhaust temperature, but experiences a sharp decline in performance as the exhaust temperature increases beyond 250 °C. This capacity reduction is likely driven by a combination of the rising desorber pressure and the physical heat transfer limits of the WHR heat exchanger. The high flowrate and temperature exhaust passes through the shell and tube heat exchanger with water temperatures between 60 and 80 °C and experiences heat transfer into the hot loop. This heat transfer rate becomes affected by the maximum convective heat transfer between the fluids due to the high inlet temperatures. The shorter residence time of the exhaust combined with the ~100 °C temperature delta within the heat exchanger means that convective heat transfer is constrained by the Leidenfrost curve and therefore experiences a reduced heat transfer capacity within the WHR heat exchanger. This phenomenon is explored more later.

The hot-loop variable trends further illustrate the chiller’s performance on the heat addition into the desorber. Notice that the series “160 CFM 250C” can reduce the capacity of the chiller, while the series “160 CFM 200C” can increase the capacity depending on the exhaust temperature. The higher exhaust temperature maximizes at lower flowrates, while the lower temperature sees improvement at higher flowrates. These trends are explored more in detail later, but in general, the chiller geometry is clearly optimized for a certain capacity of hot water flow and tries to normalize its performance through these trends.

The final series of the SOFC exhaust again illustrates the smaller mass flow capacity of the SOFC exhaust since it requires far higher exhaust temperatures to reach even lower capacities. This series also acutely experiences the diminishing returns due to convective boiling constraints since the trend is not linear, but rather logarithmic.

The chiller's performance metrics are then measured against the operating temperature delta. The operating temperature delta is defined as the difference between the desorber saturation temperature and the evaporator evaporation temperature. This metric explores the normalized performance of the chiller as it operates as a heat pump. The chiller's efficiency compared the operating temperature delta is explored in Figure 7.13 below.

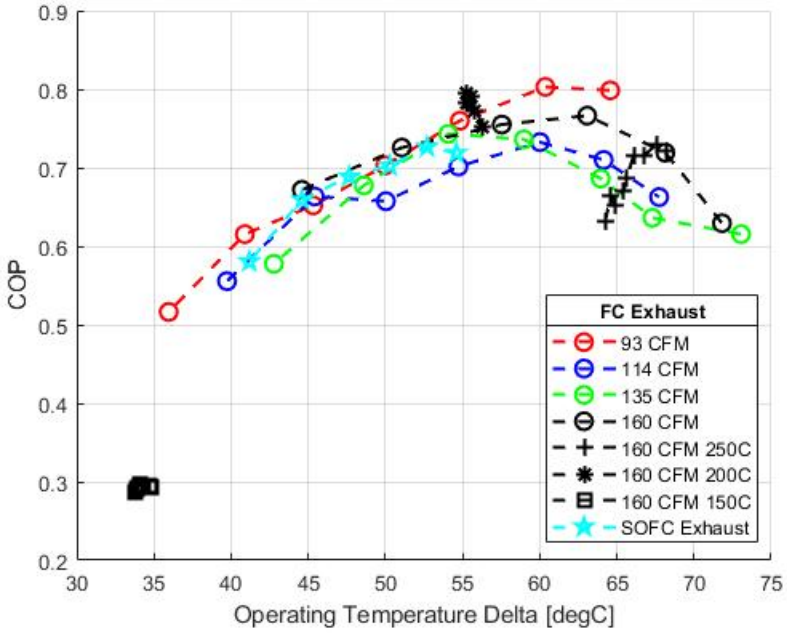

Figure 7.13 – Chiller Efficiency at Varying Operating Temperature Deltas.

Interpreting Figure 7.13, it is important to understand the competing effects on the efficiency of the absorption chiller. Absorption chilling occurs due to a combination of a heat pump and a heat engine. Typically, a heat pump operates less efficiently the higher the temperature difference it is forced to push heat across. In contrast, a heat engine typically operates at higher efficiency when the temperature delta it

operates across increases. These dual effects are both present in an absorption system and therefore can be witnessed when comparing the system efficiency to the operating temperature delta. Figure 7.13 shows that the efficiency of the system follows a similar trend for all the constant flow rate conditions. This trend shows that at lower temperature deltas the heat engine side of the cycle is not operating efficiently and therefore lowers the system performance. However, as the temperature delta increases and the heat engine component operates more efficiently, the heat pump component of the absorption chiller must push heat across a greater temperature rise and therefore operates less efficiently. The transition temperature where the heat pump's negative effect eclipses the positive effect of higher temperature rise is around 60-65 °C. This indicates that the marginal benefit of operating temperature delta is optimized at this temperature difference. Recall that this is for a single-effect absorption system and that this value would increase with each added level of effect.

Comparing the constant flow rate series with the variable hot loop flowrate series, the trends are significantly different. For example, the series "160 CFM 250C" sees an immediate performance decrease as the operating temperature delta decreases. This is likely due to the external heat transfer effects in the WHR heat exchanger rather than system efficiency effects within the absorption cycle.

Additionally, note that the series "160 CFM 150C" demonstrates that there is a minimum temperature delta of 35 °C required for the system to operate normally. Otherwise the absorption system operates in a partial capacity at lower efficiencies.

Continuing the analysis of the chiller's performance at varying operating temperature deltas, the chiller's capacity is plotted for all the operating cases in Figure 7.14 below.

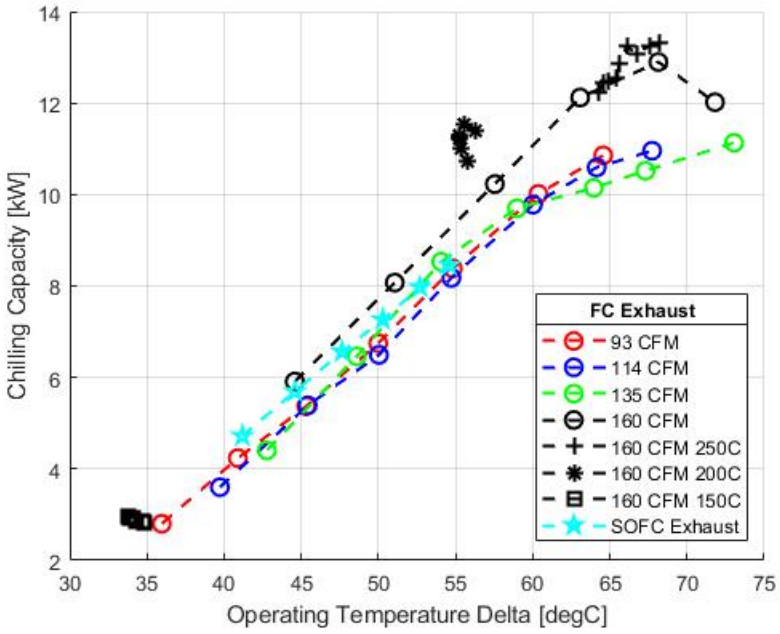

Figure 7.14 – Chiller Capacity at Varying Operating Temperature Deltas.

The chilling capacity performance of the absorption chiller is found to be fairly linear when compared to the operating temperature delta for most of the constant exhaust flow series. This trend of the system capacity increase indicates that the capacity performance of the absorption chiller is mostly limited by the heat engine component. As the operating temperature delta increases, the heat engine is able to harness more thermal energy and therefore produce more chilling. What is interesting is that once the operating temperature delta exceeds the optimal from an efficiency perspective, as shown in Figure 7.13, the capacity does not decrease, but rather increases at a marginally slower rate, for all the series except "160 CFM." This marginal performance decrease at higher operating deltas shows that the negative effects from the heat pump performance at higher temperature deltas affects the capacity of the system less than it affects the efficiency. For the series up to an exhaust flow rate of 135 CFM it should be possible to get higher chilling capacities by increasing the temperature delta over which the system operates.

However, when considering the "160 CFM" series it is apparent that with higher heat capacities, the chilling capacity decreases as the operating delta gets above 65 °C. This effect is likely a combination of the internal pressure rise within the desorber to match the hotter WHR hot loop temperatures and the

diminished heat transfer capacity of the WHR heat exchanger due to the convective limitations expressed earlier. These effects combine such that the absorption chiller has the highest capacity at 68 °C operating temperature delta.

Finally, the hot-loop variable series follow interestingly different behavior compared to the constant exhaust flow series. The series “160 CFM 200C” has a higher chilling capacity than its counterpart “160 CFM” and maintains a higher chilling capacity at the relatively constant 55 °C operating temperature delta. This behavior shows that the chilling capacity is also sensitive to the hot-loop flowrate. Even if the desorber temperature is constant, the mass flow of the refrigerant evaporating in the desorber is dependent on the internal geometry of the desorber and the hot-loop flowrate. Interestingly, the series “160 CFM 250C” does not follow a similar trend, pushing the operating delta higher as the flowrate decreases showing that the desorber heat transfer rate is more sensitive to flow changes at higher temperatures.

When considering the relationships between the chiller efficiency and the desorber temperature and comparing all of it to exhaust temperature, it is important to understand how the hot water loop temperature corelates to the exhaust temperature. This comparison is shown in Figure 7.15 below.

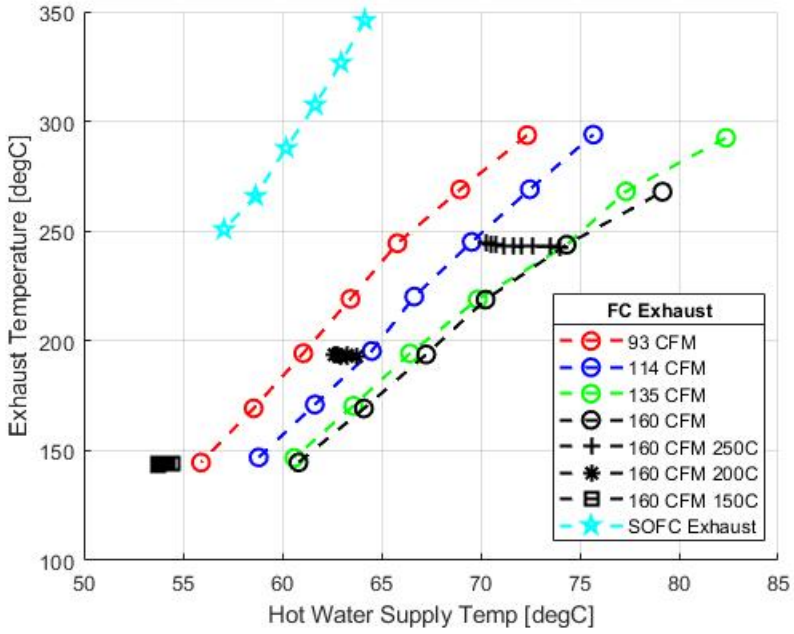

Figure 7.15 – Exhaust Temperature vs Hot Loop Supply Temperature.

Analyzing the constant exhaust flow series in Figure 7.15 the relationship between exhaust temperature and the hot water loop's supply temperature is mostly linearly dependent on the heat capacity of the exhaust. Notice though that at the higher exhaust temperatures there is a marginal increase in the slope of the constant exhaust flow series "SOFC Exhaust." These higher exhaust temperatures run into the critical heat flux limit for heat transfer in the WHR heat exchanger. While the bulk of the flow is subcooled, the temperature difference between the exhaust gas and the hot water loop is over 200 °C, so it can be assumed that there is subcooled boiling occurring and forcing a limiting heat transfer rate.

Comparatively the constant exhaust flow series "93 – 160 CFM" do not experience this limitation as severely, allowing the exhaust temperature to linearly affect the hot water supply temperature.

The final takeaway from Figure 7.15 is that for the variable hot water flow rate, the relationship between the hot water loop supply can be directly altered. By increasing the flowrate of the hot water loop the supply temperature is lowered despite having a constant exhaust temperature. This effect is expected because the higher flow rate with a similar heat transfer rate means the temperature delta across the WHR heat exchanger is lower.

In relating the hot water loop flowrate, the relationship between the exhaust temperature and the desorber heat transfer rate should be analyzed and is shown in Figure 7.16 below.

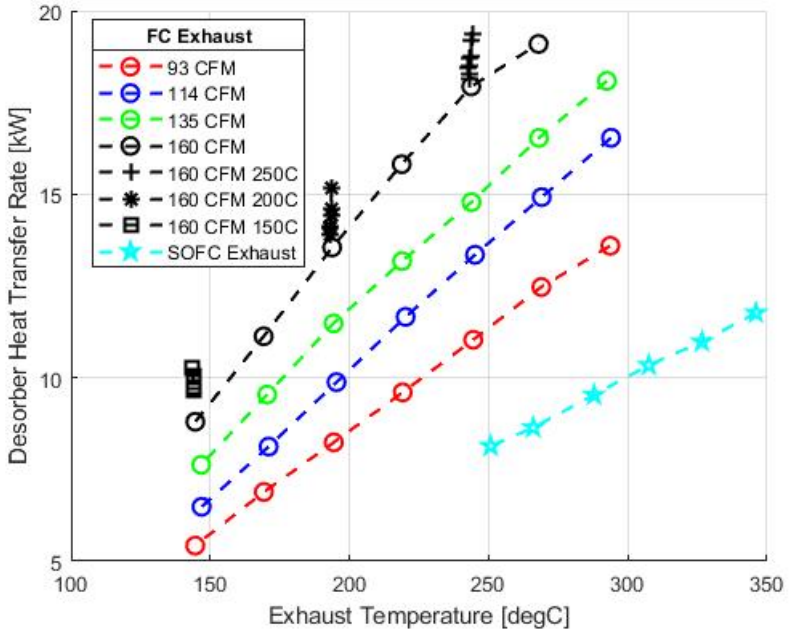

Figure 7.16 – Desorber Heat Transfer Rate at Varying Exhaust Temperatures.

Continuing with the analysis of the exhaust temperature on the desorber performance, Figure 7.16 shows how the heat transfer rate in the desorber responds to varying exhaust temperatures. For the majority of the constant exhaust flow series, the desorber heat transfer rate is directly proportional to the exhaust temperature. This indicates that there are not significant heat transfer restrictions within the desorber and that the exhaust is not currently exceeding the heat capacity of the hot water loop. However, the series “160 CFM” sees a decrease in heat transfer rate at the higher exhaust temperatures. This phenomenon signifies that there is a heat transfer limitation at the higher temperatures, either in the WHR heat exchanger or within the desorber. The WHR heat exchanger performance will be discussed later.

Finally, the variable hot water series show that the higher the hot water flowrate, the more heat transfer is able to get into the desorber. This dependency on the hot loop flowrate means that the convective heat

transfer is not just limited by the exhaust flow, as suggested by the constant exhaust flow cases, but is marginally affected by the hot loop flowrate as well. The tradeoff between these effects is explored later.

Combining Figure 7.15 and Figure 7.16, the desorber performance is rated at different desorber temperatures in Figure 7.17.

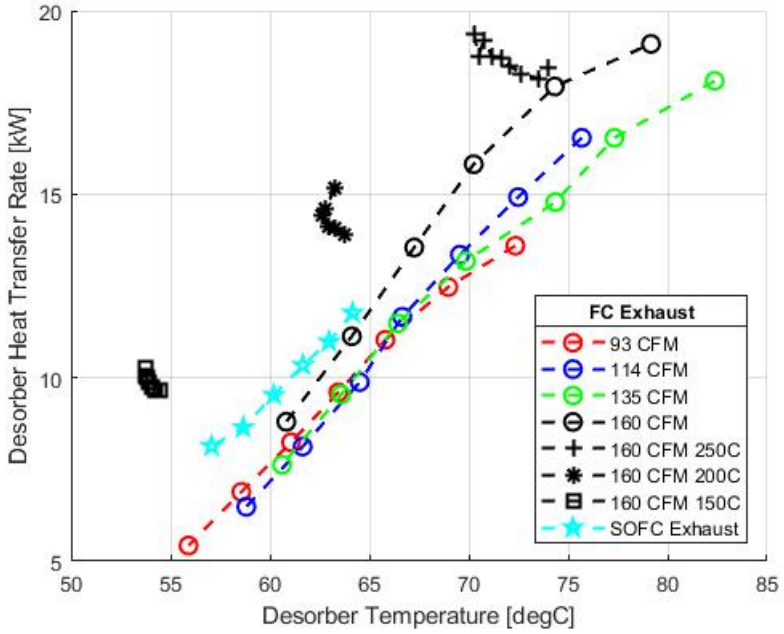

Figure 7.17 – Desorber Heat Transfer Rate at Varying Desorber Temperatures.

When considering the overall performance of the desorber in the absorption cycle, the question arises if the appropriate amount of heat is available from the exhaust stream to run the desorber at its maximum capacity. Looking at Figure 7.17 it is apparent that the higher desorber temperatures allow for the capture of more heat capacity. While this effect is counter intuitive when considering the heat transfer mechanisms, it highlights the fact that the desorber is not ever operated at its maximum capacity within these experiments. Notice however in series “160 CFM” the heat transfer rate, if extrapolated to a desorber temperature of 90 °C, should reach a peak before dropping. This theoretical performance would track with the understanding of the system’s designed capacity for 25 kW of desorber heat transfer capacity at a desorber temperature of 90 °C.

This understanding indicates that the heat availability in the SOFC exhaust is not enough to fully power this absorption chiller. This constraint was predicted given the experimental stand's connection to a 12 kW SOFC array, and the operation of the supplemental heater/blower was constrained to reflect realistic SOFC operating conditions.

The operation of the desorber component has been fully explored and its performance against the SOFC exhaust and hot water loop temperatures has been explored. The availability of heat capacity and the desorber' s ability to capture that heat has relatively few limitations on the absorption cycle's performance. However, the impact of the desorber temperature on the chillers overall efficiency and capacity has yet to be explored. The efficiency of the chiller at varying desorber temperatures is explored in Figure 7.18 below.

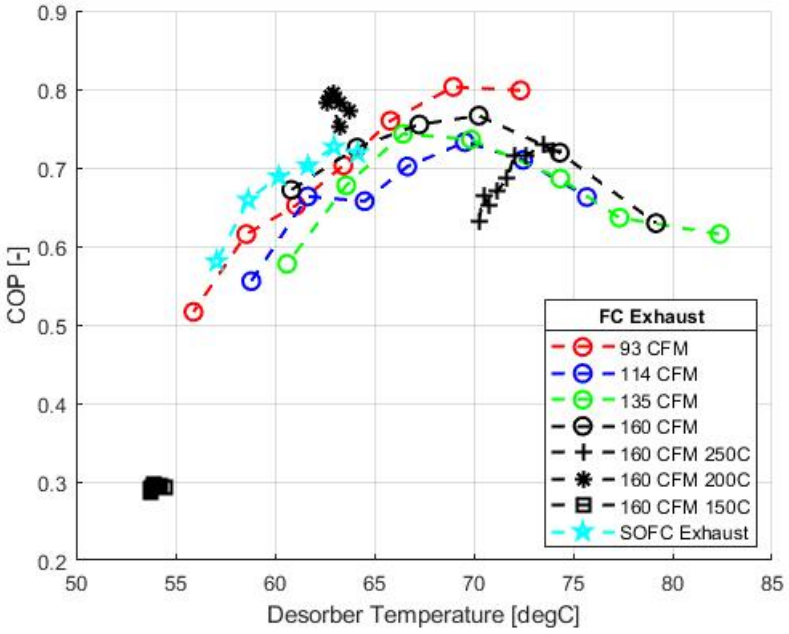

Figure 7.18 – Chiller Efficiency at Varying Desorber Temperatures.

Reviewing Figure 7.18, the efficiency of the absorption cycle is not as linearly connected to the desorber temperature as the WHR heat transfer rate it. For all the constant exhaust flow series, a parabolic trend is observed as the desorber temperature increases. The maximum COP achievable for most of the trends falls within the desorber temperature range of 65-75 °C, which is expected because that matches the designed

specification for the single-effect system. However, the performance decrease at higher desorber temperatures suggests that the efficiency decrease of the chilling cycle due to the greater temperature rise becomes dominant at temperatures in excess of 70 °C. Note that this effect can only be seen in series which achieve higher chilling capacities.

The variable hot loop series follow different trends with the desorber temperature decrease in series "160 CFM 250C" leading to a rapid fall off of system efficiency. This effect is likely due to the diminished heat transfer from the lowered hot loop flow rate in the desorber which accelerates the efficiency losses. Conversely, the variable flow series "160 CFM 200C" shows that at a lower exhaust temperature the desorber temperature has little to no change when adjusting the hot loop flow rate. This ultimately means that the chilling capacity and therefore the efficiency remain relatively unaffected. These effects will be explored more further on.

The diminished desorber heat transfer rates and the overall system efficiency can then be compared to the chilling capacity available at varying desorber temperatures, as shown in Figure 7.19 below.

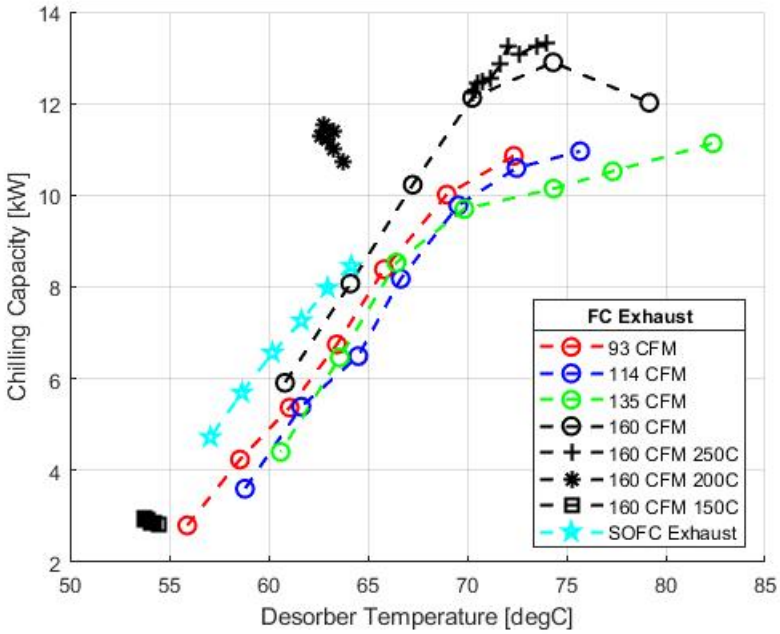

Figure 7.19 – Chiller Capacity at Varying Desorber Temperatures.

Figure 7.19 shows that the chilling capacity of the system is broken into two sections when based on the desorber temperature. Desorber temperatures of 50 to 70 °C follow a linearly dependent relationship between the chilling capacity and the desorber temperature. This indicates that the desorber pressure rises to around 70 °C at which point the thermal cycle is fully developed. However, once the desorber temperature rises above 70 °C the chilling capacity still increases for the constant exhaust series "93 – 135 CFM", albeit at a lowered rate. The diminished return of capacity indicates that the heat transfer within the desorber suffers a penalty at higher temperatures, likely due to the decrease in COP efficiency shown in Figure 7.18.

For the constant flow series "160 CFM," as the desorber reaches the highest temperature the chilling capacity actually starts to decrease. This is likely because as the pressure in the desorber rises, the heat transfer rate into the saturated solution decreases and therefore facilitates less evaporation of the refrigerant. This reduction in refrigerant evaporation causes less chilling capacity in the evaporator.

The variable hot loop flowrate series will be explored in the next set of figures below, starting with Figure 7.20.

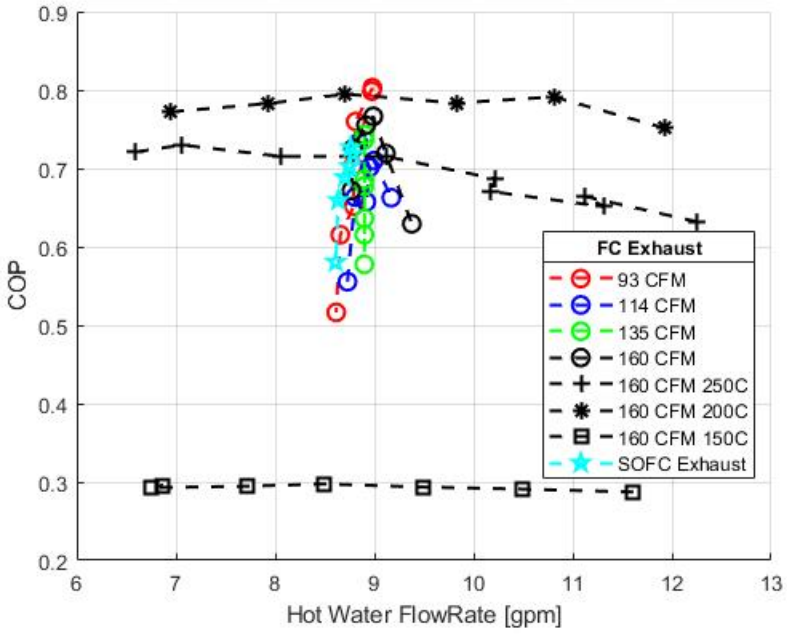

Figure 7.20 – Chiller Efficiency at Varying Hot Water Flowrates.

While it has been hard to visualize the effects of the hot water flowrate on the chiller's efficiency in the past illustrations, Figure 7.20 clearly lays out the controlled variable versus the COP. The first thing to notice is that the chiller efficiency trends in the variable hot loop series changes relatively little compared to the changes associated with different exhaust temperatures, as shown by the constant exhaust flow series.

However, comparing the effect of the hot water flowrate between the series "160 CFM 250C" and "160 CFM 200C," for the higher exhaust temperature, the increased hot water flowrate decreases the efficiency of the absorption cycle while at the lower exhaust temperature the efficiency stays relatively constant. The efficiency decrease seen by the higher hot water flowrate is likely because at the higher flowrate decreases the residence time of the hot loop medium in the WHR heat exchanger. The decreased residence time causes the temperatures within the hot loop to decrease and therefore the desorber temperature also falls, causing the efficiency to decrease. What is interesting is that this effect is counteracted by an increased heat transfer rate into the hot loop as shown in Figure 7.17 above. The lowered desorber temperature and higher heat transfer rate combine to lower the system efficiency.

This effect however is not corroborated at the lower 200 °C exhaust temperature case, where the higher flow rate has minimal effect on the efficiency, and likewise the heat transfer rate as shown in Figure 7.17. At the lower temperature, the flowrate of the hot water loop doesn't affect the efficiency of the cycle because the desorber temperature doesn't change significantly. Assuming an effectiveness model for the waste heat recovery heat exchanger, this indicates that the heat capacity of the air side is the minimum capacity and therefore the controlling capacity for heat transfer. This effect will also be discussed later when the WHR heat exchanger is analyzed.

The last effect that is likely causing decreased performance is that the increased flowrate reduces the hot loop medium's residence time within the desorber of the absorption cycle. This decreased residence time causes a decrease in heat transfer inside the desorber geometry and therefore an overall decrease in system efficiency. Finally, if you have made it this far, it is likely time to stand up and stretch.

The chilling capacity of the absorption cycle is also analyzed at the varying hot loop flow rates and is shown below in Figure 7.21.

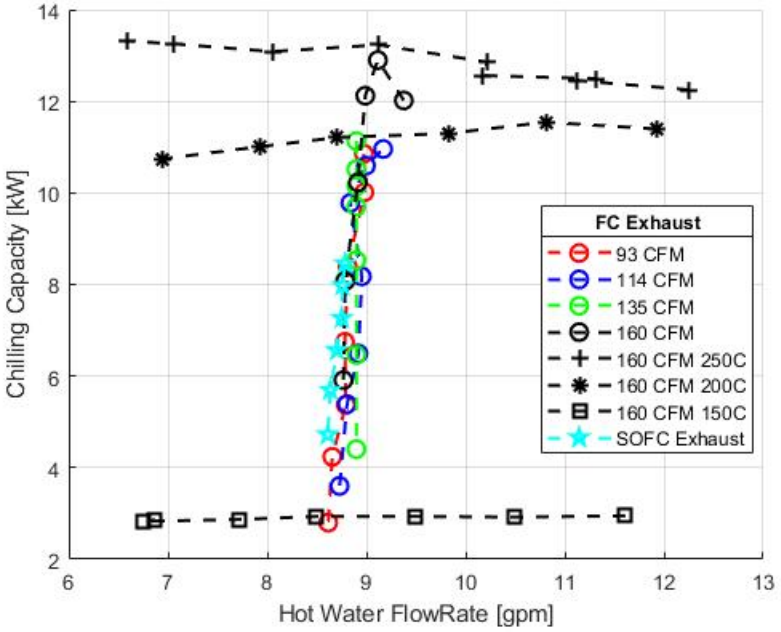

Figure 7.21 – Chiller Capacity at Varying Hot Loop Flowrates.

Similar to the efficiency, the hot water flowrate seems to have marginal effects on the chilling capacity of the cycle compared to the exhaust temperature and flowrate. However, the effect that the hot water flowrate has on the chilling capacity depends on the exhaust temperature that the hot water is capturing heat from. For the series “160 CFM 250C” the chilling capacity is highest at the lower hot loop flowrate, but “160 CFM 200C” has the highest capacity at the highest flowrate. These diverging trends suggest that two different phenomena are present in the chilling capacity of the chiller: efficiency losses due to the lowered desorber temperatures as shown in Figure 7.18 and an increase in heat transfer into the hot loop due to the increased flowrate through the WHR heat exchanger. To explore the second phenomena, the heat transfer rate in the WHR heat exchanger is compared to the hot loop flow rate in Figure 7.22 below.

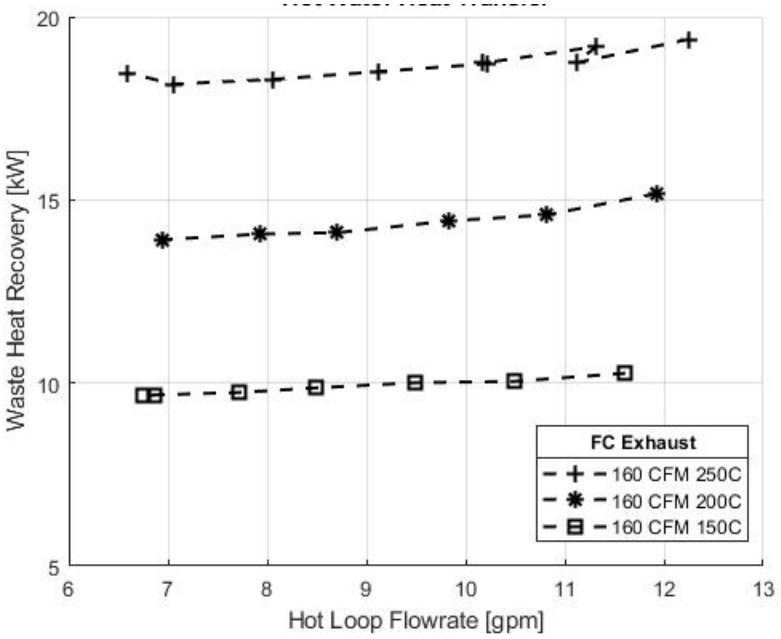

Figure 7.22 – WHR Heat Exchanger Capacity vs Hot Loop Flowrate.

The heat transfer rate in the WHR heat exchanger shown increases slightly as the hot loop flowrate rises. When considering the heat transfer in the shell and tube heat exchanger, an effectiveness-NTU methodology would suggest that there should be no change in the heat transfer rate between the exhaust and the hot loop due to a change in hot loop mass flow because the heat capacity of the water is significantly higher than the exhaust. However, the increase in heat recovery is likely an effect of the lowered hot loop

temperatures at the higher flowrates. The higher flowrate causes a smaller temperature rise in the WHR heat exchanger which pushes the desorber temperature down. Therefore, the hot water loop temperatures are lower at the higher flowrates which creates a larger temperature differential between the exhaust and the recovery fluid. This increased differential drives the heat transfer rate to increase as well and explains the marginal increase in the heat transfer rates in the WHR heat exchanger as shown in Figure 7.22.

Since the heat transfer rate varies with the different temperature rises across the WHR heat exchanger, it is prudent to explore these changes shown in Figure 7.23 below.

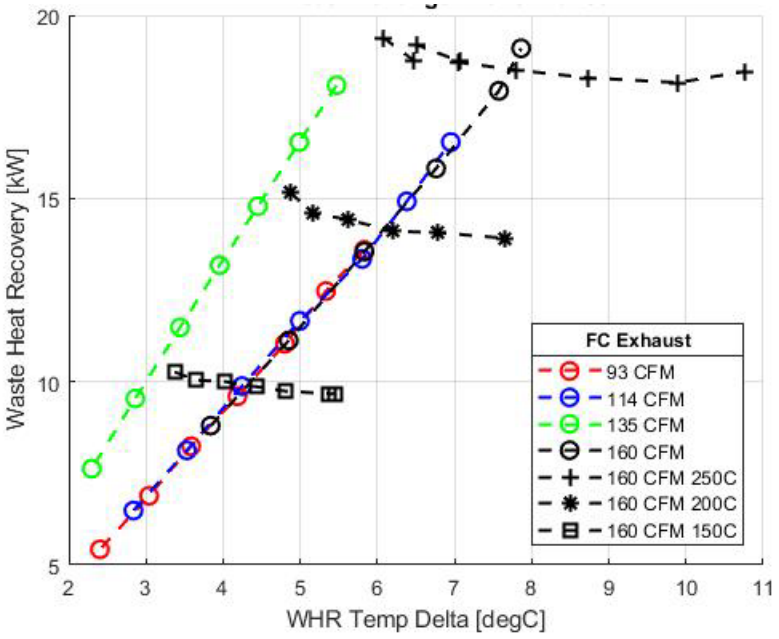

Figure 7.23 – WHR Heat Exchanger Capacity vs Hot Loop Temperature Rise.

Figure 7.23 illustrates two different phenomena that govern the heat transfer rate in the waste heat recovery heat exchanger. The first is that the heat transfer rate within the WHR heat exchanger is largely linearly dependent on the exhaust temperature as shown by the constant exhaust flow series. The only outlier is the series “135 CFM” which sees an increased heat transfer rate. This increase indicates that the critical flow for the exhaust is near 135 CFM because it allows the most heat transfer within the tubes of the heat exchanger while not limiting the residence time or the turbulent behavior.

The second phenomenon shown in Figure 7.23 is how the variable hot loop flowrates cause the temperature delta to rise when the flow is decreased. Interestingly, the heat transfer rate into the hot water does not increase, but rather decreases as the temperature delta increases across the heat exchanger. Again, referring to an assumed effectiveness NTU heat transfer model, the decreased heat transfer rate can only be a symptom of an increased hot water temperature into the WHR heat exchanger. The lower hot loop flowrate has been shown to increase the desorber temperature which similarly causes the hot loop temperatures to rise. This rise in working temperature means that even though the heat exchanger facilitates a larger temperature difference in the hot water, the overall heat transfer is less because it is capturing heat from the same source temperature. This recursive effect of raising the desorber temperature on the heat transfer performance of the WHR heat exchanger is unexpected but should be considered when simulating the absorption cycle.

The final component necessary to understand the performance of the absorption chiller's operation is how the temperature at which chilling is delivered affects the efficiency and capacity of the chiller. The efficiency of the chiller is charted against the chilling temperature in Figure 7.24 below.

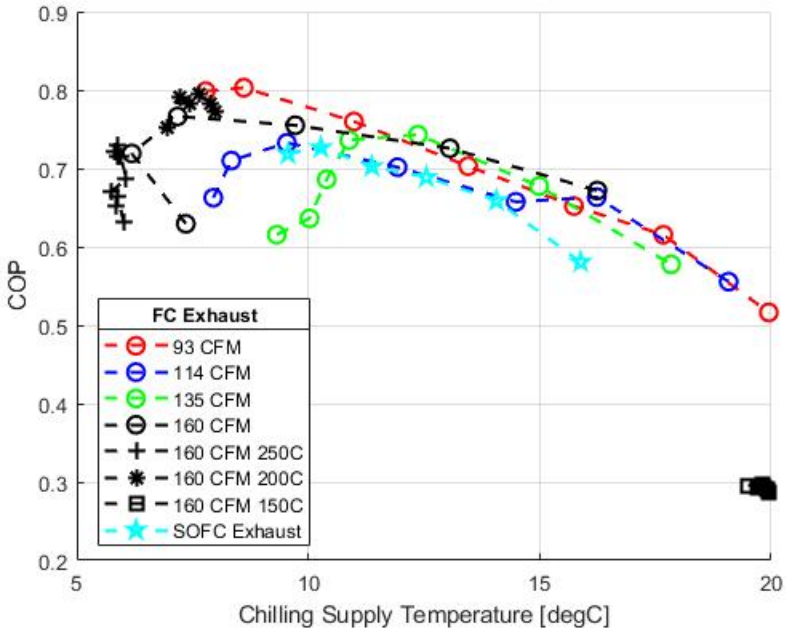

Figure 7.24 – Chiller Efficiency at Varying Chilling Supply Temperatures.

Reviewing Figure 7.24, the efficiency of the chiller decreases as the chilling temperature rises. This trend is contrary to the expected response of an absorption cycle at higher evaporation temperatures. Therefore, the cause of the decrease in efficiency is related to the heat transfer to the cold water loop which absorbs heat from the process air ducting. At higher evaporator temperatures, the chiller is not able to absorb very much chilling from the cold water loop because it tends to match the ambient air temperature, roughly 20 °C. This effect will be discussed more when the capacity of the chiller is analyzed.

However, once the chilling temperature reaches or falls below the set point of 7 °C, the pressure in the absorber also falls, causing an increase in the heat transfer in the absorber and therefore a greater concentration differential. The increase in solution concentration and the decrease in absorber pressure present the possibility for crystallization within the strong solution return line. To mitigate any physical damage that crystallization could cause, the chiller actively reduces the output capacity by throttling the refrigerant flowrate. Due to this safety mechanism, the performance of the chiller at temperatures below 7 °C is severely reduced, as shown in Figure 7.24

The capacity of the chiller is governed by the heat transfer from the cold water loop into the evaporator of the absorption cycle. The evaporator temperature corresponds directly to the chilled water supply temperature and the overall capacity compared is shown below in Figure 7.25.

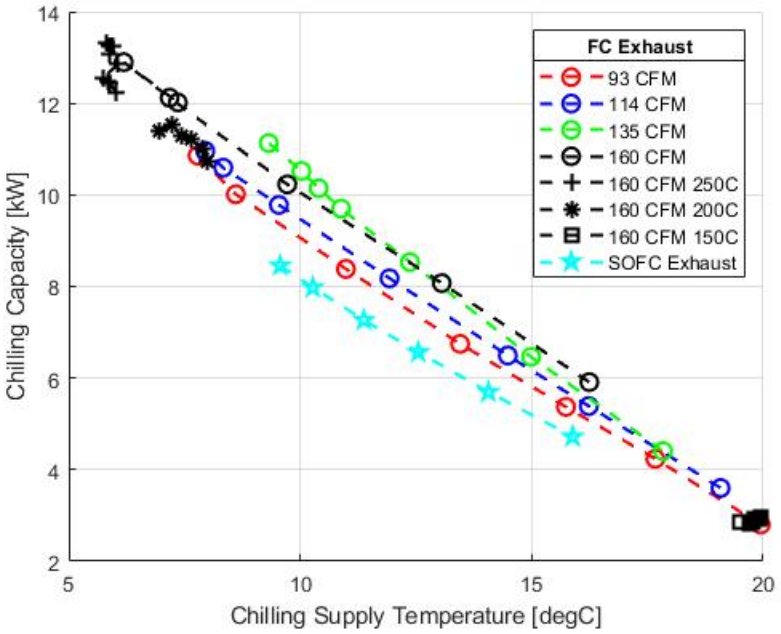

Figure 7.25 – Chiller Capacity at Varying Chilling Supply Temperatures.

Finally, when analyzing the effect that the chilling supply temperature has on the chilling capacity of the chiller, it is apparent that the lower the evaporator temperature, the higher the chilling capacity based on these experimental data. However, this is again in contrast to the expected performance of the absorption cycle, which at lower temperatures should see a diminished heat transfer rate in the evaporator. Therefore, the physics that are dominant in Figure 7.25 are governed by the phenomena occurring in the cold water loop. As mentioned previously, the heat transfer rate from the cold water loop into the evaporator is clearly limited not by the heat transfer in the evaporator but in the air handling unit. While the chiller may be capable of producing more chilling at higher temperatures, the heat transfer from the process air into the air handling unit is clearly proportional to the chilling supply temperature.

7.3.1 - Experimental Chiller Performance Takeaways

Summarizing the experimental results, there are five separate variables that the chiller's performance has been characterized against: exhaust temperature, exhaust flowrate, desorber temperature, hot water flowrate, and the chiller supply temperature.

It is important that moving forward, the trends that were demonstrated experimentally are captured by the chiller models so that they accurately reflect the performance of the real world system. The models are therefore exercised using the experimental inputs and comparing the predicted performance outputs.

7.4 - Model Verification

To fully utilize the experimental setup of the integrated absorption chiller, the data collected from the test stand is then used to verify the thermodynamic model for the absorption chiller that has been used in other integrated simulations. To exercise the absorption model, the two models of the external heat exchangers, described in their sizing section, were added to the single effect absorption model in EES. Utilizing the recorded inlet flows and temperatures as inputs to the model the model then predicted the performance of the chiller at those conditions. The predicted COP for the single effect system is shown below in Figure 7.26.

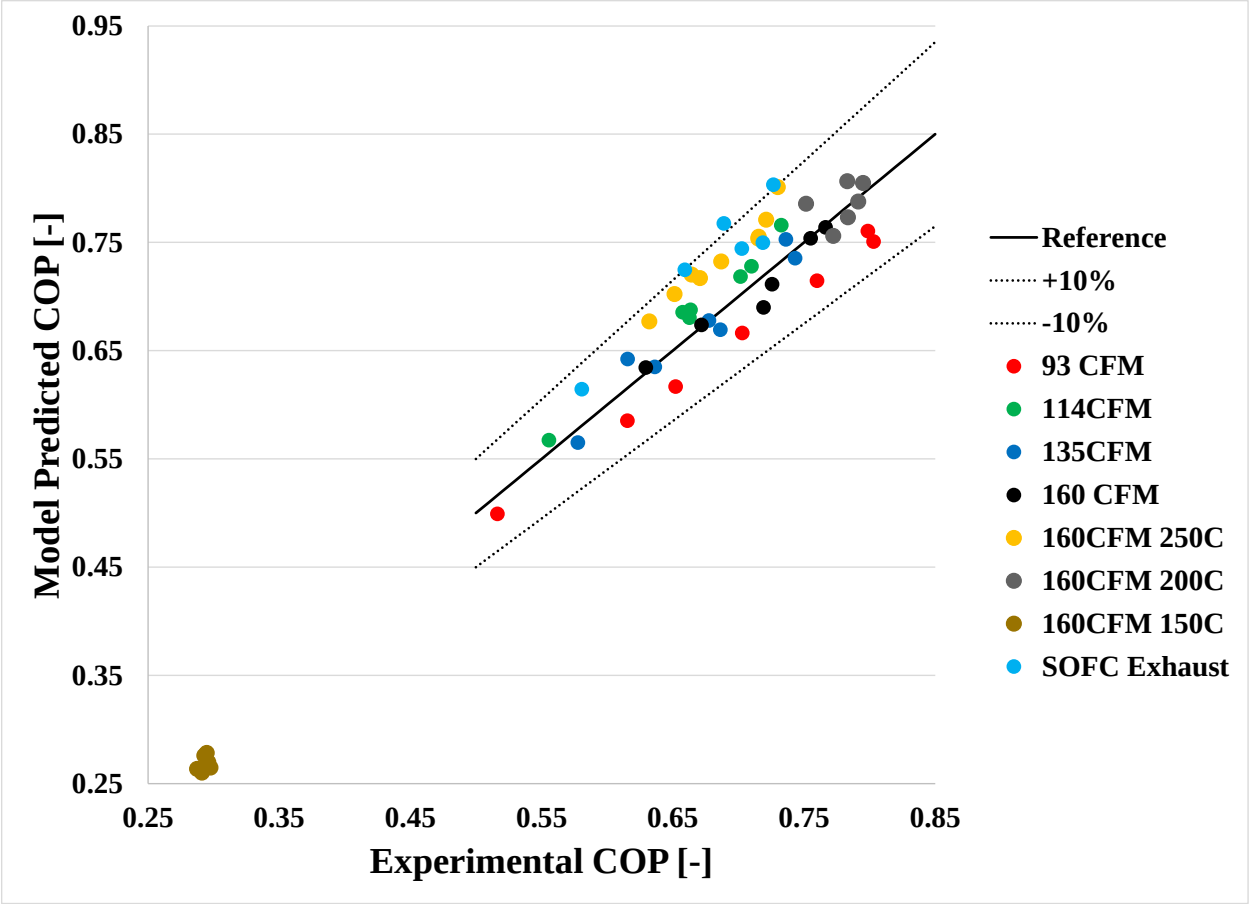

Figure 7.26 – Modeled COP Prediction Accuracy.

Note that all of the experimental series are plotted at each of their COPs and compared to the model's prediction for the cycle's performance. Additionally, note that the reference line indicates a perfect match between the measured and predicted performance, with an upper and lower bound of ±10% shown as well.

Reviewing the overall performance of the thermodynamic model, the simulation is able to accurately calculate the chiller's COP within the ±10% accuracy for the majority of data points. In general, the predictions of the model overestimate the COP slightly compared to the measured values, but this is expected because the model does not account for minute losses in the plumbing of the test stand.

Reviewing the different series, the constant exhaust flow series predicts the COP slightly lower for "93 CFM," but very accurately for "135 CFM" and "160 CFM." The error for the lower flowrate would indicate

that the heat transfer model for the shell and tube heat exchanger is perhaps not entirely capturing the ability of the heat exchanger to capture waste heat even at lower flowrates.

Conversely, for the variable hot loop flow series, “160 CFM 250C”, the higher flow and temperature leads to an overestimation of the efficiency of the cycle. The higher predicted efficiency of the cycle is because the model doesn’t predict that the desorber pressure will rise as high as it is measured to. The lower desorber temperature keeps the efficiency of the cycle higher, similar to the trends shown in Figure 7.18. However, the model is able to capture the changing hot water flowrates and accurately predict their impact on the chiller’s performance, albeit at a slightly elevated level. Lastly, the chiller model predicts much better performance for the “SOFC exhaust” case due to the same factors. Some of the data points for the “SOFC Exhaust” series fall outside of the ±10% confidence range, so it may be prudent to investigate and upgrade the model if these low flow, high temperature flows are prevalent.

The verification of the absorption chiller’s model represents an important check in the accuracy of the thermodynamic modelling for the integrated system. While this experiment and model are based upon the single effect system, it is assumed that the evaporation physics within the absorption chiller remain the same for the higher level desorbers in the more complex double- and triple-effect absorption chilling cycles.

The second performance metric that the absorption chiller was evaluated for was the chilling capacity and it is important to verify the model’s ability to predict the overall chilling capacity as well. The thermodynamic model’s accuracy in simulating the chilling capacity is shown below in Figure 7.27.

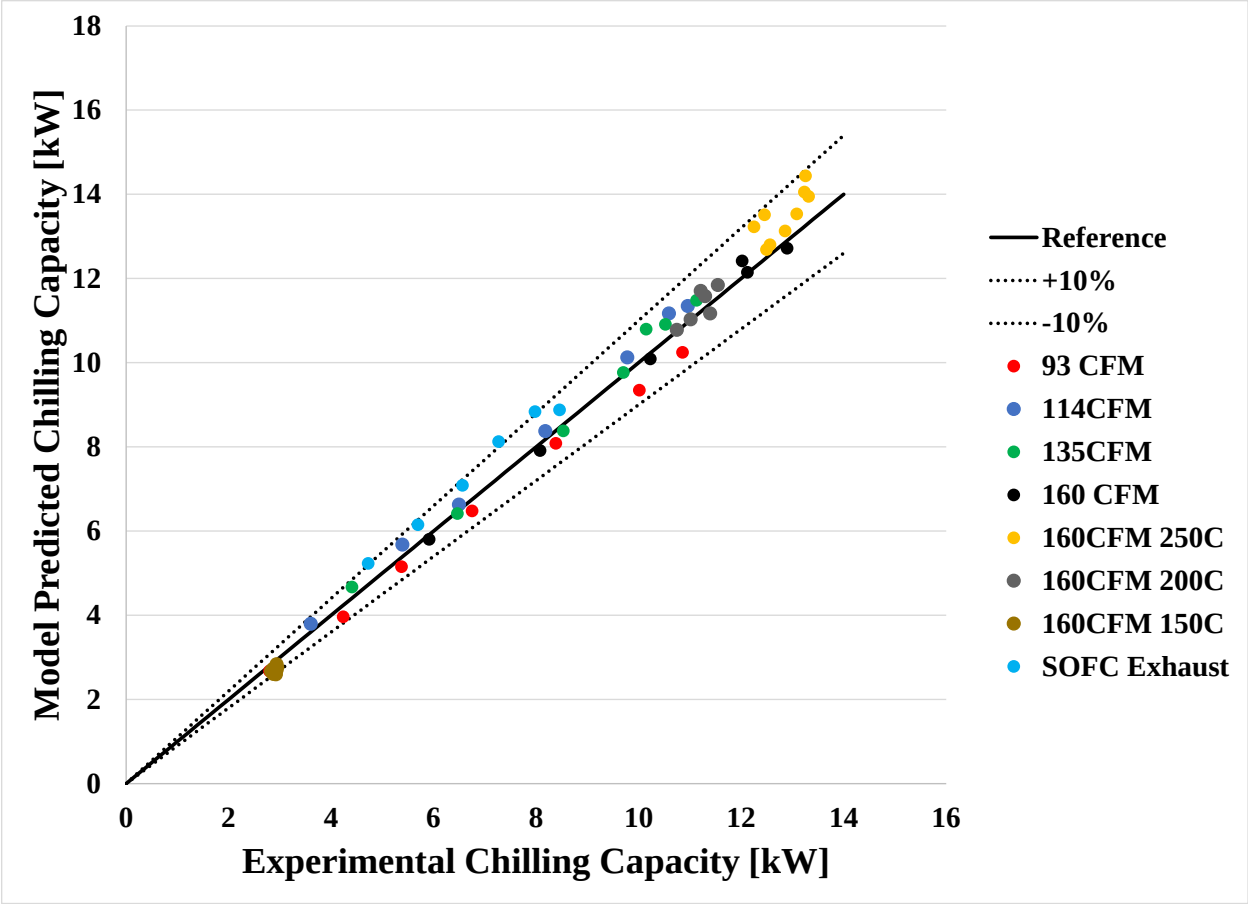

Figure 7.27 – Modelled Chilling Capacity Prediction Accuracy.

Reviewing the prediction accuracy of the absorption chiller model, when predicting the chilling capacity, the model is able to estimate the chilling capacity within the ±10% accuracy for the majority of data points. Similar to the predictions for the COP, the only outlying series are “160 CFM 150C” and the “SOFC Exhaust”. Interestingly, the predicted chilling capacity for each of the other trends follows similar trends to their over/under predictions to the COP. This would indicate that the majority of the variance between the model and the experimental results occurs within the absorption chiller model rather than the WHR heat exchanger model. This is because if the COP is overpredicted and the chilling capacity is similarly overpredicted, the heat transfer into the desorber can be estimated to be more accurate since the error is correlated.

The level of confidence presented by having a single effect absorption cycle model that can correlate with the experimental data is a great boon for the integrated modeling presented earlier. The ability of the experimental system to demonstrate the effectiveness of the thermal integration and further verify the simulated situations which help reduce the carbon footprint of data centers bodes well for making the integrated concept a reality.

Chapter 8 - UCIMC Case Study: Operational and Economic Performance Analysis of a High-Temperature Fuel Cell Cogeneration Plant

The literature review for this dissertation has identified several existing examples of thermally integrated high temperature fuel cells with absorption chilling. To leverage the knowledge that can be gained from existing systems, the analysis of such a system that exists on the UCI medical center campus presents a great opportunity for the examination of how feasible such a system is in the real world. A 1.4 MW molten carbonate fuel cell (MCFC) is paired with a 200 ton single-effect absorption chiller to produce power and chilling for the medical campus site. This installation is analyzed as a case study for the effectiveness of thermally integrated high temperature fuel cells.

8.1 - Introduction

To curb the effects of climate change, the deployment of high-efficiency, distributed-generation power plants has become prevalent within the state of California. Large scale, megawatt-class fuel cells are one of the technologies selected for the on-site generation of power. Fuel cell systems are high-efficiency thermoelectric engines that operate on an array of fuels and can provide electricity at thermal efficiencies of up to 65%. These large fuel cells can also operate at high temperature with the opportunity to capture and use the waste heat to meet secondary energy demands.

Historically, fuel cells have faced challenges in adoption due to high capital investment costs (Kalina, 2016). To stimulate their adoption, several government-sponsored programs have been introduced financial incentives to drive volume and reduce the installed cost. Once deployed, a reduction in utility cost associated with the high fuel-to-electricity efficiency combined with the opportunity to capture and use exhaust heat to displace other utility costs suggest that a fuel cell power plant may provide a positive financial return on investment over the period of operation (Alanne et al., 2006; Isa et al., 2018). The economic performance of such a fuel cell installation depends on the cost of the fuel to power the fuel cell and the competing cost of utility provided electricity. Generally, the deployment of fuel cells is most

successful in areas of historically high utility electricity prices (Kalina, 2017). In California, over 300 MW have been deployed, more of which are operating on wheeled biogas (Curtin et al., 2017). Installations include a variety of customer sites (e.g., hotels, hospitals, research and university campuses, and data centers), all of which continue to demonstrate that on-site, base-load electrical power production of a stationary fuel cell can successfully displace more emission intensive grid electricity and provide other on-site value added attributes.

Cogeneration from high-temperature fuel cells is an especially attractive attribute to further increase the overall utilization of the fuel (Alcaide et al., 2006; Appleby, n.d.; Raj et al., 2011) and thereby improve the economic performance by producing, in addition to electricity, hot water, steam, or chilled water from the high-temperature heat available in the fuel cell exhaust (Alcaide et al., 2006). The cogeneration utilized in this application is the production of chilled water via an absorption chiller. Absorption technology pairs well with HTFC power plants with several examples providing significant utility for commercial installations (Margalef & Samuelsen, 2010).

The successful commercialization of fuel cells is directly related to the operational and economic performance of fuel cell installations (Penner et al., 1995). Several studies suggest that the principal factors in the economic performance are the capital investment and the fuel cost (Khani et al., 2016; Lipman et al., 2004; Mehmeti et al., 2018; Shamoushaki et al., 2017). While adjustments to the principal investment will change over time, the high sensitivity of economic performance to fuel cost can suggest operational strategies to minimize fuel usage. Other studies address fuel cell installations with CCHP (Combined Cooling Heating and Power) applications. None, however, investigate the operational and economic performance from an existing commercial operation due to the challenges of (1) acquiring the detailed requisite data, and (2) unraveling the complex impacts of competing and convoluted utility electric rates and demand charges.

Using detailed fuel cell plant performance data from an operating system, and a detailed economic analysis from actual gas and electric utilities, this study addresses the operational and economic performance of an established HTFC paired with an absorption chiller.

The objectives of this study are as follows:

- Present and analyze four years of operational performance from the beginning of the HTFC/Chiller operation, (February 2016 through December 2019).
- Present and analyze the economic performance of the HTFC plant over the same period.
- Perform a sensitivity analysis of operational factors using historical data.
- Simulate the future economic performance.
- Identify strategies that can improve the operational and associated economic performance of the cogeneration plant in future years.

8.2 - Installation Background

The HTFC cogeneration plant consists of a 1.4 MW fuel cell and a 200-refrigeration ton (RT) Lithium Bromide single-effect absorption chiller powered by the fuel cell exhaust heat. The plant was commissioned in January 2016 with the goal to provide baseload power and chilled water to the customer. The cogeneration plant is installed on-site and includes the HTFC, the system control module, a natural gas de-sulfurizer, the absorption chiller, and cooling tower. The HTFC runs on natural gas and is connected to the customer grid and natural gas supply, both on the customer side of the meters. The fuel cell provides continuous electricity production, partially offsetting the nominal 8 MW customer power demand. The exhaust of the HTFC is ducted into the absorption chiller where heat is absorbed before release to the atmosphere. The chilled water supply and return of the 200 RT absorption chiller is integrated into the customer district chilled water distribution system.

The HTFC and chiller are operated in accordance with a 19-year power purchase agreement (PPA) enacted between the customer and the fuel cell plant operator. The PPA outlines the electrical rate in addition to heating and chilling guarantees of the plant.

To monitor and evaluate performance, the fuel cell and chiller are instrumented to meet requirements set forward by the California Self-Generation Incentive Program (SGIP) with data continuously logged in

15-minute increments and stored on a remote SGIP server to evaluate compliance with the SGIP standards. A dedicated root-style natural gas flowmeter is used to monitor fuel consumption into the HTFC, and a dedicated totalizing electricity meter is used to monitor the electrical production. Instantaneous power output is provided by the fuel cell's operating software to the data logger. The SGIP data are combined with meter data from the utility to provide temporal power demand data which is used to assess the demand cost adjustment.

8.3 - Historical Operational and Financial Analyses

To provide insight into the factors that governed the HTFC's historical performance, operational and economic analyses were performed on the data collected from February 2016 to

December 2019.

8.3.1 - Operational Performance Analysis

To assess the plant's operational performance, the following performance indicators were selected for evaluation: electricity production, average power production, natural gas consumption, fuel cell efficiency, and chilling capacity. Others, such as auxiliary electricity (<1.5%), and water consumption (<2%) on the HTFC plant site were not considered due to their minimal impact on the performance of the plant.

The monthly cumulative electricity production of the fuel cell was calculated using the instantaneous power production data from the fuel cell's data logger. The cumulative electricity production was calculated below where the start and end times were midnight on the first of the month and the consecutive month. A value of zero is assigned to empty values since the data logger creates empty values when the fuel cell system is off.

$$E_{FC} = \int_{t_{month}}^{t_{month+1}} P_{FC}\, dt \tag{8-1}$$

Using the four-year span of monthly data, Figure 8.1 was created to represent the electricity production performance of the plant.

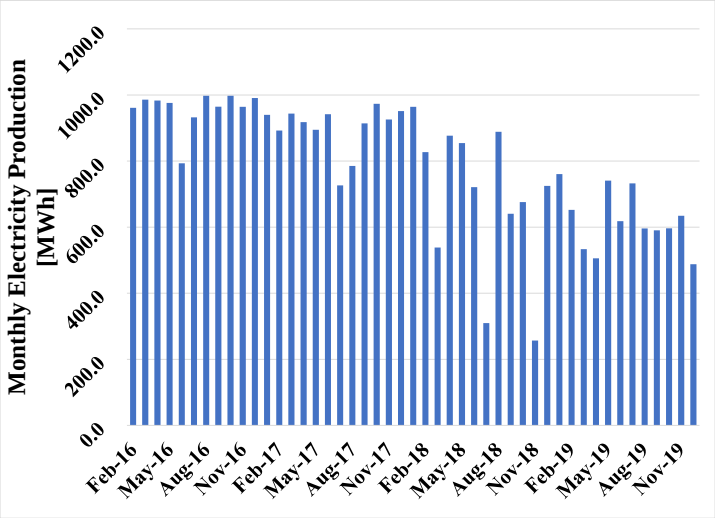

Figure 8.1 – Monthly Electricity Production Performance.

Note that the electricity production is around 1000 MWh per month for the first two years of operation but falls off in 2018. Based on the data available, the substandard monthly electricity production is not associated with fuel cell performance but rather with down time due to "tripping events" (i.e., occurrences when the fuel cell experiences an outage and restarts, pausing production while the system resets). In 2019, the frequency of tripping events decreased due to identifying and resolving a few of the more apparent causation factors.

The second performance indicator for the HTFC, shown in Figure 8.2, is the average power production within a month, calculated by taking the mean of the instantaneous power production during a given month.

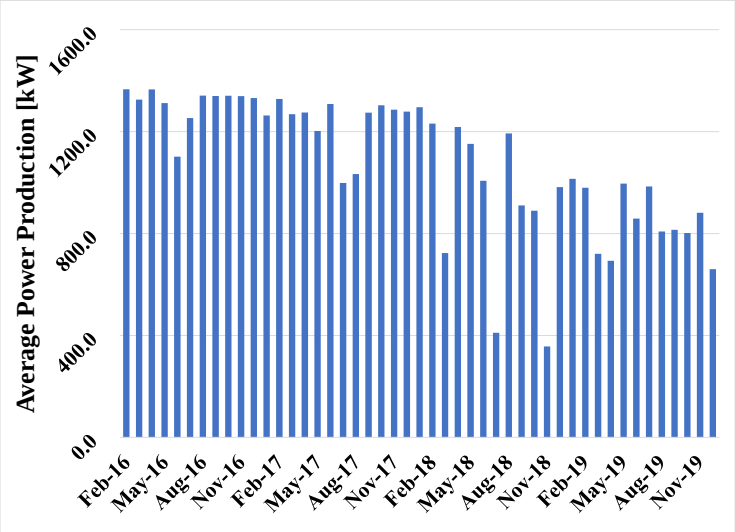

Figure 8.2 – Monthly Average Power Production.

As expected, the power production tracks the cumulative electricity production with only slight deviations due to the number of days per month. Figure 8.2 provides a more easily understood performance metric, demonstrating that the fuel cell produced close to the expected 1.4 MW for the first two years of operation. In the third and fourth year, the average power output fell to around 800 kW, suggesting a degradation in the stack.

The next performance indicator for the HTFC is natural gas consumption which is also monitored by the SGIP data logging system. The data are logged in 15-minute intervals with an instantaneous fuel flow rate in standard cubic feet per minute (SCFM). The monthly natural gas consumption within a month is calculated below.

$$V_{NG} = \int_{t_{month}}^{t_{month+1}} \dot{V}_{NG}\, dt \tag{8-2}$$

As shown in Figure 8.3, the monthly natural gas consumption is converted to therms (=~100 CF of natural gas) to relate the consumption to the utility bills, discussed later.

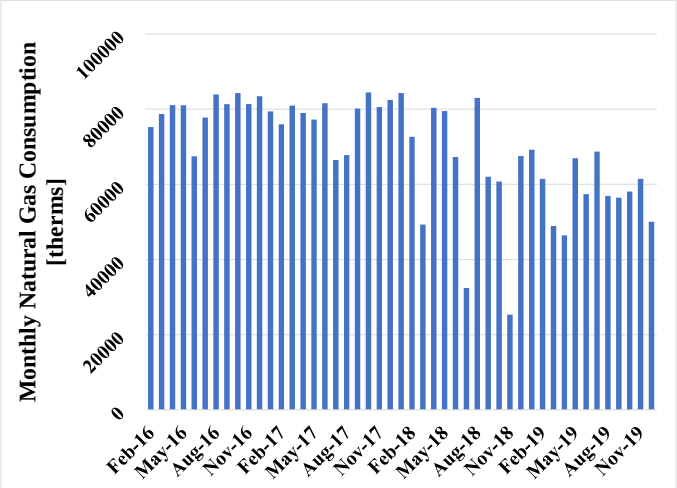

Figure 8.3 – Monthly Natural Gas Consumption.

As expected, the natural gas consumption maps to the electricity production trends. By obtaining the monthly natural gas consumption and knowing the electricity production of the plant, a plant effective electrical efficiency can be calculated below.

$$\eta_{plant,eff} = \frac{E_{FC}}{V_{NG} * LHV_{NG}\left[\frac{MWh}{therm}\right]} \tag{8-3}$$

The plant effective electrical efficiency over the four years is presented in Figure 8.4. The initial "beginning life" efficiency of 50.1% is in the expected range.

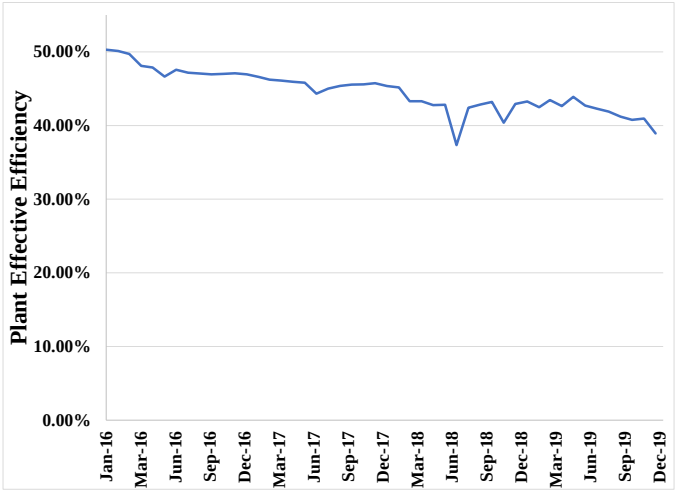

Figure 8.4 – Historical Effective Plant Electrical Efficiency.

Despite the performance issues in 2018, the fuel cell maintained a relatively steady rate of efficiency degradation due to wear on the fuel cell's stack, albeit higher than the degradation projected for the plant.

The final performance indicator is the historical chilling capacity. The chilling capacity is determined from the three following data streams: chilled water flow rate, supply temperature, and return temperature.

$$\dot{Q}_{chiller} = \dot{V}_{chill} * \rho_{H_2O} * Cp_{H_2O} * \left(T_{return} - T_{supply}\right) \quad (8\text{-}4)$$

Note that the density and specific heat capacity are evaluated at standard temperatures and pressures. Using the average chilling capacity for the month can be calculated with the results shown in Figure 8.5.

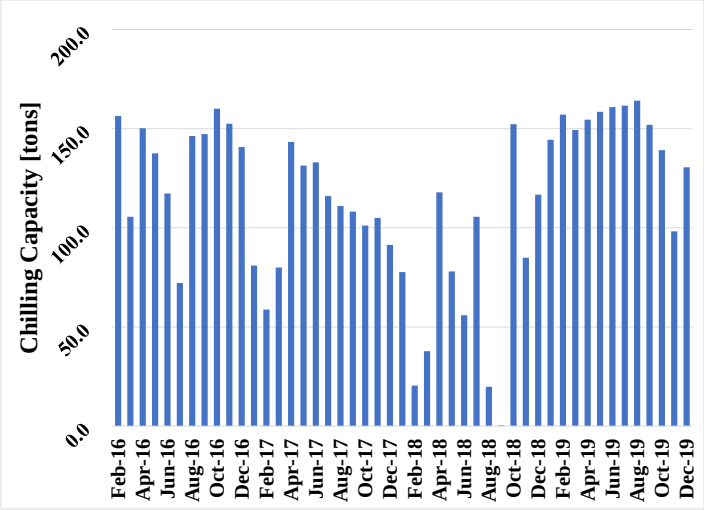

Figure 8.5 – Average Chilling Capacity.

The absorption chiller is powered by the HTFC exhaust, which can provide up to ~1500 kW at 400 °C of useful heat to the chiller. Note that, while the chiller was designed for 200 RT (702 kW) chilling capacity, its performance has been constrained to 150 RT (526 kW) for reasons that are currently under investigation including the fit to the chilled water loop differential in temperature. This reduction in capacity does not affect the heat output of the HTFC. Rather, the chiller simply absorbs less heat from the exhaust stream as it is operated, as a result, at partial capacity.

8.3.2 - Economic Performance Analysis

The HTFC cogeneration plant was installed with the expectation that it would financially return some of its principal investment through a discounted PPA electricity rate and the provision of chilling at no cost. To evaluate the economic performance of the plant, a historical analysis was performed on the data from February 2016 through December 2019. The analysis was conducted in collaboration with the customer who provided the rate structures, electric and gas utility bills, and a critical review of the analyses.

To quantify the historical savings provided by the fuel cell, the historic economic performance of the HTFC plant was compared to the cost of equivalent conventional delivery. The breakdown of the costs associated with both cases consists of:

HTFC Plant Costs:

- Fuel Cell Electricity Cost
- Natural Gas Consumed Cost

Equivalent Conventional Delivery Costs:

- Equivalent Electricity Cost
- Equivalent Chilling Cost
- Demand Cost Adjustment

Fuel cell electricity cost is the cost of electricity produced by the HTFC, which is paid at the rate prescribed by the PPA. The cost of natural gas is paid by the customer in both cases.

The equivalent electricity cost is the theoretical cost of the electricity produced by the HTFC if it were supplied instead by the electric utility. The cost of equivalent chilling is the cost associated with the electricity required to run a conventional chiller which would deliver the equivalent amount of chilling produced by the absorption chiller. Finally, the demand increase cost is the cost associated with electric utility's monthly "demand charge" which is defined as a rate in $/kW and based on the 15-minute peak

demand of the electric utility by the site during a given month. The demand cost adjustment is the reduction in the peak demand of the site associated with the power capacity of the fuel cell.

To calculate the fuel cell electricity cost, the cumulative electricity produced by the fuel cell as calculated in Equation 6-1 is multiplied by the rate structure shown in Table 8.1 which shows the PPA pricing for electricity through the years. Note that the pricing increases at a 2% rate yearly.

Table 8.1 – PPA Electricity Prices.

Year	**PPA Price [$/kWh]**
2016	$0.077
2017	$0.079
2018	$0.080
2019	$0.082

The natural gas consumption cost uses the data logged by the fuel cell and calculated in Equation 6-2 multiplied by effective natural gas rates supplied by the utility ($0.39 - $0.72 /therm).

The total monthly HTFC plant cost is shown in Figure 8.6. Note that the cost of electricity makes up for ~30% of the total plant cost.

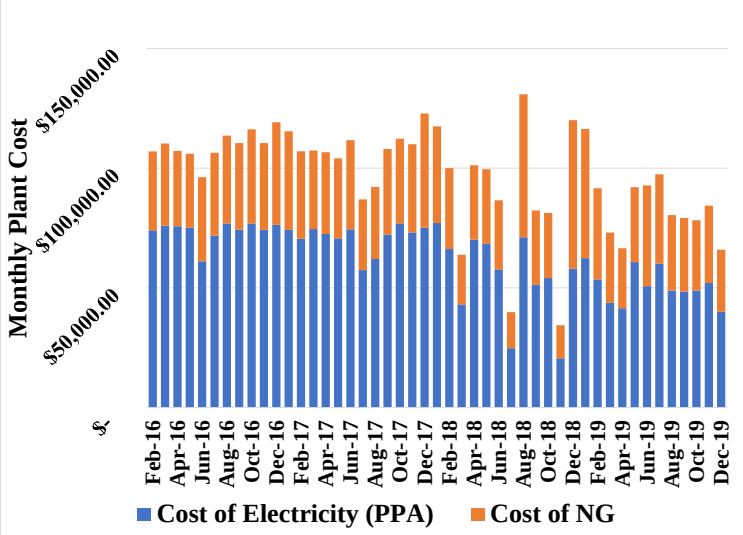

Figure 8.6 – Monthly HTFC Cogeneration Plant Costs.

The equivalent electricity cost is calculated by using the same cumulative electricity produced by the fuel cell and charging it at utility rates. For this site, electricity is bought through a direct access agreement and charged at wholesale prices ($0.063 - $0.069 /kW) with delivery charges assessed by the utility ($0.022 - $0.030 /kWh).

The equivalent chilling cost is evaluated using the historical chilling capacity, as calculated in Equation 3.4, and determining how much electricity would be required to run a mechanical chiller at that capacity. For the purposes of this analysis, the mechanical chiller is assumed to have a coefficient of performance (COP) of 7 which equates to the conversion factor stated in the PPA of 0.5 kW-e /RT. The electricity required is then charged at the conventional delivery electricity prices listed above. Additionally, the power demand associated with the equivalent mechanical chiller is also considered.

$$C_{chill,conv} = \frac{Q_{chill}}{COP_{conv}} * Pr_{utility} + \frac{\dot{Q}_{avg,chill}}{COP_{conv}} * Pr_{demand} \quad (8\text{-}5)$$

Finally, the monthly demand cost adjustment is evaluated by determining the customer's peak demand with the fuel cell installed compared to the peak demand were the fuel cell not installed. The difference between the peaks is assessed as the demand adjustment and charged at the demand rate stipulated by the utility (e.g., $16.86 - $20.83 /kW).

This adjusted demand cost is a necessary calculation to establish the actual monthly demand charge to the customer. Should the fuel cell operate continuously for the month, the fuel cell will result in a savings to the customer by reducing the peak demand for the month by an amount equivalent to the fuel cell power output. However, should the fuel cell trip during the month, the resultant peak may increase the monthly demand charge by creating an unintended spike in demand from the utility. However, despite creating an unintended peak, the fuel cell could have still reduced the peak demand at another point in the month thus resulting in a net power savings. The methodology required to evaluate the adjusted demand cost requires the 15-minute data of both the HTFC power production and the same interval electric utility demand meter data. An example of one month's data in a month that the fuel cell tripped is shown in Figure 8.7. The "Site Power Demand (Utility)" is the power supplied by the utility. The "HTFC Power Production" is the power

generated by the fuel cell plant. The “Gross Power Demand” is the sum of the “Site Power Demand (Utility)” and the “HTFC Power Production.”

Note that two trip events occurred in the month, resulting in a fuel cell restart and startup period. A HTFC requires several days to restart due to the high stack temperature and the slow reheating process to preclude undue thermal stress.

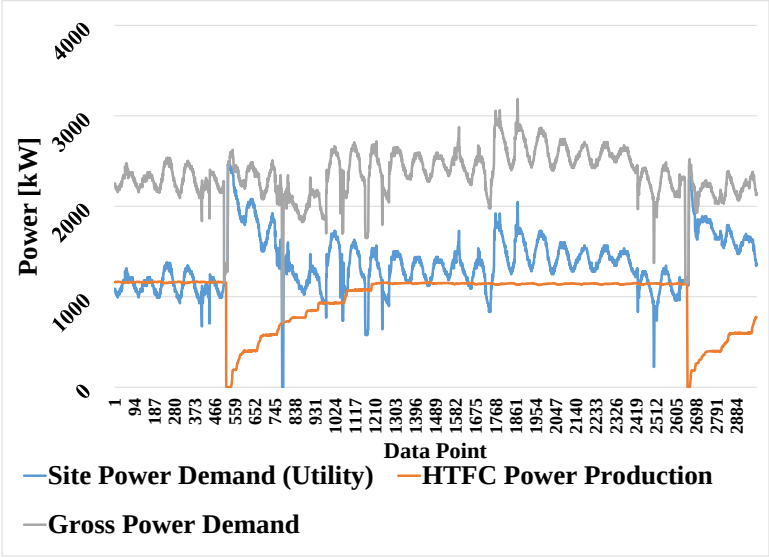

Figure 8.7 – Example Month Power Demand/Production Data.

In Figure 8.7, it is apparent that the peak demand from the electric utility, shown in blue, occurs around data point 500 and is assessed at ~2500 kW. The peak power demand for the month must then be determined without fuel cell power production during this month. To create the customer’s power demand for the month, the utility demand data are summed with the HTFC power production data to create the gross power demand. Figure 8.7 shows in gray the raw demand data for the customer. Again, in Figure 8.7, the peak gross power demand occurs around data point 1850 and would be assessed at ~3000 kW. The demand adjustment (an increase in this example) of going from 2500 kW to 3000 kW has an associated cost that is calculated by multiplying the difference by the electric utility demand charge for the month.

Note that in some cases, the customer’s peak demand is directly associated with a fuel cell trip, in which case, there is no adjusted demand cost for the month.

Finally, with all the pieces of the equivalent conventional delivery cost evaluated, it is possible to calculate the total cost of the equivalent conventional delivery case and the historical values are shown in Figure 8.8.

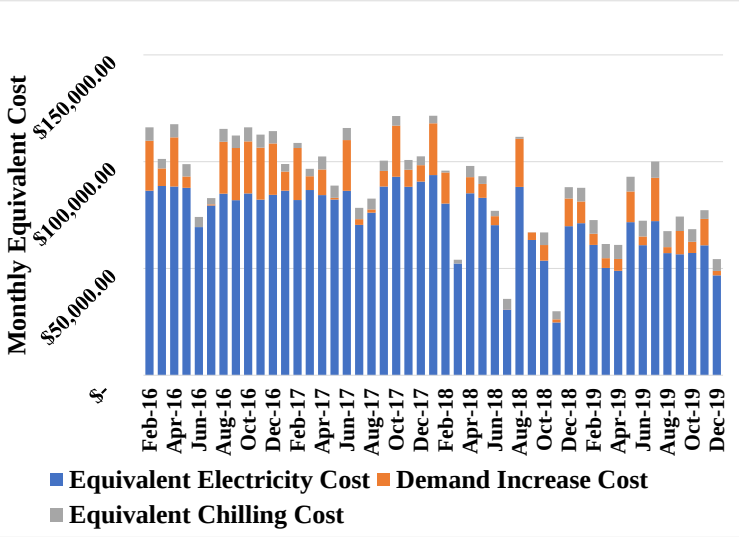

Figure 8.8 – Monthly Equivalent Conventional Delivery Costs.

8.3.3 - Historic Economic Savings Analysis

Having calculated the historical HTFC plant costs and the equivalent conventional delivery costs, it is possible to compare the two and assess the month to month savings of the cogeneration plant. Figure 8.9 shows the monthly savings of the fuel cell plant with green indicating savings and red indicating losses.

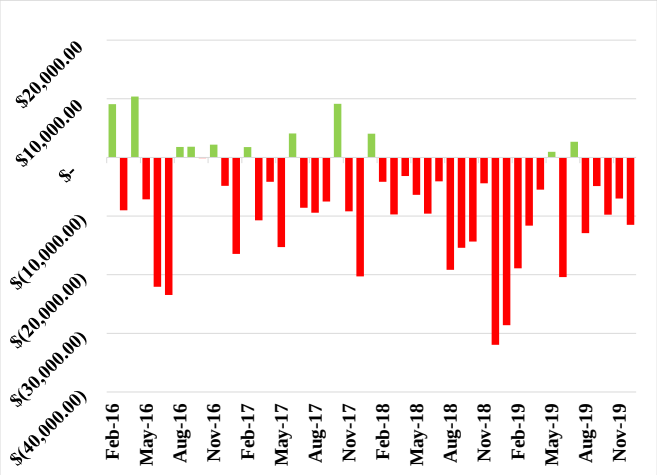

Figure 8.9 – Monthly Savings.

While Figure 8.9 reveals substantial losses over the four years investigated, it is not possible to discern what operational components have the largest impacts on the results. To investigate these impacts, several theoretical cases were formulated and analyzed.

The first theoretical case was to simulate the savings if the absorption chiller operated at full capacity for the entire operational period.

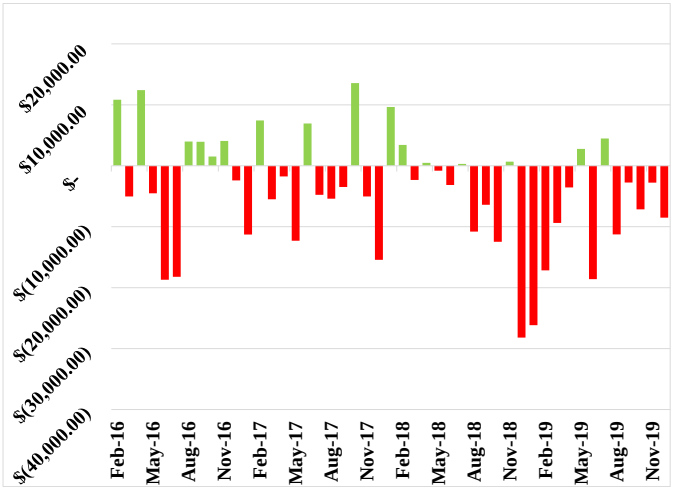

Figure 8.10 – Theoretical Monthly Savings with Ideal Chiller.

The results, shown in Figure 8.10, reveal that the performance increased in 2018. However, the overall impact on savings by improving the chiller performance is relatively minimal.

The second theoretical case simulated the savings if no trip events occurred during the operational period. To simulate this effect, the electricity production was not adjusted, but the demand increase cost was calculated using the ideal fuel cell power output for each month.

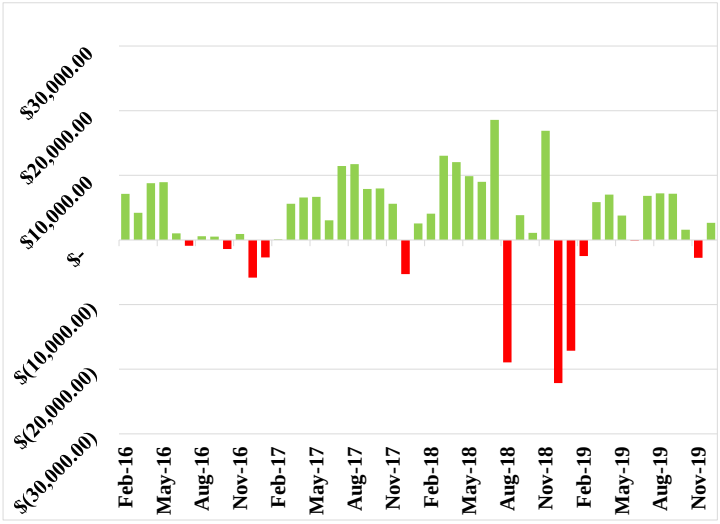

Figure 8.11 – Theoretical Monthly Savings with No Fuel Cell Trip Events.

The results, shown in Figure 3.11, makes it clear that the largest impact on the month to month savings is the tripping events. By eliminating the tripping events through the operational period, the plant operates at a net gain with only a few months experiencing losses. These months correspond to events which caused atypically high fuel prices, thus reducing the economic performance.

While the causes of tripping, particularly those most frequent and prolonged in 2018, are under investigation, candidates include a fuel cell stack disruption, fuel cell plant controller firmware defect, fuel cell controller settings that may preclude riding through voltage surges on the customer grid.

8.4 - Future Operational and Economic Performance

Using the trends and insights garnered by the historical economic performance, it is possible to identify remedies that can improve both the operational and economic performance over the remainder of the 20-year PPA period. Among the options are a replacement of the stack and reducing the PPA electrical rate.

The two benefits expected from replacing the stack: re-establishing the expected electrical efficiency and reducing the tripping frequency, are considered separately.

To address the impact of replacing the stack going forward, a “Restacking Model” was created based on several system performance inputs and trends, shown in Table 8.2, derived from an extrapolation of historical data.

Table 8.2 – Restacking Model Cogeneration Plant Inputs.

Parameter	**Input Value**
HTFC Nominal Power	1393 kW
Power Degradation Rate	12.90 kW/month
Plant Eff. Efficiency Start	48.82%
Eff. Efficiency Degradation	0.18 %/month
Intermittency Factor	0.5
Nominal Chilling Capacity	150 RT
Restacking Interval	5 years

The degradation rates listed in Table 8.2 are determined by averaging the degradation over the interval specified. By using historical data to extrapolate into the future, a “worst-case” scenario is first considered where no improvements are made. Given this, both the HTFC power degradation rate and plant effective efficiency are linear.

The intermittency factor indicates the frequency of tripping events. For example, an intermittency factor of 0.5 indicates a trip every other month, while an intermittency factor of 1 represents no trips. Based on historical data, an average intermittency factor of 0.5 is adopted for the worst-case scenario, and the nominal chilling capacity is assumed constant at the currently maximum achievable 150 RT.

Lastly, the restacking interval is assumed to be a regular 5 years, per the manufacturer’s specification. There is suggestion that improvement to the stack will allow for a longer operation of up to 7 years, but this assumption will again allow for conservative estimates.

In addition to the system parameters, the restacking model includes several economic input parameters to predict the cost of each component. These inputs, shown in Table 8.3, are based on historical data as well as external sources for predicting utility costs in the future.

Table 8.3 – Restacking Model Financial Inputs.

Parameter	**Input Value**
PPA Pricing Start (2020)	$ 0.083 /kWh
PPA Pricing Increase Rate	2% /yr
NG Pricing Start (2020)	$ 0.494 /therm
NG Pricing Increase Rate	3% /yr
Price of Utility Electricity Start (2020)	$ 0.0985 /kWh
Price of Utility Electricity Increase Rate	$ 0.0004 /month
Demand Charge Price Start (2020)	$19.39 /kW
Demand Charge Price Increase Rate	$ 0.7452 /yr

In Figure 8.12, the economic performance of the cogeneration plant is shown for the next five years. Note that from the gap in results from January 2020 to August 2020 which reflects an assumed period in which analyses were not performed and down-time for replacing the stack.

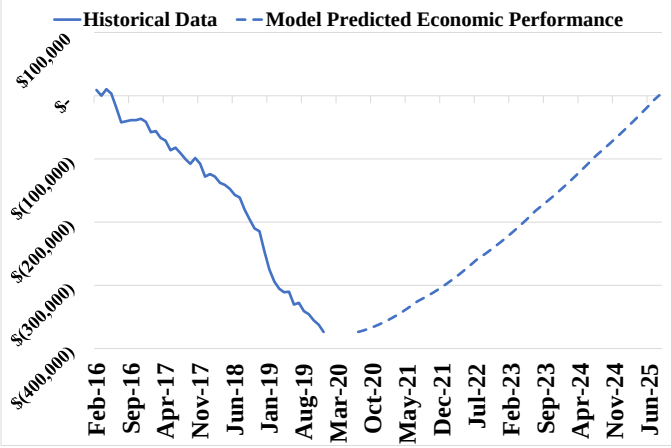

Figure 8.12 – Restacking Model Predicted Financial Performance.

The predicted performance is charted along with the historical data to demonstrate the potential to mitigate the losses which occurred historically. Figure 8.12 shows that the HTFC plant is expected to begin producing positive economic performance following the restacking. This gain in performance is due to two factors, the increased efficiency of the replacement stack and the fixed annual price increase of the PPA electricity of 2% compared to the utility prices which are expected to increase at a rate of 4.5%. However, despite the predicted improvement in economic performance, a significant performance debt remains from

the first four years. To achieve significant payback over the lifetime of the system, methods to further improve the economic performance of the plant are required.

To improve the performance of the cogeneration plant moving forward, insights from the theoretical historical economic cases are explored. To simulate a reduction in the frequency of tripping events, the intermittency factor is increased incrementally from 0.50 to 0.75. Note during the first year of operation, the intermittency factor was 0.75.

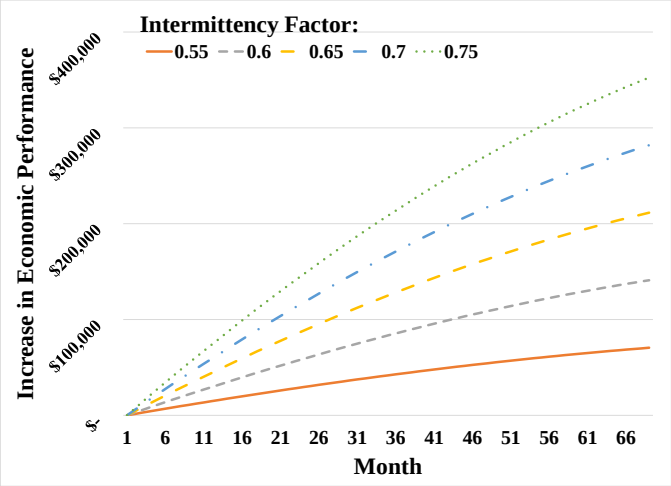

Figure 8.13 – Intermittency Factor Modelled Impact on Financial Performance.

The results, shown in Figure 8.13, demonstrate how sensitive the economic performance of the plant is to the tripping frequency. By increasing the intermittency factor from 0.5 to 0.65 the plant is able to save $200,000 more than if the HTFC plant is continued to run with its historical intermittency. To this end, the primary system improvement that should be implemented is a reduction in tripping frequency, examples of which were previously mentioned.

To address the possibility that an increase in the intermittency factor may not exceed 0.50 and thereby not improve the financial performance of the plant, an investigation the financial parameters was undertaken. Reviewing the parameters in Table 8.3, it is apparent that the financial structure has little flexibility since the majority of the parameters are outside of contractual or operational control. However, the PPA pricing structure could be altered by a renegotiation of the PPA. To maintain financial

competitiveness, the 2% pricing increase rate should be maintained. However, by reducing the PPA pricing start point it is possible to improve the financial performance, which can buffer the impact of trips. Figure 8.14 shows how different reductions of the PPA price starting point in 2020 can impact the financial performance of the plant.

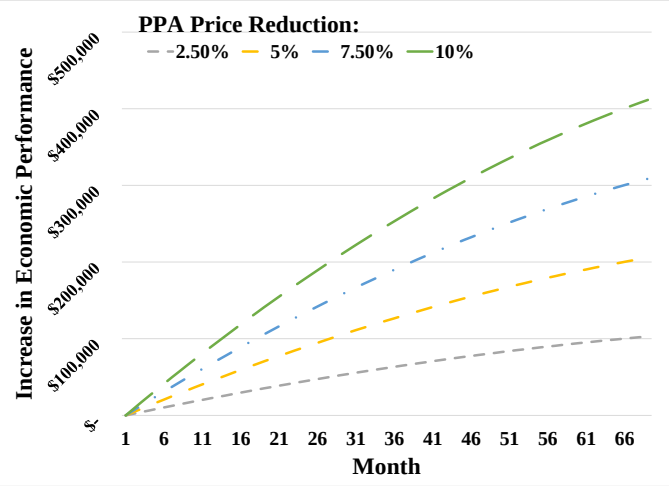

Figure 8.14 – PPA Price Start Modelled Impact on Financial Performance.

By comparing Figure 8.13 and Figure 8.14, it is apparent that a 10% reduction in the PPA pricing, while maintaining historical plant operational performance, will yield better financial performance than increasing the intermittency factor from 0.50 to 0.75. As a result, a contract negotiation to adjust the PPA pricing will, in this case, produce a more substantial increase in economic performance than a reduction in intermittency.

8.5 - Summary

This study reviewed the first four years of the operational and economic performance of an existing HTFC cogeneration plant. The historical data supported a robust analysis that led to: a high-resolution characterization of the plant electrical and chilling output, the reliability of the plant, the customer savings provided by the plant, and steps to improve the economic performance over the remaining years on the PPA.

From the historical operational data, a power production degradation was observed over the four years of operation. While this degradation is expected during the five-year life of the fuel cell stack, the observed degradation exceeded the expected rate. The plant also experienced an unexpected frequency of tripping events, particularly in the third year of operation. Rectifying a few causes resulted in a reduced but still unacceptable number of tripping events in the fourth year, leaving the fuel cell stack as the principal residual source of the tripping.

From the historical economic data, significant losses were generated over the majority of the months. While unexpectedly low electric and gas rates contributed to the losses, the principal cause was the demand charges and cost of utility electricity associated with the plant trips. Additionally, the approximate 25% reduction in the tons of refrigeration expected reduced the savings associated with the waste heat recovery. From the historical operational and economic data of the plant, operational changes can be selected and evaluated to improve the economic performance in future years. Operational changes considered included (1) restacking, (2) an increase in chilling capacity to the design, and (3) reducing the frequency of tripping. These operational strategies will help improve the performance of the HTFC system. Additionally, the CCHP plant's economic performance will benefit from technological improvements to extend the reliability and lifetime of the stack.

Assuming a "restacking" in 2020, the future economic performance while maintaining the historical chilling capacity and tripping event frequency was found to mitigate losses, but not result in a net positive savings. An improvement in chilling capability to the chiller design, in addition to restacking, also reduced the losses but not to the extent to result in a savings to the customer. A reduction in the tripping frequency was found to significantly increase the economic performance. To assure savings, a reduction in the PPA electricity rate would result in a net positive savings while retaining the integrity of the PPA instrument.

Chapter 9 - UCIMC Case Study Continued: Sampling and Degradation Analysis

9.1 - Degradation Analysis

Following the operational and economic analysis of the thermally integrated molten carbonate fuel cell (MCFC) at the UCIMC location as presented by the previous chapter, questions were raised about the ongoing performance of the fuel cell moving forward. This analysis looks at the performance of the fuel cell after the period over which the MCFC was evaluated previously.

9.1.1 - MCFC Restacking

Following the degradation of the MCFC stack over the first five years of operation, a “restacking” was performed. The restacking consisted of removing the stack component within the MCFC balance of plant and replacing it with a newer unit. This operation is laid out in the PPA to be conducted every five years to maintain the power output of the system. The new stack that was installed in summer of 2020 was developed as a “long life” component that should only require restacking every seven years. The MCFC system was offline from summer of 2020 until November 2020 at which point the system began ramping up to its nominal operating power output.

9.1.2 - 2016 vs 2020 Degradation

This section compares the operational performance of the MCFC when it was first installed an operated in 2016 with the performance after the restacking. Utilizing the data collected on the power output of the fuel cell, the primary comparison will be how the power output degrades over time. This comparison of the power output between the 2016 period and the 2020 period are presented in Figure 9.1 below.

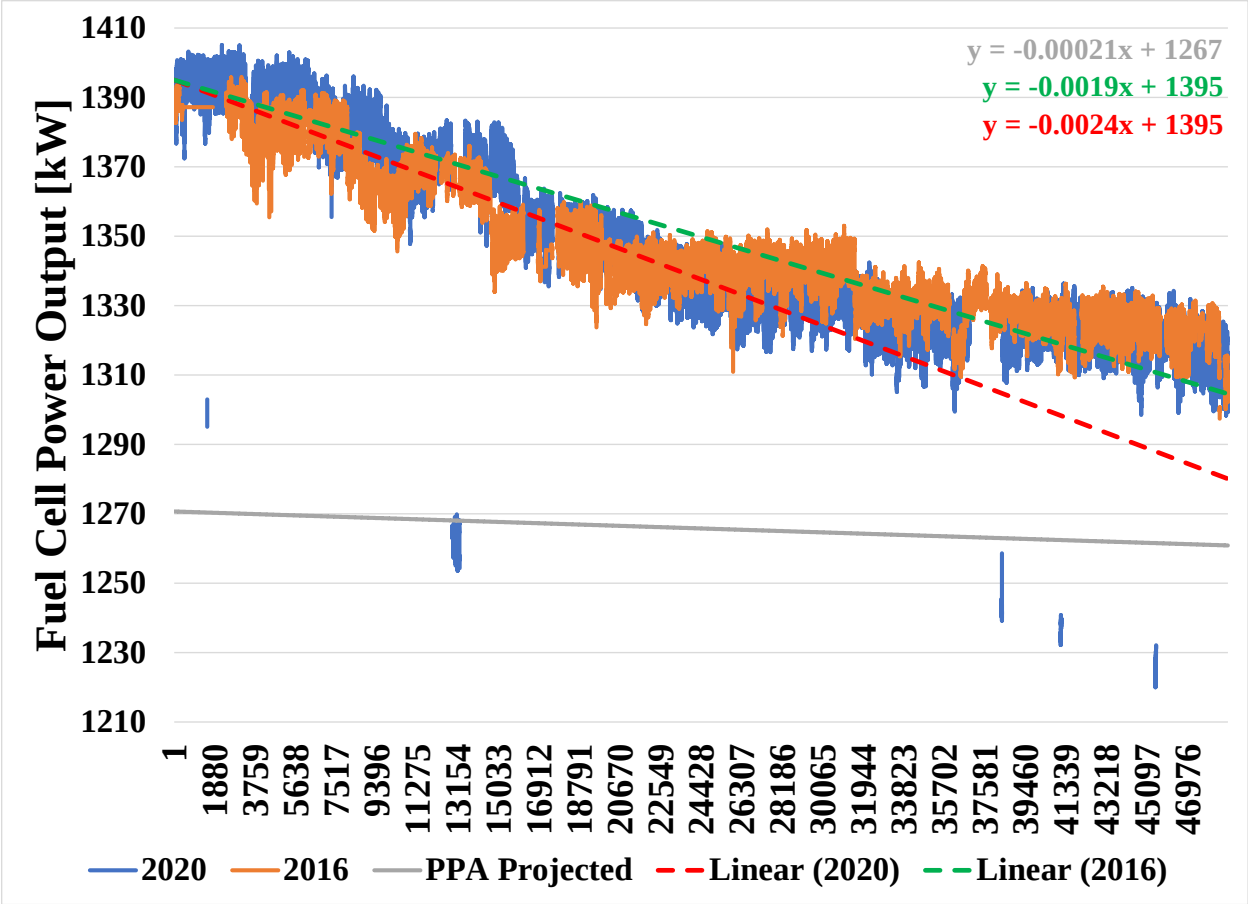

Figure 9.1 – MCFC Power Degradation Trends.

Reviewing Figure 9.1, note that the nominal power output of the MCFC is 1.4 MW (1400 kW) and that the power output of the fuel cell is expected to decline over its lifetime as the stack becomes more degraded. The two evaluation periods are shown in blue and orange for 2020 and 2016 respectively. The x-axis is displayed as sample number where each sample is taken at a 15 minute interval, meaning that the period shown in Figure 9.1 covers roughly one and a half years. Note that initially the power output of the 2020 stack maintains a higher power output but starts to decrease at a steeper rate after six months. Conversely, the 2016 stack is able to maintain a constant power output for months 9 – 11, mitigating degradation. This comparison shows that in general the performance of the 2016 and 2020 stacks is comparable in its power output degradation. This performance is curious consider that the 2020 stack is designed to be a longer life system.

Additionally, note that three linear trends are plotted in Figure 9.1, PPA projected and two linear fits of the stack data. The PPA projected trend is based on the predicted performance of the MCFC and begins with a power output of 1267 kW and degrades at a rate of 2.26 kW average power out per month. Compared to the 2016 and 2020 stacks, which both begin around 1400 kW but degrade with 23.7 and 27 kW per month, it is apparent that the degradation rate of the fuel cell far exceeds the predicted performance. Continuing the two trends into the future, the power output of the fuel cell in 2020 will degrade below the predicted performance within two years. Considering that the new stack is following the degradation rate of the 2016 stack, steps should be taken to counteract the degradation of the cell to prolong its operational lifespan.

One final comment regarding the power degradation is that the power output of the fuel cell is only shown in the initial degradation period which is fairly linear. However, once the system reaches a critical age, the degradation increases exponentially as shown in Figure 9.2. While the initial degradation may be poorer or equivalent to the 2016 stack, the most important factor will be when that critical age is reached and performance degrades dramatically.

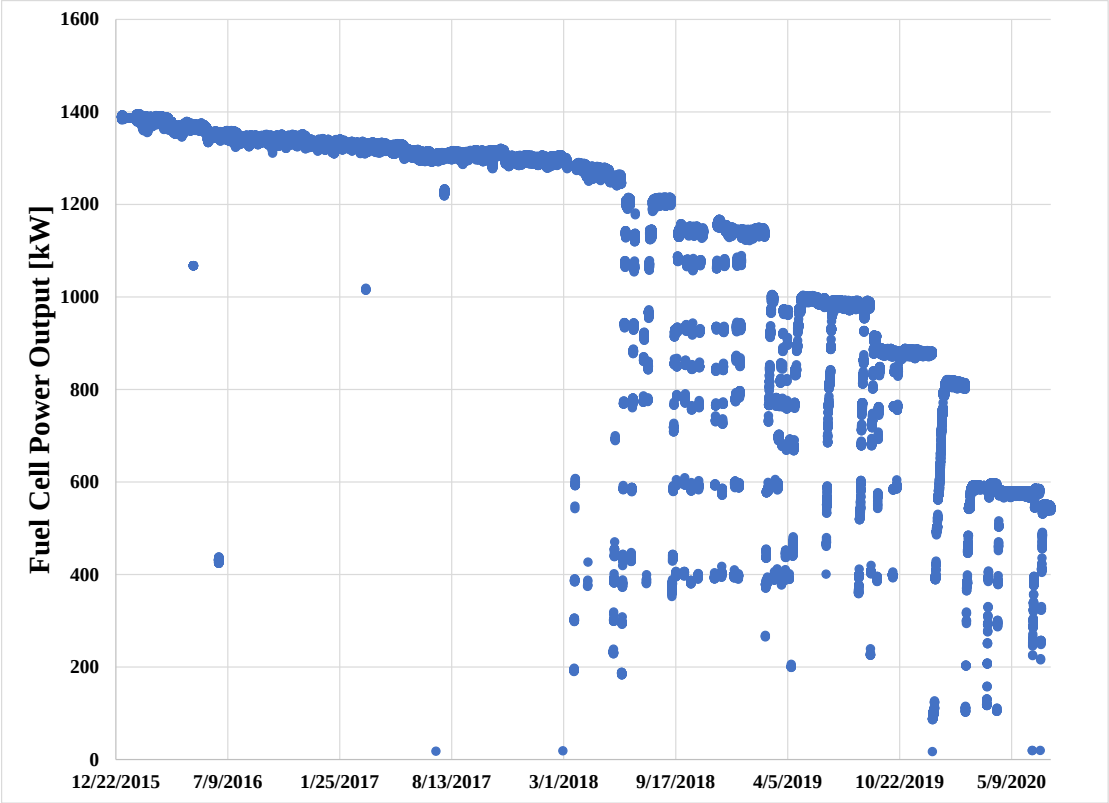

Figure 9.2 – Historical Power Output (2016 – 2020).

9.2 - Emission Sampling

In combination with the performance and economic analysis that was performed on the UCIMC MCFC plant, the parallel task of monitoring the emissions produced by the fuel cell was undertaken. The objective of the emissions sampling would be to characterize the emissions being produced and check to see if there are chemicals that are not expected in the exhaust. To take the emission samples from the fuel cell, a sampling test stand was constructed and is connected to emission characterizing equipment.

9.2.1 - Sampling Setup

To collect sample from the exhaust of the fuel cell, a sample port was necessary to tap into the exhaust stream. The exhaust connection to the absorption chiller contains several ports for access and allowed usage of one to insert a sample probe. The sample probe was ¼” stainless steel tubing that reached into the hot exhaust to capture gasses at the center of the exhaust flow. The sample probe is attached to an axillary port

via a bell reducer that takes the 2.5” NPT connection down to a ¼” Swagelok connection. The NPT fitting was installed with high temperature thread sealant to endure the hot gasses as the flow through the sample line. Additionally, the sample tube extends 1 m beyond the insulation of the exhaust ducting to allow for sufficient temperature loss before it is connected to a heated sample line. The heated sample line runs from the probe to the collection test stand. This connection layout is shown below in Figure 9.3.

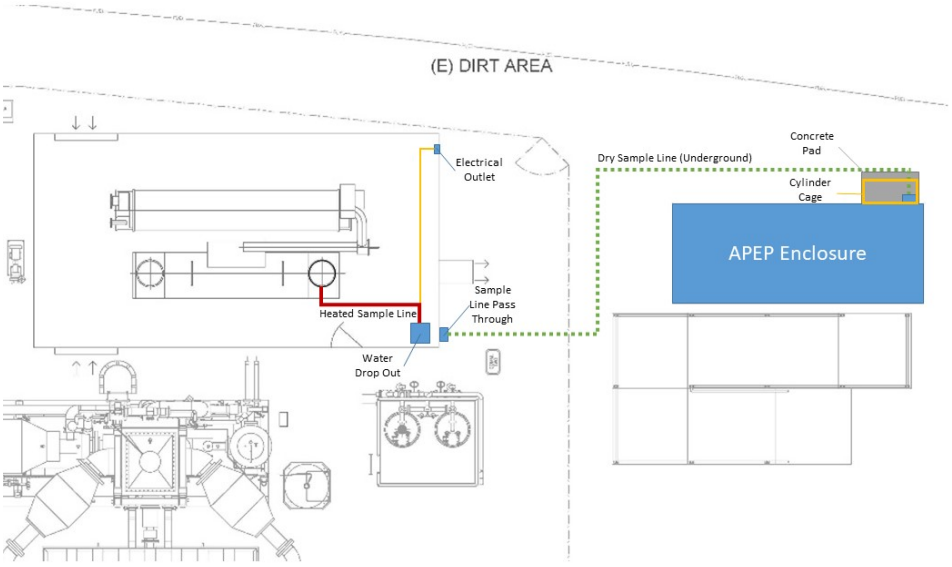

Figure 9.3 – UCIMC Sampling Layout.

The heated sample line is 3/8” stainless steel tubing with electrical heating elements and insulation. The electrical heat is controlled by an independent controller and maintained at 160 °C to ensure no water dropout. The heated line can then be connected to the hydrogen gas analyzer, which requires a wet sample. However, for the majority of testing the heated sample line is then connected to a water dropout refrigerator, shown in Figure 9.4 below.

Figure 9.4 – UCIMC Sampling Test Stand.

The heated sample line is shown entering from the top, where it is pumped out of the exhaust stack into the water dropout unit. The water dropout also cools the sample so that it can be pushed through PTFE hosing to the APEP enclosure shown in Figure 9.3.

During its operation, the water dropout discharges water into a drain line that must remain closed or exhaust will escape through it. To facilitate this, a switch valve is placed at the end of the drainage line and manually opened to allow built up condensate to escape. All of the mentioned components are mounted to the frame shown in Figure 9.4 so that they can be moved easily. Additional space in the base of the stand can also be used for more instrumentation.

The dry and cooled sample is then pushed in its PTFE hose through an underground conduit to the APEP enclosure. The tubing then enters the enclosure through a wall pass through, shown in Figure 9.5.

Figure 9.5 – UCIMC Sampling Setup inside Enclosure.

Notice in Figure 9.5 that a secondary pump it used to ensure that sufficient flowrate is achieved across the Horiba PG 350 (portable gas analyzer). A wetted tee method is used for sampling such that exhaust gasses flow across a tee from which the PG 350 pulls its sample, but the second outlet of the tee is to the ambient, the yellow exhaust line outside of the enclosure.

The PG 350 measures NO, SO_2, CO_2, CO, and O_2 using a variety of infrared absorption or paramagnetic methods. To operate the PG350, it is necessary to calibrate the unit for all of the gasses that will be assessed. For the tests run on the MCFC, only NO_X, CO_2, CO, and O_2 were calibrated using a nitrogen and a span gas.

9.2.2 - Sampling Results

The first round of emission sampling took place in May 2021. This set of emission data is intended to be used as a benchmark since the stack is relatively new. As mentioned before, only NO, CO_2, CO, and O_2 were measured. The data was collected on an SD card and visually from the user interface on the PG 350 shown below in Figure 9.6.

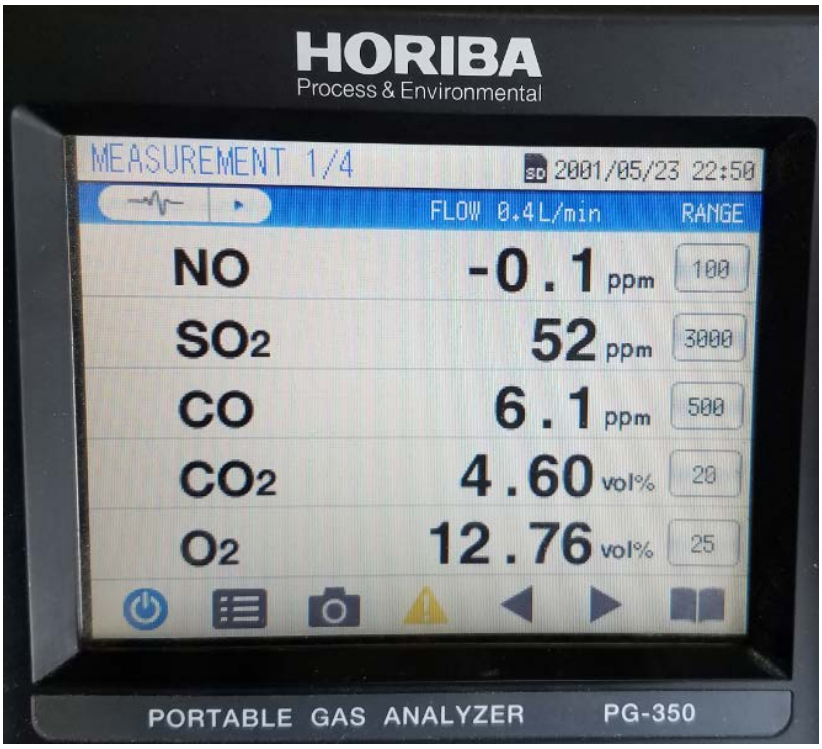

Figure 9.6 – PG 350 User Interface with MCFC Data.

The user interface provides live feedback, but the SD card allows recording of data over an extended period of time. To provide a steady state measurement, the data was collected over a 15 minute period and averaged to produce the final numbers shown below in Table 9.1 – MCFC Emission Sampling Results, May 2021.

Table 9.1 – MCFC Emission Sampling Results, May 2021.

Component	**Uncorrected**	**Corrected**
NO	-0.0635 ppm	-0.0468 ppm
CO	6.071 ppm	4.463 ppm
CO_2	4.608 %	3.372 %
O_2	12.48 %	15 %

Note that the data from the PG 350 must then be corrected to a fixed O_2 percentage. In this case, 15% was selected since it matches the emissions profile better. The data is corrected using the equation below.

$$Conc_{O_2:\,15\%} = Conc * \left(\frac{20.9\% - 15\%}{20.9\% - Conc_{O_2}}\right) \quad (9\text{-}1)$$

The second round of emissions sampling took place in April 2022. Using the same procedure as mentioned above, emissions were sampled using the PG 350 after a year of continuous operation. The results from the second round of sampling are shown in Table 9.2 - MCFC Emission Sampling Results, April 2022.

Table 9.2 - MCFC Emission Sampling Results, April 2022.

Component	**Uncorrected**	**Corrected**
NO	0.0697 ppm	0.0531 ppm
CO	4.5096 ppm	4.7747 ppm
CO_2	4.509 %	3.437 %
O_2	13.15 %	15 %

Reviewing the results from both rounds of emissions testing, the NO concentrations can both be interpreted as negligible or a non-detect because the unit is calibrated to a 0-100 ppm range. However, the CO concentration in the exhaust is slightly higher after the one year of operation, bumping from 4.4 to 4.7 ppm. Conversely, the CO_2 concentrations see a similar increase compared to the first sample, increasing from 3.37 to 3.43%. This represents a 1.9% increase in CO emissions and a 7.4% increase in CO_2 emissions over the course of an operational year.

The results of this emission testing present an interesting case for the degree to which the emissions performance corelates with the cell degradation. Figure 9.7 shows that as the efficiency of the MCFC degrades over time, the emission concentrations of both CO and CO_2 increase.

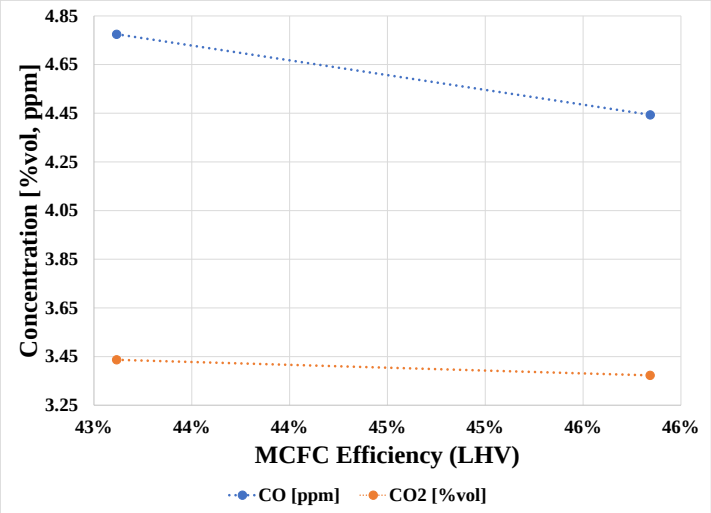

Figure 9.7 – MCFC Emission Concentration vs Efficiency Comparison.

This correlation is far from complete but would present a very interesting perspective on how the fuel cell contributes to emission productions over the course of its lifetime. This testing should be continued such that a full correlation could be investigated and developed.

Chapter 10 - Solid Oxide Electrolysis Cell Testing

This dissertation has explored the utilization of carbon based fuels in SOFC systems to produce primary power and cooling using integrated systems. This work is rooted in the current infrastructure for natural gas and electricity in order to maximize its utility for present applications. However, a common thread of discussion is the transition towards a green hydrogen infrastructure and economy. This dissertation has also described the possibility of increasing SOFC system's utility by their ability to operate on blends of natural gas and hydrogen. To meet this end, a unique opportunity arose to perform testing on solid oxide electrolysis cells (SOECs). This chapter discusses the experimental investigation of the operation of SOEC test cells in collaboration with Bloom Energy.

10.1 - Objective

The objective this experiment is to try and understand some of the fundamental physics, chemistry, and electrochemistry that occur in SOEC cells as they operate to produce green hydrogen. The primary phenomenon of interest is the nickel degradation in the hydrogen electrode. During high steam operation, it is possible for the nickel in the hydrogen electrode to migrate away from the electrode and be deposited elsewhere. This migration mechanism is the primary area of investigation for this experiment.

To explore the degradation mechanisms on SOEC button cells, a test stand was developed to experimentally evaluate and degrade samples. The design, construction and preliminary operation of this test stand are discussed here.

10.2 - Test Stand

The SOEC test stand was constructed based upon an existing test setup that was utilized for SOFC button cell testing. The primary objectives of the test stand are to facilitate the operating conditions for the button cell to be operated, and the ability to exercise cells using a potentiostat. The five principal components of the test stand are the Probostat fixture, the furnace, the gas inlet control board, the evaporator, and the potentiostat.

10.2.1 - Button Cell Probostat

A Probostat is the heart of the SOEC test stand. A Probostat is a fixture for mounting button cells while supplying gasses and collecting current all at extremely high temperatures. The Probostat fixture is shown below in Figure 10.1.

Figure 10.1 – Probostat Cell Testing Fixture.

The Probostat consists of two principal sections: the ceramic cell support and the flow/terminal base, as shown in Figure 10.1. The cell is made of aluminum oxide ceramic and extends 18” above the base of the figure to ensure thermal isolation from the operating conditions of the cell which is located at the opt of the cell support. The outer shell is cylindrical and is connected to the base via a compression O-ring fitting. The base of the Probostat facilitates the inlet and outlet gas flows through a manifold system on one side. The opposite side of the base contains the feed-throughs for the current collectors, thermocouples, and other auxiliary electrical equipment. Note that the support ring shown in Figure 10.1 is not present during normal operation because the cell support is placed within the test stand’s furnace.

The cell support consists of several concentric tubes that facilitate the fuel and air inlet/outlet to the system. The detail of how these tubes is laid out are shown in Figure 10.2 below.

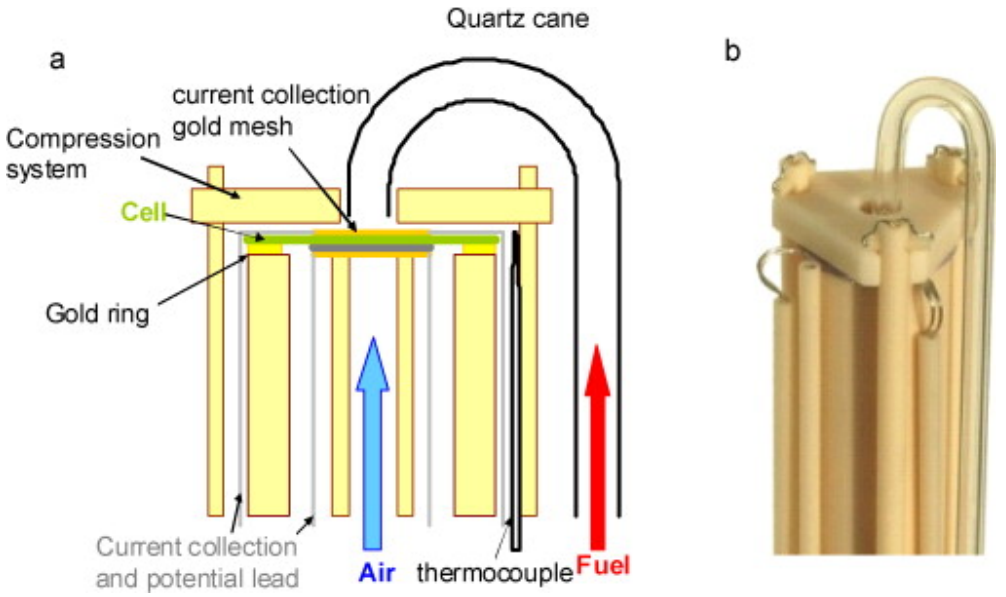

Figure 10.2 – Probostat Cell Configuration.

Figure 10.2 shows the internals of the cell support. Please note that the configuration shown above shows the air inlet in the central tube and the fuel inlet via the quartz cane. In the configuration tested, these flows are reversed with the fuel inlet in the most central column and the air supplied by the quartz cane.

Several other details are described in Figure 10.2 including the gold O-ring, the current collectors, a thermocouple, and compression mechanism. The gold O-ring is installed to prevent leakage from the fuel side to the air side during operation. At the temperatures within the furnace, the gold becomes malleable and acts as an airtight seal on the top of the fuel outer tube. The fuel outer tube is the second concentric tube and is primary cell support and is mechanically fixed to the Probostat base. The first inner tube is placed within the fuel outer tube and directs the incoming fuel onto the anode of the cell. The inner fuel tube is pressed upwards into the cell by a compressible length of flexible hose at the base of the Probostat. The anode side current collector is also place upon the inner tube so that contact is assured between the cell and the current collector's nickel mesh. The cathode side current collector is then placed on top of the cell. This current collector is pressed down into the cell by a mechanical compression mechanism that utilizes springs at the base of the Probostat to pull a flat plate with a pass through onto the cell. This mechanism ensures the sealing of the cell and keeps it from moving during operation. The final component added is

the quarts cane which is placed within the passthrough to make sure that air is correctly directed on the cell's anode. The entire assembly is then placed within the outer layer, not pictured, and sealed to the Probostat base. The fixture is then placed within the furnace as shown in Figure 10.3 below.

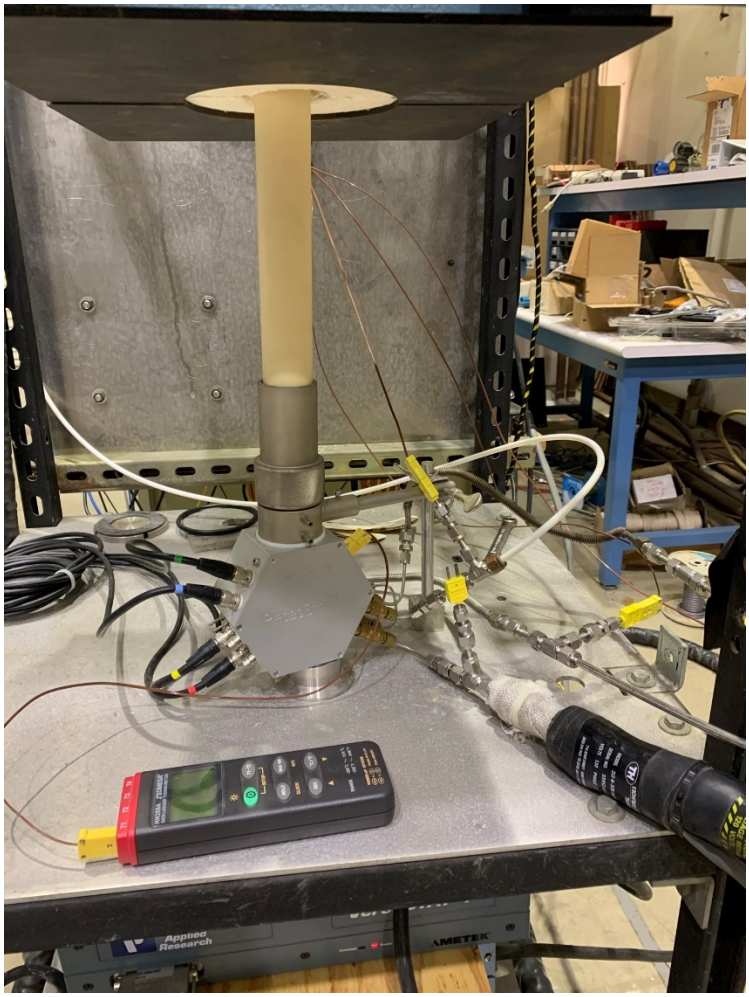

Figure 10.3 – Probostat on Test Stand with Gas Inlets.

The Probostat as installed in the test stand is shown in Figure 10.3. Notice that all gas connections are made on the right side of the Probostat base. This includes the gas/air inlet/outlet and each is directed and instrumented separately. Additionally, the electrical feedthroughs for the current collectors are shown on the left of the Probostat base. These electrical connections are wired to a potentiostat which will be utilized to test and exercise the button cells. Lastly, note that there is a handheld thermocouple reader which obtains

data from the Probostat's thermocouple feedthrough. This thermocouple allows verification of the operating temperature of the cell when comparing to the furnace's operating temperature.

10.2.2 - Furnace

The second principal component of the SOEC test stand is the electrical furnace which is used to heat the button cells to their nominal operating temperature. The furnace is an electric resistive heating furnace that contains a cylindrical enclosure into which the Probostat fixture is placed, as shown in Figure 10.4 below.

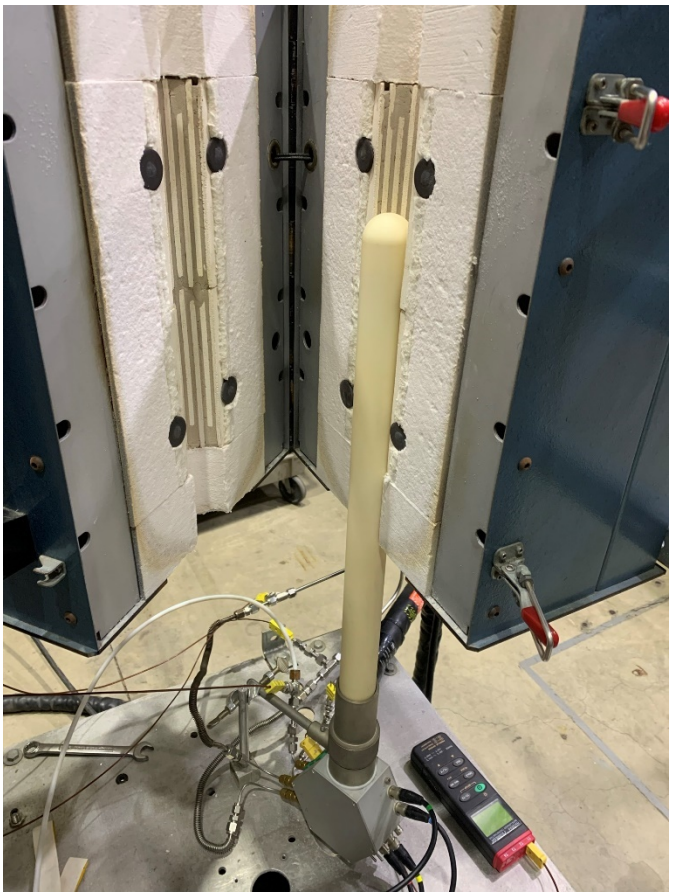

Figure 10.4 – Probostat Fixture placed within Furnace.

The furnace opens in a hinged fashion to allow for the removal of the Probostat fixture. The furnace runs on 240 VAC stepped up by the heater controller which is shown in Figure 10.5 below.

Figure 10.5 – Furnace Control.

The furnace is controlled by a Yokogawa UP550 which is an advanced heater control unit that includes a 120 to 240 VAC step up transformer. The controller utilizes two Type-K thermocouples to monitor the operating temperature and enforce a high temperature limit.

The controller has been programmed with two different operating profiles in order to facilitate the operation of the SOEC button cells. The first profile, titled PTN 1, begins a linear temperature ramp from 25 °C to 750 °C over the course of seven hours. This rate of temperature increase is defined by the cell and prevents undue thermal stresses due to rapid heating. Upon reaching the operating temperature, the controller will hold at 750 °C for 99 hours, the maximum step time. During this time period, the controller is placed into its “hold” function, which maintains the temperature indefinitely.

Additionally, during the furnace’s start up no fuel or air gasses are fed to the button cell. However, upon the cell reaching 200 – 250 °C, inlet gasses should begin to be fed into the test stand to ensure that the anode nickel oxide is reduced such that it can function normally. The gas inlet manifold will be discussed next.

10.2.3 - Gas Inlets

To provide gasses to the button cell, a gas mixing panel was developed to control the inlet composition of the different gasses into the SOEC cell. Five mass flow controllers are mounted on the control panel, but only three are currently used. The three utilized are lines which supply compressed air, nitrogen, and hydrogen to the cell and are shown below in Figure 10.6 as the blue, yellow, and red lines.

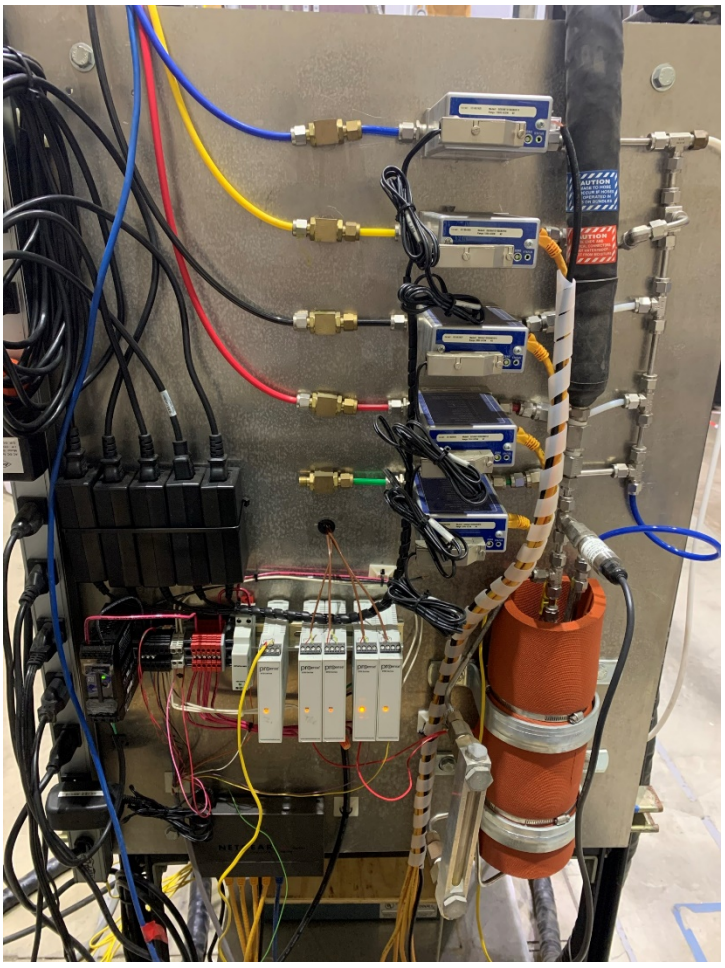

Figure 10.6 – Test Stand Gas Inlet Processing.

The mass flow controllers meter the flowrate of each incoming gas as they are mixed in the gas manifold on the right. Notice that the air line, at the top, is connected to the inlet manifold but it can be directed using a three way valve. Typically, the air is directed into its own line, shown in white, that flows into the cathode

side of the cell. The fuel mixture of nitrogen and hydrogen is routed to into the evaporator from the mixing manifold.

The nitrogen and hydrogen gasses are drawn from compressed gas cylinders stored outside the lab in a locked bunker. These compressed cylinders are regulated down to an operating pressure of 60 psi before they enter the lab. The amount of gas remaining in each must be monitored and refilled if required for the testing that usually lasts several days.

10.2.4 - Evaporator

The third gas that needs to be introduced into the hydrogen electrode side of the SOEC cell is steam which provides the fuel for electrolysis. To facilitate the injection of steam into the gas mixture, the inlet flow is bubbled through liquid water such that it is saturated with steam.

This process occurs within the evaporator which is shown in Figure 10.6 on the bottom right as an orange cylinder. The evaporator is a heated vessel which contains liquid water and facilitates the “bubbling” of inlet gasses through the pool of water. The evaporator is heated by a resistive heater and by controlling the operating temperature and monitoring the exit pressure, it is possible to calculate the mass fraction of steam within the inlet flow. The evaporator also hosts an external liquid level for the operator to monitor the amount of water left so that the evaporator doesn’t run dry during experiments.

The outlet of the evaporator is plumbed into a heated line because if the inlet flow is allowed to cool below the evaporator temperature, the steam could condense and not reach the SOEC button cell. The heated line is an insulated line that is also heated by an external controller. The heated line is shown in Figure 10.6 as the black insulated tube leaving the panel at the top. The temperature of the heated line is maintained at 100 °C to keep the steam above saturation temperature. The outlet of the heated line is also monitored via a separate thermocouple to ensure that the inlet flow is above the saturation temperature. The instrumentation and control of the test stand will be discussed next.

10.2.5 - Control and Instrumentation

To run the SOEC test stand, several levels of control and instrumentation are implemented to make sure each subsystem is running correctly. The first three systems have already been mentioned: the potentiostat, the furnace controller, and the heated line controller. The furnace temperature is corroborated by the internal thermocouple which is read using a handheld TC reader.

All other temperatures are read and logged by a LabVIEW based DAQ system. Five Type-K thermocouples are utilized to measure various process temperatures within the test stand. To read the voltages of the thermocouples, individual thermocouple transmitters are used to convert the mV measurements to a full scale range of 4-20 mA. The wiring setup for the thermocouple transmitters and their connections to the DAQ are shown below in Figure 10.7.

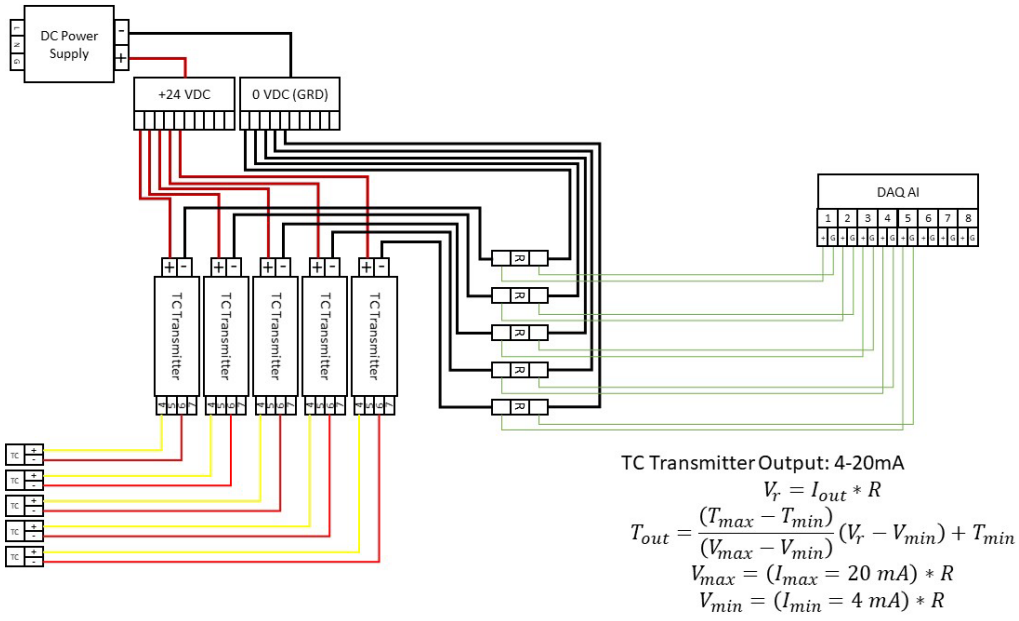

Figure 10.7 – SOEC Test Stand Thermocouple Wiring Diagram.

Note that each transmitter requires 24VDC power to operate and outputs the rated current through the negative lead from each transmitter. The output current is put across a resistor, which we can choose the resistance for, and the voltage drop across the resistor gives the temperature output using the equations shown in Figure 10.7. The temperature is then recorded and logged for interpretation later.

The evaporator temperature is also utilized in an open feedback control loop to maintain the saturation conditions in the inlet gasses. The control mechanism for the evaporator heater is a 120 VAC solid state relay (SSR) which can be actuated by the LabVIEW DAQ. A binary control strategy is utilized to control the temperature in the evaporator. Whenever the temperature rises above the setpoint, current is disconnected from the resistive heater. This strategy is able to maintain a setpoint ±2 °C which is sufficiently accurate for the purposes of the evaporator. The virtual control interface is shown below in Figure 10.8.

Figure 10.8 – LabVIEW Thermal Control Virtual Interface.

In addition to the thermal management of the test stand, the LabVIEW virtual interface controls all of the mass flow controllers via a Modbus connection. The control interface is shown below in Figure 10.9.

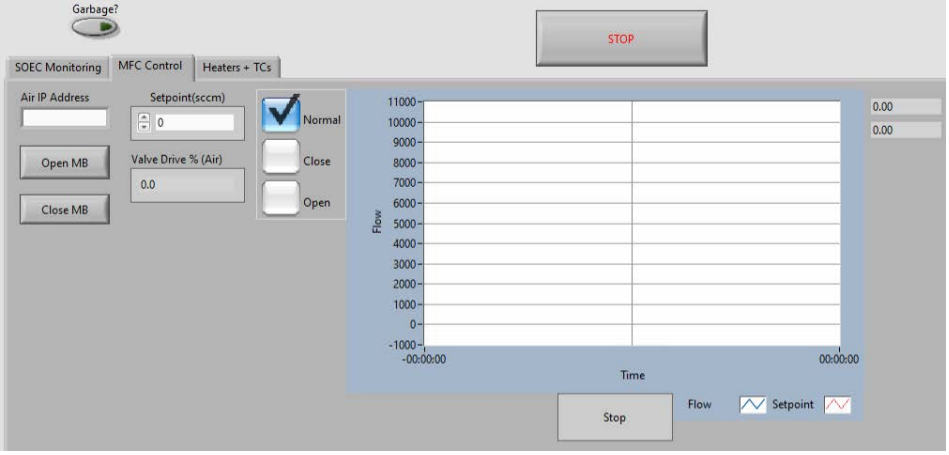

Figure 10.9 – Mass Flow Controller Virtual Control Interface.

To operate the controllers, the Modbus address must be listed for the corresponding controller, the Modbus connection must then be initialized. Once the connection is established, the valve control can be selected with “normal” utilizing active control to reach a desired setpoint.

10.2.6 - Challenges

Several challenges arose during the construction and operation of the SOEC test stand. First, the heated line between the evaporator and the gas inlet to the Probostat fixture sees extremely small flowrates compared to its inner diameter. This low flow means that the heat capacity of the inlet gasses is relatively low. The low heat capacity requires that all fittings before and especially after the heated line must be well insulated or the amount of heat loss that occurs before the cell allows for the entrained steam to condense. This condensation will ultimately reach the cell, but negatively affects the performance of the cell. This effect will be discussed later.

10.3 - Preliminary Tests

To exercise the SOEC test stand, some initial tests were performed on commercially available button cells. These tests unveiled the aforementioned challenges and are allowing for the development of more robust testing infrastructure.

10.3.1 - Cell Breakage

The first large obstacle that was discovered in the preliminary tests was that when setting up the button cell on the Probostat fixture, the thin nature of the cell made it extremely prone to breakage. The spring loaded mechanism for ensuring contact and sealing the cell forced the cell onto the central column which applied uneven pressure. This force combined with the three sided spring loading mechanism, shown in Figure 10.2, caused the cell to crack and break as it was being installed into the fixture. To remedy this issue, a aluminum oxide circular space is placed on top of the cathode-side current collector to better distribute the forces and to support the button cell. This spacer is shown below in Figure 10.10.

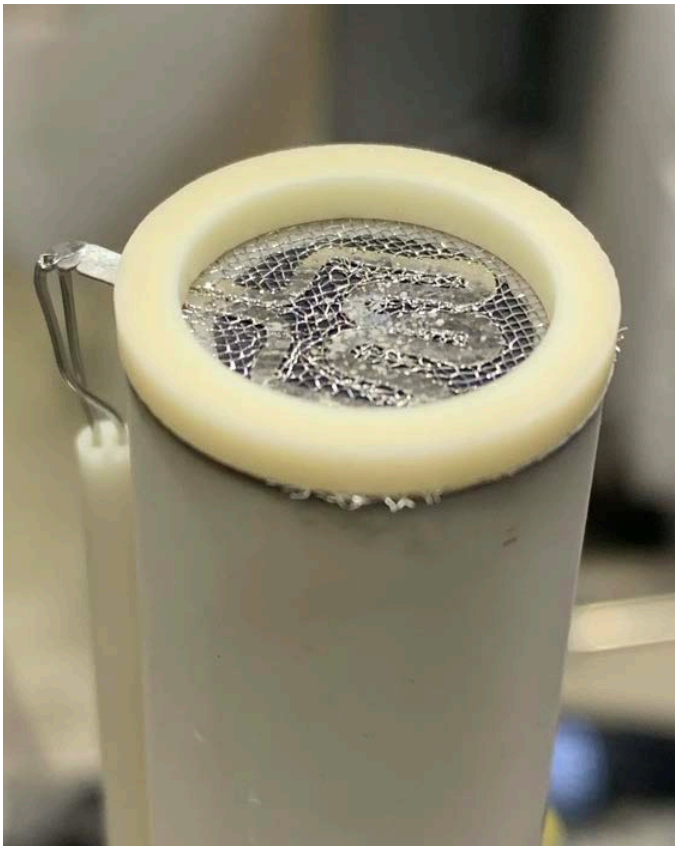

Figure 10.10 – SOFC Button Cell Assembled in Probostat Following Tests.

This solution has so far prevented further breakage when installing the cell.

10.3.2 - Preliminary SOFC Operation

So far, only one multi-day testing period has been achieved with the commercial button cells. This testing period lasted three days until the monitoring computer failed which caused the inlet gasses to cease. This shutoff allowed air back into the cell at higher temperatures and the cell oxidized, ending the test. Several tests were successfully run before the computer failure, and the results will be discussed later.

Delamination

Following the first test of the commercial cell, the Probostat fixture was deconstructed, and the cell was inspected to determine the points of failure. After removing the compression mechanism, the alumina spacer and the current collector, the cathode side was exposed and inspected. The cathode is shown below in Figure 10.11. Aside from some adhesion to the current collector, the cathode is relatively undamaged.

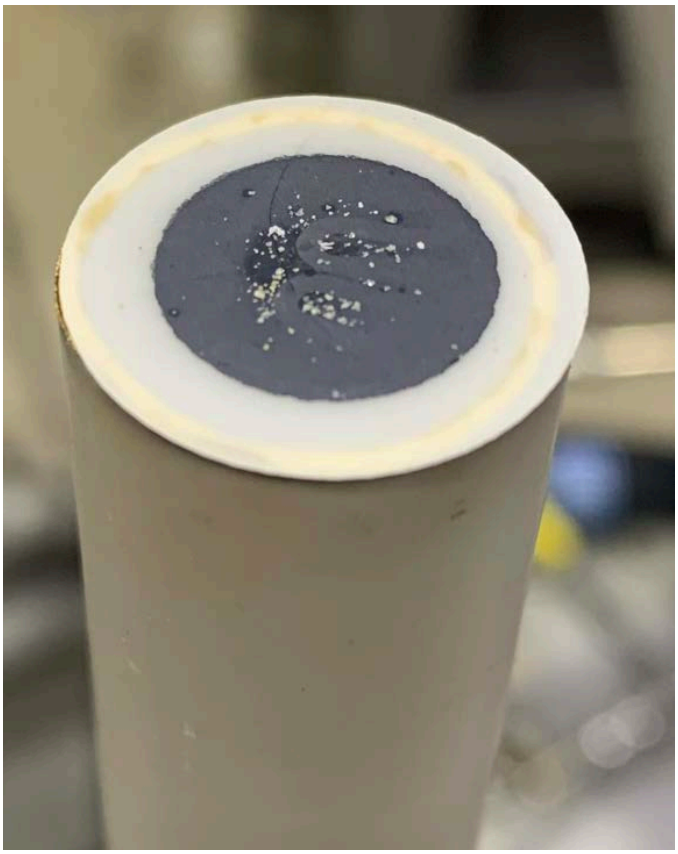

Figure 10.11 – Cell Cathode Exposed.

The cell was then removed from the fixture, but some breakage was induced in the removal process. The anode side of the cell seemed to adhere quite strongly and integrate itself into the nickel current collector on which it was placed. Unfortunately, this adhesion caused some of the anode to pull apart from the cell as it was removed. The adhered anode material is shown below in Figure 10.12.

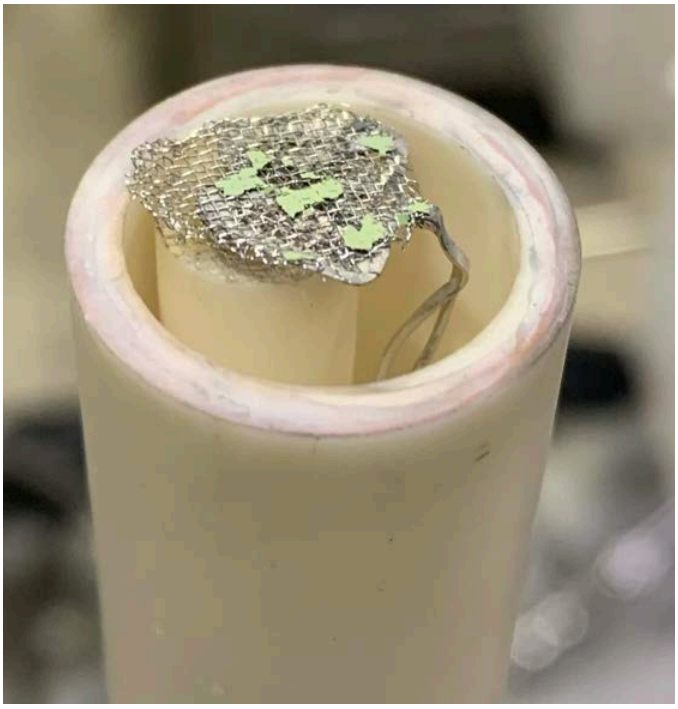

Figure 10.12 – Anode Current Collector with Adhered Anode.

The correspondingly damaged anode is shown below in Figure 10.13. Note that the anode material returned its green color due to the oxidation that took place during the test.

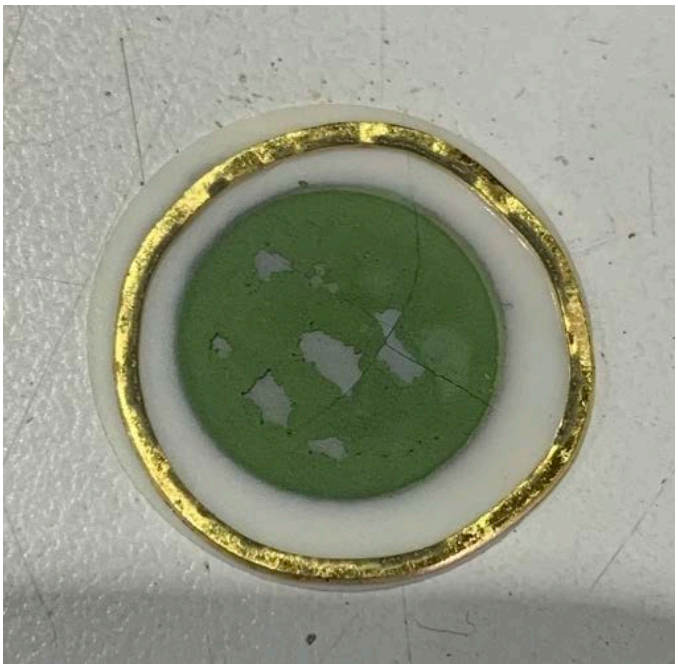

Figure 10.13 – Cell Removed from Probostat with Gold Seal.

Notice in Figure 10.13 that the areas of anode material that were left on the current collector seem to be larger than the actual contact areas with the mesh. Additionally, the electrolyte below the removed areas seems unperturbed. These two observations led to the hypothesis that there had been significant delamination of the cell during its operation. This theory will be explored later with microscopic imaging.

With the removal of the cell from the fixture, it was necessary to remove the gold sealing ring from the cell as well. Unfortunately, the cell and the sealing ring had adhered to each other sufficiently strongly that in order to remove the ring, it was necessary to break the cell. The broken cell is shown in Figure 10.14 and Figure 10.15 from the anode and cathode side respectively.

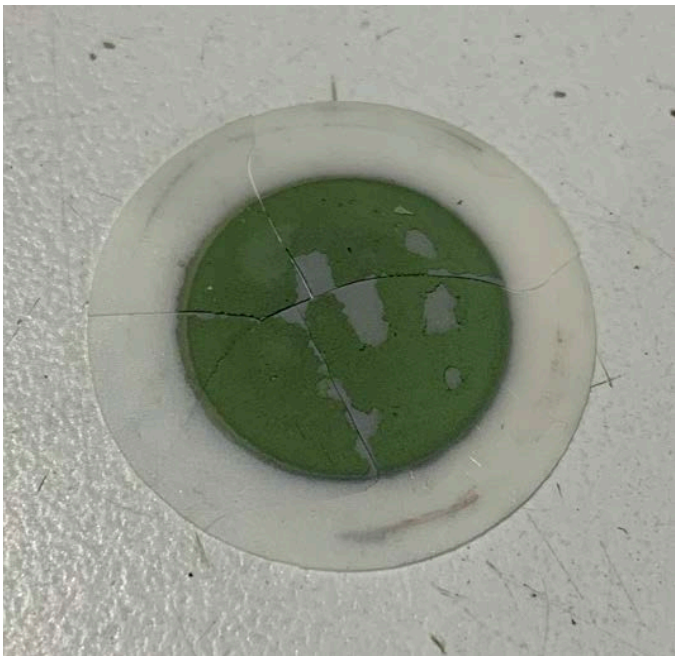

Figure 10.14 – Cracked Cell Following Removal of Gold Seal.

Figure 10.15 – Cell Cathode Following Seal Removal.

Note that the breaking of the cell was also conducive for some of the post-mortem analysis that was performed on the cell.

10.4 - Preliminary Results

Despite the challenges of the first round of experimental tests, electrochemical data was successfully collected and there are several takeaways that will help improve the future testing of SOEC cells. Three types of electrochemical experiments were run: open circuit voltage (OCV), polarization curve, and electrochemical impedance spectroscopy (EIS) tests.

10.4.1 - Cell Voltages

The first round of tests that were run are open circuit voltage (OCV) experiments that measure the cell's voltage given the temperature and concentration gradient but with minimal current. This experiment helps determine if the cell is functioning and if the inlet gasses are supplying the needed concentrations to achieve the nominal cell voltage. For the commercial cells that were tested in this iteration, a cell voltage of 1.1 – 1.2 V is expected. If the cell potential is lower than the expected, the assumption is that there is some leakage causing the lower potential.

However, during the preliminary test run there were some voltage instabilities that were occurring during the measurement periods. These voltage instabilities are shown in two of the experiments below in Figure 10.16.

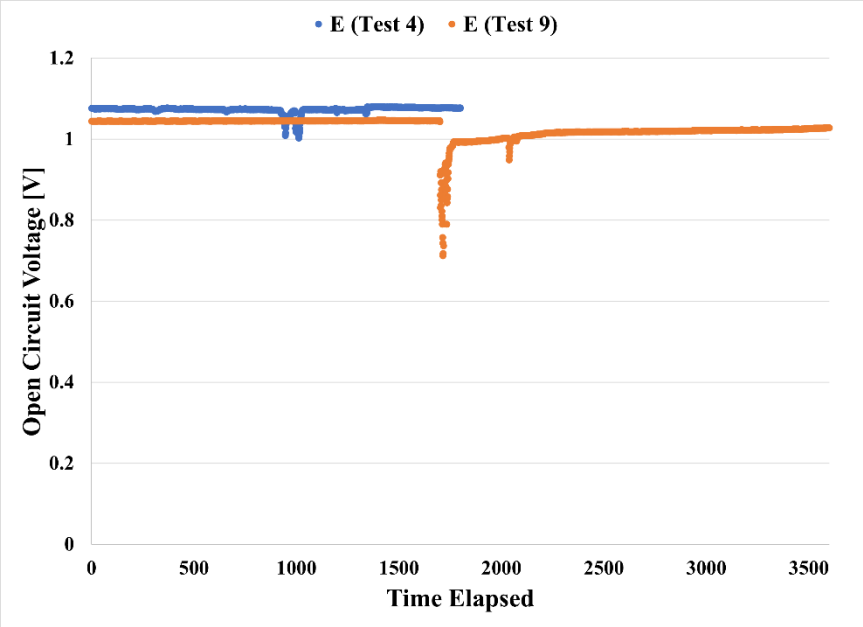

Figure 10.16 – Cell Transient Voltage Instabilities.

Notice in Figure 10.16 that the cell voltage is initially close to the expected cell potential, coming in at around 1.08 V. However, at some points during the test there are sharp drops in the voltage. These sharp drops are associated with water condensation in the inlet gas line and as the water droplets reach the button cell, they cause the voltage to drop dramatically until the evaporate and leave the cell. These instabilities occurred in the first several hours of cell testing and may have damaged the cell by the repeated exposure to low concentrations of inlet gas and liquid water. Once this phenomenon was observed, the evaporator was turned off to limit the amount of water that was entering the inlet stream. This solution mitigated the voltage instabilities and allowed for normal SOFC operation of the cell. However, for future SOEC testing, this issue will need to be resolved while still allowing steam into the fixture.

10.4.2 - Polarization Curves

The next series of tests that were performed on the cells were to explore their operation at varying levels of current density. Typically, a fuel cell's voltage decreases as the current density increases, but the measure of how quickly the voltage decreases as current increases help characterize the cell's performance. The cell's initial performance is shown below in Figure 10.17.

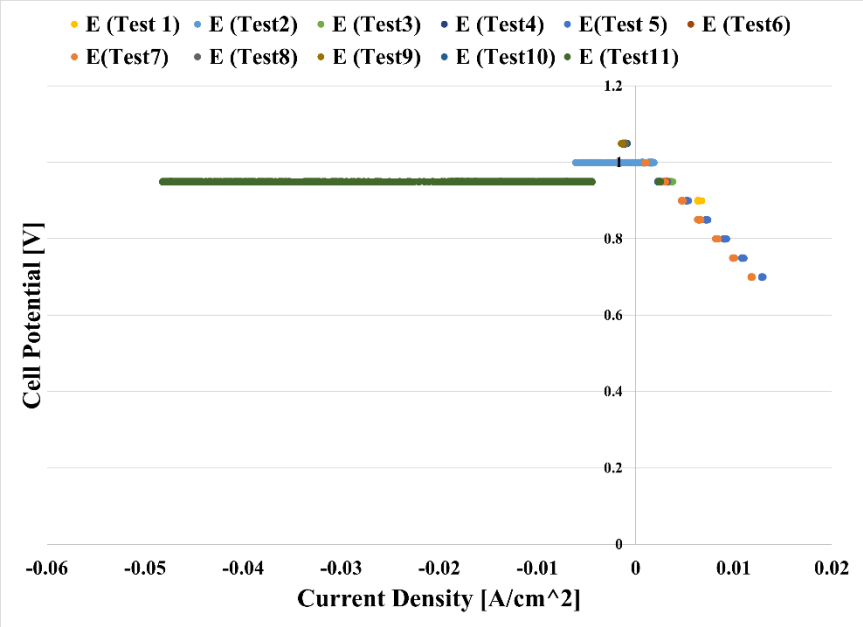

Figure 10.17 – Polarization Curves for Cell.

Notice that eleven separate tests were run over the three days and that each was aimed at characterizing a different range of the cell. Initial tests (1-4) were spot tests that simply ensured the cell was able to maintain a specified voltage and measured the current at that condition. Tests 5-9 explored the polarization curve of the cell, by specifying the cell's voltage to range from OCV (1.08 V) to 0.7 V and measure the current at each. It should be noted that the potentiostat measures the absolute current through the cell, so in order to derive the current density, it is necessary to know the surface are of the electrode. For these cells, the electrode is 12.5 mm in diameter. Using this sizing it is possible to determine the current density of the cell. The final experiment performed (Test 11) was to explore the possibility of electrolysis in the cell. To achieve this, current is pushed through the cell and the voltage at which the cell operates is measured. However, due to the lack of steam in the inlet gasses, no electrolysis could take place, so the cell voltage remained at the current OCV during the duration of the test.

What is interesting about the results shown is the values for the current density of the cell are incredibly low. Figure 10.18 shows the results of the two successful polarization experiment when compared to the manufacturers published performance data.

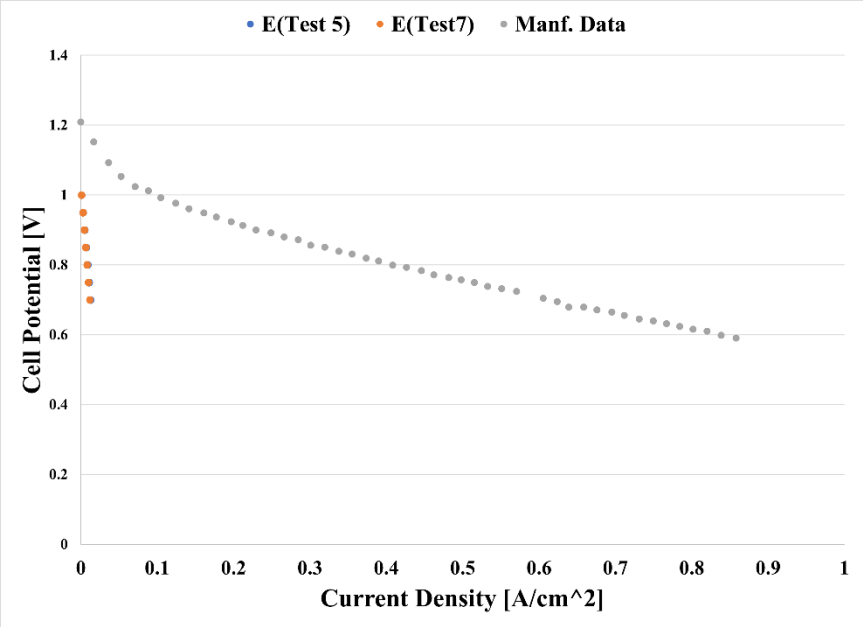

Figure 10.18 – SOFC Polarization versus Manufacturing Data.

The performance of the cell in the test stand is significantly lower than expected when comparing to the manufacturer's data in Figure 10.18. The principal cause for these extremely low current densities is the inability for charge to rout into the cell and reach active triple point boundaries. To try and resolve these lowered cell currents, a conductive paste will be applied to the cell to help facilitate electrical conduction from the cell to the current collector for future tests.

Following the application of the conductive paste on the current collector, a second round of testing was performed. Unfortunately, the amperage through the cell was still too small compared to the expected currents, but a sweep of cell temperature revealed that operating the cell at higher temperatures has a drastic effect on the operational current density of the cell. The results of the temperature sweep are shown below in Figure 10.19.

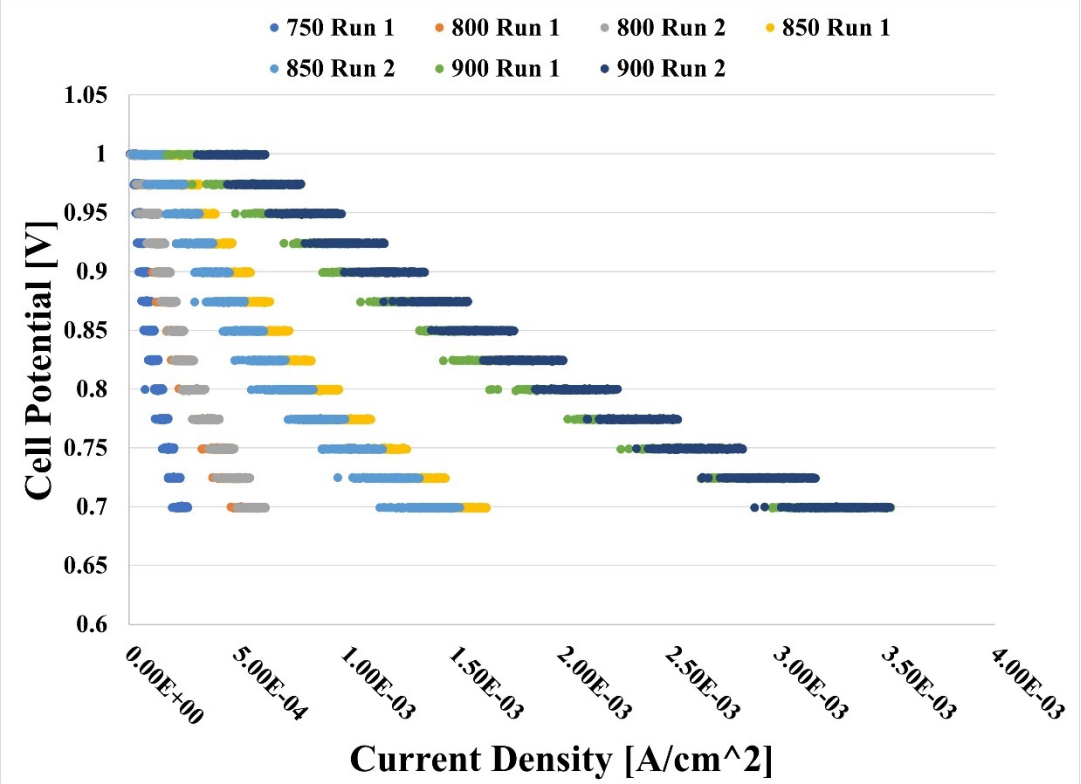

Figure 10.19 – SOFC Button Cell Polarization Temperature Sweep.

Notice that by operating the cell at 900 °C, the maximum current density can increase by over a factor of 10. However, the current densities exhibited are still much smaller than the expected data from the manufacturer. One potential cause of this is that by adding the conductive paste to the cell surface, the active area in the cell may be reduced, causing dramatic loss of reaction sites and therefore current.

10.4.3 - EIS

The final round of electrochemical tests run on the button cell is electrochemical impedance spectroscopy (EIS) which is able to determine cell impedance using a range of voltage frequencies to characterize the electrical circuit. EIS is typically used to characterize the different transport resistances within the electrochemical cell. The preliminary set of results from the commercial cell are shown in Figure 10.20 below.

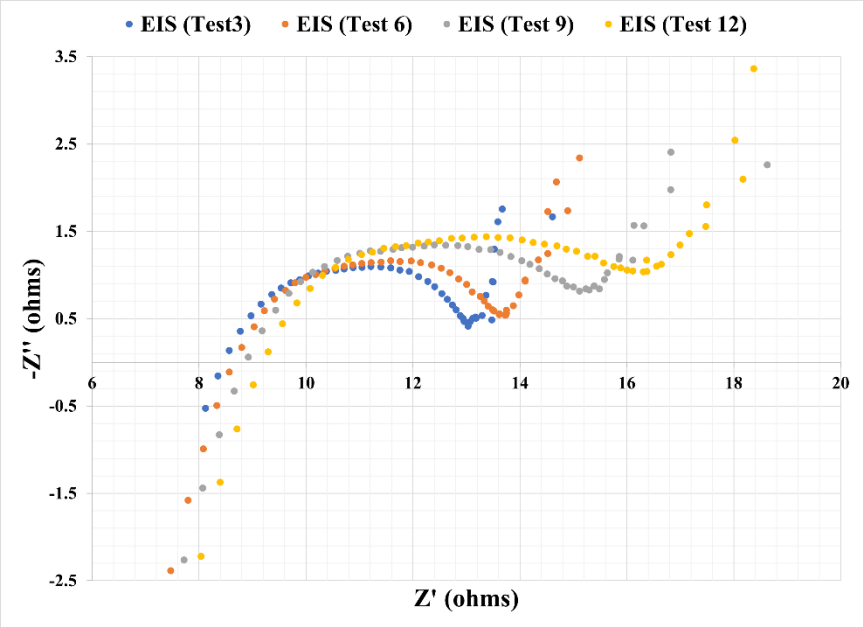

Figure 10.20 – Cell Impedance through Testing.

Reviewing the data in Figure 10.20 there are two big takeaways that dictate how testing moving forward should be conducted. The first is that the initial impedance of the circuit is more than 8 ohms. This resistance is incredibly high compared to typical measurements and indicates that the cell does not have good electrical connection to the measurement device. To investigate this effect, the resistance between the current collector and the measurement probes was checked independently. The resistance was found to less than 0.1 ohms as measurable by a handheld multimeter. Therefore, this result corroborates the issues reported in the polarization curves that the cell needs better connection between the electrodes and the current collectors.

The second takeaway from Figure 10.20 is that the impedance of the cell is constantly increasing at a rapid rate when considering that the cell was only tested for three days. The higher impedance of Test 12 indicates that there was significant degradation of the cell during its operation. The hypotheses that the anode became delaminated due to oxidation and the exposure to liquid water due to condensation was investigated by performing post-mortem analysis on the cell using a scanning electron microscope (SEM).

10.4.4 - SEM Post-Mortem Imaging

To explore the hypothesis that the electrode had become delaminated during the testing of the button cell, SEM imaging was utilized to inspect the boundaries between the electrodes and the electrolyte. The first boundary that was inspected was the cathode-electrolyte boundary and is shown below in Figure 10.21.

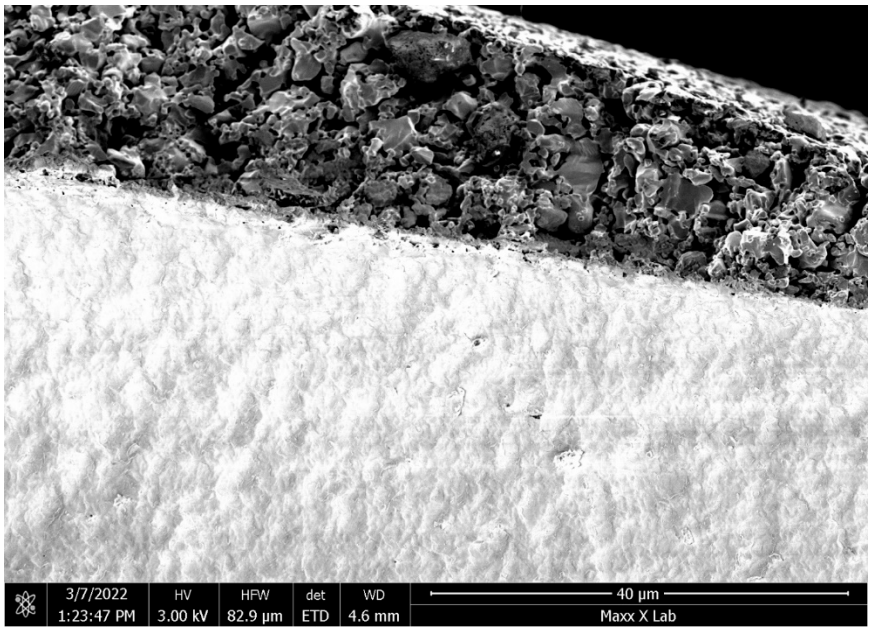

Figure 10.21 – SOFC Cathode / Electrolyte Boundary.

Examining Figure 10.21, two clear layers are visible: the cathode gas distribution layer (GDL) and the electrolyte. The cathode GDL is shown as the darker porous media on top of the solid electrolyte. The cathode for this cell is made of lanthanum strontium cobalt ferrite which is layered on top of the electrolyte which is made of scandia doped zirconia-based substrate. The image in Figure 10.21 shows that the cathode-electrolyte interface is still well connected and there seems to be no damage to the cell on this side.

Reducing the scale of the zoom, it is possible to look at the entire cross section of the cell, shown in Figure 10.22 below.

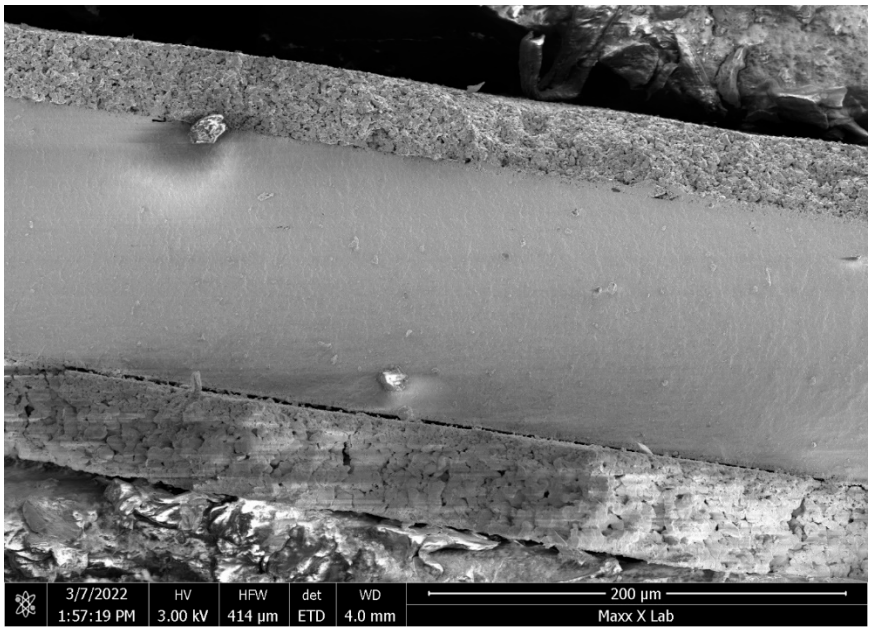

Figure 10.22 – SOFC Cell Cross Profile.

Looking at the cell's cross section, the anode is shown on top, the electrolyte in the middle and the anode on the bottom of Figure 10.22. Notice that the interface between the cathode and the electrolyte is intact, but the anode boundary in comparison looks to be slightly separated. Focusing in on this area, it is possible to observe the boundary separation in greater detail using the SEM as shown in Figure 10.23.

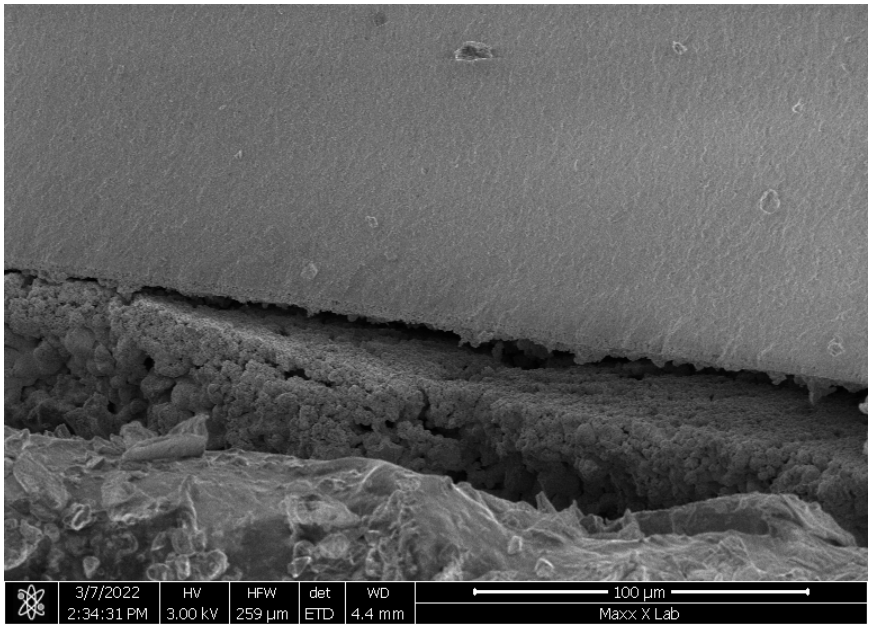

Figure 10.23 – Delamination of SOFC Anode from Electrolyte.

Figure 10.23 shows clear evidence of delamination supports the hypothesis that the cell was damaged during its operation and most likely affected the performance indices measured. However, there is some uncertainty in when the delamination occurred. Two possible causes are highlighted, the condensation in the early operation, or the loss of inlet gasses due to the computer failure. Further analysis will be required to fully understand which caused the delamination or if it was a combination of the two. Preliminary assumptions suggest that the loss of inlet gasses is the more likely cause because when the anode re-oxidizes the nickel oxide has a lower density than the reduced nickel. This lower density could cause the cell to expand during oxidation and force the delamination. Regardless, the ability to image and analyze the cells after they come out of the electrochemical tests will be critical to understand the degradation phenomenon in the cells.

Chapter 11 - Summary and Conclusions

This dissertation explores the concept of an integrated solid oxide fuel cell and absorption chiller system for the purpose of producing primary power and chilling for a hyper scale data center. The objectives and conclusions of the dissertation were as follows:

Objective 1. Leverage existing research and knowledge about the systems toward developing a novel understanding of thermal integration.

As explored by in background investigation, the concept of a thermal integration between a solid-oxide fuel cell and absorption chiller is not unexplored in the literature, but often the analysis into the operation and performance of the absorption chiller itself is limited. Existing studies have shown that thermal integrations allow SOFC systems to achieve very high cogeneration efficiencies, up to 88%. Additionally, some optimization has been performed on these systems, but never towards a specific application such as the data center application proposed here.

- **Conclusion.** While there are several examples of thermal integration between solid-oxide fuel cell systems and absorption chillers, the synergistic operation of the integrated system is under-explored. The advantages of adjusting the fuel utilization and desorber temperatures of the systems has not been studied in depth and presents promising incentives in mitigating data center emissions.

Objective 2. Use thermophysical simulation to evaluate different thermal integration configurations to determine which can successfully provide the required power and cooling to a data center.

The current work describes different thermal integration configurations, beginning with a single fuel cell and single-effect system for each server rack. Simulating the SOFC operating conditions and aiming to produce the power and chilling for a single rack, it became apparent that a larger scale configuration would have more significant advantages when implemented in hyper-scale data centers. Additionally, the single-effect chiller system was not able to produce enough capacity to offset the thermal load of the server rack,

maximizing at 5.08 kW, not meeting the 15 kW electric load. The chilling configuration was then altered and explored numerically as a parallel double-effect absorption chiller. The double effect model predicted that such a system could offset 11.8 kW of the chilling load, meeting lower capacity operation. However, the single server rack layout and simulation was still not allowing for a full offset of the electrical and thermal loads.

The final configuration explored was a triple-effect absorption chiller, with the highest efficiency commercially available, to produce chilling for servers at a row level. To simulate this case, a 210 kW SOFC model was developed to simulate the electrochemical operation alongside the entire balance of plant. The SOFC model allowed for the characterization of the exhaust gasses as they are utilized by the waste heat recovery of the absorption chiller. The thermal integration between the larger scale SOFC and the higher-efficiency triple effect absorption configuration allows for a full offset of the thermal load when producing primary power and chilling.

- **Conclusion.** In order to achieve full thermal offset of the electricity produced by the SOFC, a triple-effect absorption chiller configuration must be utilized. However, the complexity of triple-effect absorption systems and commercial sizing requires that the power and chilling strategy be modified for a row of server racks (200 kWe).

Objective 3. Optimize the operation of the thermally integrated SOFC and absorption chiller to minimize carbon emissions and levelized costs.

This novel thermal integration was further explored to optimize to controlling parameters of the SOFC to produce the primary power and chilling. The two controllable parameters of the SOFC are the stack temperature and the fuel utilization, which are manipulated by adjusting the fuel, air, and power flows into and out of the SOFC system. The sensitivity of the SOFC exhaust to changes of these operating parameters is explored to find an optimal operating condition for the SOFC and absorption chiller integrated system. The optimization was conducted against three parameters: carbon emission intensity, primary energy

savings (PES), and the levelized costs of the system. Quite synergistically, the optimal operating condition for all of the metrics lands on the same point, showing that the system tradeoffs for efficient running match the economic and emissions goals. However, when considering the cost of the system compared to conventional delivery systems, the integrated system is still largely above competitive costs.

- **Conclusion.** An integrated SOFC and absorption chiller system can be operationally optimized to minimize emissions, maximize PES, and minimize levelized costs. Through the optimization of the fuel utilization and stack temperature, the integrated system can provide cleaner electricity and chilling at a lower cost than conventional delivery when installed locally at a data center.

Objective 4. Understand how dynamic control of the optimized thermally integrated system can allow for dynamic dispatch to further reduce carbon emissions of data centers.

In addition to the steady state optimization of the SOFC and triple-effect absorption chiller, an active dispatch control strategy was conceptualized and explored using the modelling tools previously developed. This concept explored the idea that it is possible to control the chilling capacity of the absorption chiller using the operating conditions of the SOFC. By actively adjusting the operating conditions of the SOFC, the integrated system can produce the exact amount of chilling that is required by the data center. Utilizing a data center model built to predict the thermal load in an existing data center, the thermally integrated SOFC and absorption chiller operation is exercised. By keeping the integrated system running at its maximum efficiency when chilling is not required but adjusting the conditions to allow for more chilling capacity when it is needed, the average efficiency and emissions are improved across a yearlong profile. This exercising of the integrated model found that when the optimized system is applied to the row level configuration, all three configurations, single-effect, double-effect, and triple-effect are able to provide the necessary cooling for the data center although the single-effect configuration requires some thermal storage. Simulating each configuration, it was possible to show how each system reduces the carbon emissions of a data center over the course of a year when still running fully off natural gas. The triple and double effect

configurations with active control are able to save up to 27.9% of the carbon emissions compared to a conventional delivery case. Even the single-effect configuration can save up to 24.5% of the carbon emissions when producing primary power and coupled to a thermal storage system. Additionally, such a system would further benefit from the introduction of hydrogen blending which would reduce the carbon emission intensity even more.

- **Conclusion.** The integrated SOFC and absorption chiller system can be dynamically controlled to provide the required chilling as the ambient conditions change. Using dynamic dispatch control, the integrated system can produce electricity more efficiently when less chilling is required but still meet the year-round chilling demands. Successful implementation of this control reduces the carbon emissions of a data center row by 27.9%.

Objective 5. Develop an experimental platform to explore the operation of an integrated system.

Objective 6. Verify the thermophysical integrated model against experimental test results.

This numerical investigation was supported in parallel by an experimental effort to demonstrate the real world feasibility of a thermally integrated SOFC and absorption chiller. An experimental test stand was constructed in the laboratory space to test the operation and verify the models of the SOFC and absorption chiller. To achieve this, eight commercial BlueGEN SOFC units were installed and operated on natural gas. Their operation was investigated by another student and their findings supported this research. The second component of the experimental test stand was an 18 kW single-effect absorption chiller. The chiller utilizes waste heat that is captured from the SOFC or simulated exhaust in a WHR heat exchanger. The chiller then provides chilling to an air handling unit (AHU) which cools a stream of process air before it enters a single demonstration server rack. The server rack carries 21 server computers which can be operated using stress-testing software to produce their maximum thermal output. The chiller's performance was the focus of the investigation to better understand how the heat source of SOFC exhaust heat affects the performance of such a system. Additionally, it is from this integration and exercise that the concept of active chiller control

using SOFC operating parameters was uncovered. The data collected form the experimental test stand was then used to verify a single-effect absorption model and assuming that the desorber physics remains similar in double and triple effect systems, verify the majority of the simulated chilling performance.

- **Conclusion.** The controllability of the absorption chiller's capacity using modulated SOFC exhaust temperature and mass flow rates was discovered experimentally and led to the exploration of transient chilling profiles. The laboratory scale experimental setup was also utilized to verify the accuracy of the thermophysical models developed. When comparing the real-world performance to the simulated operation, the model can predict performance within 11.8%.

Objective 7. Evaluate an existing cogeneration case study for the thermodynamic and economic performance to further verify and support the presented thermophysical model.

In addition to the experimental and numerical investigation of SOFC systems for data centers, a case study was investigated of another high-temperature fuel cell producing power and chilling on site at the UCIMC. The 1.4 MW molten-carbonate fuel cell (MCFC) was analyzed over 5 years of its operation to characterize how such an integrated system performs both operationally and economically. The economic performance of the fuel cell was hindered by intermittency, particularly in the third year of operation. Random shut-offs of the system caused substantial demand charges that ultimately caused negative economic performance over a historical 4 year operating period. The investigation found that the economic challenges of the demand charges substantially outweighed the value of the thermal chilling provided at no charge by the absorption chiller. Following the period of investigation, a new stack was installed to improve the system performance and extend the system lifetime. The power output degradation of the second stack was similar to the initial stack. This case study affirms that, for a cogeneration to be economically feasible, the power output must be robust in availability and absent of trips.

- **Conclusion.** The UCIMC case study highlights the importance of robust power from fuel cell power in the economic performance of a cogeneration plant. When considering the data center

application, significant costs could be incurred if a grid connection is utilized to supplement the SOFC's primary power and the electricity production from the fuel cell is unreliable. Additionally, the year-to-year degradation of power from the fuel cells must also be considered in order to meet the demands of the data center.

Objective 8. Explore how solid-oxide technology can be utilized to produce hydrogen to further mitigate carbon emissions.

The final component of the current work is the construction of a test stand which explores solid oxide electrolysis in button cells. The ability of SOFC systems to run on mixtures of natural gas and hydrogen will provide them increased utility as the energy economy shifts from carbon fuel to greener hydrogen sources. This testing explores more fundamental issues involved in electrolysis, specifically the degradation of cells due to the migration of nickel in the steam electrode. This test stand allows for cells to be tested and pushed through a rapid lifetime cycle. Finally, the electrochemical characterization of the cell and imaging of the cells will help develop novel material configurations to improve the cell performance over its lifetime. The ability of SOEC systems to compliment power production to help reduce the carbon footprint of the grid will empower greener hydrogen and SOFC solutions in the future.

- **Conclusion.** Further testing is required to definitively determine the causation of electrode degradation on SOFC and SOEC samples. However, the ability of solid-oxide technology to produce both power and green hydrogen in the future presents a promising outlook for data center carbon emission reductions.

Chapter 12 - Future Work

Following the completion of the work that has been described in this dissertation, there are several avenues of research that should continue to be explored moving forward. The findings of this research present promising investigations into each of the following areas with more to be learned in each case.

12.1 - Modeling Next Steps

Continuing with the simulated thermally integrated system when applied to the transient data center chilling load profile, it would be interesting to see how the results of each configuration change in different geographic regions where there are different ambient conditions.

For example, taking the same three chiller configurations and applying them to a case where the mechanical chilling needs of the data center are significantly lower, like in a colder climate, and seeing if the single effect chiller is able to offset the thermal loads throughout the year. This simulation would also be best when paired with an economic model of the configuration in order to compare the costs of such a system with more traditional methods.

Additionally, the sensitivity of the economic viability of the integrated system to the capacity factor of the absorption chiller should be investigated thoroughly. Certain locations that require smaller capacity factors could diminish the economic advantage of the integrated system. To meet this end, understanding which configuration is the most competitive in varying capacity factors would present a good tool for setting up an optimized system.

12.2 - Future Experimental Work

Now that the experimental test stand has been exercised to explore the performance of the absorption chiller, there are some opportunities to further explore the SOFC integration. First, the fuel cells are currently operating on natural gas from the laboratory's grid supply. Utilizing the expertise from the combustion laboratory, a mixing box is under construction, as shown in Figure 12.1 to create variable mixes of natural gas and alternative fuels. Some examples that could be explored are mixing natural gas with

hydrogen, ammonia, or other biogases. The interesting takeaways of such an exploration would be how the fuel blends affect both the performance of the SOFC and the thermal characteristics of the balance of plant. For example, the introduction of hydrogen reduces the amount of reformation required and could therefore provide more waste heat to the thermally integrated absorption chiller. In addition, the introduction of less carbon-intensive fuels can further reduce the carbon emissions of data centers running on SOFCs.

Figure 12.1 – Fuel Mixing Test Stand.

12.3 - UCIMC Future Work

The data collection from the UCIMC MCFC plant will continue through May 2022. Further analysis of the data for the newer stack's degradation can be performed to assist with the future improvement of these components. Additionally, a second round of emission data should be taken in order to quantify the impact that the degradation of the stack has on the emission intensity of the fuel cell. Theoretically, being able to map this change in emission intensity over time would be the ultimate goal of this research endeavor.

12.4 - SOEC Future Testing

Moving forward with the SOEC testing, adjustments should be made to the control and routing of the steam into the Probostat fixture so that the concentration is more accurate. This represents the principal

upgrade to the test stand that should be implemented, but other upgrades could investigate the setup within the Probostat fixture to improve the current collection and assembly.

Currently, the current collection is the limiting factor when being able to test button cells at higher currents. To mitigate this challenge, it will be advantageous to begin coating the cells with conductive paste or a finer mesh with better connection. This improvement will allow for the full testing of cells at their designed currents and ensure better reliability of the test stand.

In addition to the commercial cells that have been tested, there will be opportunities to experiment with novel materials and configurations either printed here in lab or provided by our industry sponsor. Seeing that the ultimate goal is to investigate the mechanisms for nickel degradation in electrolysis operation, it will be important to refine the evaluation methods. These evaluations will consist of torture testing the cells and measuring their performance across a simulated lifetime, and post-mortem failure analysis to better understand how the degradation occurred. The failure analysis will also require the use of advanced machinery to image and evaluate the electrode materials pre and post testing.

Chapter 13 - Nomenclature

Symbol	Description	Subscript	Description
A	Area [m^2], Electrolyte Constant [K/ohm-m]	AC	Absorption Chiller
Cp	Specific heat capacity [kJ/kg-K]	c	Cold
COP	Coefficient of Performance [-]	cat	Cathode
$\boldsymbol{D^{eff}}$	Effective Diffusivity [m^2/s]	comb	Combustion
E	Energy [kJ, kWh, MWh]	des	Desorber
F	Faraday's Constant [C/mol], Fuel Expenditures [$]	el, elec	Electrical
$\boldsymbol{\Delta G_{act}}$	Activation Energy [kJ/mol]	evap	Evaporation
h	Specific Enthalpy [kJ/kg]	exh	Exhaust
I	Investment Expenditures [$]	FC	Fuel Cell
j	Current Density [A/cm^2]	h	Hot
K	Equilibrium Constant [-]	HX	Heat Exchanger
LCOC	Levelized Cost of Chilling [$/MWh]	in	Inlet
LCOE	Levelized Cost of Energy [$/MWh]	LHV	Lower Heating Value
m	Mass Flow Rate [kg/s]	ohm	Ohmic
M	Maintenance Expenditures [$]	out	Outlet
P	Pressure [kPa], Power [kW]	th	Thermal
PES	Primary Energy Savings [-]	0	Exchange Reference Case
Q, $\boldsymbol{\dot{Q}}$	Heat Transfer [kWh], Heat Transfer Rate [kW]	Abs	Absorber
R	Ideal Gas Constant [J/mol-K]	cell	Single fuel cell
t	Thickness [m], time [sec]	Des	Desorber
T	Temperature [C]	pmp	Pump
U	Heat Transfer Coefficient [W/m^2K]	react	Reacting
x	Concentration [-]	ref	Refrigerant
$\boldsymbol{\alpha}$	Transfer Coefficient [-]	sat	Saturated
$\boldsymbol{\epsilon}$	Heat Exchanger Effectiveness [-]	sol	Solution
$\boldsymbol{\eta}$	Efficiency [-]	suc	Suction
$\boldsymbol{\rho}$	Density [kg/m^3]	Chill	Chiller
Pr	Price [$]	Demand	Price of Demand [$/kW]
V	Volume [CF,m^3]	NG	Natural Gas
$\boldsymbol{\dot{V}}$	Volumetric Flowrate [CFM, m^3/s]	Plant, eff	Effective Plane
		Utility	Price of Electricity [$/kWh]

Chapter 14 - References

Abdollahi Haghghi, M., Ghazanfari Holagh, S., Chitsaz, A., & Parham, K. (2019, 10). Thermodynamic assessment of a novel multi-generation solid oxide fuel cell-based system for production of electrical power, cooling, fresh water, and hydrogen. *Energy Conversion and Management, 197*.

Aguiar, P., Adjiman, C., & Brandon, N. (2004, 11). Anode-supported intermediate temperature direct internal reforming solid oxide fuel cell. I: Model-based steady-state performance. *Journal of Power Sources, 138*(1-2), 120-136.

Alanne, K., Saari, A., Ugursal, V., & Good, J. (2006, 7). The financial viability of an SOFC cogeneration system in single-family dwellings. *Journal of Power Sources, 158*(1), 403-416.

Alcaide, F., Cabot, P., & Brillas, E. (2006, 1). Fuel cells for chemicals and energy cogeneration. *Journal of Power Sources, 153*(1), 47-60.

Al-Falahi, A., Alobaid, F., & Epple, B. (2020, 12). Design and thermo-economic comparisons of large scale solar absorption air conditioning cycles. *Case Studies in Thermal Engineering, 22*.

Aniti, L. (2021). Major U.S. utilities spending more on electricity delivery, less on power production. *Today in Energy - U.S. Energy Information Administration (EIA)*.

Appleby, A. (n.d.). *FUEL CELL TECHNOLOGY: STATUS AND FUTURE PROSPECTS+,S.*

Arsalis, A. (2012, 9). Modeling and simulation of a 100 kWe HT-PEMFC subsystem integrated with an absorption chiller subsystem. *International Journal of Hydrogen Energy, 37*(18), 13484-13490.

Asghari, M., Lavernia, A., Saeedmanesh, A., James, S., & Brouwer, J. (2019, 7). Integration of Solid Oxide Fuel Cell with Liquid Desiccant Cooling for Generation of Combined Cooling and Power for a Server. *ECS Transactions, 91*(1), 167-177.

Asghari, M., McVay, D., & Brouwer, J. (2017, 5). Integration of a Solid Oxide Fuel Cell with an Absorption Chiller for Dynamic Generation of Combined Cooling and Power for a Residential Application. *ECS Transactions, 78*(1), 243-255.

Bakhtiari, B., Fradette, L., Legros, R., & Paris, J. (2011, 2). A model for analysis and design of H2O-LiBr absorption heat pumps. *Energy Conversion and Management, 52*(2), 1439-1448.

Barelli, L., Bidini, G., Gallorini, F., & Ottaviano, A. (2011, 2). An energetic-exergetic comparison between PEMFC and SOFC-based micro-CHP systems. *International Journal of Hydrogen Energy, 36*(4), 3206-3214.

Beigzadeh, M., Pourfayaz, F., & Ahmadi, M. (2020, 2). Modeling and improvement of solid oxide fuel cell-single effect absorption chiller hybrid system by using nanofluids as heat transporters. *Applied Thermal Engineering, 166*.

Bellos, E., Tzivanidis, C., Symeou, C., & Antonopoulos, K. (2017, 1). Energetic, exergetic and financial evaluation of a solar driven absorption chiller – A dynamic approach. *Energy Conversion and Management, 137*, 34-48.

Bujlo, P., Pasupathi, S., Ulleberg, Scholta, J., Nomnqa, M., Rabiu, A., & Pollet, B. (2013, 8). Validation of an externally oil-cooled 1 kWel HT-PEMFC stack operating at various experimental conditions. *International Journal of Hydrogen Energy, 38*(23), 9847-9855.

Burer, M., Tanaka, K., Favrat, D., & Yamada, K. (2003). Multi-criteria optimization of a district cogeneration plant integrating a solid oxide fuel cell-gas turbine combined cycle, heat pumps and chillers. *Energy, 28*(6), 497-518.

Capozzoli, A., & Primiceri, G. (2015, 12). Cooling systems in data centers: State of art and emerging technologies. *Energy Procedia, 83*, 484-493.

Castro, J., Farnós, J., Papakokkinos, G., Zheng, J., & Oliet, C. (2020, 12). Transient model for the development of an air-cooled LiBr-H2O absorption chiller based on heat and mass transfer empirical correlations. *International Journal of Refrigeration, 120*, 406-419.

Chacartegui, R., Monje, B., Sánchez, D., Becerra, J., & Campanari, S. (2013, 11). Molten carbonate fuel cell: Towards negative emissions in wastewater treatment CHP plants. *International Journal of Greenhouse Gas Control, 19*, 453-461.

Cheung, H., & Wang, S. (2019, 11). Reliability and availability assessment and enhancement of water-cooled multi-chiller cooling systems for data centers. *Reliability Engineering and System Safety, 191*.

Chitsaz, A., Mehr, A., & Mahmoudi, S. (2015, 12). Exergoeconomic analysis of a trigeneration system driven by a solid oxide fuel cell. *Energy Conversion and Management, 106*, 921-931.

Chitsaz, A., S. Mahmoudi, S., & Rosen, M. (2015, 4). Greenhouse gas emission and exergy analyses of an integrated trigeneration system driven by a solid oxide fuel cell. *Applied Thermal Engineering, 86*, 81-90.

Choudhury, A., Chandra, H., & Arora, A. (2013). Application of solid oxide fuel cell technology for power generation - A review. *Renewable and Sustainable Energy Reviews, 20*, 430-442.

Damberger, T. (1998). *PII: S0378-7753(97)02786-9*.

Desideri, U., Proietti, S., Sdringola, P., Cinti, G., & Curbis, F. (2012, 12). MCFC-based CO2 capture system for small scale CHP plants. *International Journal of Hydrogen Energy, 37*(24), 19295-19303.

DeValeria, M., Michaelides, E., & Michaelides, D. (2020, 1). Energy and thermal storage in clusters of grid-independent buildings. *Energy, 190*.

Dhahad, H., Ahmadi, S., Dahari, M., Ghaebi, H., & Parikhani, T. (2021, 3). Energy, exergy, and exergoeconomic evaluation of a novel CCP system based on a solid oxide fuel cell integrated with absorption and ejector refrigeration cycles. *Thermal Science and Engineering Progress, 21*.

Ebrahimi, K., Jones, G., & Fleischer, A. (2014). A review of data center cooling technology, operating conditions and the corresponding low-grade waste heat recovery opportunities. *Renewable and Sustainable Energy Reviews, 31*, 622-638.

Ebrahimi, K., Jones, G., & Fleischer, A. (2015, 2). Thermo-economic analysis of steady state waste heat recovery in data centers using absorption refrigeration. *Applied Energy, 139*, 384-397.

El-Gohary, M. (2013). Economical analysis of combined fuel cell generators and absorption chillers. *Alexandria Engineering Journal, 52*(2), 151-158.

Facci, A., Cigolotti, V., Jannelli, E., & Ubertini, S. (2017). Technical and economic assessment of a SOFC-based energy system for combined cooling, heating and power. *Applied Energy, 192*, 563-574.

Fischer, Y., Dutra, J., & Rohatgi, J. (2020, 12). Thermodynamic modelling of a LiBr-H2O absorption chiller by improvement of characteristic equation method. *International Journal of Refrigeration, 120*, 420-429.

Florides, G., Kalogirou, S., Tassou, S., & Wrobel, L. (2003, 9). Design and construction of a LiBr-water absorption machine. *Energy Conversion and Management, 44*(15), 2483-2508.

Foley, G., DeVault, R., & Sweetser, R. (n.d.). *The Future of Absorption Technology in America A CRITICAL LOOK AT THE IMPACT OF BCHP AND INNOVATION HISTORY OF ABSORPTION TECHNOLOGY.*

Fong, K., & Lee, C. (2014). Investigation on zero grid-electricity design strategies of solid oxide fuel cell trigeneration system for high-rise building in hot and humid climate. *Applied Energy, 114*, 426-433.

Franchi, G., Capocelli, M., De Falco, M., Piemonte, V., & Barba, D. (2020, 1). Hydrogen production via steam reforming: A critical analysis of MR and RMM technologies. *Membranes, 10*(1).

Franchini, G., Notarbartolo, E., Padovan, L., & Perdichizzi, A. (2015). Modeling, design and construction of a micro-scale absorption chiller. *Energy Procedia, 82*, 577-583.

Fu, D., Poncia, G., & Lu, Z. (2006, 2). Implementation of an object-oriented dynamic modeling library for absorption refrigeration systems. *Applied Thermal Engineering, 26*(2-3), 217-225.

Garousi Farshi, L., Mahmoudi, S., Rosen, M., Yari, M., & Amidpour, M. (2013, 1). Exergoeconomic analysis of double effect absorption refrigeration systems. *Energy Conversion and Management, 65*, 13-25.

Gaynor, R., Mueller, F., Jabbari, F., & Brouwer, J. (2008, 5). On control concepts to prevent fuel starvation in solid oxide fuel cells. *Journal of Power Sources, 180*(1), 330-342.

Gebreslassie, B., Medrano, M., & Boer, D. (2010, 8). Exergy analysis of multi-effect water-LiBr absorption systems: From half to triple effect. *Renewable Energy, 35*(8), 1773-1782.

Gomri, R. (2010, 8). Investigation of the potential of application of single effect and multiple effect absorption cooling systems. *Energy Conversion and Management, 51*(8), 1629-1636.

Guizzi, G., & Manno, M. (2012). Fuel cell-based cogeneration system covering data centers' energy needs. *Energy, 41*(1), 56-64.

Ham, S., Kim, M., Choi, B., & Jeong, J. (2015). Simplified server model to simulate data center cooling energy consumption. *Energy and Buildings, 86*, 328-339.

Haywood, A., Sherbeck, J., Phelan, P., Varsamopoulos, G., & Gupta, S. (2015, 5). The relationship among CPU utilization, temperature, and thermal power for waste heat utilization. *Energy Conversion and Management, 95*, 297-303.

He, F., Nagano, K., & Togawa, J. (2020, 10). Experimental study and development of a low-cost 1 kW adsorption chiller using composite adsorbent based on natural mesoporous material. *Energy, 209*.

He, Y., Jiang, Y., Gao, N., Chen, G., & Tang, L. (2015, 6). Theoretical analyses of a new two-stage absorption-transcritical hybrid refrigeration system. *International Journal of Refrigeration, 56*, 105-113.

Hong, D., Tang, L., He, Y., & Chen, G. (2010, 10). A novel absorption refrigeration cycle. *Applied Thermal Engineering, 30*(14-15), 2045-2050.

Huang, B., Qi, Y., & Murshed, M. (2011, 12). Solid oxide fuel cell: Perspective of dynamic modeling and control. *Journal of Process Control, 21*(10), 1426-1437.

Huicochea, A., Rivera, W., Gutiérrez-Urueta, G., Bruno, J., & Coronas, A. (2011, 11). Thermodynamic analysis of a trigeneration system consisting of a micro gas turbine and a double effect absorption chiller. *Applied Thermal Engineering, 31*(16), 3347-3353.

Isa, N., Tan, C., & Yatim, A. (2018, 1). A comprehensive review of cogeneration system in a microgrid: A perspective from architecture and operating system. *Renewable and Sustainable Energy Reviews, 81*, 2236-2263.

Izquierdo, M., Marcos, J., Palacios, M., & González-Gil, A. (2012). Experimental evaluation of a low-power direct air-cooled double-effect LiBr-H2O absorption prototype. *Energy, 37*(1), 737-748.

Jeong, S., Kang, B. H., & Karngt, S. W. (1998). *DYNAMIC SIMULATION OF AN ABSORPTION HEAT PUMP FOR RECOVERING LOW GRADE WASTE HEAT.*

Joudi, K., & Lafta, A. (n.d.). *Simulation of a simple absorption refrigeration system.* Retrieved from www.elsevier.com/locate/enconman

Kaita, Y. (n.d.). *Simulation results of triple-effect absorption cycles.* Retrieved from www.elsevier.com/locate/ijrefrig

Kaita, Y. (n.d.). *Thermodynamic properties of lithium bromide±water solutions at high temperatures.* Retrieved from www.elsevier.com/locate/ijrefrig

Kalina, J. (2016, 9). Complex thermal energy conversion systems for efficient use of locally available biomass. *Energy, 110*, 105-115.

Kalina, J. (2017, 12). Techno-economic assessment of small-scale integrated biomass gasification dual fuel combined cycle power plant. *Energy, 141*, 2499-2507.

Khani, L., Mahmoudi, S., Chitsaz, A., & Rosen, M. (2016, 1). Energy and exergoeconomic evaluation of a new power/cooling cogeneration system based on a solid oxide fuel cell. *Energy, 94*, 64-77.

Kheirabadi, A., & Groulx, D. (2016, 7). Cooling of server electronics: A design review of existing technology. *Applied Thermal Engineering, 105*, 622-638.

Kim, B., & Park, J. (2007, 5). Dynamic simulation of a single-effect ammonia-water absorption chiller. *International Journal of Refrigeration, 30*(3), 535-545.

Kim, D., & Ferreira, C. (2006, 1). A Gibbs energy equation for LiBr aqueous solutions. *International Journal of Refrigeration, 29*(1), 36-46.

Kim, M., Dong, H., Park, J., & Jeong, J. (2016, 10). Primary energy savings in desiccant and evaporative cooling-assisted 100% outdoor air system combined with a fuel cell. *Applied Energy, 180*, 446-456.

Kini, G., Chandrasekaran, S., Tambasco, M., & Garimella, S. (2020, 12). A residential absorption chiller for high ambient temperatures. *International Journal of Refrigeration, 120*, 31-38.

Kiwan, S., Al-Nimr, M., & Radaideh, M. (2020, 5). Investigation of a new hybrid fuel cell–ThermoElectric generator–absorption chiller system for combined power and cooling. *International Journal of Refrigeration, 113*, 103-114.

Kohlenbach, P., & Ziegler, F. (2008, 3). A dynamic simulation model for transient absorption chiller performance. Part I: The model. *International Journal of Refrigeration, 31*(2), 217-225.

Kohlenbach, P., & Ziegler, F. (2008, 3). A dynamic simulation model for transient absorption chiller performance. Part II: Numerical results and experimental verification. *International Journal of Refrigeration, 31*(2), 226-233.

Labus, J., Bruno, J., & Coronas, A. (2013). Performance analysis of small capacity absorption chillers by using different modeling methods. *Applied Thermal Engineering, 58*(1-2), 305-313.

Lan, Z., Ma, X., Hao, Z., & Jiang, R. (2017, 4). Expérience sur la pression de vapeur saturée d'une solution aqueuse de bromure de lithium à haute température. *International Journal of Refrigeration, 76*, 73-83.

Lance, J., & Vanbmber, L. (1984). *THE ECONOMICS OF A FUEL CELL COGENERATION SYSTEM USING A BY-PRODUCT HYDROGEN STREAM.*

Li, B., Wang, S., Wang, K., & Song, L. (2020, 11). Thermo-economic analysis of a combined cooling, heating and power system based on carbon dioxide power cycle and absorption chiller for waste heat recovery of gas turbine. *Energy Conversion and Management, 224*.

Li, Y., Guangyi, C., & Qingchun, Y. (2006). *Daily Operation Optimization of a Residential Molten Carbonate Fuel Cell Power System Using Genetic Algorithm*.*

Lipman, T., Edwards, J., & Kammen, D. (2004). *Fuel cell system economics: comparing the costs of generating power with stationary and motor vehicle PEM fuel cell systems.*

Loreti, G., Facci, A., Baffo, I., & Ubertini, S. (2019, 2). Combined heat, cooling, and power systems based on half effect absorption chillers and polymer electrolyte membrane fuel cells. *Applied Energy, 235*, 747-760.

Mahmoudi, S., & Ghavimi, A. (2016, 8). Thermoeconomic analysis and multi objective optimization of a molten carbonate fuel cell – Supercritical carbon dioxide – Organic Rankin cycle integrated power system using liquefied natural gas as heat sink. *Applied Thermal Engineering, 107*, 1219-1232.

Margalef, P., & Samuelsen, S. (2010, 9). Integration of a molten carbonate fuel cell with a direct exhaust absorption chiller. *Journal of Power Sources, 195*(17), 5674-5685.

Matsushima, H., Fujii, T., Komatsu, T., & Nishiguchi, A. (2010, 3). Dynamic simulation program with object-oriented formulation for absorption chillers (modelling, verification, and application to triple-effect absorption chiller). *International Journal of Refrigeration, 33*(2), 259-268.

McLarty, D., Brouwer, J., & Samuelsen, S. (2014, 5). Fuel cell-gas turbine hybrid system design part II: Dynamics and control. *Journal of Power Sources, 254*, 126-136.

McLarty, D., Kuniba, Y., Brouwer, J., & Samuelsen, S. (2012, 7). Experimental and theoretical evidence for control requirements in solid oxide fuel cell gas turbine hybrid systems. *Journal of Power Sources, 209*, 195-203.

Mehmeti, A., Pedro Pérez-Trujillo, J., Elizalde-Blancas, F., Angelis-Dimakis, A., & McPhail, S. (2018, 7). Exergetic, environmental and economic sustainability assessment of stationary Molten Carbonate Fuel Cells. *Energy Conversion and Management, 168*, 276-287.

Morel, B., Roberge, Ŕ., Savoie, S., Napporn, T., & Meunier, M. (2007). An experimental evaluation of the temperature gradient in solid oxide fuel cells. *Electrochemical and Solid-State Letters, 10*(2).

Mueller, F., Brouwer, J., Jabbari, F., & Samuelsen, S. (2006, 5). Dynamic simulation of an integrated solid oxide fuel cell system including current-based fuel flow control. *Journal of Fuel Cell Science and Technology, 3*(2), 144-154.

Mueller, F., Gaynor, R., Auld, A., Brouwer, J., Jabbari, F., & Samuelsen, G. (2008, 1). Synergistic integration of a gas turbine and solid oxide fuel cell for improved transient capability. *Journal of Power Sources, 176*(1), 229-239.

Mueller, F., Jabbari, F., & Brouwer, J. (2009, 2). On the intrinsic transient capability and limitations of solid oxide fuel cell systems. *Journal of Power Sources, 187*(2), 452-460.

Mueller, F., Jabbari, F., Gaynor, R., & Brouwer, J. (2007, 10). Novel solid oxide fuel cell system controller for rapid load following. *Journal of Power Sources, 172*(1), 308-323.

Myat, A., Thu, K., Kim, Y., Chakraborty, A., Chun, W., & Ng, K. (2011, 10). A second law analysis and entropy generation minimization of an absorption chiller. *Applied Thermal Engineering, 31*(14-15), 2405-2413.

Nanaeda, K., Mueller, F., Brouwer, J., & Samuelsen, S. (2010, 5). Dynamic modeling and evaluation of solid oxide fuel cell - combined heat and power system operating strategies. *Journal of Power Sources, 195*(10), 3176-3185.

Ochoa, A., Dutra, J., Henríquez, J., & Dos Santos, C. (2016, 1). Dynamic study of a single effect absorption chiller using the pair LiBr/H2O. *Energy Conversion and Management, 108*, 30-42.

Oró, E., Depoorter, V., Garcia, A., & Salom, J. (2015). Energy efficiency and renewable energy integration in data centres. Strategies and modelling review. *Renewable and Sustainable Energy Reviews, 42*, 429-445.

Oryshchyn, D., Harun, N., Tucker, D., Bryden, K., & Shadle, L. (2018, 10). Fuel utilization effects on system efficiency in solid oxide fuel cell gas turbine hybrid systems. *Applied Energy, 228*, 1953-1965.

Owebor, K., Oko, C., Diemuodeke, E., & Ogorure, O. (2019, 4). Thermo-environmental and economic analysis of an integrated municipal waste-to-energy solid oxide fuel cell, gas-, steam-, organic fluid- and absorption refrigeration cycle thermal power plants. *Applied Energy, 239*, 1385-1401.

Palacín, F., Monné, C., & Alonso, S. (2011). Improvement of an existing solar powered absorption cooling system by means of dynamic simulation and experimental diagnosis. *Energy, 36*(7), 4109-4118.

Pandya, B., El-Kharouf, A., Venkataraman, V., & Steinberger-Wilckens, R. (2020, 10). Comparative study of solid oxide fuel cell coupled absorption refrigeration system for green and sustainable refrigerated transportation. *Applied Thermal Engineering, 179*.

Penner, S., Appleby Texas, A., Baker, B., Bates, J., Buss, L., Dollard, W., . . . Kimball, J. (1995). *COMMERCIALIZATION OF FUEL CELLS? by.*

Perna, A., Minutillo, M., & Jannelli, E. (2015, 8). Investigations on an advanced power system based on a high temperature polymer electrolyte membrane fuel cell and an organic Rankine cycle for heating and power production. *Energy, 88*, 874-884.

Pourfayaz, F., Imani, M., Mehrpooya, M., & Shirmohammadi, R. (2019, 1). Process development and exergy analysis of a novel hybrid fuel cell-absorption refrigeration system utilizing nanofluid as the absorbent liquid. *International Journal of Refrigeration, 97*, 31-41.

Prasartkaew, B. (2013). Mathematical modeling of an absorption chiller system energized by a hybrid thermal system: Model validation. *Energy Procedia, 34*, 159-172.

Prasartkaew, B. (2014). Performance test of a small size LiBr-H2o absorption chiller. *Energy Procedia, 56*(C), 487-497.

Promsen, M., Komatsu, Y., Sciazko, A., Kaneko, S., & Shikazono, N. (2020, 12). Feasibility study on saturated water cooled solid oxide fuel cell stack. *Applied Energy, 279*.

Raj, N., Iniyan, S., & Goic, R. (2011, 10). A review of renewable energy based cogeneration technologies. *Renewable and Sustainable Energy Reviews, 15*(8), 3640-3648.

Ramadhani, F., Hussain, M., Mokhlis, H., & Hajimolana, S. (2017). Optimization strategies for Solid Oxide Fuel Cell (SOFC) application: A literature survey. *Renewable and Sustainable Energy Reviews, 76*, 460-484.

Ritchie, A., & Brouwer, J. (2018, 4). Design of fuel cell powered data centers for sufficient reliability and availability. *Journal of Power Sources, 384*, 196-206.

Roberts, R., & Brouwer, J. (2006, 2). Dynamic simulation of a pressurized 220 kW solid oxide fuel-cell-gas-turbine hybrid system: Modeled performance compared to measured results. *Journal of Fuel Cell Science and Technology, 3*(1), 18-25.

Rokni, M. (2013, 11). Thermodynamic analysis of SOFC (solid oxide fuel cell)-Stirling hybrid plants using alternative fuels. *Energy, 61*, 87-97.

Rokni, M. (2018, 3). Design and analysis of a waste gasification energy system with solid oxide fuel cells and absorption chillers. *International Journal of Hydrogen Energy, 43*(11), 5922-5938.

Romdhane, J., & Louahlia-Gualous, H. (2018, 10). Energy assessment of PEMFC based MCCHP with absorption chiller for small scale French residential application. *International Journal of Hydrogen Energy, 43*(42), 19661-19680.

Rosner, F., Rao, A., & Samuelsen, S. (2020, 9). Economics of cell design and thermal management in solid oxide fuel cells under SOFC-GT hybrid operating conditions. *Energy Conversion and Management, 220*.

Salogni, A., & Colonna, P. (2010, 4). Modeling of solid oxide fuel cells for dynamic simulations of integrated systems. *Applied Thermal Engineering, 30*(5), 464-477.

Selman, J. (2006, 10). Molten-salt fuel cells-Technical and economic challenges. *Journal of Power Sources, 160*(2 SPEC. ISS.), 852-857.

Seo, J., Shin, Y., & Chung, J. (2012, 6). Dynamics and control of solution levels in a high temperature generator for an absorption chiller. *International Journal of Refrigeration, 35*(4), 1123-1129.

Sevencan, S., Lindbergh, G., Lagergren, C., & Alvfors, P. (2016, 1). Economic feasibility study of a fuel cell-based combined cooling, heating and power system for a data centre. *Energy and Buildings, 111*, 218-223.

Shamoushaki, M., Ehyaei, M., & Ghanatir, F. (2017). Exergy, economic and environmental analysis and multi-objective optimization of a SOFC-GT power plant. *Energy, 134*, 515-531.

Shin, Y., Seo, J., Cho, H., Nam, S., & Jeong, J. (2009, 9). Simulation of dynamics and control of a double-effect LiBr-H2O absorption chiller. *Applied Thermal Engineering, 29*(13), 2718-2725.

Shirazi, A., Taylor, R., White, S., & Morrison, G. (2016, 4). A systematic parametric study and feasibility assessment of solar-assisted single-effect, double-effect, and triple-effect absorption chillers for heating and cooling applications. *Energy Conversion and Management, 114*, 258-277.

Shu, G., Che, J., Tian, H., Wang, X., & Liu, P. (2017, 2). A compressor-assisted triple-effect H2O-LiBr absorption cooling cycle coupled with a Rankine Cycle driven by high-temperature waste heat. *Applied Thermal Engineering, 112*, 1626-1637.

Siefert, N., & Litster, S. (2014, 12). Exergy & economic analysis of biogas fueled solid oxide fuel cell systems. *Journal of Power Sources, 272*, 386-397.

Spath, P. L., & Mann, M. K. (2000). *Life Cycle Assessment of a Natural Gas Combined-Cycle Power Generation System (NREL/TP-570-27715).* NREL.

Srikhirin, P., Aphornratana, S., & Chungpaibulpatana, S. (2001). *A review of absorption refrigeration technologies.* Retrieved from www.elsevier.com/locate/rser

Su, B., Han, W., Zhang, X., Chen, Y., Wang, Z., & Jin, H. (2018, 11). Assessment of a combined cooling, heating and power system by synthetic use of biogas and solar energy. *Applied Energy, 229*, 922-935.

Tian, M., Yu, Z., Zhao, H., & Yin, J. (2018, 9). Thermodynamic analysis of an integrated solid oxide fuel cell, Organic Rankine Cycle and absorption chiller trigeneration system with CO2 capture. *Energy Conversion and Management, 171,* 350-360.

Toppi, T., Aprile, M., & Motta, M. (2020, 5). Self-adapting double and triple-lift absorption cycles for low-grade heat driven cooling. *International Journal of Refrigeration, 113*, 206-218.

U.S. Energy Information Administration. (2021). *Levelized Costs of New Generation Resources in the Annual Energy Outlook 2021.*

Varbanov, P., & Klemeš, J. (2008). Analysis and integration of fuel cell combined cycles for development of low-carbon energy technologies. *Energy, 33*(10), 1508-1517.

Venkataraman, V., Pacek, A., & Steinberger-Wilckens, R. (2016, 6). Coupling of a Solid Oxide Fuel Cell Auxiliary Power Unit with a Vapour Absorption Refrigeration System for Refrigerated Truck Application. *Fuel Cells, 16*(3), 273-293.

Wahlroos, M., Pärssinen, M., Manner, J., & Syri, S. (2017). Utilizing data center waste heat in district heating – Impacts on energy efficiency and prospects for low-temperature district heating networks. *Energy, 140*, 1228-1238.

Wahlroos, M., Pärssinen, M., Rinne, S., Syri, S., & Manner, J. (2018, 2). Future views on waste heat utilization – Case of data centers in Northern Europe. *Renewable and Sustainable Energy Reviews, 82*, 1749-1764.

Wang, C., Lee, J., Chang, T., & Lin, P. (n.d.). *Heat transfer and friction correlation for compact louvered _n!and!tube heat exchangers.*

Wang, C.-C., Chi, K.-Y., & Chang, C.-J. (n.d.). *Heat transfer and friction characteristics of plain ®n-and-tube heat exchangers, part II: Correlation.* Retrieved from www.elsevier.com/locate/ijhmt

Wang, D., Wang, Y., Zhang, J., Tian, X., & Wu, J. (2008, 5). Experimental study of adsorption chiller driven by variable heat source. *Energy Conversion and Management, 49*(5), 1063-1073.

Wee, J. (2011). Molten carbonate fuel cell and gas turbine hybrid systems as distributed energy resources. *Applied Energy, 88*(12), 4252-4263.

Wu, S., & Eames, I. (n.d.). *A novel absorption±recompression refrigeration cycle.*

Yu, Z., Han, J., & Cao, X. (2011, 9). Investigation on performance of an integrated solid oxide fuel cell and absorption chiller tri-generation system. *International Journal of Hydrogen Energy, 36*(19), 12561-12573.

Yu, Z., Han, J., Cao, X., Chen, W., & Zhang, B. (2010, 4). Analysis of total energy system based on solid oxide fuel cell for combined cooling and power applications. *International Journal of Hydrogen Energy, 35*(7), 2703-2707.

Zeng, Z., Qian, Y., Zhang, Y., Hao, C., Dan, D., & Zhuge, W. (2020, 12). A review of heat transfer and thermal management methods for temperature gradient reduction in solid oxide fuel cell (SOFC) stacks. *Applied Energy, 280*.

Zhai, H., & Rubin, E. (2010). Performance and cost of wet and dry cooling systems for pulverized coal power plants with and without carbon capture and storage. *Energy Policy, 38*(10), 5653-5660.

Zhao, H., Jiang, T., & Hou, H. (2015, 11). Performance analysis of the SOFC-CCHP system based on H2O/Li-Br absorption refrigeration cycle fueled by coke oven gas. *Energy, 91*, 983-993.

Zhao, L., Brouwer, J., James, S., Peterson, E., Wang, D., & Liu, J. (2016, 2). Fuel Cell Powered Data Centers: In-Rack DC Generation. *ECS Transactions, 71*(1), 131-139.

Zhao, L., Brouwer, J., Liu, J., James, S., Siegler, J., Kansal, A., & Peterson, E. (n.d.). *Fuel Cells for Data Centers: Power Generation Inches From the Server.*

Zinet, M., Rulliere, R., & Haberschill, P. (2012, 10). A numerical model for the dynamic simulation of a recirculation single-effect absorption chiller. *Energy Conversion and Management, 62*, 51-63.

Appendix A – Technical Specifications

The following pages contain the technical specifications for the components used in the experimental setup.

Specifications[5]

Model			WFC-	SC5	SC/SH10	SC/SH20	SC/SH30	SC50	M100
Cooling			kW	17.6	35.2	70.3	105.5	175.8	351.6
Heating (WFC-SH only)			kW	---	48.7	97.5	146.2	---	---
Chilled / Hot Water	Cooling		°C	12.5 Inlet / 7.0 Outlet (12.2 Inlet / 6.7 Outlet for M100)					
	Heating		°C	---	47.4 Inlet / 55.0 Outlet (WFC-SH Models Only)			---	
	Rated Water Flow		L/s	0.76	1.5	3.1	4.6	7.6	15.3
	Evaporator Pressure Loss[9]		kPa	52.6	55.8	66.2	69.6	44.2	72.6
	Maximum Operating Pressure[4]		kPa	1034					
	Allowable Water Flow		% Rated	80% - 120%					
	Water Retention Volume		L	8.0	17.0	46.9	73.1	127.2	121.0
Cooling Water	Total Heat Rejection		kW	42.7	85.4	170.8	256.2	427.0	854.9
	Temperature		°C	31.0 Inlet / 35.0 Outlet (29.4 Inlet / 35.4 Outlet for M100)					
	Rated Water Flow[1]		L/s	2.6	5.1	10.2	15.3	25.5	34.0
	Allowable Water Flow		% of Rated	100% - 120%					
	Absorber Pressure Loss[9]		kPa	38.6	84.8	45.5	46.2	45.3	66.0
	Condenser Pressure Loss[9]		kPa	38.6	Included in Absorber	45.5	46.2	21.9	Included in Absorber
	Maximum Operating Pressure[4]		PSI	1034					
	Water Retention Volume		L	37.0	65.9	124.9	194.2	330.1	422
Heat Medium[6]	Heat Input		kW	25.1	50.2	100.5	150.7	251.2	503.0
	Temperature		°C	88.0 Inlet / 83.0 Outlet (90.0 Inlet / 80.0 Outlet for M100)					
	Allowable Temperature		°C	70.0 – 95.0					
	Generator Pressure Loss[9]		kPa	77.0	90.3	46.2	60.7	93.7	29.7
	Maximum Operating Pressure[4]		kPa	1034					
	Rated Water Flow		L/s	1.2	2.4	4.8	7.2	12.0	12.4
	Allowable Water Flow		% of Rated	30% - 120% (25% - 120% for M100)					
	Water Retention Volume		L	10.0	20.8	54.1	84.0	150.3	250.0
Electrical[7]	Power Supply			115/60/1	208VAC / 60 Hz / 3-Phase				
	Consumption[2]		Watts	48	210	260	310	670	640
	Minimum Circuit Amps		Amps	0.89	0.6	0.9	2.6	4.7	2.7
	MOCP – Max. Fuse Size		Amps	15					
Capacity Control				On - Off					Proportional or On/Off
Construction	Dimensions[3]	Width	mm	594	760	1064	1380	1785	1510
		Depth	mm	744	970	1300	1545	1960	3654
		Height	mm	1755	1900	2010	2045	2085	2200
	Weight	Dry	kg	365	500	930	1450	2150	4940
		Operating	kg	420	603	1155	1800	2700	5740
	Cabinet			NEMA 3R, Silver Metallic Pre-Painted Hot Dip Zinc-Coated Sheet Steel					
	Noise Level[8]		dB(A)	38	49		46	51	56
Piping	Chilled / Hot Water		Inches	1-1/4 NPT	1-1/2 NPT	2 NPT		3 NPT	4 Flanged
	Cooling Water		Inches	1-1/2 NPT	2 NPT		2-1/2 NPT	3 NPT	5 Flanged
	Heat Medium		Inches	1-1/2 NPT		2 NPT	2-1/2 NPT	3 NPT	4 Flanged

NOTES:

1. Minimum cooling water flow is 100%.
2. Power Consumption does not include external pumps or fan motors.
3. Height does not include removable lifting lugs, but does include level bolts. Width/Depth does not include junction box or mounting plates.
4. Do not exceed 150 PSI (1034 kPa) in any fluid circuit.
5. Specifications are based upon water in all fluid circuits and fouling factor of 0.0005 ft^2-hr-°F/Btu.
6. Density of Heat Medium is 60.47 lbs/ft^3, Specific Heat 1.003 BTU/lbs°F (185°F).
7. Electric field wiring must be made in accordance with local regulation and must be sized to provide less than 2% voltage drop.
8. Noise level is measured in a free field at a point 1m away from the cabinet and 1.5m above ground level.
9. Pressure Loss ratings are +/- 10%.

Equipment Dimensions

Drawings are not to scale. Piping shown is all field-supplied. All metric values are converted from Imperial units.

WFC-SC5

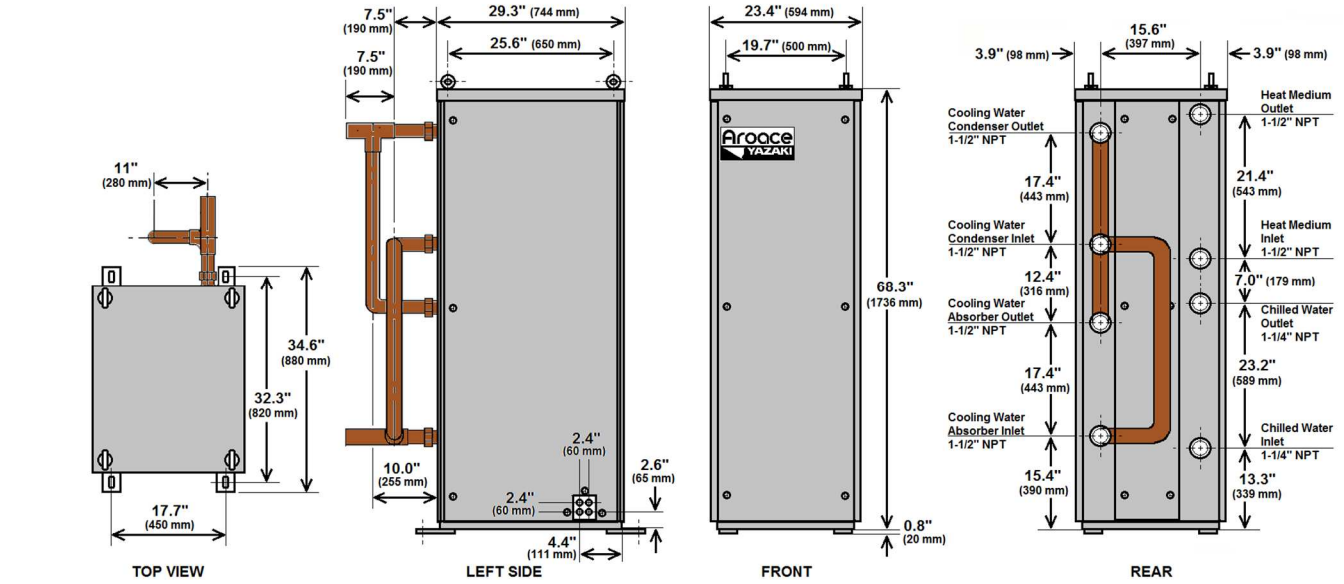

WFC-SC/SH10

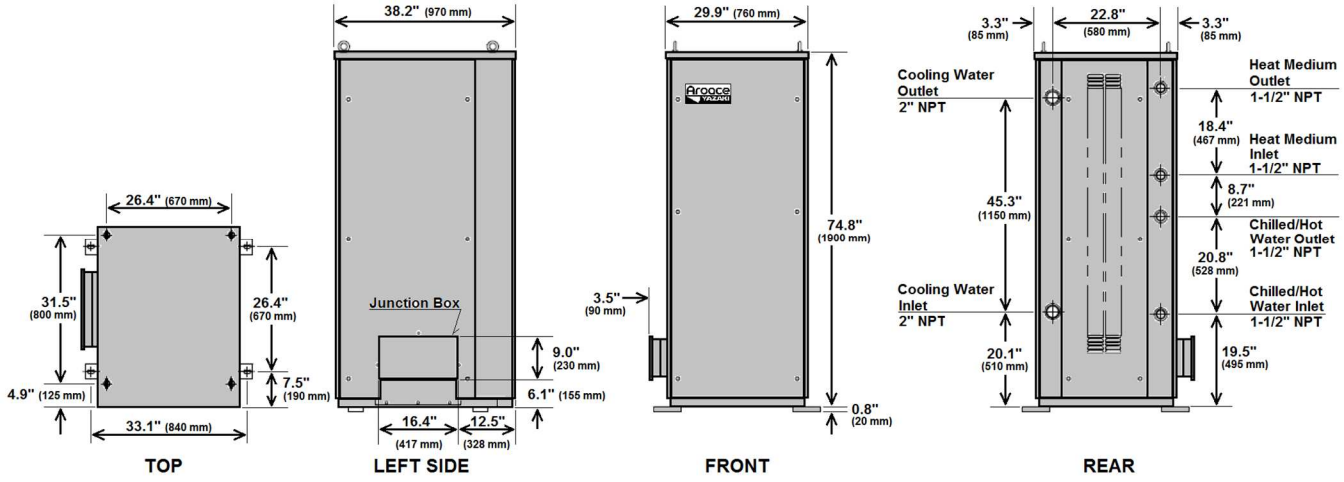

WFC-SC/SH20

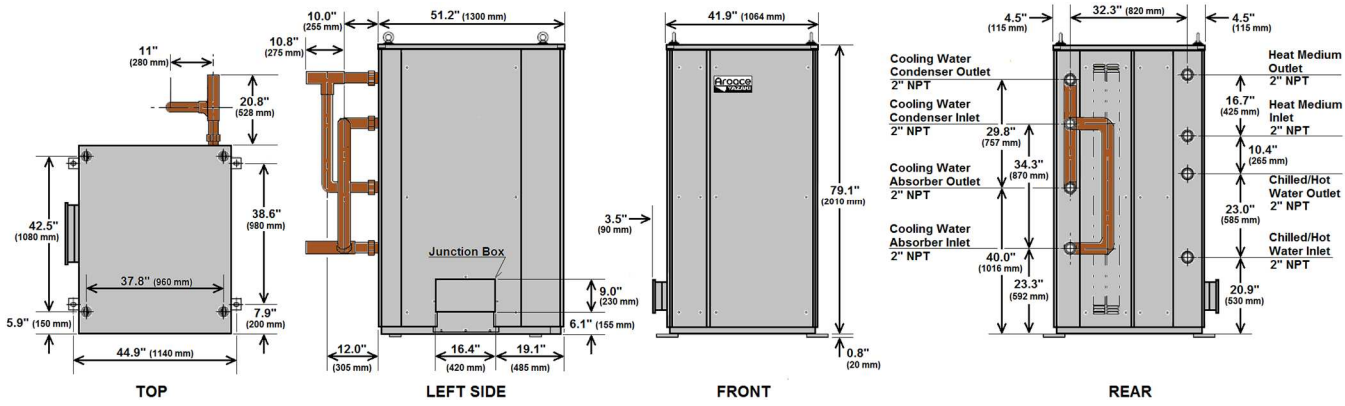

Customer:	UC Irvine -	Date:	5/20/2019
Contact:	Alejandro Lavernia	From:	Zeke Lujano
Telephone:		Company:	Coilmen Plus, Inc.
Cell:		Return Tel:	323-497-0707
Fax:		Return Fax:	323-758-4497
Job:	Advanced power & enery program CW	Email:	zeke@coilmenplus.com
Quote #:			

		MODEL NUMBER						
ITEM	QTY	TYPE	FPI	ROWS	FIN	FH (IN)	FL (IN)	HAND
CW Coil	1	5WH	10	06	B	24.00	24.00	Left

MATERIALS OF CONSTRUCTION		OPTIONS			
Fins	0.0075 Aluminum	**Coating**	None	**TurboSpirals**	No
Tubes	0.020 Copper	**Casing Type**	Flanged	**Moisture Eliminator**	No
Casing	304L S/S	**Vent & Drain**	.50 FPT on Face	**Mounting Holes**	No
Conn. Material	Copper			**Label Kit**	No
Conn. Type	Sweat			**Drain Headers**	No
Conn. Size	1.63			**Tube Ferrules**	No
Weight (LBS)	94.0				

Vent/Drain

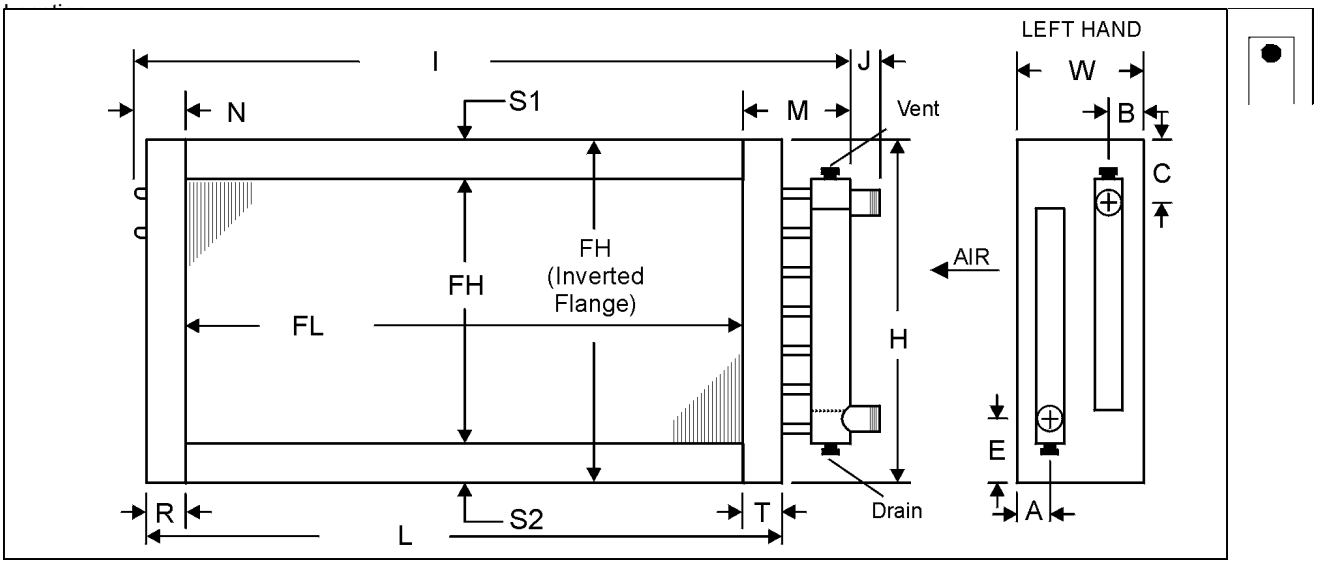

DIMENSIONAL DATA(IN)														
A	B	C	E	H	I	J	L	M	N	R	S1	S2	T	W
1.75	1.75	2.25	2.25	27.00	31.00	3.00	27.00	4.50	2.50	1.50	1.50	1.50	1.50	10.00

NOTES:

GENERAL NOTES:

1. All dimensions are in (IN)
2. Manually verifying dimensions is highly recommended.
3. The supply line should be connected to the lower connection on the leaving air side for counterflow operation.
4. Coils will vent and drain through factory-installed vent and drain fittings when mounted level for horizontal flow.
5. Connection location other than standard could affect vent and drain locations. Consult factory.

Customer:	UC Irvine -	Date:	5/20/2019
Contact:	Alejandro Lavernia	From:	Zeke Lujano
Telephone:		Company:	Coilmen Plus, Inc.
Cell:		Return Tel:	323-497-0707
Fax:		Return Fax:	323-758-4497
Job:	Advanced power & enery program CW	Email:	zeke@coilmenplus.com
Quote #:			

Item	Coils Per Bank	FA SQ FT	Air Flow ft^3/min	Face Vel. ft/min	Fin Fouling Factor ft^2-°F-hr/BTU	Ent Air DB/WB °F	Lvg Air DB/WB °F	Capacity Total MBH	APD "H2O	Fluid Type	Fluid Fouling Factor ft^2-°F-hr/BTU	Fluid Temp. Ent/Lvg °F	FPD FT H2O	Fluid Vel	Fluid Flow gal/min	Model Number FHxFL IN
CW Coil	1	4.0	S- 2100.0	525.0	0.00	77.00/65.00	56.06/55.16	61.55/48.08	0.71	10% Ethylene	0.00	44.60/55.12	1.99	1.61	12.10	5WH1006B 24.00 x 24.00

Tower Specifications: Model T-215

Cooling Tower Systems, Inc.

Design and Operating Conditions		Water Distribution System Construction Materials	
Tower Type:	Counter Flow Induced Draft	Stand Pipe:	PVC
Water Flow Rate (GPM):	44 GPM	Sprinkler Head:	Nylon
Entering Water Temperature	95°F	Sprinkler Pipes:	PVC
Leaving Water Temperature	85°F	**Mechanical Equipment**	
Wet Bulb Temperature:	75°F	Fan Unit:	One Unit per Tower
Total Fan BHP:	1/4 HP	Type:	Axial Flow
Total Pump Head:	5.3’	Manufacturer:	CTS
Drift Loss of Water Flow:	0.1%	Diameter:	26 3/8”
Evaporation Loss of Water Flow:	0.93%	Blade Material:	Nylon
Design Wind Load:	30.7 lbs/sq. ft.	Hub Material:	Nylon
Structural Details		Nominal Air Volume:	4,700 CFM
Overall Diameter:	46”	**Fan Motor**	
Overall Height:	59”	Number of motors:	One Unit per Tower
Dry Weight:	139 lbs.	Type:	Induction
Operating Weight:	536 lbs.	Manufacturer:	CTS
Basic Tower Construction Materials		Insulation:	E Class
Tower Support Frame Assembly	-	Rated HP:	1/4 HP
Casing:	FRP	Voltage and phase:	110/220V/1
Casing Supporters	Nylon	**Piping Connections**	
Cold Water Basin	FRP	Primary Water Inlet Diameter	2”
Filling:	PVC	Primary Water Outlet Diameter:	2”
Filling Supports:	PVC	Auto fill inlet diameter:	1/2”
Fan Guard	PP	Quick fill inlet diameter:	-
Mechanical Equipment Supports:	HDGS	Overflow outlet diameter:	1”
Inlet Louvers:	PVC	Drain diameter:	1”
Bolts, Nuts & Washers:	STS	Water Flow (GPM):	44 GPM

Materials Key			
FRP	Fiberglass Reinforced Polyester	STS	Stainless Steel
HDGS	Hot Dipped Galvanized Steel	AC	Aluminum Alloy Cast

Cooling Tower Systems, Inc.
3170 Mercer University Dr., Macon, GA 31204
TF: 800.752.1905 F: 478.755.8304 www.coolingtowersystems.com info@coolingtowersystems.com

GENERAL SPECIFICATIONS

Pressure and Temperature Rating

Max Pressure at Indicated Temperature

PVC	PIPE DIAMETER IN INCHES				
TEMPERATURE IN DEGREES F	1/2	3/4	1	1 1/2	2
73	425	345	315	235	200
80	377	306	279	208	177
90	317	258	235	175	149
100	264	214	196	146	124
110	216	175	160	119	101
120	172	139	127	95	81
130	131	106	97	72	62
140	93	76	69	52	44
150	-	-	-	-	-
160	-	-	-	-	-
170	-	-	-	-	-
180	-	-	-	-	-

CPVC	PIPE DIAMETER IN INCHES				
TEMPERATURE IN DEGREES F	1/2	3/4	1	1 1/2	2
73	425	345	315	235	200
80	403	327	298	223	189
90	371	301	275	205	175
100	340	276	252	188	160
110	308	250	228	170	145
120	276	224	205	153	130
130	244	198	181	135	115
140	213	173	158	118	100
150	182	148	135	101	86
160	154	125	114	85	72
170	129	105	96	71	61
180	110	89	81	61	52

Minimum Operating Pressure:	See INSTALLATION and PRESSURE DROP CHARTS
Minimum Operating Temperature:	35°F (2ºC) fluid and ambient
Maximum Flow:	Meters may occasionally be over-ranged up to 125% of capacity without damaging the meter. Note: Output is clamped at 21mA (6.3% over-range)
Capacities:	1/2" = 12 GPM (45 LPM) 3/4" = 25 GPM (95 LPM) 1" = 50 GPM (190 LPM) 1 1/2" = 100 GPM (380 LPM) 2" = 200 GPM (750 LPM)
Turndown Ratio:	10:1 standard
Process Connections:	Socket weld standard and female NPT thread optional
Wetted Parts:	PVC or CPVC
Display:	No Display
Enclosure Rating:	Type 1, 3, 4, 12, 13, IP65
Power:	10 - 30 VDC @ 21 mA ⎓

Caution: The unit shall be supplied by a SELV (separated extra-low voltage) source in accordance with CSA Standard C22.2 No.1010.1-92 Annex H.

Environmental Conditions:	This device has been designed for use in Installation Category I, pollution degree 4, at altitudes up to 2000 meters (6560 ft.), either indoors or outdoors as defined in CSA Standard C22.2 No.1010.1-92.

FLOW

Electrical Service:	General Purpose Non-hazardous
Enclosure Classification:	Type 1, 2, 3, 4 (equal to IP 65), 12, and 13
Power Requirements:	The P420 is a loop-powered, 2-wire transmitter. It operates from loop voltages of 10 to 30 Volts DC (4-20 mA).
Accuracy:	± 2% of full-scale
Analog Output:	4-20 mA proportional to flow
Response Time:	0.9-7.5 seconds to 63% of step change
Repeatability:	± 0.25% of actual flow
Electrical Connection:	Screw terminal, polarity independent with ½" conduit port

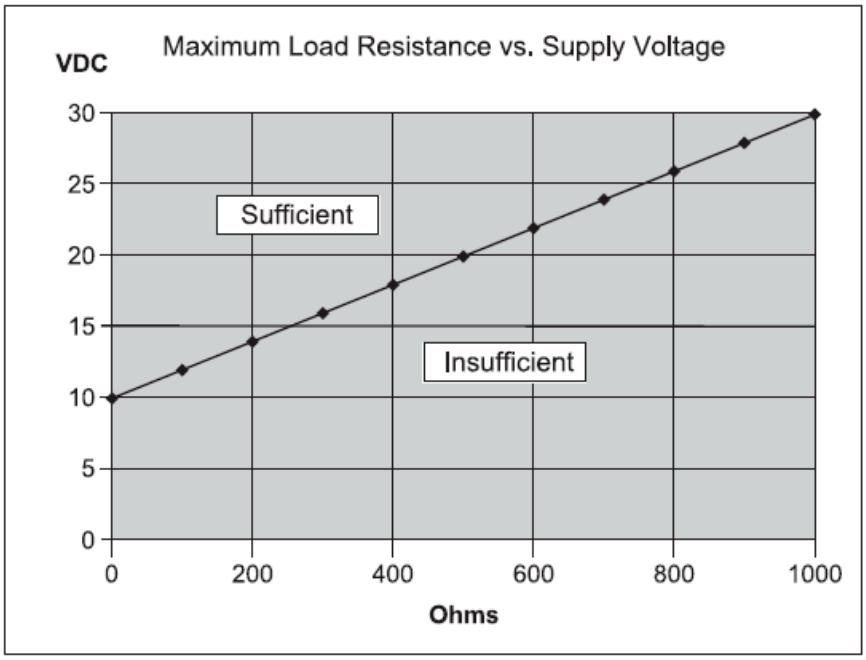

FLOW TORCH™ FT800

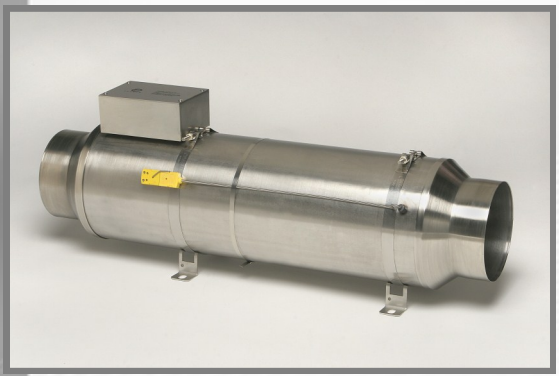

Shown with optional inlet & exhaust fittings

- The Flow Torch™ 800 is a 8" diameter stainless steel air heater designed for high flow rates at low pressure drop due to its efficient design with minimal flow restrictions.
- The Flow Torch™ 800 is capable of operating with airflow of 2000 SCFM and up to 3 psig.
- UL component recognized (UL File # E365755)

Wattage	Min. SCFM Req.
20.0kW	76.3
35.0kW	133.6
50.0kW	190.8
65.0kW	248.0
75.0kW	286.2

Airflow (SCFM)	Pressure Drop (H2O) w/o fittings	Pressure Drop (H2O) 6" fittings
290	0.1	0.6
460	0.2	1.5
630	0.3	2.8
800	0.6	4.5
970	0.8	6.6
1140	1.2	9.1
1310	1.5	12.0
1480	2.0	15.3
1650	2.4	19.1
1820	3.0	23.2
2000	3.6	28.0

Wattage & Voltage Options

208V, three phase, 10.0kW-30.0kW
240V, three phase, 10.0kW-35.0kW
380V, three phase, 10.0kW-60.0kW
480V, three phase, 10.0kW-75.0kW
575V, three phase, 10.0kW-75.0kW

Fitting Options

Inlet Fitting:
6T- 6" O.D. Tube
NF- No Fitting (8" O.D.)

Exhaust Fitting:
6T- 6" O.D. Tube
NF- No Fitting (8" O.D.)

Other Options

Thermocouple Fitting
Thermocouple
Insulation Blanket

Specifications

Category:	**Open Coil Heaters, Inline Heaters, Process Heaters**
Max. wattage:	75.0kW
Max. exhaust air temp.:	900°F
Max. inlet air temp.:	250°F
(consult factory for higher inlet temp.)	
Max. SCFM:	2000
Max. allowable pressure :	3 psig
Mounting:	Horizontal/Vertical
Heater Body:	304 Stainless Steel
Inlet Fitting:	304 Stainless Steel
Exhaust Fitting:	304 Stainless Steel

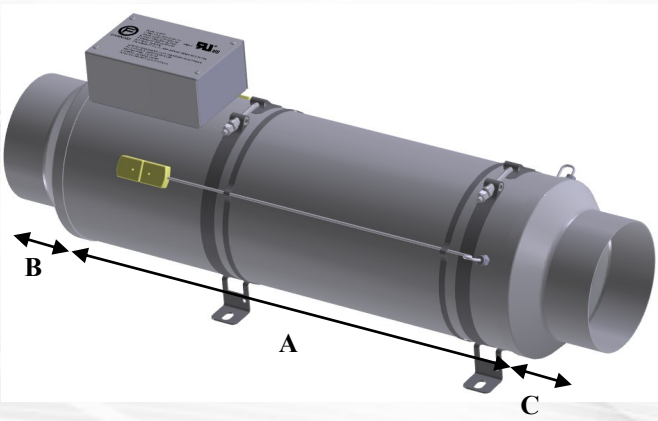

Visit **www.farnam-custom.com** for detailed drawings

A	Inlet Fitting	B	Exhaust Fitting	C
24.0"	NF	0	NF	0
24.0"	6T	3.5"	6T	3.5"

Part Number Key

FT800	40000	480	3	6T	6T	TF2	(XXX)
Flow Torch 400	Wattage	Voltage	Phase	Inlet Fitting	Exhaust Fitting	Thermocouple Fitting	Modification

ISO 9001:2008 REGISTERED

TUTCO HEATING SOLUTIONS GROUP

FARNAM CUSTOM PRODUCTS

www.farnam-custom.com
Ph: (828) 684-3766 Fax: (828) 684-3768

REV 02/04/16

Job Name: 500 CFM - University of CA-Irvine

Fans & Blowers
Twin City

Customer:
Job ID: 05-15-19ts-03
Date: May 17, 2019

Tag: inlet screen

Fan information

Size/Model	15W6/TBNA	Class	HP	Outlet Vel (FPM)	3189
Volumetric Flow (CFM)	625	Speed (RPM)	3501	Density (lb/ft³)	0.075
SP (in WC)	18	Max Speed	4,000 RPM @ 70 °F		
		Power (BHP)	2.98		

Adjusted for Apply Compressibility

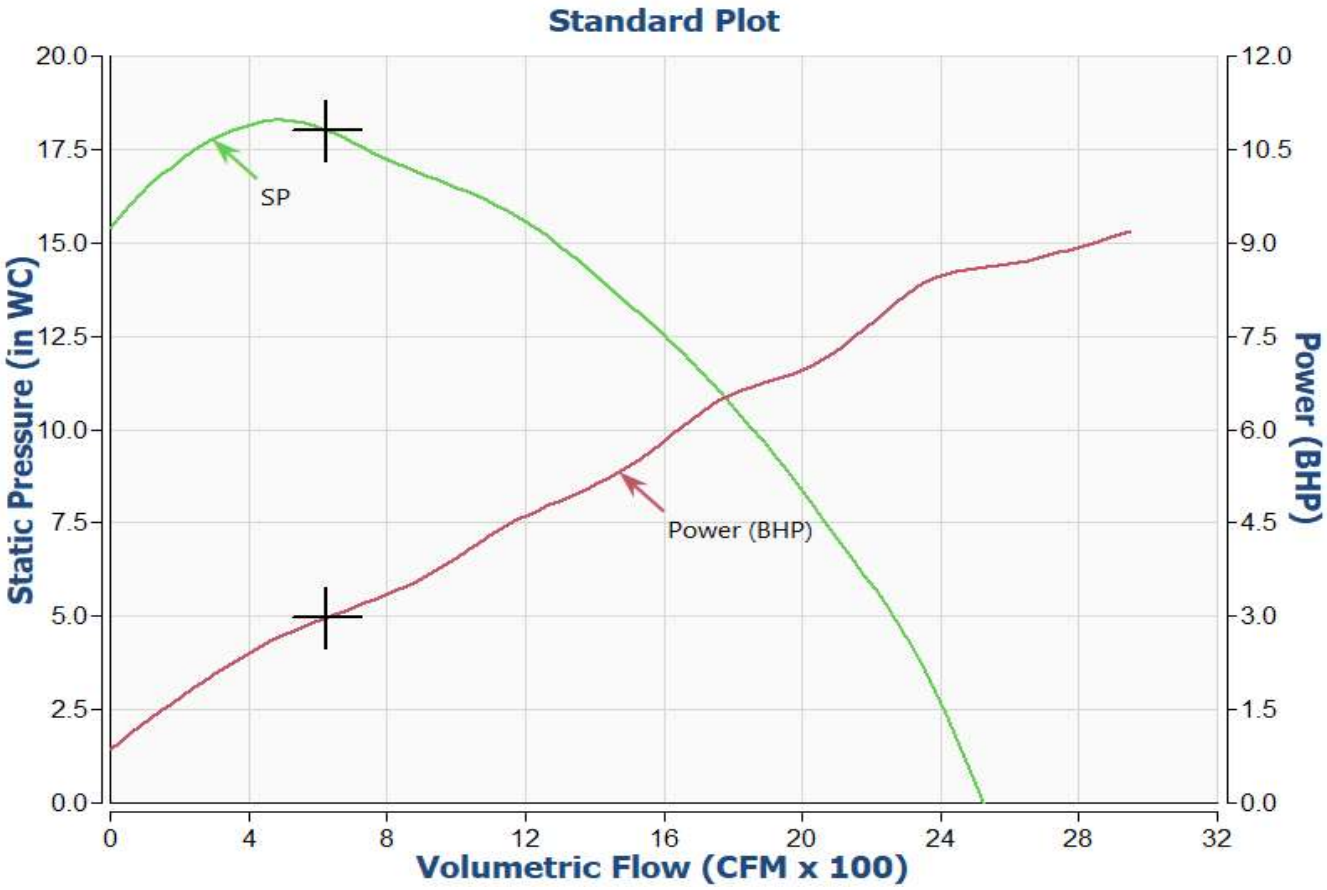

Sound Power Ea.	Octave Bands	1	2	3	4	5	6	7	8	LwA	dBA
	Inlet dB	76	81	89	94	85	79	75	71	93	78

LwA: The overall (single value) fan sound power level in dB re. 10^{-12} Watts, 'A' weighted.
dBA: Estimated sound pressure level (re:0.0002 microbar) based on a single ducted installation at 5 ft., using a directivity factor of 1.

Appendix B – Modeling Code

The following pages contain the MATLAB and EES codes used for the modeling described.

Table of Contents


```
function [Outputs] = BloomServerModel_v4func(Inputs)
```

SOFC Model

Alejandro Lavernia 2/27/2020

Unload Inputs

```
T_init = Inputs.T_init;
m_init = Inputs.m_init;
C_init = Inputs.C_init;
CP_init = Inputs.CP_init;
m_NG_in = Inputs.m_NG_in;
m_AIR_in = Inputs.m_AIR_in;
m_AIR_comb_in = Inputs.m_AIR_comb_in;
m_H2O_in = Inputs.m_H2O_in;
x_recirc = Inputs.x_recirc;
eff_AND_RECOUP = Inputs.eff_AND_RECOUP;
eta_SMR_react = Inputs.eta_SMR_react;
eff_SMR_HX = Inputs.eff_SMR_HX;
eff_AND_cool = Inputs.eff_AND_cool;
eff_CAT_rec = Inputs.eff_CAT_rec;
eta_fuel_utl = Inputs.eta_fuel_utl;
eff_AND_cond = Inputs.eff_AND_cond;
eta_dropout = Inputs.eta_dropout;
eff_STM_gen = Inputs.eff_STM_gen;
n_max = Inputs.n_max;
dT_max = Inputs.dT_max;
```

Initialize State Point Arrays

```
%tic

if isempty(T_init)
% Temperature Array - degC
T_NG_in = 25;
```

```
T_NG_STM_mix = 75;
T_NG_EXH_mix = 120;
T_SMR_in = 240;
T_AND_in = 200;
T_AND_out = 500;
T_AND_exh_rec_out = 300;
T_AND_exh_cool = 150;
T_AND_exh_cond = 80;

T_AIR_in = 25;
T_AIR_AND_cool = 80;
T_CAT_in = 150;
T_CAT_out = 500;
T_CAT_exh_SMR_out = 250;
T_AIR_comb_in = 25;
T_EXH_comb = 800;
T_CAT_EXH_mix = 550;
T_CAT_EXH_rec = 320;
T_CAT_EXH = 120;

T_W_in = 25;
T_STM = 100;

    % Compile Array
    T_init = [T_NG_in; T_NG_STM_mix; T_NG_EXH_mix; T_SMR_in; T_AND_in;
 T_AND_out; T_AND_exh_rec_out; T_AND_exh_cool; T_AND_exh_cond; T_AIR_in;
 T_AIR_AND_cool; T_CAT_in; T_CAT_out; T_CAT_exh_SMR_out; T_AIR_comb_in;
 T_EXH_comb; T_CAT_EXH_mix; T_CAT_EXH_rec; T_CAT_EXH; T_W_in; T_STM];
    % T_init =
 [25;88.4346965766868;238.605052737377;787.243712360561;753.101552918544;1457.80207402761;

 clear T_NG_in T_NG_STM_mix T_NG_EXH_mix T_SMR_in T_AND_in T_AND_out T_AND_exh_rec_out T_A
end
if isempty(m_init)
% Mass Flow Array kg/s
% m_NG_in = 0.008;        % INPUT
m_mix_2 = 0.009;
m_NG_EXH_mix = 0.012;
m_SMR_in = m_NG_EXH_mix;
m_AND_in = m_SMR_in;
m_AND_out = 0.015;
m_AND_exh_rec_out = m_AND_out;
m_AND_exh_cool = m_AND_out;
m_AND_exh_cond = 0.010;

% m_AIR_in = 0.150;       % INPUT
m_AIR_AND_cool = m_AIR_in;
m_CAT_in = m_AIR_in;
m_CAT_out = 0.05;
m_CAT_exh_SMR_out = m_CAT_out;
% m_AIR_comb_in = 0.250;  % INPUT
m_EXH_comb = 0.06;
m_CAT_EXH_mix = 0.11;
m_CAT_EXH_rec = m_CAT_EXH_mix;
```

```
m_CAT_EXH = m_CAT_EXH_mix;

% m_H2O_in = 0.01;
m_STM = m_H2O_in;
    % Compile Array
    m_init = [m_NG_in; m_mix_2; m_NG_EXH_mix; m_SMR_in; m_AND_in; m_AND_out;
 m_AND_exh_rec_out; m_AND_exh_cool; m_AND_exh_cond; m_AIR_in; m_AIR_AND_cool;
 m_CAT_in; m_CAT_out; m_CAT_exh_SMR_out; m_AIR_comb_in; m_EXH_comb;
 m_CAT_EXH_mix; m_CAT_EXH_rec; m_CAT_EXH; m_H2O_in; m_STM];
    % m_init =
 [0.00800000000000000;0.0625162630299007;0.0712491353915930;0.0712491353915930;0.071249135

 clear m_NG_in m_NG_STM_mix m_NG_EXH_mix m_SMR_in m_AND_in m_AND_out m_AND_exh_rec_out m_A
else
    m_init(1) = m_NG_in;
    m_init(10) = m_AIR_in;
    m_init(15) = m_AIR_comb_in;
    m_init(20) = m_H2O_in;
end

if isempty(C_init)
% Composition Array - mass basis [CH4 CO2 N2 O2 H2 H2O] [kg/kg]
eta_H2 = Inputs.H2Injection;
% eta_H2 = 0;
C_NG_in = (1-eta_H2) * [0.94 0.025 0.035 0 0 0] + eta_H2 * [0 0 0 0 1 0];
C_NG_STM_mix = [0.6 0.035 0.015 0 0 0.35];
C_NG_EXH_mix = [0.6 0.035 0.015 0 0 0.35];
C_SMR_in = [0.5 0.025 0.015 0 0.005 0.45];
C_AND_in = [0.03 0.63 0.01 0 0.25 0.08];
C_AND_out = [0.03 0.45 0.01 0 0.01 0.50];
C_AND_exh_rec_out = [0.03 0.45 0.01 0 0.01 0.50];
C_AND_exh_cool = [0.03 0.45 0.01 0 0.01 0.50];
C_AND_exh_cond = [0.09 0.70 0.03 0 0.03 0.15];

C_AIR_in = [0 0 0.79 0.21 0 0];
C_AIR_AND_cool = [0 0 0.79 0.21 0 0];
C_CAT_in = [0 0 0.79 0.21 0 0];
C_CAT_out = [0 0 0.79 0.05 0 0.16];
C_CAT_exh_SMR_out = [0 0 0.79 0.05 0 0.16];
C_AIR_comb_in = [0 0 0.79 0.21 0 0];
C_EXH_comb = [0 0.15 0.75 0.01 0 0.09];
C_CAT_EXH_mix = [0 0.09 0.78 0.02 0 0.11];
C_CAT_EXH_rec = [0 0.09 0.78 0.02 0 0.11];
C_CAT_EXH = [0 0.09 0.78 0.02 0 0.11];

C_W_in = [0 0 0 0 0 1];
C_STM = [0 0 0 0 0 1];
    % Compile Array - and normalizes in case of not adding up to 1
    C_init = [C_NG_in; C_NG_STM_mix; C_NG_EXH_mix; C_SMR_in; C_AND_in;
 C_AND_out; C_AND_exh_rec_out; C_AND_exh_cool; C_AND_exh_cond; C_AIR_in;
 C_AIR_AND_cool; C_CAT_in; C_CAT_out; C_CAT_exh_SMR_out; C_AIR_comb_in;
 C_EXH_comb; C_CAT_EXH_mix; C_CAT_EXH_rec; C_CAT_EXH; C_W_in; C_STM];
    % C_init =
 [0.940000000000000,0.0250000000000000,0.0350000000000000,0,0,0;0.120288699860439,0.003199
```

```
 clear C_NG_in C_NG_STM_mix C_NG_EXH_mix C_SMR_in C_AND_in C_AND_out C_AND_exh_rec_out C_A
end
if Inputs.H2Injection ~= 0
    eta_H2 = Inputs.H2Injection;
    C_init(1,:) = (1-eta_H2) * [0.94 0.025 0.035 0 0 0] + eta_H2 * [0 0 0 0 1
 0];
end

if isempty(CP_init)
% Cp Array (Cp = [1] + [2]T + [3]T^2 ...) [kJ/kg-C]
CH4_CP_poly = [2.197 0.0023 4e-6 -3e-9];
CO2_CP_poly = [0.8179 0.001 -9e-7 3e-10];
N2_CP_poly = [1.0378 1e-5 4e-7 -2e-10];
O2_CP_poly = [0.9181 0.0002 2e-7 -2e-10];
H2_CP_poly = [14.145 0.0059 -3e-5 7e-8 -6e-11 2e-14];
H2O_CP_poly = [1.8611 0.0003 7e-7 4e-10];

CP_CH4 = CH4_CP_poly(1) + CH4_CP_poly(2)*T_init + CH4_CP_poly(3)*T_init.^2 +
 CH4_CP_poly(4)*T_init.^3;
CP_CO2 = CO2_CP_poly(1) + CO2_CP_poly(2)*T_init + CO2_CP_poly(3)*T_init.^2 +
 CO2_CP_poly(4)*T_init.^3;
CP_N2 = N2_CP_poly(1) + N2_CP_poly(2)*T_init + N2_CP_poly(3)*T_init.^2 +
 N2_CP_poly(4)*T_init.^3;
CP_O2 = O2_CP_poly(1) + O2_CP_poly(2)*T_init + O2_CP_poly(3)*T_init.^2 +
 O2_CP_poly(4)*T_init.^3;
CP_H2 = H2_CP_poly(1) + H2_CP_poly(2)*T_init + H2_CP_poly(3)*T_init.^2 +
 H2_CP_poly(4)*T_init.^3 + H2_CP_poly(5)*T_init.^4 + H2_CP_poly(6)*T_init.^5;
CP_H2O = H2O_CP_poly(1) + H2O_CP_poly(2)*T_init + H2O_CP_poly(3)*T_init.^2 +
 H2O_CP_poly(4)*T_init.^3;

    % Compile Array
    CP_init = sum([CP_CH4 CP_CO2 CP_N2 CP_O2 CP_H2 CP_H2O].*C_init,2);

 clear CP_CH4 CP_CO2 CP_N2 CP_O2 CP_H2 CP_H2O CH4_CP_poly CO2_CP_poly N2_CP_poly O2_CP_pol
end
```

Iterative Convergance for State Points

Iteration Values

```
i=1;
% n_max = 500;
dT = 1;
% dT_max = 1e-7;

% Universal Constants
T_amb = 25;
P_amb = 101.325;

% Initialize Converging Matrices
T_c = zeros(21,n_max);
m_c = zeros(21,n_max);
```

```
CP_c = zeros(21,n_max);
C_c = zeros(21,6,n_max);

% Put Initial Values of Statepoints into converging variables
T_c(:,1) = T_init;
m_c(:,1) = m_init;
CP_c(:,1) = CP_init;
C_c(:,:,1) = C_init;
```

Loop

```
while i < n_max && dT > dT_max
```

Component Models

```
% Constants - values that should not change during iteration
T_c(1,i+1) = T_c(1,i);
C_c(1,:,i+1) = C_c(1,:,i);
m_c(1,i+1) = m_c(1,i);
T_c(10,i+1) = T_c(10,i);
C_c(10,:,i+1) = C_c(10,:,i);
m_c(10,i+1) = m_c(10,i);
T_c(15,i+1) = T_c(15,i);
C_c(15,:,i+1) = C_c(15,:,i);
m_c(15,i+1) = m_c(15,i);
T_c(20,i+1) = T_c(20,i);
C_c(20,:,i+1) = C_c(20,:,i);
m_c(20,i+1) = m_c(20,i);

% NG + Steam Mixing Model
    % Calculates New State 2 based on States 1 and 20

m_NG_1 = m_c(1,i);
m_STM_21 = m_c(21,i);
m_mix_2 = m_NG_1 + m_STM_21;    % Mass Balance
m_c(2,i+1) = m_mix_2;           % Determine mix mass flow

c_NG_1 = C_c(1,:,i);
c_STM_20 = C_c(21,:,i);
m_x_NG_1 = c_NG_1 * m_NG_1;
m_x_H2O_20 = c_STM_20 * m_STM_21;
m_x_mix_2 = m_x_NG_1 + m_x_H2O_20;
C_mix_2 = m_x_mix_2 ./ m_mix_2; % Mass Balance
C_c(2,:,i+1) = C_mix_2;         % Determine mixture composition

T_NG_1 = T_c(1,i);
T_STM_20 = T_c(21,i);
CP_NG_1 = CP_c(1,i);
CP_STM_20 = CP_c(21,i);
CP_mix_2 = CP_c(2,i);
T_mix_2 = (m_NG_1 * CP_NG_1 * T_NG_1 + m_STM_21 * CP_STM_20 * T_STM_20) /
 (m_mix_2 * CP_mix_2);     %Energy Balance
```

```
T_c(2,i+1) = T_mix_2;           % Determine Exit temperature

% MIX 2 (NG + STM) + Anode EXH Recirc
    % Calculate State 3 based on States 2 and 8
    % Currently assuming a fixed recirc rate of 0.1

% x_recirc = 0.1;
m_AND_rcirc_8 = x_recirc * m_c(8,i);
m_mix_2old = m_c(2,i);
m_mix_3 = m_mix_2old + m_AND_rcirc_8;
m_c(3,i+1) = m_mix_3;

C_AND_rcirc_8 = C_c(8,:,i);
C_mix_2old = C_c(2,:,i);
m_x_AND_rcirc_8 = C_AND_rcirc_8 * m_AND_rcirc_8;
m_x_mix_2old = C_mix_2old * m_mix_2old;
m_x_mix_3 = m_x_AND_rcirc_8 + m_x_mix_2old;
C_mix_3 = m_x_mix_3 ./ m_mix_2old;
C_c(3,:,i+1) = C_mix_3;

T_mix_2old = T_c(2,i);
T_AND_rcirc_8 = T_c(8,i);
CP_mix_2old = CP_c(2,i);
CP_AND_rcirc_8 = CP_c(8,i);
CP_mix_3 = CP_c(3,i);
T_mix_3 = (m_mix_2old * CP_mix_2old * T_mix_2old + m_AND_rcirc_8 *
 CP_AND_rcirc_8 * T_AND_rcirc_8) / (m_mix_3 * CP_mix_3);
T_c(3,i+1) = T_mix_3;

% Anode Recouperator HX
    % Calculate States 7 and 4 from 3 and 6
    % Assuming a fixed HX effectiveness

T_AND_out_6 = T_c(6,i);
T_mix_3old = T_c(3,i);
CP_AND_out_6 = CP_c(6,i);
CP_mix_3 = CP_c(3,i);
m_AND_out_6 = m_c(6,i);
m_mix_3old = m_c(3,i);

% eff_AND_RECOUP = 0.45;
Q_MAX_AND_RECOUP = min(m_AND_out_6*CP_AND_out_6*(T_AND_out_6 -
 T_mix_3old),m_mix_3old*CP_mix_3*(T_AND_out_6 - T_mix_3old));
Q_AND_RECOUP = eff_AND_RECOUP * Q_MAX_AND_RECOUP;
T_AND_rec_out_7 = T_AND_out_6 - Q_AND_RECOUP / (m_AND_out_6 * CP_AND_out_6);
T_SMR_in_4 = T_mix_3old + Q_AND_RECOUP / (m_mix_3old * CP_mix_3);
T_c(7,i+1) = T_AND_rec_out_7;
T_c(4,i+1) = T_SMR_in_4;

% Steam Reformer HX
     % Calculate States 5 and 14 from 4 and 13
     % Assumed a fixed HX effectiveness
     % Assumes fixed reaction completion
```

```
MM_CH4 = 16.04;     % kg/kmol
MM_H2O = 18.01;     % kg/kmol
MM_CO2 = 44.01;     % kg/kmol
MM_N2 = 14.0;       % kg/kmol
MM_O2 = 15.99;      % kg/kmol
MM_H2 = 2.016;      % kg/kmol

m_SMR_in_4old = m_c(4,i);
C_SMR_in_4old = C_c(4,:,i);
m_x_SMR_in_4old = m_SMR_in_4old * C_SMR_in_4old;
n_SMR_in_CH4 = m_x_SMR_in_4old(1) / MM_CH4;
n_SMR_in_CO2 = m_x_SMR_in_4old(2) / MM_CO2;
n_SMR_in_N2 = m_x_SMR_in_4old(3) / MM_N2;
n_SMR_in_O2 = m_x_SMR_in_4old(4) / MM_O2;
n_SMR_in_H2 = m_x_SMR_in_4old(5) / MM_H2;
n_SMR_in_H2O = m_x_SMR_in_4old(6) / MM_H2O;



% eta_SMR_react = 0.95;
n_SMR_react_max = min(n_SMR_in_CH4,n_SMR_in_H2O/2);
n_SMR_react = eta_SMR_react * n_SMR_react_max;  % Moles of CH4 reacted [kmol]
n_SMR_out_CH4 = n_SMR_in_CH4 - n_SMR_react;
n_SMR_out_CO2 = n_SMR_in_CO2 + n_SMR_react;
n_SMR_out_H2 = n_SMR_in_H2 + 4 * n_SMR_react;
n_SMR_out_H2O = n_SMR_in_H2O - 2 * n_SMR_react;

Q_SMR_react = -165e3 * n_SMR_react;   %kW

m_SMR_out_CH4 = n_SMR_out_CH4 * MM_CH4;
m_SMR_out_CO2 = n_SMR_out_CO2 * MM_CO2;
m_SMR_out_H2 = n_SMR_out_H2 * MM_H2;
m_SMR_out_H2O = n_SMR_out_H2O * MM_H2O;
m_SMR_out_N2 = n_SMR_in_N2 * MM_N2;
m_SMR_out_O2 = n_SMR_in_O2 * MM_O2;
m_SMR_out_5 = m_SMR_out_CH4 + m_SMR_out_CO2 + m_SMR_out_H2O + m_SMR_out_H2 +
 m_SMR_out_N2 + m_SMR_out_O2;
C_SMR_out_5 = [m_SMR_out_CH4 m_SMR_out_CO2 m_SMR_out_N2 m_SMR_out_O2
 m_SMR_out_H2 m_SMR_out_H2O] / m_SMR_out_5;
C_c(5,:,i+1) = C_SMR_out_5;

T_SMR_in_4old = T_c(4,i);
T_CAT_out_13old = T_c(13,i);
CP_SMR_in_4old = CP_c(4,i);
CP_CAT_out_13old = CP_c(13,i);
m_CAT_out_13old = m_c(13,i);

% eff_SMR_HX = 0.45;
Q_SMR_HX_MAX = min(m_SMR_in_4old * CP_SMR_in_4old * (T_CAT_out_13old
 - T_SMR_in_4old) - Q_SMR_react, m_CAT_out_13old * CP_CAT_out_13old *
 (T_CAT_out_13old - T_SMR_in_4old));
Q_SMR_HX = eff_SMR_HX * Q_SMR_HX_MAX;
T_SMR_out_5 = T_SMR_in_4old + (Q_SMR_HX + Q_SMR_react) / (m_SMR_in_4old *
 CP_SMR_in_4old);
```

```
T_CAT_SMR_out_14 = T_CAT_out_13old - (Q_SMR_HX) / (m_CAT_out_13old *
 CP_CAT_out_13old);
T_c(5,i+1) = T_SMR_out_5;
T_c(14,i+1) = T_CAT_SMR_out_14;

% Annode Cooler HX
    % Calculate States 8 and 11 from 10 and 7
    % Assumed a fixed HX effectiveness

T_AND_rec_7old = T_c(7,i);
T_AIR_10 = T_c(10,i);
CP_AND_rec_7old = CP_c(7,i);
CP_AIR_10 = CP_c(10,i);
m_AND_rec_7old = m_c(7,i);
m_AIR_10 = m_c(10,i);

% eff_AND_cool = 0.55;
Q_MAX_AND_cool = min(m_AND_rec_7old*CP_AND_rec_7old ,
 m_AIR_10*CP_AIR_10)*(T_AND_rec_7old - T_AIR_10);
Q_AND_cool = eff_AND_cool * Q_MAX_AND_cool;
T_AND_cool_8 = T_AND_rec_7old - Q_AND_cool / (m_AND_rec_7old*CP_AND_rec_7old);
T_AIR_cool_11 = T_AIR_10 + Q_AND_cool / (m_AIR_10*CP_AIR_10);
T_c(8,i+1) = T_AND_cool_8;
T_c(11,i+1) = T_AIR_cool_11;

% Combustor Cathode Mixing
    % Calculate State 17 from 14 and 16

m_SMR_out_14old = m_c(14,i);
m_EXH_comb_16 = m_c(16,i);
m_CAT_mix_17 = m_SMR_out_14old + m_EXH_comb_16;

c_SMR_out_14old = C_c(14,:,i);
c_EXH_comb_16 = C_c(16,:,i);
m_x_SMR_out_14old = c_SMR_out_14old * m_SMR_out_14old;
m_x_EXH_comb_16 = c_EXH_comb_16 * m_EXH_comb_16;
m_x_CAT_mix_17 = m_x_SMR_out_14old + m_x_EXH_comb_16;
C_CAT_mix_17 = m_x_CAT_mix_17 ./ m_CAT_mix_17; % Mass Balance
C_c(17,:,i+1) = C_CAT_mix_17;         % Determine mixture composition

% Cathode Recoup HX
    % Calculate States 12 and 18 from 11 and 17
    % Assumed a fixed HX effectiveness

T_AIR_cool_11old = T_c(11,i);
T_CAT_mix_17old = T_c(17,i);
CP_AIR_cool_11 = CP_c(11,i);
CP_CAT_mix_17 = CP_c(17,i);
m_AIR_cool_11 = m_c(11,i);
m_CAT_mix_17old = m_c(17,i);

% eff_CAT_rec = 0.25;
Q_MAX_CAT_rec = min(m_AIR_cool_11*CP_AIR_cool_11,
 m_CAT_mix_17old*CP_CAT_mix_17)*(T_CAT_mix_17old - T_AIR_cool_11old);
```

```
Q_CAT_rec = eff_CAT_rec * Q_MAX_CAT_rec;
T_CAT_rec_18 = T_CAT_mix_17old - Q_CAT_rec / (m_CAT_mix_17old*CP_CAT_mix_17);
T_CAT_in_12 = T_AIR_cool_11 + Q_CAT_rec / (m_AIR_cool_11*CP_AIR_cool_11);
T_c(18,i+1) = T_CAT_rec_18;
T_c(12,i+1) = T_CAT_in_12;

% Fuel Cell Model
    % Calculate States 6 and 13 from 5 and 12.
    % Heat transfer model: reaction enthalpy, heat transfer through stack
    % Fixed Fuel Utilization

T_CAT_in_12 = T_c(12,i);
T_AND_in_5 = T_c(5,i);
CP_CAT_in_12 = CP_c(12,i);
CP_AND_in_5 = CP_c(5,i);
C_CAT_in_12 = C_c(12,:,i);
C_AND_in_5 = C_c(5,:,i);
m_CAT_in_12 = m_c(12,i);
m_AND_in_5 = m_c(5,i);

T_CAT_out_13old = T_c(13,i);
T_AND_out_6old = T_c(6,i);
CP_CAT_out_13old = CP_c(13,i);
CP_AND_out_6old = CP_c(6,i);
C_CAT_out_13old = C_c(13,:,i);
C_AND_out_6old = C_c(6,:,i);
m_CAT_out_13old = m_c(13,i);
m_AND_out_6old = m_c(6,i);

MM_CH4 = 16.04;     % kg/kmol
MM_H2O = 18.01;     % kg/kmol
MM_CO2 = 44.01;     % kg/kmol
MM_N2 = 14.0;       % kg/kmol
MM_O2 = 15.99;      % kg/kmol
MM_H2 = 2.016;      % kg/kmol

m_x_CAT_in = m_CAT_in_12 * C_CAT_in_12;
n_CAT_in_CH4 = m_x_CAT_in(1) / MM_CH4;
n_CAT_in_CO2 = m_x_CAT_in(2) / MM_CO2;
n_CAT_in_N2 = m_x_CAT_in(3) / MM_N2;
n_CAT_in_O2 = m_x_CAT_in(4) / MM_O2;
n_CAT_in_H2 = m_x_CAT_in(5) / MM_H2;
n_CAT_in_H2O = m_x_CAT_in(6) / MM_H2O;
n_CAT_in_tot = n_CAT_in_CH4 + n_CAT_in_CO2 + n_CAT_in_N2 + n_CAT_in_O2 +
 n_CAT_in_H2 + n_CAT_in_H2O;
y_CAT_in_O2 = n_CAT_in_O2 / n_CAT_in_tot;

m_x_AND_in = m_AND_in_5 * C_AND_in_5;
n_AND_in_CH4 = m_x_AND_in(1) / MM_CH4;
n_AND_in_CO2 = m_x_AND_in(2) / MM_CO2;
n_AND_in_N2 = m_x_AND_in(3) / MM_N2;
n_AND_in_O2 = m_x_AND_in(4) / MM_O2;
n_AND_in_H2 = m_x_AND_in(5) / MM_H2;
n_AND_in_H2O = m_x_AND_in(6) / MM_H2O;
```

```
n_AND_in_tot = n_AND_in_CH4 + n_AND_in_CO2 + n_AND_in_N2 + n_AND_in_O2 +
 n_AND_in_H2 + n_AND_in_H2O;
y_AND_in_H2 = n_AND_in_H2 / n_AND_in_tot;

% Internal Anode Reformation
n_AND_REF = n_AND_in_CH4 * 1;     % Assume complete internal reformation
n_AND_REF_react = min( n_AND_REF, n_AND_in_H2O / 2);
n_AND_REF_CH4 = n_AND_in_CH4 - n_AND_REF_react;
n_AND_REF_CO2 = n_AND_in_CO2 + n_AND_REF_react;
n_AND_REF_H2 = n_AND_in_H2 + 4 * n_AND_REF_react;
n_AND_REF_H2O = n_AND_in_H2O - 2 * n_AND_REF_react;

Q_AND_REF_react = n_AND_REF_react * -165e3;   % kW

% Anode Side Reaction
% eta_fuel_utl = 0.85;

n_AND_H2_react = eta_fuel_utl * n_AND_REF_H2;
n_O_ion_trans = n_AND_H2_react;

n_AND_H2O_form = n_AND_H2_react;
n_AND_electrons = 2 * n_AND_H2_react;

n_AND_out_H2 = n_AND_REF_H2 - n_AND_H2_react;
n_AND_out_H2O = n_AND_REF_H2O + n_AND_H2O_form;

m_x_AND_out_H2 = n_AND_out_H2 * MM_H2;
m_x_AND_out_H2O = n_AND_out_H2O * MM_H2O;
m_x_AND_out_CH4 = n_AND_REF_CH4 * MM_CH4;
m_x_AND_out_CO2 = n_AND_REF_CO2 * MM_CO2;
m_x_AND_out_O2 = n_AND_in_O2 * MM_O2;
m_x_AND_out_N2 = n_AND_in_N2 * MM_N2;

m_AND_out = sum([m_x_AND_out_CH4 m_x_AND_out_CO2 m_x_AND_out_N2 m_x_AND_out_O2
 m_x_AND_out_H2 m_x_AND_out_H2O]);
C_AND_out = [m_x_AND_out_CH4 m_x_AND_out_CO2 m_x_AND_out_N2 m_x_AND_out_O2
 m_x_AND_out_H2 m_x_AND_out_H2O] / m_AND_out;

m_c(6,i+1) = m_AND_out;
C_c(6,:,i+1) = C_AND_out;

% Cathode Side Reaction
n_CAT_out_O2 = n_CAT_in_O2 - 0.5 * n_O_ion_trans;
n_CAT_out_CH4 = n_CAT_in_CH4;
n_CAT_out_CO2 = n_CAT_in_CO2;
n_CAT_out_N2 = n_CAT_in_N2;
n_CAT_out_H2 = n_CAT_in_H2;
n_CAT_out_H2O = n_CAT_in_H2O;

eta_oxidant = (n_CAT_in_O2 - n_CAT_out_O2) / n_CAT_in_O2;

m_x_CAT_out_CH4 = n_CAT_out_CH4 * MM_CH4;
m_x_CAT_out_CO2 = n_CAT_out_CO2 * MM_CO2;
m_x_CAT_out_N2 = n_CAT_out_N2 * MM_N2;
```

```
m_x_CAT_out_O2 = n_CAT_out_O2 * MM_O2;
m_x_CAT_out_H2 = n_CAT_out_H2 * MM_H2;
m_x_CAT_out_H2O = n_CAT_out_H2O * MM_H2O;

m_CAT_out = sum([m_x_CAT_out_CH4 m_x_CAT_out_CO2 m_x_CAT_out_N2 m_x_CAT_out_O2
 m_x_CAT_out_H2 m_x_CAT_out_H2O]);
C_CAT_out = [m_x_CAT_out_CH4 m_x_CAT_out_CO2 m_x_CAT_out_N2 m_x_CAT_out_O2
 m_x_CAT_out_H2 m_x_CAT_out_H2O] / m_CAT_out;

m_c(13,i+1) = m_CAT_out;
C_c(13,:,i+1) = C_CAT_out;

% Electrochemistry
F = 96485.3e3;  % C/kmol
F_mol = F / 1e3;    %C/mol
R = 8.314;              % kJ/kmol-K
A_FC = n_AND_electrons * F; % [kmol/s]*[C/kmol] = C/s = A
% E_thermo = 1.0;      % V
E_0 = 1.23;            % V
dS = -147;          % kJ/kmol - K
T_FC = T_AND_out_6old + 273.15;
E_t = E_0 + dS * (T_FC - T_amb)/(8*F_mol);

P_cat = 1;              % atm
P_and = 1;              % atm
P_cat_Pa = 101325 * P_cat;
P_and_Pa = 101324 * P_and;

x_H2_FC_bar = (C_AND_in_5(5) + C_AND_out(5))/2;
x_O2_FC_bar = (C_CAT_in_12(4) + C_CAT_out(4))/2;
x_H2O_FC_bar = (C_AND_in_5(6) + C_AND_out(6))/2;

prod_React = (x_H2_FC_bar*P_and_Pa) * (x_O2_FC_bar * P_cat_Pa)^(0.5);
prod_Prod = x_H2O_FC_bar * P_and_Pa;

E_thermo = E_t - (R*T_FC/(2*F))*log(prod_Prod/prod_React);

% D_eff_H2O_H2 = 1e-4;    % m^2/s
D_eff_O2_N2 = 2e-5;     % m^2/s
alpha_SOFC = 0.5;
j_0 = 0.1;              % A/cm^2
A_SOFC = 9e7;           % K/ohm-m
dG_act = 100e3;           % kJ/mol
t_M = 8e-6;               % um
% t_AND = 50e-6;             % um
t_CAT = 50e-6;            % um

gamma_tune = 1;         % Tuning variable to get V =0.8 @ j = 0.3;
j = A_FC / 800000;
eta_ohmic = gamma_tune * j * (1e4) * (t_M * T_FC) / (A_SOFC * exp(-dG_act / (R
 * T_FC)));
% eta_CAT = ((R * T_FC) / (4 * alpha_SOFC * F)) * log( j / (j_0 * P_cat *
 (y_CAT_in_O2 - t_CAT * ((j * 1e4 * R * T_FC ) / (4 * F * P_cat * 101325 *
 D_eff_O2_N2)))));
```

```
p1 = (4 * F_mol * P_cat * 101325 * D_eff_O2_N2);
p2 = (y_CAT_in_O2 - t_CAT * ((j * 1e4 * R * T_FC ) / p1));
p3 = (j_0 * P_cat * p2);
eta_CAT = ((R * T_FC) / (4 * alpha_SOFC * F_mol)) * log( j / p3);

V_FC = E_thermo - eta_ohmic - eta_CAT;
%V_FC = 0.82;
P_FC = A_FC * V_FC / 1000;  % kW

% Thermochemistry
LHV_H2 = 120.0e3;   % kJ/kg
LHV_CH4 = 50.0e3;   % kJ/kg
E_gen_react = n_AND_H2_react * MM_H2 * LHV_H2;
Q_gen_react = E_gen_react - P_FC;
E_CH4 = m_c(1,i) * LHV_CH4;
eta_FC = P_FC / E_CH4;

% Heat Transfer Model for Stack
%Q_lost = (Q_gen_react + Q_AND_REF_react) * 0.2;
% Q_lost = ((T_AND_out_6old + T_CAT_out_13old)/2 - T_amb)/145; %Heat transfer
 out based on constant insulation resistance and thermal gradient
Q_lost = 0.1 * Q_gen_react;
Q_gen = Q_gen_react + Q_AND_REF_react - Q_lost;
% Assume that enough surface for temperature equilibrium between cathode
% and anode outlet
T_FC_out = (T_AND_in_5 * m_AND_in_5 * CP_AND_in_5 + T_CAT_in_12 * m_CAT_in_12
 * CP_CAT_in_12 + Q_gen) / (m_AND_in_5 * CP_AND_in_5 + m_CAT_in_12 *
 CP_CAT_in_12);
% Q_gen_AND = Q_gen * (CP_AND_out_6old * m_AND_out / (CP_AND_out_6old *
 m_AND_out + CP_CAT_out_13old * m_CAT_out));
Q_AND = (T_FC_out - T_AND_in_5) * m_AND_in_5 * (CP_AND_in_5 +
 CP_AND_out_6old)/2;
Q_CAT = (T_FC_out - T_CAT_in_12) * m_CAT_in_12 * (CP_CAT_in_12 +
 CP_CAT_out_13old)/2;

% T_CAT_out_13 = T_CAT_in_12 + Q_CAT / (m_CAT_out * CP_CAT_in_12);
% T_AND_out_6 = T_AND_in_5 + Q_AND / (m_AND_out * CP_AND_in_5);

T_CAT_out_13 = T_FC_out;
T_AND_out_6 = T_FC_out;
T_c(13,i+1) = T_CAT_out_13;
T_c(6,i+1) = T_AND_out_6;

% Air Cooled Water Dropout
    % Calculate State 9 from State 8
    % Assume fixed water drop out

T_AND_cool_out_8 = T_c(8,i);
m_AND_cool_out_8 = m_c(8,i) * (1 - x_recirc);
C_AND_cool_out_8 = C_c(8,:,i);
CP_AND_cool_out_8 = CP_c(8,i);

m_comb_in_9old = m_c(9,i);
```

```
CP_comb_in_9old = CP_c(9,i);

% eff_AND_cond = 0.45;
Q_AND_cond_max = m_comb_in_9old * CP_comb_in_9old * (T_AND_cool_out_8 -
 T_amb);
Q_AND_cond = Q_AND_cond_max * eff_AND_cond;

m_x_AND_cool_out_8 = m_AND_cool_out_8 * C_AND_cool_out_8;
m_x_AND_cool_CH4_8 = m_x_AND_cool_out_8(1);
m_x_AND_cool_CO2_8 = m_x_AND_cool_out_8(2);
m_x_AND_cool_N2_8 = m_x_AND_cool_out_8(3);
m_x_AND_cool_O2_8 = m_x_AND_cool_out_8(4);
m_x_AND_cool_H2_8 = m_x_AND_cool_out_8(5);
m_x_AND_cool_H2O_8 = m_x_AND_cool_out_8(6);

% eta_dropout = 0.4;
m_x_comb_in_H2O_9 = (1-eta_dropout) * m_x_AND_cool_H2O_8;

m_x_comb_in_CH4_9 = m_x_AND_cool_CH4_8;
m_x_comb_in_CO2_9 = m_x_AND_cool_CO2_8;
m_x_comb_in_N2_9 = m_x_AND_cool_N2_8;
m_x_comb_in_O2_9 = m_x_AND_cool_O2_8;
m_x_comb_in_H2_9 = m_x_AND_cool_H2_8;

m_comb_in_9 =
 sum([m_x_comb_in_CH4_9,m_x_comb_in_CO2_9,m_x_comb_in_N2_9,m_x_comb_in_O2_9,m_x_comb_in_H2
C_comb_in_9 =
 [m_x_comb_in_CH4_9,m_x_comb_in_CO2_9,m_x_comb_in_N2_9,m_x_comb_in_O2_9,m_x_comb_in_H2_9,m
 m_comb_in_9;
T_comb_in_9 = T_AND_cool_out_8 - Q_AND_cond / (CP_AND_cool_out_8 *
 m_AND_cool_out_8);

T_c(9,i+1) = T_comb_in_9;
m_c(9,i+1) = m_comb_in_9;
C_c(9,:,i+1) = C_comb_in_9;

    % MM_CH4 = 16.04;     % kg/kmol
    % MM_H2O = 18.01;     % kg/kmol
    % MM_CO2 = 44.01;     % kg/kmol
    % MM_N2 = 14.0;       % kg/kmol
    % MM_O2 = 15.99;      % kg/kmol
    % MM_H2 = 2.016;      % kg/kmol
    %
    % m_x_AND_cool_out_8 = m_AND_cool_out_8 * C_AND_cool_out_8;
    % n_x_cool_8_CH4 = m_x_AND_cool_out_8(1) / MM_CH4;
    % n_x_cool_8_CO2 = m_x_AND_cool_out_8(1) / MM_CO2;
    % n_x_cool_8_N2 = m_x_AND_cool_out_8(1) / MM_N2;
    % n_x_cool_8_O2 = m_x_AND_cool_out_8(1) / MM_O2;
    % n_x_cool_8_H2 = m_x_AND_cool_out_8(1) / MM_H2;
    % n_x_cool_8_H2O = m_x_AND_cool_out_8(1) / MM_H2O;
    %
    % y_H2O_cool_8 = n_x_cool_8_H2O / (n_x_cool_8_CH4 + n_x_cool_8_CO2 +
 n_x_cool_8_N2 + n_x_cool_8_O2 + n_x_cool_8_H2);
    % y_air_cool_8 = 1 - y_H2O_cool_8;
```

```
    %
    % p_v_cool_8 = y_H2O_cool_8 * 101.325;    % kPa
    % p_vsat_cool_8 = 0.6108 * exp(17.27 * T_AND_cool_out_8 /
 (T_AND_cool_out_8 + 273.3));
    %
    % rh_cool_8 = p_v_cool_8 / p_vsat_cool_8;
    % b_cool_8 = log(p_v_cool_8 / 0.6108) / 17.27;
    % T_d_AND_cool_8 = 237.3 * (b_cool_8 / (1 - b_cool_8));

% Combustor
    % Calculate State 16 from 9 and 15
    % Assume complete combustion

T_comb_in_9old = T_c(9,i);
C_comb_in_9old = C_c(9,:,i);
m_comb_in_9old = m_c(9,i);
CP_comb_in_9old = CP_c(9,i);

T_comb_ox_in_15 = T_c(15,i);
C_comb_ox_in_15 = C_c(15,:,i);
m_comb_ox_in_15 = m_c(15,i);
CP_comb_ox_in_15 = CP_c(15,i);

MM_CH4 = 16.04;     % kg/kmol
MM_H2O = 18.01;     % kg/kmol
MM_CO2 = 44.01;     % kg/kmol
MM_N2 = 14.0;       % kg/kmol
MM_O2 = 15.99;      % kg/kmol
MM_H2 = 2.016;      % kg/kmol

m_x_comb_in_9old = m_comb_in_9old * C_comb_in_9old;
n_x_comb_in_CH4_9old = m_x_comb_in_9old(1) / MM_CH4;
n_x_comb_in_CO2_9old = m_x_comb_in_9old(2) / MM_CO2;
n_x_comb_in_N2_9old = m_x_comb_in_9old(3) / MM_N2;
n_x_comb_in_O2_9old = m_x_comb_in_9old(4) / MM_O2;
n_x_comb_in_H2_9old = m_x_comb_in_9old(5) / MM_H2;
n_x_comb_in_H2O_9old = m_x_comb_in_9old(6) / MM_H2O;

m_x_comb_ox_in_15 = m_comb_ox_in_15 * C_comb_ox_in_15;
n_x_comb_ox_in_CH4_15 = m_x_comb_ox_in_15(1) / MM_CH4;
n_x_comb_ox_in_CO2_15 = m_x_comb_ox_in_15(2) / MM_CO2;
n_x_comb_ox_in_N2_15 = m_x_comb_ox_in_15(3) / MM_N2;
n_x_comb_ox_in_O2_15 = m_x_comb_ox_in_15(4) / MM_O2;
n_x_comb_ox_in_H2_15 = m_x_comb_ox_in_15(5) / MM_H2;
n_x_comb_ox_in_H2O_15 = m_x_comb_ox_in_15(6) / MM_H2O;

n_comb_react = min( (n_x_comb_in_CH4_9old + n_x_comb_in_H2_9old) ,
 (n_x_comb_ox_in_O2_15 + n_x_comb_in_O2_9old) / 2.5);
n_comb_react_CH4 = n_comb_react * (n_x_comb_in_CH4_9old /
 (n_x_comb_in_CH4_9old + n_x_comb_in_H2_9old));
n_comb_react_H2 = n_comb_react * (n_x_comb_in_H2_9old / (n_x_comb_in_CH4_9old
 + n_x_comb_in_H2_9old));
```

```
n_x_comb_out_CH4_16 = n_x_comb_in_CH4_9old + n_x_comb_ox_in_CH4_15 -
 n_comb_react_CH4;
n_x_comb_out_CO2_16 = n_x_comb_in_CO2_9old + n_x_comb_ox_in_CO2_15 +
 n_comb_react;
n_x_comb_out_N2_16 = n_x_comb_in_N2_9old + n_x_comb_ox_in_N2_15;
n_x_comb_out_O2_16 = n_x_comb_in_O2_9old + n_x_comb_ox_in_O2_15 - 2.5 *
 n_comb_react;
n_x_comb_out_H2_16 = n_x_comb_in_H2_9old + n_x_comb_ox_in_H2_15 -
 n_comb_react_H2;
n_x_comb_out_H2O_16 = n_x_comb_in_H2O_9old + n_x_comb_ox_in_H2O_15 + 3 *
 n_comb_react;

m_x_comb_out_16 = [n_x_comb_out_CH4_16 * MM_CH4, n_x_comb_out_CO2_16 * MM_CO2,
 n_x_comb_out_N2_16 * MM_N2, n_x_comb_out_O2_16 * MM_O2, n_x_comb_out_H2_16 *
 MM_H2, n_x_comb_out_H2O_16 * MM_H2O];
m_comb_out_16 = sum(m_x_comb_out_16);
C_comb_out_16 = m_x_comb_out_16 / m_comb_out_16;
m_c(16,i+1) = m_comb_out_16;
C_c(16,:,i+1) = C_comb_out_16;

LHV_CH4 = 50e3 * MM_CH4;    % kJ/kmol
LHV_H2 = 120e3 * MM_H2;     % kJ/kmol

Q_comb_react =  (LHV_CH4 * n_comb_react_CH4 + LHV_H2 * n_comb_react_H2);
% disp(Q_comb_react)
eta_Q_comb_lost = 0;

CP_comb_out_16old = CP_c(16,i);
H_comb_reacts = m_comb_in_9old * CP_comb_in_9old * T_comb_in_9old +
 m_comb_ox_in_15 * CP_comb_ox_in_15 * T_comb_ox_in_15;
H_comb_prods = H_comb_reacts + (1-eta_Q_comb_lost) * Q_comb_react;
T_comb_out_16 = H_comb_prods / (m_comb_out_16 * CP_comb_out_16old);
T_c(16,i+1) = T_comb_out_16;

% Combustor Products Mixer
    % Calculate State 17 from 14 and 16

T_mix_in_14old = T_c(14,i);
T_mix_in_16old = T_c(16,i);
C_mix_in_14old = C_c(14,:,i);
C_mix_in_16old = C_c(16,:,i);
m_mix_in_14old = m_c(14,i);
m_mix_in_16old = m_c(16,i);
CP_mix_in_14old = CP_c(14,i);
CP_mix_in_16old = CP_c(16,i);

m_x_mix_14old = m_mix_in_14old * C_mix_in_14old;
m_x_mix_16old = m_mix_in_16old * C_mix_in_16old;
m_x_mix_17 = m_x_mix_14old + m_x_mix_16old;
m_mix_17 = sum(m_x_mix_17);
C_mix_17 = m_x_mix_17 / m_mix_17;
m_c(17,i+1) = m_mix_17;
C_c(17,:,i+1) = C_mix_17;
```

```
CP_mix_out_17old = CP_c(17,i);
T_mix_17 = (T_mix_in_14old * CP_mix_in_14old * m_mix_in_14old + T_mix_in_16old
 * CP_mix_in_16old * m_mix_in_16old) / (m_mix_17 * CP_mix_out_17old);
T_c(17,i+1) = T_mix_17;

% Steam Generator
    % Calculate States 19 and 20 from 18 assuming liquid water inlet
    % Assume a fixed HX effectiveness

T_CAT_rec_18old = T_c(18,i);
T_H2O_liq = T_c(20,i);
CP_CAT_rec_18old = CP_c(18,i);
m_CAT_rec_18old = m_c(18,i);
m_H2O_liq_20 = m_c(20,i);
CP_H2O_gas_21 = CP_c(21,i);

% eff_STM_gen = 0.45;
Q_MAX_STM_gen = m_CAT_rec_18old * CP_CAT_rec_18old * (T_CAT_rec_18old -
 T_H2O_liq);
Q_STM_gen = eff_STM_gen * Q_MAX_STM_gen;

CP_H2O_liq = 4;     % kJ/kg-K
T_H2O_vap = 100;
h_fg_H2O = 2256;    % kJ/kg - Enthalpy of evaporation

m_STM_gen_21 = Q_STM_gen / (CP_H2O_liq*(T_H2O_vap - T_H2O_liq) + h_fg_H2O); %
 Calculate steam generated using enthalpy of evaporation

if m_STM_gen_21 < m_H2O_liq_20
    m_c(21,i+1) = m_STM_gen_21;
    T_c(21,i+1) = 100;
else
    Q_STM_gen = (CP_H2O_liq*(T_H2O_vap - T_H2O_liq) + h_fg_H2O) *
 m_H2O_liq_20;
    m_c(21,i+1) = m_H2O_liq_20;
    T_c(21,i+1) = 100;
end

% if m_STM_gen_21 < m_H2O_liq_20
%     m_c(21,i+1) = m_STM_gen_21;
%     T_c(21,i+1) = 100;
% else
%     m_c(21,i+1) = m_H2O_liq_20;
%     Q_STM_sup = Q_STM_gen - (CP_H2O_liq*(T_H2O_vap - T_H2O_liq) + h_fg_H2O)
 * m_H2O_liq_20;
%     T_c(21,i+1) = 100 + 0.1*Q_STM_sup / (m_H2O_liq_20 * CP_H2O_gas_21);
% end

T_CAT_EXH_19 = T_CAT_rec_18old - Q_STM_gen / (m_CAT_rec_18old *
 CP_CAT_rec_18old);
T_c(19,i+1) = T_CAT_EXH_19;

% Mass Continuity
```

```
m_c(4,i+1) = m_c(3,i+1);
m_c(5,i+1) = m_c(4,i+1);
m_c(7,i+1) = m_c(6,i+1);
m_c(8,i+1) = m_c(7,i+1) * (1 - x_recirc);
m_c(11,i+1) = m_c(10,i+1);
m_c(12,i+1) = m_c(11,i+1);
m_c(14,i+1) = m_c(13,i+1);
m_c(18,i+1) = m_c(17,i+1);
m_c(19,i+1) = m_c(18,i+1);

C_c(4,:,i+1) = C_c(3,:,i+1);
C_c(7,:,i+1) = C_c(6,:,i+1);
C_c(8,:,i+1) = C_c(7,:,i+1);
C_c(11,:,i+1) = C_c(10,:,i+1);
C_c(12,:,i+1) = C_c(11,:,i+1);
C_c(14,:,i+1) = C_c(13,:,i+1);
C_c(18,:,i+1) = C_c(17,:,i+1);
C_c(19,:,i+1) = C_c(18,:,i+1);
C_c(21,:,i+1) = C_c(20,:,i+1);
```

Convergance Control

```
T_new = T_c(:,i+1);
C_new = C_c(:,:,i+1);
m_new = m_c(:,i+1);
T_old = T_c(:,i);
C_old = C_c(:,:,i);
m_old = m_c(:,i);

% Average of Old and New Values - linear interpolation
T_c(:,i+1) = (T_new + T_old) / 2;
C_c(:,:,i+1) = (C_new + C_old) / 2;
m_c(:,i+1) = (m_new + m_old) / 2;

% Max Temp Change Convergance Shutoff
dT = max(abs(T_new - T_old));
% dT_r(i) = dT;

% Evaluation of CP
    % Cp Array (Cp = [1] + [2]T + [3]T^2 ...) [kJ/kg-C]
CH4_CP_poly = [2.197 0.0023 4e-6 -3e-9];
CO2_CP_poly = [0.8179 0.001 -9e-7 3e-10];
N2_CP_poly = [1.0378 1e-5 4e-7 -2e-10];
O2_CP_poly = [0.9181 0.0002 2e-7 -2e-10];
H2_CP_poly = [14.145 0.0059 -3e-5 7e-8 -6e-11 2e-14];
H2O_CP_poly = [1.8611 0.0003 7e-7 4e-10];

CP_CH4 = CH4_CP_poly(1) + CH4_CP_poly(2)*T_c(:,i+1) + CH4_CP_poly(3)*T_c(:,i
+1).^2 + CH4_CP_poly(4)*T_c(:,i+1).^3;
CP_CO2 = CO2_CP_poly(1) + CO2_CP_poly(2)*T_c(:,i+1) + CO2_CP_poly(3)*T_c(:,i
+1).^2 + CO2_CP_poly(4)*T_c(:,i+1).^3;
CP_N2 = N2_CP_poly(1) + N2_CP_poly(2)*T_c(:,i+1) + N2_CP_poly(3)*T_c(:,i+1).^2
 + N2_CP_poly(4)*T_c(:,i+1).^3;
```

```
CP_O2 = O2_CP_poly(1) + O2_CP_poly(2)*T_c(:,i+1) + O2_CP_poly(3)*T_c(:,i+1).^2
 + O2_CP_poly(4)*T_c(:,i+1).^3;
CP_H2 = H2_CP_poly(1) + H2_CP_poly(2)*T_c(:,i+1) + H2_CP_poly(3)*T_c(:,i
+1).^2 + H2_CP_poly(4)*T_c(:,i+1).^3 + H2_CP_poly(5)*T_c(:,i+1).^4 +
 H2_CP_poly(6)*T_c(:,i+1).^5;
CP_H2O = H2O_CP_poly(1) + H2O_CP_poly(2)*T_c(:,i+1) + H2O_CP_poly(3)*T_c(:,i
+1).^2 + H2O_CP_poly(4)*T_c(:,i+1).^3;

    % Compile Array
    CP_c(:,i+1) = sum([CP_CH4 CP_CO2 CP_N2 CP_O2 CP_H2 CP_H2O].*C_c(:,:,i
+1),2);

 clear CP_CH4 CP_CO2 CP_N2 CP_O2 CP_H2 CP_H2O CH4_CP_poly CO2_CP_poly N2_CP_poly O2_CP_pol
```

Iterate

```
i=i+1;

end
%toc
```

Convergance Outputs

```
Temp_out = T_c(:,i);
Mass_out = m_c(:,i);
Conc_out = C_c(:,:,i);
CP_out = CP_c(:,i);
Q_out = [Q_AND_RECOUP, Q_SMR_react, Q_SMR_HX, Q_AND_cool, Q_CAT_rec,
 Q_AND_REF_react, Q_gen_react, Q_lost, Q_AND, Q_CAT, Q_AND_cond, Q_comb_react,
 Q_STM_gen];
% figure(2)
% subplot(2,1,1)
% plot(transpose(T_c(:,1:i)));
% subplot(2,1,2)
% plot(transpose(m_c(:,1:i)));


% Compile Outputs
Outputs.Temp_out = Temp_out;
Outputs.T_c = T_c;
Outputs.Mass_out = Mass_out;
Outputs.m_c = m_c;
Outputs.Conc_out = Conc_out;
Outputs.CP_out = CP_out;
Outputs.Q_out = Q_out;
Outputs.P_FC = P_FC;
Outputs.eta_ox = eta_oxidant;
Outputs.eta_FC = eta_FC;
Outputs.r_SC = n_SMR_in_H2O / n_SMR_in_CH4;
Outputs.V_FC = V_FC;
Outputs.j_FC = j;
Outputs.i = i;
Outputs.CO2 = Conc_out(19,2)*Mass_out(19)*(3600) / P_FC;
```

```
Outputs.j = j;
Outputs.eta_CAT = eta_CAT;
Outputs.eta_ohm = eta_ohmic;
Outputs.E_thermo = E_thermo;

% Total Fuel Utilization Calculation
C_2 = Conc_out(2,:);
m_2 = Mass_out(2);
m_x_2 = m_2 * C_2;

n_x_CH4_2 = m_x_2(1) / MM_CH4;
n_x_CO2_2 = m_x_2(2) / MM_CO2;
n_x_N2_2 = m_x_2(3) / MM_N2;
n_x_O2_2 = m_x_2(4) / MM_O2;
n_x_H2_2 = m_x_2(5) / MM_H2;
n_x_H2O_2 = m_x_2(6) / MM_H2O;
if n_x_H2O_2 >= 2*n_x_CH4_2
    n_H2eq_in = n_x_H2_2 + 4 * n_x_CH4_2;
else
    n_H2eq_in = n_x_H2_2 + 2 * n_x_H2O_2;
end
Outputs.eta_fuel_utl_loop = (n_H2eq_in - n_x_comb_in_H2_9old) / n_H2eq_in;

end
```

Published with MATLAB® R2021b

```
Inputs = export_Inputs;     % Requires BloomSOFCGui Export to
 Workspace

P_FC_goal = 210;
R_SC_goal = 2.5;

% dT_step = 25 * 0.104;      %deg C
% dF = 12.5 * 5.2e-4;    % utilization

dT_step = 0.18*8;       % degC
dF = 6.696e-4*8;        % utilization step

n = 24;    % MUST BE an EVEN NUMBER
[X,Y,n_tot] = Spiral(n);

% Prealocations
time = nan(1,n_tot+1);
r_SC_r = nan(1,n_tot+1);
T_exh_r = nan(1,n_tot+1);
m_exh_r = nan(1,n_tot+1);
cp_exh_r = nan(1,n_tot+1);
C_exh_r = nan(1,n_tot+1);
m_fuel_r = nan(1,n_tot+1);
m_air_r = nan(1,n_tot+1);
m_h2o_r = nan(1,n_tot+1);
P_FC_r = nan(1,n_tot+1);
T_FC_r = nan(1,n_tot+1);
eta_FC_r = nan(1,n_tot+1);
eta_fuel_utl_full_r = nan(1,n_tot+1);
eta_ox_utl_r = nan(1,n_tot+1);
V_fc_r = nan(1,n_tot+1);
dT_stack_an = nan(1,n_tot+1);
dT_stack_cat = nan(1,n_tot+1);
T_ox_r = nan(1,n_tot+1);
CO2_r = nan(1,n_tot+1);
Inputs_r = cell(1,n_tot+1);
Temp_out_r(1:n_tot+1) = {nan};
Mass_out_r(1:n_tot+1) = {nan};
i_out_r = nan(1,n_tot+1);
j_out_r = nan(1,n_tot+1);
Inputs_r(1:n_tot+1) = {nan};

T_array = Inputs.T_init(6);
F_array = Inputs.eta_fuel_utl;

for j = 1 : n_tot
    T_array(j+1) = T_array(j) + X(j) * dT_step;
    F_array(j+1) = F_array(j) + Y(j) * dF;
end

count = 0;
f = waitbar(count,'Points Completed','Name','Progress');
```

```
for i = 1:n_tot+1
    tic
    Inputs.eta_fuel_utl = F_array(i);
    dP = 100;
while abs(dP) >0.1
    dR = 100;
        while abs(dR) >0.1
            [Outputs] = BloomServerModel_v4func(Inputs);
            R_SC = Outputs.r_SC;
            dR = R_SC - R_SC_goal;
            dM_H2O = -dR / 1000;
            if ~isnan(dM_H2O)
                Inputs.m_H2O_in = Inputs.m_H2O_in + dM_H2O;
            else
                dR = 0;
            end
            if
 ~or(any(isnan(Outputs.Temp_out)),any(isnan(Outputs.Mass_out)))
                Inputs.T_init = Outputs.Temp_out;
                Inputs.m_init = Outputs.Mass_out;
                Inputs.C_init = Outputs.Conc_out;
                Inputs.CP_init = Outputs.CP_out;
            end
            fprintf('R_SC Error: %d \n',dR)
        end
    P_FC = Outputs.P_FC;
    dP = P_FC - P_FC_goal;
    dM_NG = -dP / 20000;
    if ~isnan(dM_NG)
        Inputs.m_NG_in = Inputs.m_NG_in + dM_NG;
    else
        dP = 0;
    end
    if ~or(any(isnan(Outputs.Temp_out)),any(isnan(Outputs.Mass_out)))
        Inputs.T_init = Outputs.Temp_out;
        Inputs.m_init = Outputs.Mass_out;
        Inputs.C_init = Outputs.Conc_out;
        Inputs.CP_init = Outputs.CP_out;
    end
    fprintf('P_FC Error: %d \n',dP)
end

dT = 100;
while abs(dT)>(dT_step/20)
    [Outputs] = BloomServerModel_v4func(Inputs);
    T_FC = Outputs.Temp_out(13);
    dT = T_FC - T_array(i);
    dM_air = dT / 500;
    if ~isnan(dM_air)
        Inputs.m_AIR_in = Inputs.m_AIR_in + dM_air;
    else
        dT = 0;
    end
```

```
        if ~or(any(isnan(Outputs.Temp_out)),any(isnan(Outputs.Mass_out)))
            Inputs.T_init = Outputs.Temp_out;
            Inputs.m_init = Outputs.Mass_out;
            Inputs.C_init = Outputs.Conc_out;
            Inputs.CP_init = Outputs.CP_out;
        end
        fprintf('T_FC Error: %d \n',dT)
    end

    % Catalog Outputs for Memory
    r_SC_r(i) = Outputs.r_SC;
    T_exh_r(i) = Outputs.Temp_out(19);
    m_exh_r(i) = Outputs.Mass_out(19);
    cp_exh_r(i) = Outputs.CP_out(19);
    C_exh_r(i) = Outputs.Conc_out(19,2);
    m_fuel_r(i) = Outputs.Mass_out(1);
    m_air_r(i) = Outputs.Mass_out(10);
    m_h2o_r(i) = Outputs.Mass_out(20);
    T_FC_r(i) = Outputs.Temp_out(6);
    P_FC_r(i) = Outputs.P_FC;
    eta_FC_r(i) = Outputs.eta_FC;
    eta_fuel_utl_full_r(i) = Outputs.eta_fuel_utl_loop;
    eta_ox_utl_r(i) = Outputs.eta_ox;
    V_fc_r(i) = Outputs.V_FC;
    dT_stack_an(i) = Outputs.Temp_out(6) - Outputs.Temp_out(5);
    dT_stack_cat(i) = Outputs.Temp_out(13) - Outputs.Temp_out(12);
    T_ox_r(i) = Outputs.Temp_out(16);
    CO2_r(i) = Outputs.CO2;
    Temp_out_r{i} = Outputs.Temp_out;
    Mass_out_r{i} = Outputs.Mass_out;
    i_out_r(i) = Outputs.i;
    j_out_r(i) = Outputs.j;
    Inputs_r{i} = Inputs;
    % Update Progress Bar with Estimated Completion Time
    time(i) = toc;
    completion = i / (n_tot+1);
    time_tot = mean(time,'omitnan')*(n_tot - i);
    time_tot_hr = floor(time_tot/3600);
    time_tot_min = floor((time_tot - time_tot_hr*3600)/60);
    waitbar(completion,f,['Estimated Time Remaining:
     ',num2str(time_tot_hr),' hr ',num2str(time_tot_min),' min'])
    % Inputs = original_inputs;

    end
    close(f)

    % Process output vectors into arrays based on Temperature and
     Utilization
    export_Inputs = Inputs;
    export_Outputs = Outputs;
    Data.T_array = DataSpiralWinder(T_array,n,n_tot,X,Y);
    Data.F_array = DataSpiralWinder(F_array,n,n_tot,X,Y);
    Data.r_SC = DataSpiralWinder(r_SC_r,n,n_tot,X,Y);
    Data.T_exh = DataSpiralWinder(T_exh_r,n,n_tot,X,Y);
```

```
Data.m_exh = DataSpiralWinder(m_exh_r,n,n_tot,X,Y);
Data.cp_exh = DataSpiralWinder(cp_exh_r,n,n_tot,X,Y);
Data.C_exh = DataSpiralWinder(C_exh_r,n,n_tot,X,Y);
Data.m_fuel = DataSpiralWinder(m_fuel_r,n,n_tot,X,Y);
Data.m_air = DataSpiralWinder(m_air_r,n,n_tot,X,Y);
Data.m_h2o = DataSpiralWinder(m_h2o_r,n,n_tot,X,Y);
Data.P_FC = DataSpiralWinder(P_FC_r,n,n_tot,X,Y);
Data.T_FC = DataSpiralWinder(T_FC_r,n,n_tot,X,Y);
Data.eta_FC = DataSpiralWinder(eta_FC_r,n,n_tot,X,Y);
Data.eta_fuel_utl_full =
 DataSpiralWinder(eta_fuel_utl_full_r,n,n_tot,X,Y);
Data.eta_ox_utl = DataSpiralWinder(eta_ox_utl_r,n,n_tot,X,Y);
Data.V_FC = DataSpiralWinder(V_fc_r,n,n_tot,X,Y);
Data.dT_stack_an = DataSpiralWinder(dT_stack_an,n,n_tot,X,Y);
Data.dT_stack_cat = DataSpiralWinder(dT_stack_cat,n,n_tot,X,Y);
Data.T_ox = DataSpiralWinder(T_ox_r,n,n_tot,X,Y);
Data.CO2 = DataSpiralWinder(CO2_r,n,n_tot,X,Y);
Data.i_out = DataSpiralWinder(i_out_r,n,n_tot,X,Y);
Data.j_out = DataSpiralWinder(j_out_r,n,n_tot,X,Y);
Data.Inputs = DataSpiralWinder_cellmod(Inputs_r,n,n_tot,X,Y);
Data.Temp_out = DataSpiralWinder_cellmod(Temp_out_r,n,n_tot,X,Y);
Data.Mass_out = DataSpiralWinder_cellmod(Mass_out_r,n,n_tot,X,Y);

% Contour Plot of Data
X_g = Data.eta_fuel_utl_full;
Y_g = Data.T_array;

[M,c] = contourf(X_g,Y_g,Data.j_out);
c.LineWidth = 1;
c.ShowText = 'on';
ax = gca;
ax.FontSize = 12;

cb = colorbar;
cb.Label.String = 'Current Density';
cb.FontSize = 12;
cy = ylabel('Stack Temperature [C]');
cx = xlabel('Fuel Utilization [-]');

cx.FontWeight = 'Bold';
cx.FontSize = 14;
cy.FontWeight = 'Bold';
cy.FontSize = 14;
```

Published with MATLAB® R2020b

```
% Post Processing CCHP SOFC 200 kW
% Alejandro Lavernia
% 1/25/2020

% Contour XY Values
Y_g = Data.T_FC;
X_g = Data.eta_fuel_utl_full;
% Useful waste heat
T_WHR_3 = 120:0.2:190;
COP_trip = -4.6659e-8 * T_WHR_3.^4 + 3.4054e-5*T_WHR_3.^3 - 9.3451e-3
 * T_WHR_3.^2 + 1.1429e0 * T_WHR_3 - 50.708; % From Triple model
T_WHR_2 = 95:0.2:155;
COP_doub = -3.5661e-8 * T_WHR_2.^4 + 1.9609e-5*T_WHR_2.^3 - 4.0619e-3
 * T_WHR_2.^2 + 3.7584e-1* T_WHR_2 - 11.685; % From Double model
T_WHR_1 = 50:0.2:110;
COP_sing = -2.0016e-8 * T_WHR_1.^4 + 7.4031e-6* T_WHR_1.^3 - 1.0373e-3
 * T_WHR_1.^2 + 6.5326e-2 * T_WHR_1 - 7.6154e-1; % from Single Model

% Select Type of Chiller
% chiller_type = 2;
if chiller_type == 3
    T_WHR = T_WHR_3;
    COP = COP_trip;
    C_AC_cap = 1200;    %$/kW (Triple Effect)
elseif chiller_type == 2
    T_WHR = T_WHR_2;
    COP = COP_doub;
    C_AC_cap = 754;     %$/kW (Double Effect)
else
    T_WHR = T_WHR_1;
    COP = COP_sing;
    C_AC_cap = 584;
end
[rows,cols] = size(Data.T_exh);
for j = 1:cols
for i = 1:rows
Q_exh_array = Data.m_exh(i,j) .* Data.cp_exh(i,j) .* ( Data.T_exh(i,j)
 - T_WHR);
Q_chill_array = Q_exh_array .* COP;
[Q_chill(i,j),Q_chill_index] = max(Q_chill_array);
Q_exh(i,j) = Q_exh_array(Q_chill_index);
T_WHR_r(i,j) = T_WHR(Q_chill_index);
COP_r(i,j) = COP(Q_chill_index);
end
end
% Absorption Chiller
% COP_AC = 1.862;     % Triple Effect AC
% COP_AC = 1.4;       % Double Effect AC
%COP_AC = 0.8;       % Single Effect AC
%Q_chill = Q_exh * COP_AC;
Q_cool = Q_exh + Q_chill;
% Cost Inputs
```

```
C_SOFC_cap = 498.9; %$/kW
C_SOFC_OM = 6;      %$/MWh
C_NG = 0.45;        %$/therm
%C_AC_cap = 1200;    %$/kW (Triple Effect)
%C_AC_cap = 754;     %$/kW (Double Effect)
%C_AC_cap = 584;
C_AC_OM = 14;       %$/MWh
AC_oversize = 1.0;  %-
C_ctower_cap = 224.4;   %$/kW
C_ctower_OM = 7.2;  %$/MWh
Ctower_oversize = 1.25;

T_life = 20;

eta_elec_ref = 0.525;
COP_ref = 5;
eta_grid = 0.892;

% Cost Calculations
Cost_SOFC_cap = C_SOFC_cap * Data.P_FC;
Cost_AC_cap = C_AC_cap * Q_chill * AC_oversize;
Cost_ctower_cap = C_ctower_cap * Q_cool * Ctower_oversize;

E_SOFC = Data.P_FC * 365.25 * 24 /1000;    %MWh
NG_cons = (E_SOFC ./ (Data.eta_FC .* 2.9890e-04))/100; %therms
Cost_NG = NG_cons * C_NG;
Cost_SOFC_OM = E_SOFC * C_SOFC_OM;
E_AC = Q_chill * 365.25 * 24 / 1000;    %MWh
Cost_AC_OM = E_AC * C_AC_OM;
E_ctower = Q_cool * 365.25 * 24 / 1000; %MWh
Cost_ctower_OM = E_ctower * C_ctower_OM;

E_fuel = NG_cons * 27.75 / 1000;    % MWh

% Levelized Costs
LCOE =  (Cost_SOFC_cap + T_life .* (Cost_NG + Cost_SOFC_OM)) ./
 (T_life * E_SOFC);
LCOC = (Cost_AC_cap + Cost_ctower_cap + T_life .* (Cost_AC_OM +
 Cost_ctower_OM)) ./ (T_life * E_AC);
LCOU = (Cost_SOFC_cap + T_life .* (Cost_NG + Cost_SOFC_OM)
 + Cost_AC_cap + Cost_ctower_cap + T_life .* (Cost_SOFC_OM +
 Cost_ctower_OM)) ./ (T_life * (E_SOFC + 0.2* E_AC));
PES = 1 - E_fuel ./ (E_SOFC / (eta_elec_ref * eta_grid) + E_AC /
 COP_ref);

% Plots
plots = {Data.T_exh Data.m_exh Data.m_fuel Data.m_air Q_exh
 Q_chill Data.dT_stack_an Data.dT_stack_cat Data.eta_FC Data.V_FC
 Data.eta_ox_utl+0.08 Data.T_ox Data.CO2 LCOE LCOC PES LCOU T_WHR_r
 COP_r};
axes = ["Exhaust Temperature [degC]"; "Exhaust Mass Flow Rate
 [kg/s]"; "Fuel Mass Flow Rate [kg/s]"; "Air Mass Flow Rate [kg/
s]"; "Exhaust Capacity [kW]"; "Chilling Capacity [kW]"; "Temperature
 Rise in Anode [degC]"; "Temperature Rise in Cathode [degC]"; "Fuel
```

```
 Cell Efficiency"; "Stack Voltage [V]"; "Oxidant Utilization"; "Burner
 Temp [degC]"; "CO2 Production kg/kWh"; "Levelized Cost of Electricity
 [$/MWh]"; "Levelized Cost of Chilling [$/MWh]"; "Primary Energy
 Savings Ratio"; "Levelized Cost of Utility [$/MWh]"; "Desorber Temp
 [C]"; "Chiller COP"];

for n = 1:length(plots)
%     subplot(3,4,n)
    figure(n)
    [M,c] = contourf(X_g,Y_g,plots{n});
    c.LineWidth = 1;
    c.ShowText = 'on';
    ax = gca;
    ax.FontSize = 12;

    cb = colorbar;
    cb.Label.String = axes(n);
    cb.FontSize = 12;
    cy = ylabel('Stack Temperature [C]');
    cx = xlabel('Fuel Utilization [-]');

    cx.FontWeight = 'Bold';
    cx.FontSize = 14;
    cy.FontWeight = 'Bold';
    cy.FontSize = 14;
end
```

```
Unable to resolve the name Data.T_FC.

Error in CostPostAnalysis_v2 (line 6)
Y_g = Data.T_FC;
```

Published with MATLAB® R2020b

```
Bool.dT_an = Data.dT_stack_an < 70;
Bool.dT_cat = Data.dT_stack_cat < 80;
Bool.CO2 = Data.CO2 < 0.44;
i=1;


Q_bool = Q_chill;
Q_bool(~(Bool.dT_an & Bool.dT_cat & Bool.CO2)) = NaN;
Q_min = min(Q_bool(:));
Q_max = max(Q_bool(:));
dQ = (Q_max - Q_min) / 100;  %normally 100

for Q_goal = Q_min : dQ : Q_max
    Bool.chill = Q_chill >= Q_goal;
    Bool.master = Bool.dT_an & Bool.dT_cat & Bool.CO2 & Bool.chill;

    CO2_min = Data.CO2;
    CO2_min(~Bool.master) = NaN;

%     figure()
%     [M,c] = contourf(X_g,Y_g,CO2_min);
%     c.LineWidth = 1;
%     c.ShowText = 'on';
%     ax = gca;
%     ax.FontSize = 12;
%
%     cb = colorbar;
%     cb.Label.String = 'CO2 Emission Intensity [kg/kWh]';
%     cb.FontSize = 12;
%     cy = ylabel('Stack Temperature [C]');
%     cx = xlabel('Fuel Utilization [-]');
%
%     cx.FontWeight = 'Bold';
%     cx.FontSize = 14;
%     cy.FontWeight = 'Bold';
%     cy.FontSize = 14;
%     title(['Chilling Capacity: ',num2str(Q_goal),'kW'])
    [min_val,min_indx] = min(CO2_min(:));
    [row_min,col_min] = ind2sub(size(CO2_min),min_indx);
    Opt.row_max_r(i) = row_min;
    Opt.col_max_r(i) = col_min;
    Opt.Q_chill_goal(i) = Q_goal;
    Opt.Q_chill(i) = Q_chill(row_min,col_min);
    Opt.T_FC(i) = Data.T_array(row_min,col_min);
    Opt.eta_fuel(i) = Data.F_array(row_min,col_min);
    Opt.r_SC(i) = Data.r_SC(row_min,col_min);
    Opt.T_exh(i) = Data.T_exh(row_min,col_min);
    Opt.m_exh(i) = Data.m_exh(row_min,col_min);
    Opt.cp_exh(i) = Data.cp_exh(row_min,col_min);
    Opt.C_exh(i) = Data.C_exh(row_min,col_min);
    Opt.Q_exh(i) = Q_exh(row_min,col_min);
    Opt.m_fuel(i) = Data.m_fuel(row_min,col_min);
```

```
    Opt.m_air(i) = Data.m_air(row_min,col_min);
    Opt.m_h2o(i) = Data.m_h2o(row_min,col_min);
    Opt.P_FC(i) = Data.P_FC(row_min,col_min);
    Opt.eta_FC(i) = Data.eta_FC(row_min,col_min);
    Opt.eta_fuel_utl_full(i) =
 Data.eta_fuel_utl_full(row_min,col_min);
    Opt.eta_ox_utl(i) = Data.eta_ox_utl(row_min,col_min);
    Opt.V_FC(i) = Data.V_FC(row_min,col_min);
    Opt.dT_stack_an(i) = Data.dT_stack_an(row_min,col_min);
    Opt.dT_stack_cat(i) = Data.dT_stack_cat(row_min,col_min);
    Opt.T_cat_in(i) = Data.T_array(row_min,col_min) -
 Data.dT_stack_cat(row_min,col_min);
    Opt.T_ox(i) = Data.T_ox(row_min,col_min);
    Opt.CO2(i) = Data.CO2(row_min,col_min);
    Opt.Inputs{i} = Data.Inputs{row_min,col_min};
    Opt.LCOE(i) = LCOE(row_min,col_min);
    Opt.LCOC(i) = LCOC(row_min,col_min);
    Opt.LCOU(i) = LCOU(row_min,col_min);
    Opt.PES(i) = PES(row_min,col_min);
    Opt.T_des(i) = T_WHR_r(row_min,col_min);


    i=i+1;
end



% plots = {Opt.T_FC, Opt.eta_fuel_utl_full, Opt.eta_FC, Opt.T_exh,
 Opt.m_fuel, Opt.m_air, Opt.T_cat_in, Opt.m_h2o, Opt.CO2, Opt.PES,
 Opt.T_des};
% axes = ["Stack Temperature [degC]"; "Fuel Utilization [-]"; "Fuel
 Cell Efficiency [-]"; "Exhaust Temp [degC]"; "Fuel Mass Flow Rate
 [kg/s]"; "Air Mass Flow Rate [kg/s]"; "Cathode Inlet Temp [degC]";
 "Water Mass Flow Rate [kg/s]"; "Carbon Dioxide Production [kg/kWh]";
 "Primary Energy Savings Ratio [-]"; "Desorber Temp [C]"];
%
% for n = 1:length(plots)
%     figure(n)
%     plot(Opt.Q_chill,plots{n});
%     ax = gca;
%     ax.FontSize = 12;
%
%     cy = ylabel(axes(n));
%     cx = xlabel('Chilling Capacity Available [kW]');
%
%     cx.FontWeight = 'Bold';
%     cx.FontSize = 14;
%     cy.FontWeight = 'Bold';
%     cy.FontSize = 14;
% end
```

Unable to resolve the name Data.dT_stack_an.

Error in Result_Maximizer_v2 (line 1)

```
Bool.dT_an = Data.dT_stack_an < 70;
```

Published with MATLAB® R2020b

Load Applicator

```
% Calcualted Cooling Profile
Q_load.Texas.Load_200full = Q_load.Texas.r_max * 200;

Opt_profile = Opt;

% Use optimized data to provide optimal point for each hour
for i = 1:length(Q_load.Texas.Load_200full)
    Q_demand = Q_load.Texas.Load_200full(i);
    Q_int_bool = Opt_profile.Q_chill_goal >= Q_demand;
    Q_int = Opt_profile.Q_chill_goal;
    Q_int(~Q_int_bool) = NaN;
    [Q_int_min,Q_int_min_index] = min(Q_int);

    Profile.Q_abs(i) = Q_int(Q_int_min_index);
    Profile.T_FC(i) = Opt_profile.T_FC(Q_int_min_index);
    Profile.eta_fuel(i) = Opt_profile.eta_fuel(Q_int_min_index);
    Profile.r_SC(i) = Opt_profile.r_SC(Q_int_min_index);
    Profile.T_exh(i) = Opt_profile.T_exh(Q_int_min_index);
    Profile.m_exh(i) = Opt_profile.m_exh(Q_int_min_index);
    Profile.cp_exh(i) = Opt_profile.cp_exh(Q_int_min_index);
    Profile.C_exh(i) = Opt_profile.C_exh(Q_int_min_index);
    Profile.m_fuel(i) = Opt_profile.m_fuel(Q_int_min_index);
    Profile.m_air(i) = Opt_profile.m_air(Q_int_min_index);
    Profile.m_h2o(i) = Opt_profile.m_h2o(Q_int_min_index);
    Profile.P_FC(i) = Opt_profile.P_FC(Q_int_min_index);
    Profile.eta_FC(i) = Opt_profile.eta_FC(Q_int_min_index);
    Profile.eta_fuel_utl_full(i) =
 Opt_profile.eta_fuel_utl_full(Q_int_min_index);
    Profile.eta_ox_utl(i) = Opt_profile.eta_ox_utl(Q_int_min_index);
    Profile.V_FC(i) = Opt_profile.V_FC(Q_int_min_index);
    Profile.dT_stack_an(i) = Opt_profile.dT_stack_an(Q_int_min_index);
    Profile.dT_stack_cat(i) =
 Opt_profile.dT_stack_cat(Q_int_min_index);
    Profile.T_cat_in(i) = Opt_profile.T_FC(Q_int_min_index) -
 Opt_profile.dT_stack_cat(Q_int_min_index);
    Profile.T_ox(i) = Opt_profile.T_ox(Q_int_min_index);
    Profile.CO2(i) = Opt_profile.CO2(Q_int_min_index);
    Profile.Inputs{i} = Opt_profile.Inputs{Q_int_min_index};
    Profile.LCOE(i) = Opt_profile.LCOE(Q_int_min_index);
    Profile.LCOC(i) = Opt_profile.LCOC(Q_int_min_index);
    Profile.LCOU(i) = Opt_profile.LCOU(Q_int_min_index);
    Profile.PES(i) = Opt_profile.PES(Q_int_min_index);
end

plots = {Q_load.Texas.Load_200full, Profile.T_FC,
 Profile.eta_fuel_utl_full, Profile.eta_FC, Profile.T_exh,
 Profile.m_fuel, Profile.m_air, Profile.T_cat_in, Profile.m_h2o,
 Profile.CO2, Profile.PES};
axes = ["Cooling Demand [kW]"; "Stack Temperature [degC]"; "Fuel
 Utilization [-]"; "Fuel Cell Efficiency [-]"; "Exhaust Temp
```

```
 [degC]"; "Fuel Mass Flow Rate [kg/s]"; "Air Mass Flow Rate [kg/
s]"; "Cathode Inlet Temp [degC]"; "Water Mass Flow Rate [kg/
s]"; "Carbon Dioxide Production [kg/kWh]"; "Primary Energy Savings
 Ratio [-]"];

for n = 1:length(plots)
%     figure(n);
    figure('Renderer', 'painters', 'Position', [10 10 1910 510])
    plot(plots{n});
    ax = gca;
    ax.FontSize = 12;

    cy = ylabel(axes(n));
    cx = xlabel('Hour');

    cx.FontWeight = 'Bold';
    cx.FontSize = 14;
    cy.FontWeight = 'Bold';
    cy.FontSize = 14;
end
```

Published with MATLAB® R2020b

Load Applicator

```
% Calcualted Cooling Profile
Q_load.Texas.Load_200full = Q_load.Texas.r_max * 200;
dE = 100;
E_storage_max = 1e4;    % Initial guess of storage capacity (kWh)
t = 1:8760;
eta_loss = 0.000;
eta_turnoff = 0.98;
Q_loss = 15;

% while dE > 1
E_storage = nan(1,8761);
% E_storage(1) = 0;
E_storage(1) = E_storage_max;
E_dstorage = nan(1,8760);
Opt_profile = Opt_1;
% Use optimized data to provide optimal point for each hour
for i = t
    Q_demand = Q_load.Texas.Load_200full(i);
    if (Q_demand + Q_loss) < max(Opt_profile.Q_chill)     % see if
 chiller capacity can cover demand
        Q_int_bool = Opt_profile.Q_chill_goal >= Q_demand;
        Q_int = Opt_profile.Q_chill_goal;
        Q_int(~Q_int_bool) = NaN;
        [Q_int_min,Q_int_min_index] = min(Q_int);
        if E_storage(i) < E_storage_max     % check to see if storage
 is full
            E_dstorage(i) = Q_int_min - Q_demand - Q_loss;   %kWh
            E_storage(i+1) = E_storage(i) + E_dstorage(i); % update
 state of storage
        else
            if (Q_int_min-Q_demand)>Q_loss
                E_dstorage(i) = 0;
            else
                E_dstorage(i) = Q_int_min - Q_demand -Q_loss;
            end
            E_storage(i+1) = E_storage(i) + E_dstorage(i);
        end
    else                                    % if not, still use max
 capacity
        Q_int_min = max(Opt_profile.Q_chill_goal);
        Q_int_min_index = length(Opt_profile.Q_chill_goal);
        E_dstorage(i) = Q_int_min - Q_demand - Q_loss;   %kWh
        E_storage(i+1) = E_storage(i) + E_dstorage(i) ; % update state
 of storage
    end


    Profile.Q_abs(i) = Q_int(Q_int_min_index);
    Profile.T_FC(i) = Opt_profile.T_FC(Q_int_min_index);
    Profile.eta_fuel(i) = Opt_profile.eta_fuel(Q_int_min_index);
```

```
    Profile.r_SC(i) = Opt_profile.r_SC(Q_int_min_index);
    Profile.T_exh(i) = Opt_profile.T_exh(Q_int_min_index);
    Profile.m_exh(i) = Opt_profile.m_exh(Q_int_min_index);
    Profile.cp_exh(i) = Opt_profile.cp_exh(Q_int_min_index);
    Profile.C_exh(i) = Opt_profile.C_exh(Q_int_min_index);
    Profile.m_fuel(i) = Opt_profile.m_fuel(Q_int_min_index);
    Profile.m_air(i) = Opt_profile.m_air(Q_int_min_index);
    Profile.m_h2o(i) = Opt_profile.m_h2o(Q_int_min_index);
    Profile.P_FC(i) = Opt_profile.P_FC(Q_int_min_index);
    Profile.eta_FC(i) = Opt_profile.eta_FC(Q_int_min_index);
    Profile.eta_fuel_utl_full(i) =
 Opt_profile.eta_fuel_utl_full(Q_int_min_index);
    Profile.eta_ox_utl(i) = Opt_profile.eta_ox_utl(Q_int_min_index);
    Profile.V_FC(i) = Opt_profile.V_FC(Q_int_min_index);
    Profile.dT_stack_an(i) = Opt_profile.dT_stack_an(Q_int_min_index);
    Profile.dT_stack_cat(i) =
 Opt_profile.dT_stack_cat(Q_int_min_index);
    Profile.T_cat_in(i) = Opt_profile.T_FC(Q_int_min_index) -
 Opt_profile.dT_stack_cat(Q_int_min_index);
    Profile.T_ox(i) = Opt_profile.T_ox(Q_int_min_index);
    Profile.CO2(i) = Opt_profile.CO2(Q_int_min_index);
    Profile.Inputs{i} = Opt_profile.Inputs{Q_int_min_index};
    Profile.LCOE(i) = Opt_profile.LCOE(Q_int_min_index);
    Profile.LCOC(i) = Opt_profile.LCOC(Q_int_min_index);
    Profile.LCOU(i) = Opt_profile.LCOU(Q_int_min_index);
    Profile.PES(i) = Opt_profile.PES(Q_int_min_index);
end

% dE = E_storage(8761)
% E_storage_max = E_storage_max - dE/2
% end


% figure(1)
figure('Renderer', 'painters', 'Position', [10 10 1910 1080])
% subplot(2,1,1)
plot(E_storage)
title('Storage Energy')
xlabel('Hour in Year')
ylabel('State of Charge (kWh)')
xlim([1,8760])

J_storage = E_storage*3600;
dT_storage = J_storage / (4.2*5e5);  % Assume storage is 500,000 kg
T_storage = 28 - dT_storage;

figure('Renderer', 'painters', 'Position', [10 10 1910 1080])
plot(T_storage)
xlabel('Hour in Year')
ylabel('Storage Temperature [degC]')
xlim([1,8760])


figure('Renderer', 'painters', 'Position', [10 10 1910 1080])
```

```
subplot(2,1,1)
plot(E_dstorage)
title('Storage Rate')
xlabel('Hour')
ylabel('Rate of Charge (kW)')
xlim([1,8760])
subplot(2,1,2)
plot(E_dstorage(1,5000:5168))
xlabel('Hour in Week')
ylabel('Rate of Charge (kW)')
xlim([1,168])

% % figure(3)
% figure('Renderer', 'painters', 'Position', [10 10 1910 1080])
% subplot(2,1,1)
% plot(Q_load.Texas.Load_200full)
% title('Texas Data Center Cooling Demand')
% xlabel('Hour')
% ylabel('Cooling Demand (kW)')
% xlim([1,8760])
% subplot(2,1,2)
% plot(Q_load.Texas.Load_200full(1,5000:5168))
% xlabel('Hour in Week')
% ylabel('Cooling Demand (kW)')
% xlim([1,168])

plots = {Q_load.Texas.Load_200full, Profile.T_FC,
 Profile.eta_fuel_utl_full, Profile.eta_FC, Profile.T_exh,
 Profile.m_fuel, Profile.m_air, Profile.T_cat_in, Profile.m_h2o,
 Profile.CO2, Profile.PES};
axes = ["Cooling Demand [kW]"; "Stack Temperature [degC]"; "Fuel
 Utilization [-]"; "Fuel Cell Efficiency [-]"; "Exhaust Temp
 [degC]"; "Fuel Mass Flow Rate [kg/s]"; "Air Mass Flow Rate [kg/
s]"; "Cathode Inlet Temp [degC]"; "Water Mass Flow Rate [kg/
s]"; "Carbon Dioxide Production [kg/kWh]"; "Primary Energy Savings
 Ratio [-]"];

for n = 1:length(plots)
%     figure(n);
    figure('Renderer', 'painters', 'Position', [10 10 1910 510])
    plot(plots{n});
    ax = gca;
    ax.FontSize = 12;

    cy = ylabel(axes(n));
    cx = xlabel('Hour');

    cx.FontWeight = 'Bold';
    cx.FontSize = 14;
    cy.FontWeight = 'Bold';
    cy.FontSize = 14;
end
```

Published with MATLAB® R2020b

Effect Comparison

February 8, 2022

```
chiller_type = 3;
CostPostAnalysis_v2
close all
Result_Maximizer_v2
Opt_3 = Opt;
Q_chill_3 = Q_chill;
close all
CoolingLoadOptApplicator
Profile_3 = Profile;
close all

chiller_type = 2;
CostPostAnalysis_v2
close all
Result_Maximizer_v2
Opt_2 = Opt;
Q_chill_2 = Q_chill;
close all
CoolingLoadOptApplicator
Profile_2 = Profile;
close all

chiller_type = 1;
CostPostAnalysis_v2
close all
Result_Maximizer_v2
Opt_1 = Opt;
Q_chill_1 = Q_chill;
close all
Thermal_Storage_Model_11_16
Profile_1 = Profile;
close all
```

Plots

```
plots_3 = {Opt_3.T_FC, Opt_3.eta_fuel_utl_full, Opt_3.eta_FC,
 Opt_3.T_exh, Opt_3.Q_exh, Opt_3.m_fuel, Opt_3.m_air, Opt_3.T_cat_in,
 Opt_3.m_h2o, Opt_3.CO2, Opt_3.PES, Opt_3.T_des};
plots_2 = {Opt_2.T_FC, Opt_2.eta_fuel_utl_full, Opt_2.eta_FC,
 Opt_2.T_exh, Opt_2.Q_exh, Opt_2.m_fuel, Opt_2.m_air, Opt_2.T_cat_in,
 Opt_2.m_h2o, Opt_2.CO2, Opt_2.PES, Opt_2.T_des};
plots_1 = {Opt_1.T_FC, Opt_1.eta_fuel_utl_full, Opt_1.eta_FC,
 Opt_1.T_exh, Opt_1.Q_exh, Opt_1.m_fuel, Opt_1.m_air, Opt_1.T_cat_in,
 Opt_1.m_h2o, Opt_1.CO2, Opt_1.PES, Opt_1.T_des};

profile_axes = ["Stack Temperature [degC]"; "Fuel Utilization
 [-]"; "Fuel Cell Efficiency [-]"; "Exhaust Temp [degC]"; "Waste Heat
 Recovered [kW]"; "Fuel Mass Flow Rate [kg/s]"; "Air Mass Flow Rate
```

```
 [kg/s]"; "Cathode Inlet Temp [degC]"; "Water Mass Flow Rate [kg/
s]"; "Carbon Dioxide Production [kg/kWh]"; "Primary Energy Savings
 Ratio [-]"; "Desorber Temp [C]"; 'Chilling Capactiy [kW]'];

for n = 1:length(plots_3)
    figure(n)
    plot(Opt_3.Q_chill,plots_3{n});
    hold on
    plot(Opt_2.Q_chill,plots_2{n});
    plot(Opt_1.Q_chill,plots_1{n});
    hold off
    ax = gca;
    ax.FontSize = 12;

    cy = ylabel(profile_axes(n));
    cx = xlabel('Chilling Capacity Available [kW]');

    cx.FontWeight = 'Bold';
    cx.FontSize = 14;
    cy.FontWeight = 'Bold';
    cy.FontSize = 14;

    legend('Triple Effect', 'Double Effect', 'Single Effect')
end

P_3 = mean(Profile_3.P_FC);
P_2 = mean(Profile_2.P_FC);
P_1 = mean(Profile_1.P_FC);
CO2_3 = mean(Profile_3.CO2);
CO2_2 = mean(Profile_2.CO2);
CO2_1 = mean(Profile_1.CO2);

E_P = [P_1;P_2;P_3] * 8760;
CO2_tot = E_P .*[CO2_1;CO2_2;CO2_3];


profile_plots_3 = {Profile_3.T_FC, Profile_3.eta_fuel_utl_full,
 Profile_3.eta_FC, Profile_3.T_exh, Profile_3.m_fuel, Profile_3.m_air,
 Profile_3.m_h2o, Profile_3.CO2, Profile_3.PES};
profile_plots_2 = {Profile_2.T_FC, Profile_2.eta_fuel_utl_full,
 Profile_2.eta_FC, Profile_2.T_exh, Profile_2.m_fuel, Profile_2.m_air,
 Profile_2.m_h2o, Profile_2.CO2, Profile_2.PES};
profile_plots_1 = {Profile_1.T_FC, Profile_1.eta_fuel_utl_full,
 Profile_1.eta_FC, Profile_1.T_exh, Profile_1.m_fuel, Profile_1.m_air,
 Profile_1.m_h2o, Profile_1.CO2, Profile_1.PES};

profile_axes = ["Stack Temperature [degC]"; "Fuel Utilization
 [-]"; "Fuel Cell Efficiency [-]"; "Exhaust Temp [degC]"; "Fuel Mass
 Flow Rate [kg/s]"; "Air Mass Flow Rate [kg/s]"; "Water Mass Flow
 Rate [kg/s]"; "Carbon Dioxide Production [kg/kWh]"; "Primary Energy
 Savings Ratio [-]"];

for n = 1:length(profile_plots_3)
```

```
    figure('Renderer', 'painters', 'Position', [10 10 1910 820])
    subplot(3,1,1)
    plot(profile_plots_3{n});
    set(gca, 'XTick', []);
    title('Triple Effect')
    subplot(3,1,2)
    plot(profile_plots_2{n});
    set(gca, 'XTick', []);
    title('Double Effect')
    subplot(3,1,3)
    plot(profile_plots_1{n});
    title('Single Effect')

    ax = gca;
    ax.FontSize = 16;

    cy = ylabel(profile_axes(n));
    cx = xlabel('Hour');

    cx.FontWeight = 'Bold';
    cx.FontSize = 18;
    cy.FontWeight = 'Bold';
    cy.FontSize = 18;
end
```

Published with MATLAB® R2020b

"Double Effect LiBr Absorption Cycle "

{Input Parameters}
m[1]=1. {kg/sec}
SI=2
cp=4.2 {J/g-K}
{Vapor quality inputs, fraction}
q[1]=0
q[4]=0
q[11]=0
q[14]=0
q[18]=0
q[8]=0
q[10]=1.0
{Heat transfer fluid flow rate inputs, kg/sec}
m[21]=8
m[25]=14
m[27]=20
m[23]=12
{Heat transfer fluid inlet temperatures, °C}
T[21]=140
T[25]=25
T[27]=5
T[23]=25
{Heat exchanger sizes (UA), kW/K}
UAd=25
UAc=65
UAe=80
UAa=50
UAcd=10.

{Start Model Equations}
{Set Pressure Levels}
Ph=pressure(WATER,T=T[18],x=q[18])
Pm=pressure(WATER,T=T[8],x=q[8])
Pl=pressure(WATER,T=T[10],x=q[10])

{Upper Generator}
x[14]=X_LIBR(T[14],Ph,SI)
m[13]=m[14]+m[17]
m[13]*x[13]=m[14]*x[14]
Qgenh=m[17]*h[17]+m[14]*h[14]-m[13]*h[13]
Qgenh=m[21]*cp*(T[21]-T[22])
UAd=Qgenh/Lmtdd
Lmtdd=((T[21]-T[14])-(T[22]-T[17]))/ln((T[21]-T[14])/(T[22]-T[17]))

{Solution Heat Exchangers}
Eff_HX=.5
Eff_HX=(T[4]-T[5])/(T[4]-T[2])
Qhxl=m[1]*(h[3]-h[2]) {energy balances}
Qhxl=m[4]*(h[4]-h[5])
Lmtds1=((T[4]-T[3])-(T[5]-T[2]))/ln((T[4]-T[3])/(T[5]-T[2]))
UAs1=Qhxl/Lmtds1

Eff_HX=(T[14]-T[15])/(T[14]-T[12])
Qhxl2=m[11]*(h[13]-h[12]) {energy balances}
Qhxl2=m[14]*(h[14]-h[15])
Lmtds2=((T[14]-T[13])-(T[15]-T[12]))/ln((T[14]-T[13])/(T[15]-T[12]))
UAs2=Qhxl2/Lmtds2

{Low Generator - High Condenser}
x[11]=x[3]
x[4]=x[16]
m[3]+m[16]=m[4]+m[11]+m[7] {overall mass balance}

```
m[3]*x[3]+m[16]*x[16]=m[4]*x[4]+m[11]*x[11] {LiBr balance}
T[11]=T[7]
h[3]*m[3]+m[16]*h[16]+m[17]*h[17]=h[4]*m[4]+h[11]*m[11]+m[18]*h[18]+m[7]*h[7]
Qcd=m[17]*(h[17]-h[18])
Lmtdcd=((T[18]-T[4])-(T[18]-T[7]))/ln((T[18]-T[4])/(T[18]-T[7]))
UAcd=Qcd/Lmtdcd

{Low Condenser}
m[8]=m[7]+m[19]
Qcond=m[7]*h[7]+m[19]*h[19]-m[8]*h[8]
Qcond=m[25]*cp*(T[26]-T[25])
UAc=Qcond/Lmtdc
Lmtdc=((T[8]-T[25])-(T[8]-T[26]))/ln((T[8]-T[25])/(T[8]-T[26]))

{Refrigerant Valves}
h[8]=h[9]
h[18]=h[19]

{Evaporator}
Qevap=m[9]*(h[10]-h[9])
Qevap=m[27]*cp*(T[27]-T[28])
UAe=Qevap/Lmtde
Lmtde=((T[27]-T[10])-(T[28]-T[9]))/ln((T[27]-T[10])/(T[28]-T[9]))

{Absorber}
m[10]*h[10]+h[6]*m[6]-Qabs-m[1]*h[1]=0
Qabs=m[23]*cp*(T[24]-T[23])
UAa=Qabs/Lmtda
Lmtda=((T[6]-T[24])-(T[1]-T[23]))/ln((T[6]-T[24])/(T[1]-T[23]))

{Solution expansion valve models}
h[6]=h[5]
h[16]=h[15]

{Pump calculation}
Pump1=m[1]*v1*(Pm-Pl)/1000    {kW}
h[2]=h[1]+Pump1/m[1]
Pump2=m[11]*v11*(Ph-Pm)/1000
h[12]=h[11]+Pump2/m[11]

{Compute COP}
COP=Qevap/Qgenh

{Trivial mass balances}
m[2]=m[1]
m[3]=m[2]
m[5]=m[4]
m[6]=m[5]
m[9]=m[8]
m[10]=m[9]
m[12]=m[11]
m[13]=m[12]
m[15]=m[14]
m[16]=m[15]
m[18]=m[17]
m[19]=m[18]

x[2]=X[1]
x[3]=x[2]
x[5]=x[4]
x[6]=x[5]
x[12]=X[11]
x[13]=x[12]
x[15]=x[14]
```

```
x[16]=x[15]

{Working fluid property relations}
h[1]=H_LIBR(T[1],X[1],SI)
x[1]=X_LIBR(T[1],Pl,SI)
v1= V_LIBR(T[1],x[1],SI)
h[2]=H_LIBR(T[2],x[2],SI)
h[3]=H_LIBR(T[3],x[3],SI)
h[4]=H_LIBR(T[4],x[4],SI)
T[4]=T_LIBR(Pm,x[4],SI)
h[5]=H_LIBR(T[5],x[5],SI)
CALL Q_LIBR(h[5],Pl,x[5],2:q[6]*100,T[6],Xl6,hl6,hv6)
T[7]=T_LIBR(Pm,x[3],SI)
h[7]=enthalpy(WATER,T=T[7],P=Pm)
h[8]=enthalpy(WATER,T=T[8],x=q[8])
T[9]=temperature(WATER,h=h[9],P=Pl)
q[9]=quality(WATER,h=h[9],T=T[9])
h[10]=enthalpy(WATER,T=T[10],x=q[10])
v11=V_LIBR(T[11],x[1],SI)
h[11]=H_LIBR(T[11],x[11],SI)
h[12]=H_LIBR(T[12],x[12],SI)
h[13]=H_LIBR(T[13],x[13],SI)
h[14]=H_LIBR(T[14],x[14],SI)
h[15]=H_LIBR(T[15],x[15],SI)
CALL Q_LIBR(h[15],Pm,x[15],2:q[16]*100,T[16],Xl16,hl16,hv16)
T[17]=T_LIBR(Ph,x[13],SI)
h[17]=enthalpy(WATER,T=T[17],P=Ph)
h[18]=enthalpy(WATER,T=T[18],x=q[18])
T[19]=temperature(WATER,h=h[19],P=Pm)
q[19]=quality(WATER,h=h[19],T=T[19])

{Set several parameters for output}
x[7]=0.
x[8]=0.
x[9]=0.
x[10]=0.
x[17]=0.
x[18]=0.
x[19]=0.

{Set pressures for output}
P[1]=Pl
P[2]=Pm
P[3]=Pm
P[4]=Pm
P[5]=Pm
P[6]=Pl
P[7]=Pm
P[8]=Pm
P[9]=Pl
P[10]=Pl
P[11]=Pm
P[12]=Ph
P[13]=Ph
P[14]=Ph
P[15]=Ph
P[16]=Pm
P[17]=Ph
P[18]=Ph
P[19]=Pm
```

SOLUTION

Unit Settings: SI C kPa kJ mass deg

COP = 1.358
cp = 4.200 [J/g-K]
Eff_{HX} = 0.500
hl16 = 200.593 [J/g]
hl6 = 143.029 [J/g]
hv16 = 2646.688 [J/g]
hv6 = 2593.109 [J/g]
Lmtda = 9.414 [K]
Lmtdc = 3.148 [K]
Lmtdcd = 20.942 [K]
Lmtdd = 11.455 [K]
Lmtde = 4.861 [K]
Lmtds1 = 25.764 [K]
Lmtds2 = 50.073 [K]
Ph = 66.042 [kPa]
Pl = 1.034 [kPa]
Pm = 4.296 [kPa]
Pump1 = 0.002 [kW]
Pump2 = 0.022 [kW]
Qabs = 470.698 [kW]
Qcd = 209.419 [kW]
Qcond = 204.605 [kW]
Qevap = 388.913 [kW]
Qgenh = 286.365 [kW]
Qhxl = 36.053 [kW]
Qhxl2 = 38.317 [kW]
SI = 2.000
UAa = 50.000 [kW/K]
UAc = 65.000 [kW/K]
UAcd = 10.000 [kW/K]
UAd = 25.000 [kW/K]
UAe = 80.000 [kW/K]
UAs1 = 1.399 [kW/K]
UAs2 = 0.765 [kW/K]
v1 = 0.654 [cm^3/g]
v11 = 0.659 [cm^3/g]
Xl16 = 62.452 [%]
Xl6 = 61.658 [%]

No unit problems were detected.

Arrays Table: Main

	h_i [J/g]	m_i [mixed]	P_i [kPa]	q_i [fraction]	T_i [°C]	X_i [%]
1	63.5	1.000	1.034	0.000	30.30	51.492
2	63.5	1.000	4.296		30.31	51.492
3	99.5	1.000	4.296		47.04	51.492
4	192.0	0.837	4.296	0.000	75.97	61.510
5	148.9	0.837	4.296		53.14	61.510
6	148.9	0.837	1.034	0.002	49.58	61.510
7	2604.4	0.074	4.296		55.75	0.000
8	126.6	0.163	4.296	0.000	30.20	0.000
9	126.6	0.163	1.034	0.038	7.46	0.000
10	2514.6	0.163	1.034	1.000	7.46	0.000
11	118.4	0.547	4.296	0.000	55.75	51.492
12	118.4	0.547	66.042		55.77	51.492
13	188.5	0.547	66.042		88.12	51.492
14	321.2	0.458	66.042	0.000	144.42	61.510
15	237.5	0.458	66.042		100.10	61.510
16	237.5	0.458	4.296	0.015	78.11	61.510
17	2722.1	0.089	66.042		121.01	0.000
18	370.3	0.089	66.042	0.000	88.41	0.000
19	370.3	0.089	4.296	0.100	30.20	0.000
20						
21		8.000			140.00	
22					141.48	
23		12.000			25.00	
24					34.34	
25		14.000			25.00	
26					28.48	
27		20.000			5.00	
28					10.37	

"Triple Effect Absorption Model"
"Alejandro Lavernia"

{Input Parameters}
Tgen=170
//Tc=Tevap+dT_cond
Tc=35
//dT_cond = 15
Tevap=15
//m[1]=1
Eff_HX=.5
DeltaT1=5
DeltaT2=5
SI=2

//Qe=200 [kW]
Qd3 = 100 [kW]

{Set some key states}
Pm=pressure(WATER,T=Tc,x=1)
x[24]=X_LIBR(Tgen,Ph2,SI)
Pl=pressure(WATER,T=Tevap,x=1)
X[1]=X_LIBR(Tc,Pl,SI)

{Solution Heat Exchangers}
m[2]=m[1]; m[2]=m[3] {overall mass balances}
m[4]=m[5]; m[5]=m[6]
x[2]=X[1]; x[2]=x[3] {LiBr balances}
x[4]=x[5]; x[5]=x[6]
Eff_HX=(T[4]-T[5])/(T[4]-T[2])
Qshx1=m[1]*(h[3]-h[2]) {energy balances}
Qshx1=m[4]*(h[4]-h[5])
h[3]=H_LIBR(T[3],x[3],SI) {Property relations}
h[5]=H_LIBR(T[5],x[5],SI); {finds T[5]}

m[12]=m[11]; m[12]=m[13] {overall mass balances}
m[14]=m[15]; m[15]=m[16]
x[12]=X[11];x[13]=x[12] {LiBr balances}
x[14]=x[15]; x[15]=x[16]
Eff_HX=(T[14]-T[15])/(T[14]-T[12])
Qshx2=m[11]*(h[13]-h[12]) {energy balances}
Qshx2=m[14]*(h[14]-h[15])
h[13]=H_LIBR(T[13],x[13],SI) {Property relations}
h[15]=H_LIBR(T[15],x[15],SI); {finds T[15]}

m[22]=m[21]; m[22]=m[23] {overall mass balances}
m[24]=m[25]; m[25]=m[26]
x[22]=X[21];x[23]=x[22] {LiBr balances}
x[24]=x[25]; x[25]=x[26]
Eff_HX=(T[24]-T[25])/(T[24]-T[22])
Qshx3=m[21]*(h[23]-h[22]) {energy balances}
Qshx3=m[24]*(h[24]-h[25])
h[23]=H_LIBR(T[23],x[23],SI) {Property relations}
h[25]=H_LIBR(T[25],x[25],SI); {finds T[25]}

{Generator G1 - Condenser C2}
m[3]+m[16]=m[4]+m[11]+m[7] {overall mass balance}
m[3]*x[3]+m[16]*x[16]=m[4]*x[4]+m[11]*x[11] {LiBr balance}
h[4]=H_LIBR(T[4],x[4],SI)
T[4]=T_LIBR(Pm,x[4],SI)
T[7]=T_LIBR(Pm,x[3],SI)

```
h[7]=enthalpy(WATER,T=T[7],P=Pm)  {superheated}
T[11]=T[7]
h[11]=H_LIBR(T[11],x[11],SI)
0=Qd1+h[3]*m[3]+m[16]*h[16]-h[4]*m[4]-h[11]*m[11]-m[7]*h[7]
Qc2=m[17]*h[17]-m[18]*h[18]+m[29]*h[29]
Qc2=Qd1
T[18]=T[4]+DeltaT1
h[18]=enthalpy(WATER,T=T[18],x=0)
x[11]=x[3];  x[4]=x[16]
T[17]=T_LIBR(Ph,x[13],SI)
h[17]=enthalpy(WATER,T=T[17],P=Ph)

{Generator G2 - Condenser C3}
m[13]+m[26]=m[14]+m[21]+m[17]  {overall mass balance}
m[13]*x[13]+m[26]*x[26]=m[14]*x[14]+m[21]*x[21] {LiBr balance}
h[14]=H_LIBR(T[14],x[14],SI)
T[14]=T_LIBR(Ph,x[14],SI)
T[21]=T[17]
h[21]=H_LIBR(T[21],x[21],SI)
0=Qd2+h[13]*m[13]+m[26]*h[26]-h[14]*m[14]-h[21]*m[21]-m[17]*h[17]
Qc3=m[27]*h[27]-m[28]*h[28]
Qc3=Qd2
T[28]=T[14]+DeltaT2
h[28]=enthalpy(WATER,T=T[28],x=0)
x[21]=x[13];  x[14]=x[26]
T[27]=T_LIBR(Ph2,x[23],SI)
h[27]=enthalpy(WATER,T=T[27],P=Ph2)


{Condenser C1}
m[8]=m[7]+m[19]; m[18]=m[17]+m[29]
T[8]=Tc
h[8]=enthalpy(WATER,T=T[8],x=0)
Qc1=m[7]*h[7]+m[19]*h[19]-m[8]*h[8]
m[27]=m[28]

{Valve}
m[8]=m[9]
h[8]=h[9]
T[9]=temperature(WATER,h=h[9],P=Pl)
q[9]=quality(WATER,h=h[9],P=Pl)

m[19]=m[18]
h[18]=h[19]
T[19]=temperature(WATER,h=h[19],P=Pm)
q[19]=quality(WATER,h=h[19],P=Pm)

m[29]=m[28]
h[29]=h[28]
T[29]=temperature(WATER,h=h[29],P=Ph)
q[29]=quality(WATER,h=h[29],P=Ph)

{Evaporator}
m[9]=m[10]
T[10]=Tevap
h[10]=enthalpy(WATER,T=T[10],x=1)
Qe=m[9]*(h[10]-h[9])

{Absorber}
m[10]*h[10]+h[6]*m[6]-Qabs-m[1]*h[1]=0
T[1]=Tc
h[1]=H_LIBR(T[1],X[1],SI)

COP=Qe/Qd3
```

```
{Solution expansion valve model}
CALL Q_LIBR(h[5],Pl,x[5],2:q[6]*100,T[6],Xl6,hl6,hv6)
h[6]=h[5]

CALL Q_LIBR(h[15],Pm,x[15],2:q[16]*100,T[16],Xl16,hl16,hv16)
h[16]=h[15]

CALL Q_LIBR(h[25],Pm,x[25],2:q[26]*100,T[26],Xl26,hl26,hv26)
h[26]=h[25]

{Pump calculation}
v1= V_LIBR(T[1],x[1],SI)
Pump1=m[1]*v1*(Pm-Pl)/1000    {kW}
h[2]=h[1]+Pump1/m[1]
h[2]=H_LIBR(T[2],x[2],SI)

v11=V_LIBR(T[11],x[1],SI)
Pump2=m[11]*v11*(Ph-Pm)/1000
h[12]=h[11]+Pump2/m[11]
h[12]=H_LIBR(T[12],x[12],SI)

v21=V_LIBR(T[21],x[21],SI)
Pump3=m[21]*v21*(Ph2-Ph)/1000
h[22]=h[21]+Pump3/m[21]
h[22]=H_LIBR(T[22],x[22],SI)

{Upper Generator}
T[24]=Tgen
m[23]=m[24]+m[27]
m[23]*x[23]=m[24]*x[24]
h[24]=H_LIBR(T[24],x[24],SI)
Qd3=m[27]*h[27]+m[24]*h[24]-m[23]*h[23]

Ph=pressure(WATER,T=T[18],x=0)
Ph2=pressure(WATER,T=t[28],x=0)

P[1]=Pl
P[2]=Pm
P[3]=Pm
P[4]=Pm
P[5]=Pm
P[6]=Pl
P[7]=Pm
P[8]=Pm
P[9]=Pl
P[10]=Pl

P[11]=Pm
P[12]=Ph
P[13]=Ph
P[14]=Ph
P[15]=Ph
P[16]=Pm
P[17]=Ph
P[18]=Ph
P[19]=Pm

P[21]=Ph
P[22]=Ph2
P[23]=Ph2
P[24]=Ph2
P[25]=Ph2
P[26]=Ph
```

P[27]=Ph2
P[28]=Ph2
P[29]=Ph

SOLUTION

Unit Settings: SI C kPa kJ mass deg

COP = 1.8576
δT1 = 5.000 [°C]
δT2 = 5.000 [°C]
Eff$_{HX}$ = 0.500
hl16 = 166.068 [J/g]
hl26 = 182.211 [J/g]
hl6 = 116.311 [J/g]
hv16 = 2635.194
hv26 = 2643.3 [J/g]
hv6 = 2590.471 [J/g]
Ph = 39.610 [kPa]
Ph2 = 211.939 [kPa]
Pl = 1.706 [kPa]
Pm = 5.629 [kPa]
Pump1 = 0.0016 [kW]
Pump2 = 0.0099 [kW]
Pump3 = 0.0301 [kW]
Qabs = 220.912 [kW]
Qc1 = 64.9 [kW]
Qc2 = 60.5 [kW]
Qc3 = 73.8 [kW]
Qd1 = 60.5 [kW]
Qd2 = 73.8 [kW]
Qd3 = 100.0 [kW]
Qe = 185.8 [kW]
Qshx1 = 19.2 [kW]
Qshx2 = 23.0 [kW]
Qshx3 = 15.3 [kW]
Sl = 2.000
Tc = 35.000 [°C]
Tevap = 15.000 [°C]
Tgen = 170.000 [°C]
v1 = 0.671 [cm^3/g]
v11 = 0.676 [cm^3/g]
v21 = 0.685 [cm^3/g]
Xl16 = 57.101 [%]
Xl26 = 59.141 [%]
Xl6 = 56.637 [%]

20 potential unit problems were detected.

Arrays Table: Main

	h_i [J/g]	m_i [kg/s]	P_i [kPa]	q_i [mixed]	T_i [C]	X_i [%]
1	70.0	0.609	1.71		35.0	49.21
2	70.0	0.609	5.63		35.0	49.21
3	101.6	0.609	5.63		49.3	49.21
4	161.1	0.531	5.63		70.6	56.44
5	125.0	0.531	5.63		52.8	56.44
6	125.0	0.531	1.71	0.0035	48.2	56.44
7	2606.8	0.023	5.63		57.2	
8	146.6	0.078	5.63		35.0	
9	146.6	0.078	1.71	0.0339	15.0	
10	2528.3	0.078	1.71		15.0	
11	119.1	0.433	5.63		57.2	49.21
12	119.2	0.433	39.61		57.2	49.21
13	172.3	0.433	39.61		81.1	49.21
14	255.6	0.378	39.61		117.1	56.44
15	194.7	0.378	39.61		87.1	56.44
16	194.7	0.378	5.63	0.0116	72.0	56.44
17	2688.3	0.023	39.61		102.3	
18	316.6	0.055	39.61		75.6	
19	316.6	0.055	5.63	0.0703	35.0	
20						
21	219.7	0.255	39.61		102.3	49.21
22	219.8	0.255	211.94		102.4	49.21
23	280.0	0.255	211.94		129.2	49.21
24	363.7	0.222	211.94		170.0	56.44
25	294.7	0.222	211.94		136.2	56.44
26	294.7	0.222	39.61	0.0457	76.3	56.44

Arrays Table: Main

	h_i [J/g]	m_i [kg/s]	P_i [kPa]	q_i [mixed]	T_i [C]	X_i [%]
27	2776.0	0.033	211.94		153.8	
28	512.5	0.033	211.94		122.1	
29	512.5	0.033	39.61	0.0845	75.6	

Parametric Table: T_high

	Tgen [°C]	m_1 [kg/s]	COP	Qe [kW]	T_{23} [C]
Run 1	200.000	*0.432*	*1.8582*	*185.8*	*142.3*
Run 2	196.552	*0.446*	*1.8606*	*186.1*	*140.9*
Run 3	193.103	*0.461*	*1.8627*	*186.3*	*139.4*
Run 4	189.655	*0.477*	*1.8642*	*186.4*	*137.9*
Run 5	186.207	*0.495*	*1.8652*	*186.5*	*136.4*
Run 6	182.759	*0.515*	*1.8655*	*186.5*	*134.9*
Run 7	179.310	*0.537*	*1.8649*	*186.5*	*133.4*
Run 8	175.862	*0.561*	*1.8633*	*186.3*	*131.9*
Run 9	172.414	*0.588*	*1.8605*	*186.0*	*130.3*
Run 10	168.966	*0.619*	*1.8561*	*185.6*	*128.7*
Run 11	165.517	*0.654*	*1.8499*	*185.0*	*127.1*
Run 12	162.069	*0.694*	*1.8412*	*184.1*	*125.5*
Run 13	158.621	*0.740*	*1.8296*	*183.0*	*123.8*
Run 14	155.172	*0.794*	*1.8141*	*181.4*	*122.2*
Run 15	151.724	*0.858*	*1.7936*	*179.4*	*120.5*
Run 16	148.276	*0.935*	*1.7665*	*176.7*	*118.8*
Run 17	144.828	*1.029*	*1.7304*	*173.0*	*117.0*
Run 18	141.379	*1.147*	*1.6816*	*168.2*	*115.3*
Run 19	137.931	*1.301*	*1.6139*	*161.4*	*113.5*
Run 20	134.483	*1.506*	*1.5178*	*151.8*	*111.7*
Run 21	131.034	*1.795*	*1.3743*	*137.4*	*109.8*
Run 22	127.586	*2.229*	*1.1450*	*114.5*	*107.9*
Run 23	124.138	*2.937*	*0.7384*	*73.8*	*106.0*
Run 24	120.690				
Run 25	117.241				
Run 26	113.793				
Run 27	110.345				
Run 28	106.897				
Run 29	103.448				
Run 30	100.000				

Parametric Table: Table 2

	dT_{cond} [C]	COP
Run 1	20	*1.8600*
Run 2	25	*1.6636*
Run 3	30	*1.2457*
Run 4	35	*73.8848*
Run 5	40	*3.2536*
Run 6	15	*2.0011*
Run 7	10	*2.1302*

Parametric Table: Table 2

	dT_{cond} [C]	COP
Run 8	5	*2.1302*

Parametric Table: Table 3

	Tc [°C]	COP
Run 1	50.000	
Run 2	48.621	
Run 3	47.241	
Run 4	45.862	
Run 5	44.483	
Run 6	43.103	
Run 7	41.724	
Run 8	40.345	
Run 9	38.966	
Run 10	37.586	*0.9152*
Run 11	36.207	*1.4248*
Run 12	34.828	*1.6824*
Run 13	33.448	*1.8407*
Run 14	32.069	*1.9517*
Run 15	30.690	*2.0352*
Run 16	29.310	*2.1025*
Run 17	27.931	*2.1597*
Run 18	26.552	*2.2096*
Run 19	25.172	*2.2546*
Run 20	23.793	*2.2962*
Run 21	22.414	*2.3349*
Run 22	21.034	*2.3702*
Run 23	19.655	
Run 24	18.276	
Run 25	16.897	
Run 26	15.517	
Run 27	14.138	
Run 28	12.759	
Run 29	11.379	
Run 30	10.000	

Appendix C – Unabridged Modeling Results

The following pages contain the full set of results generated by the integrated model described.

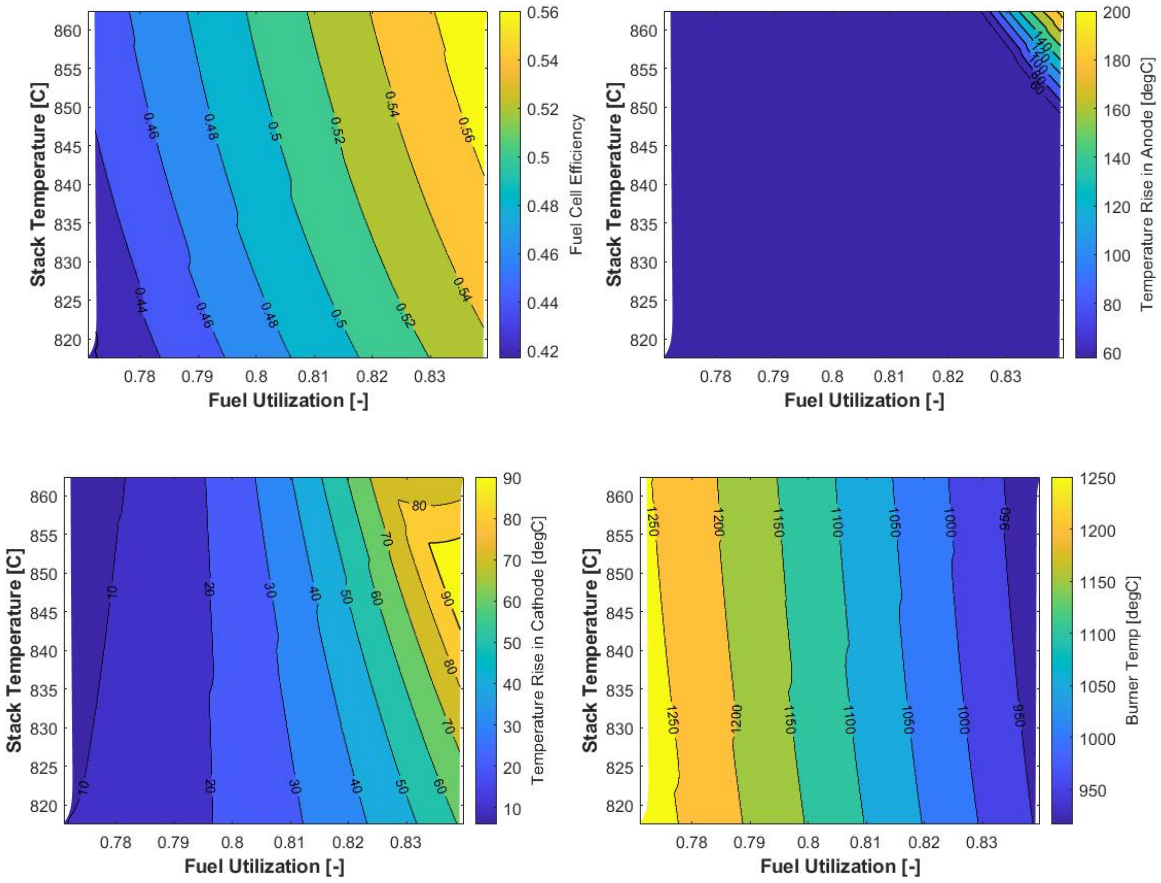

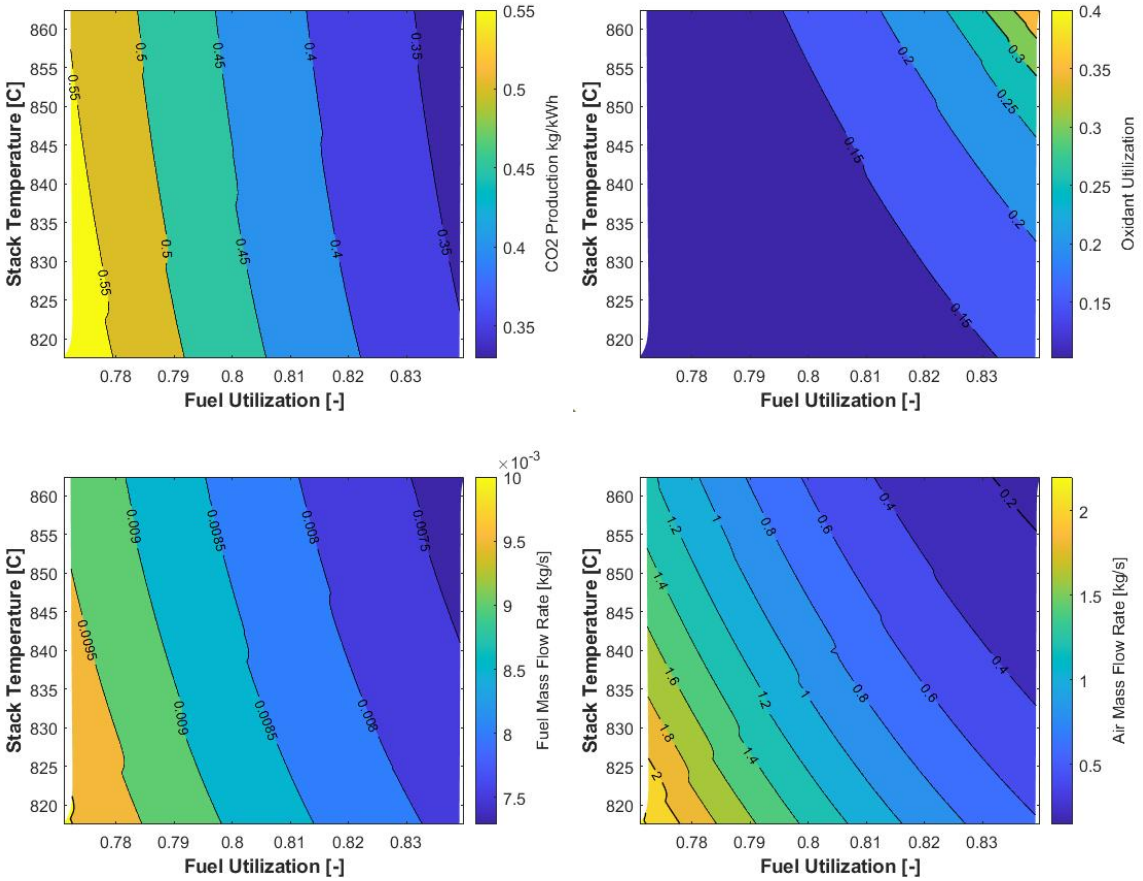
Stack Temperature [C]
Fuel Utilization [-]
CO2 Production kg/kWh
Oxidant Utilization
Fuel Mass Flow Rate [kg/s]
Air Mass Flow Rate [kg/s]
×10^-3

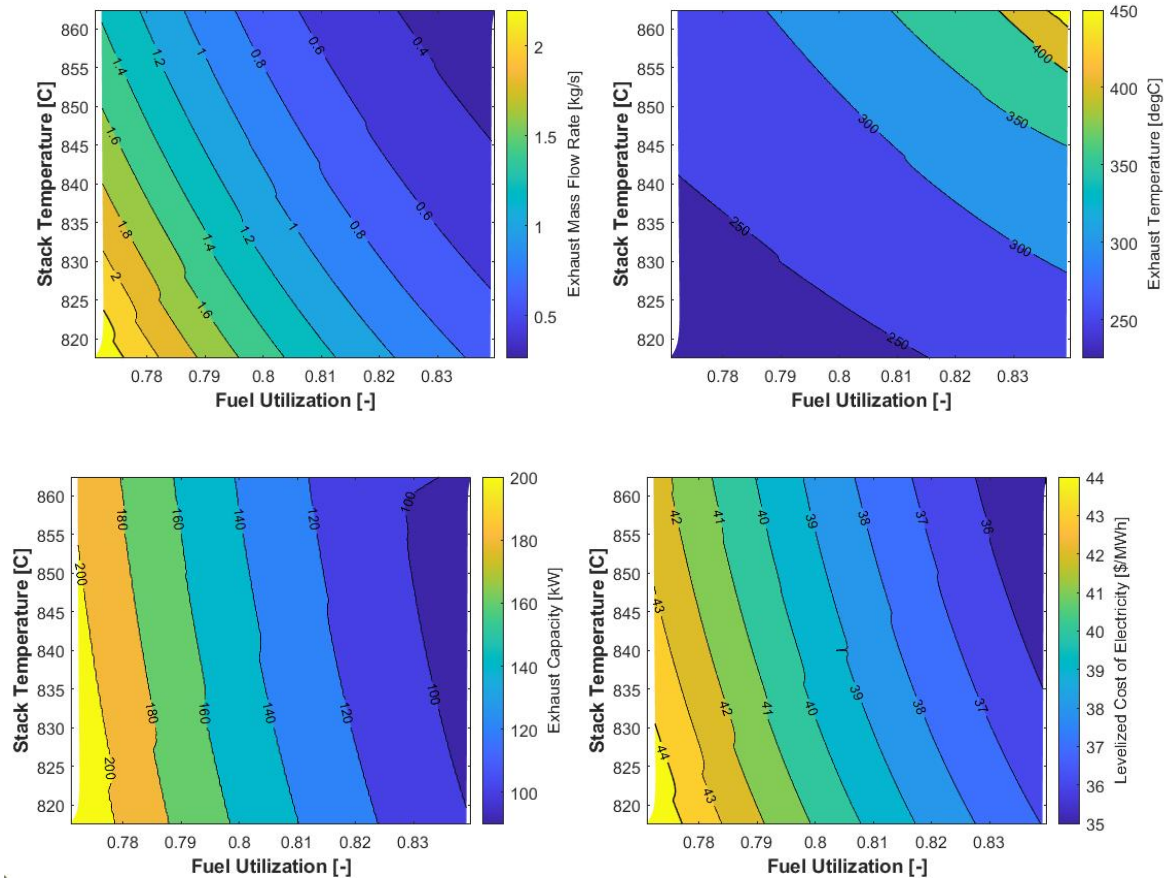
Stack Temperature [C]
Fuel Utilization [-]
Exhaust Mass Flow Rate [kg/s]
Exhaust Temperature [degC]
Exhaust Capacity [kW]
Levelized Cost of Electricity [$/MWh]

Triple Effect:

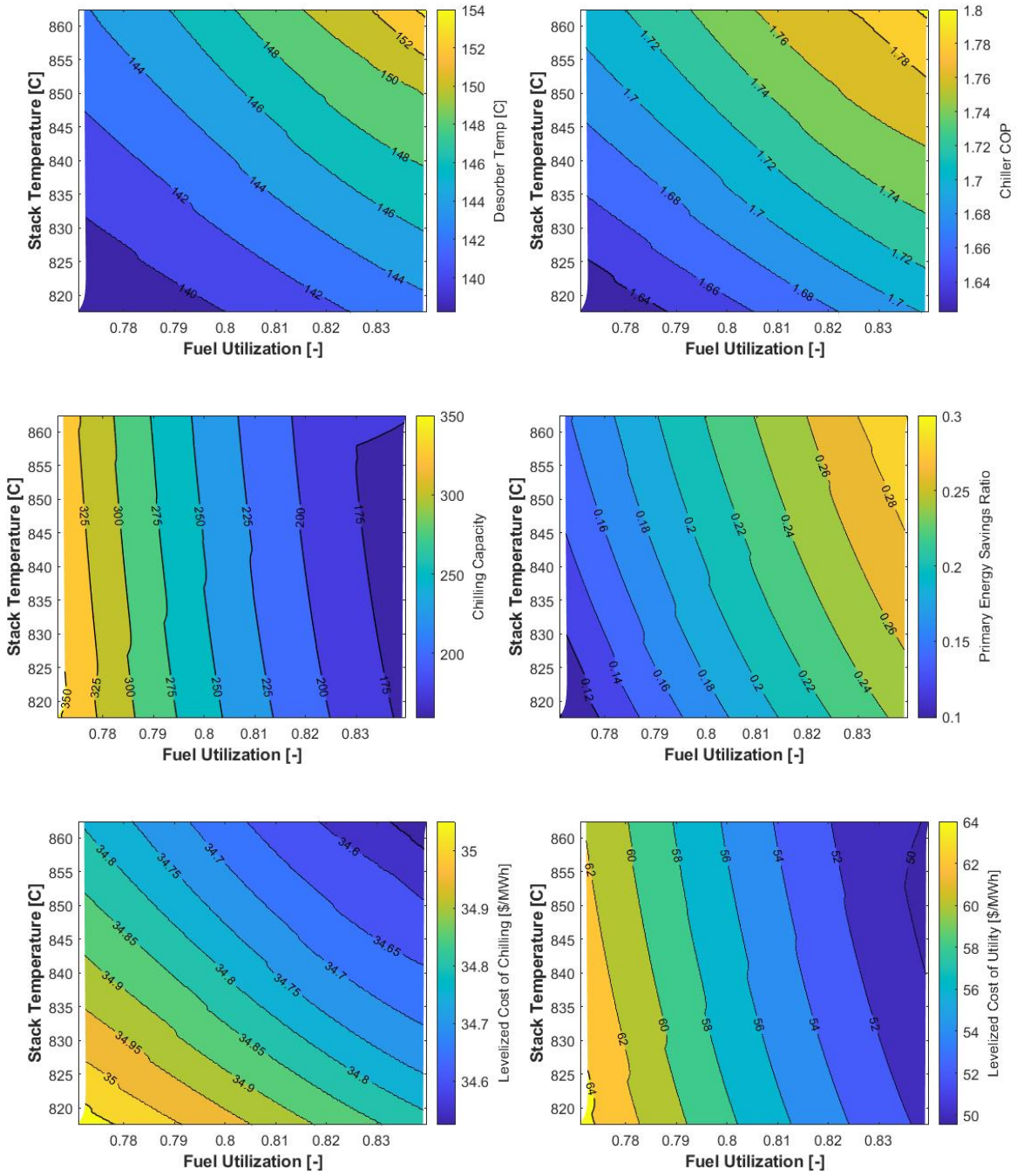

Double Effect:

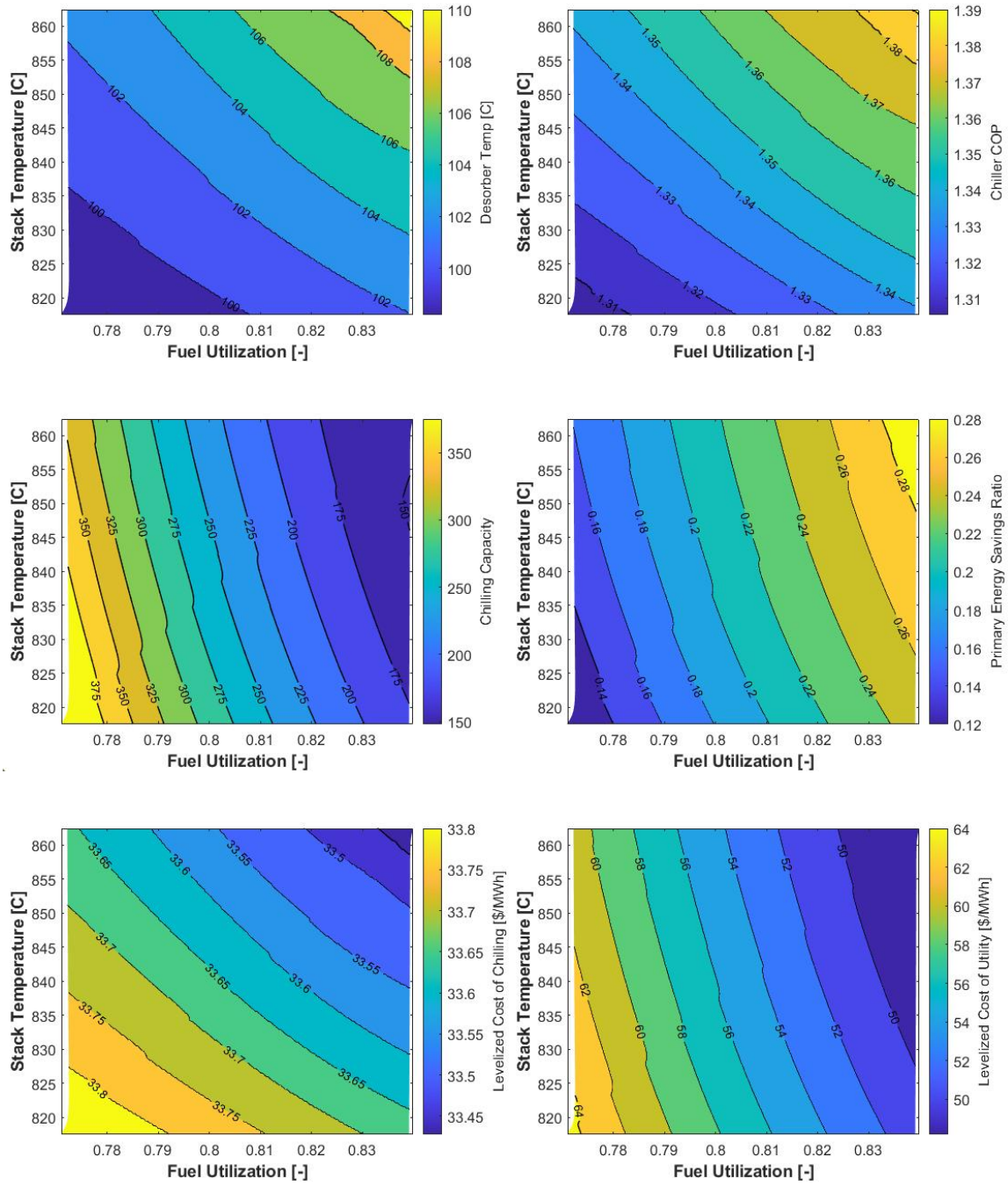

Single Effect:

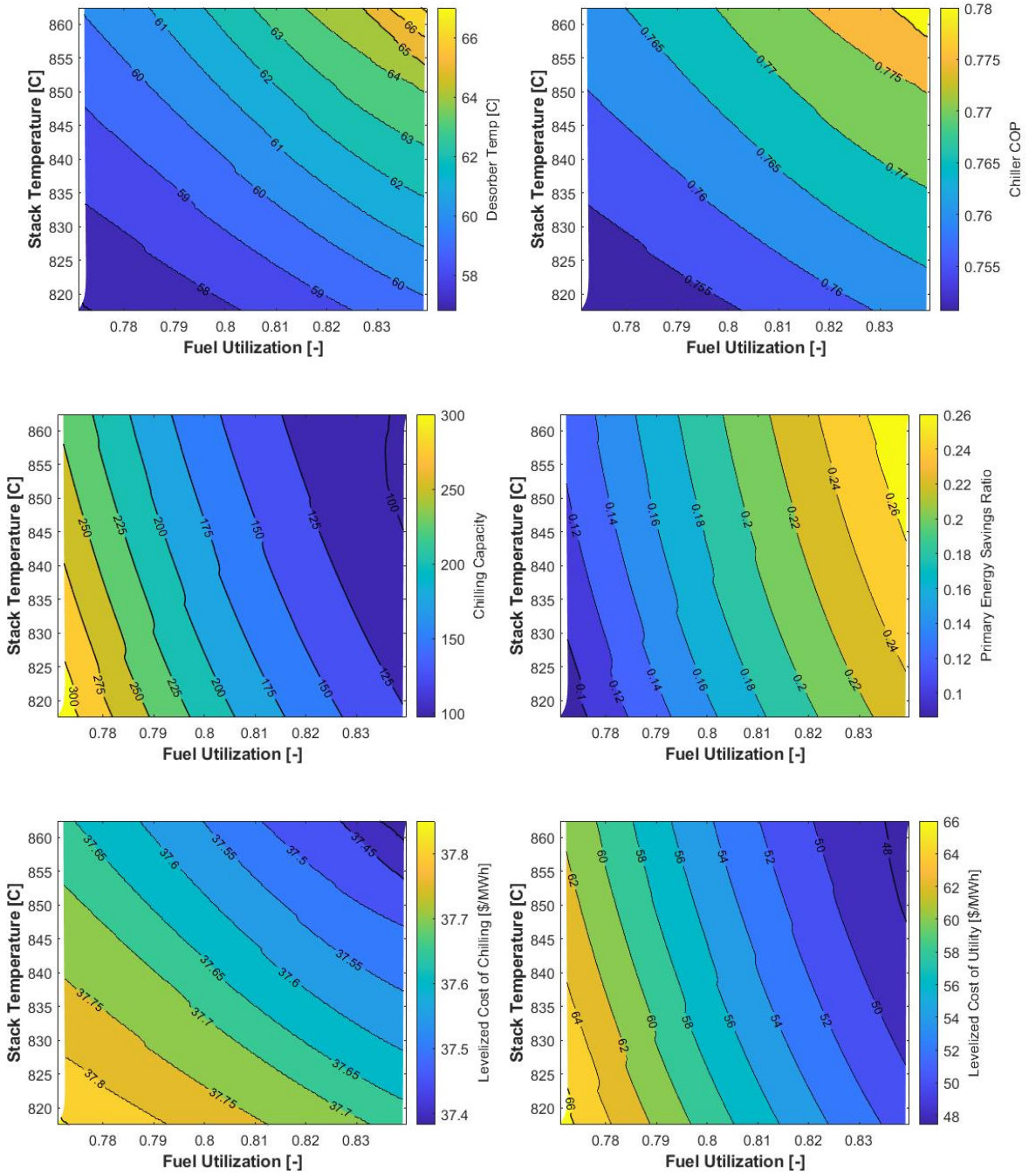

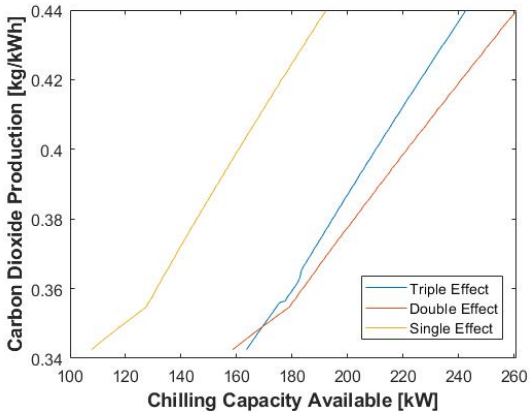
Carbon Dioxide Production [kg/kWh]
0.44
0.42
0.4
0.38
0.36
0.34
100 120 140 160 180 200 220 240 260
Chilling Capacity Available [kW]
Triple Effect
Double Effect
Single Effect

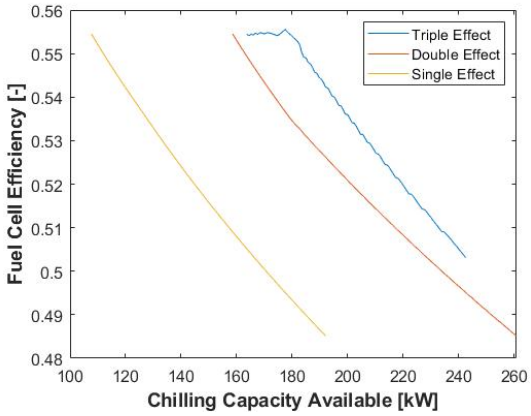
Fuel Cell Efficiency [-]
0.56
0.55
0.54
0.53
0.52
0.51
0.5
0.49
0.48
100 120 140 160 180 200 220 240 260
Chilling Capacity Available [kW]
Triple Effect
Double Effect
Single Effect

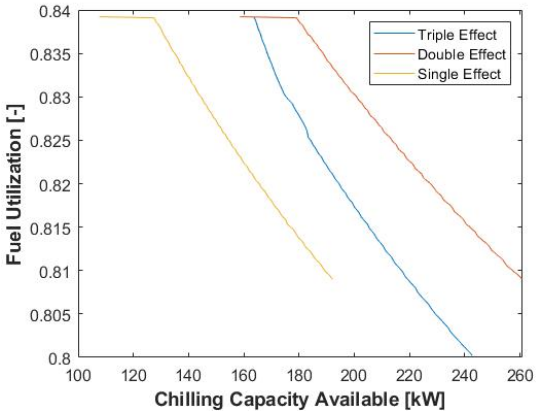
Fuel Utilization [-]
0.84
0.835
0.83
0.825
0.82
0.815
0.81
0.805
0.8
100 120 140 160 180 200 220 240 260
Chilling Capacity Available [kW]
Triple Effect
Double Effect
Single Effect

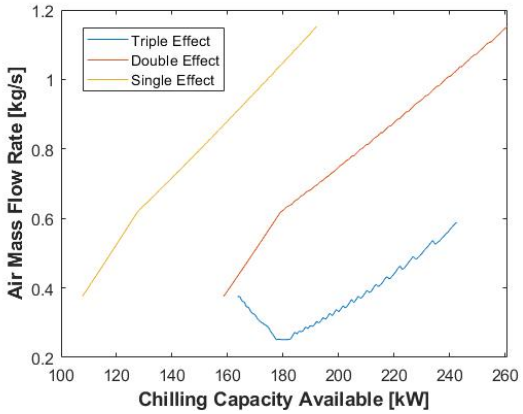
Air Mass Flow Rate [kg/s]
1.2
1
0.8
0.6
0.4
0.2
100 120 140 160 180 200 220 240 260
Chilling Capacity Available [kW]
Triple Effect
Double Effect
Single Effect

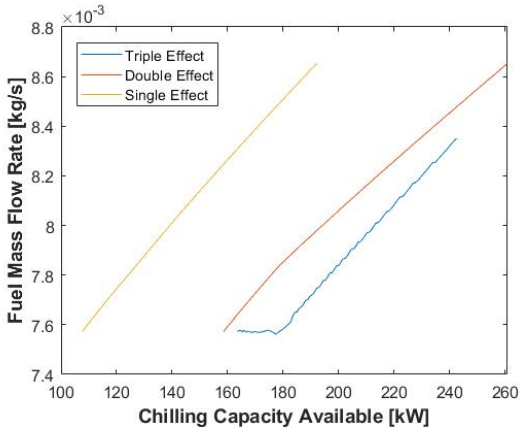
×10^-3
Fuel Mass Flow Rate [kg/s]
8.8
8.6
8.4
8.2
8
7.8
7.6
7.4
100 120 140 160 180 200 220 240 260
Chilling Capacity Available [kW]
Triple Effect
Double Effect
Single Effect

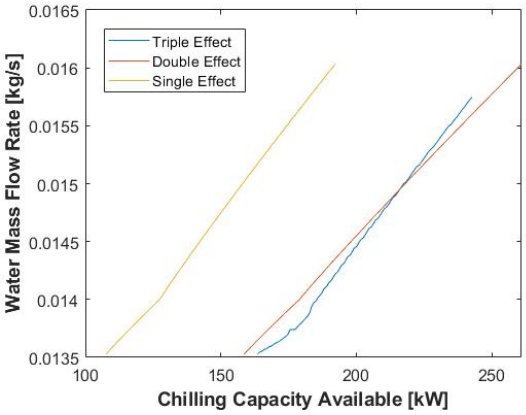
Water Mass Flow Rate [kg/s]
0.0165
0.016
0.0155
0.015
0.0145
0.014
0.0135
100 150 200 250
Chilling Capacity Available [kW]
Triple Effect
Double Effect
Single Effect

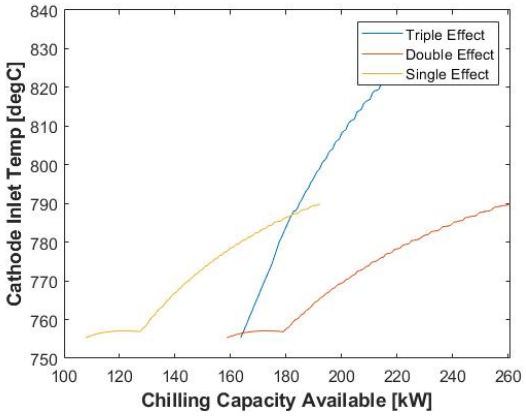
Triple Effect
Double Effect
Single Effect
Cathode Inlet Temp [degC]
Chilling Capacity Available [kW]

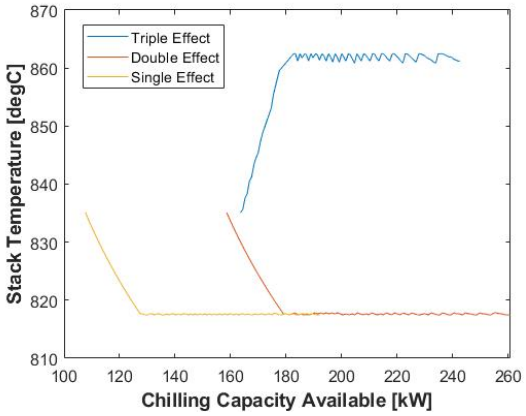
Triple Effect
Double Effect
Single Effect
Stack Temperature [degC]
Chilling Capacity Available [kW]

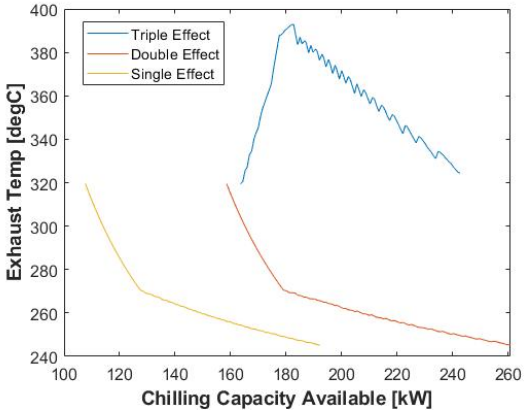
Triple Effect
Double Effect
Single Effect
Exhaust Temp [degC]
Chilling Capacity Available [kW]

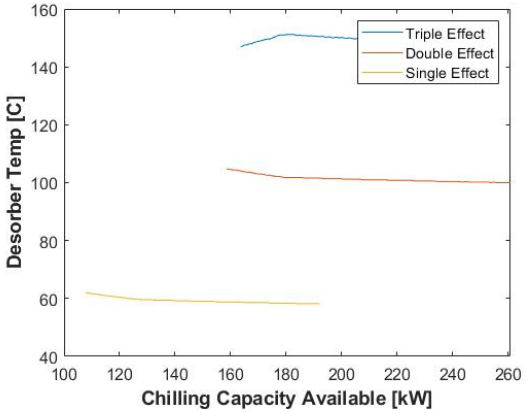
Triple Effect
Double Effect
Single Effect
Desorber Temp [C]
Chilling Capacity Available [kW]

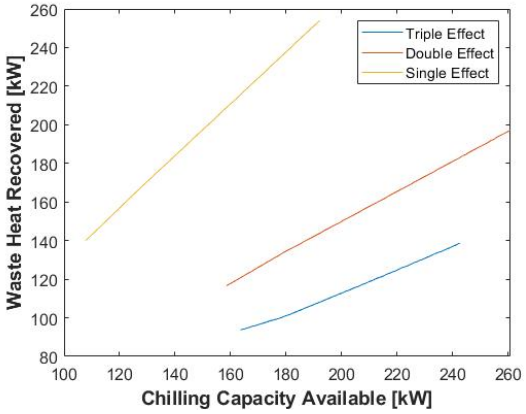
Triple Effect
Double Effect
Single Effect
Waste Heat Recovered [kW]
Chilling Capacity Available [kW]

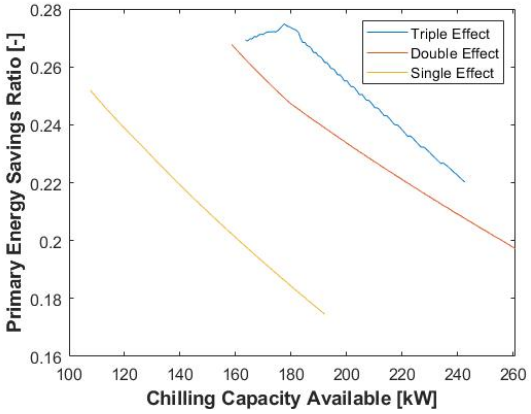
Triple Effect
Double Effect
Single Effect
Primary Energy Savings Ratio [-]
Chilling Capacity Available [kW]

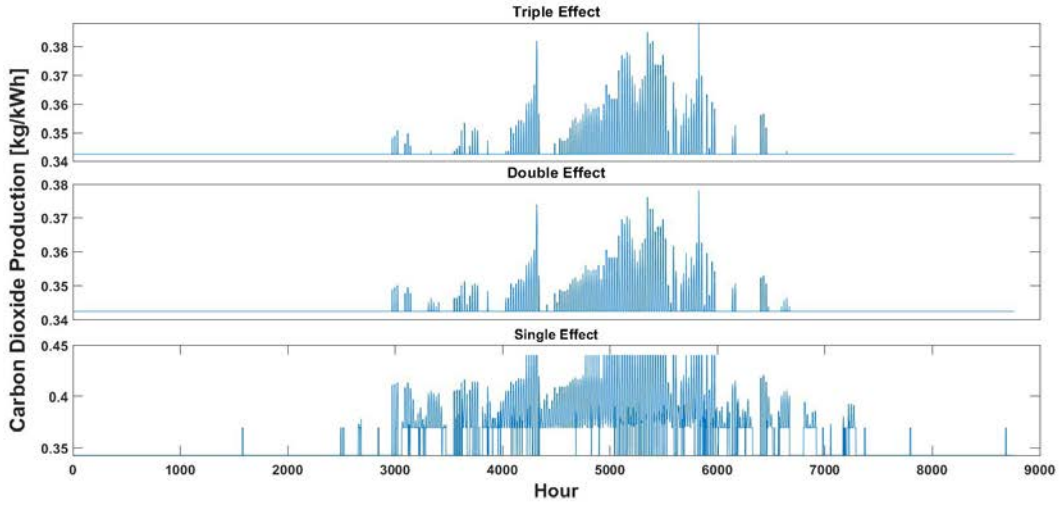
Triple Effect
Double Effect
Single Effect
Carbon Dioxide Production [kg/kWh]
Hour

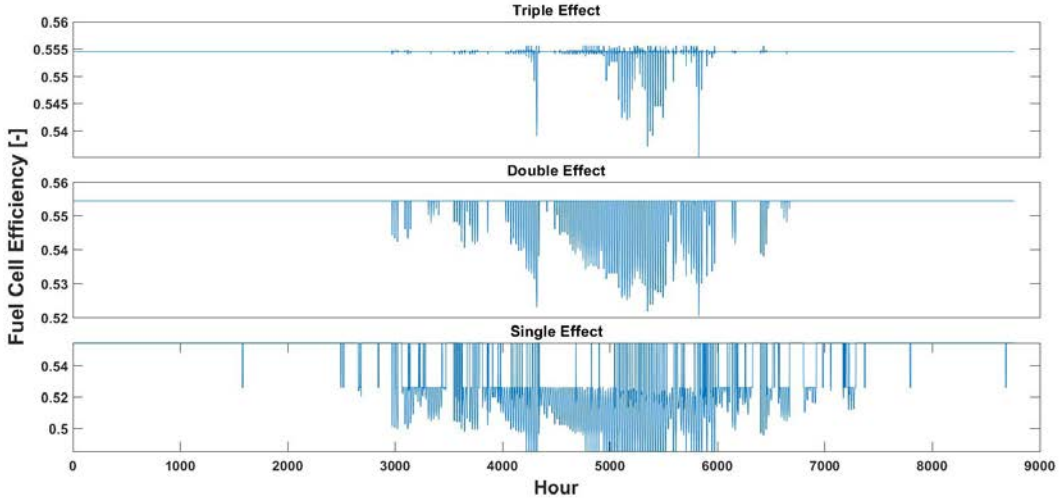
Triple Effect
Double Effect
Single Effect
Fuel Cell Efficiency [-]
Hour

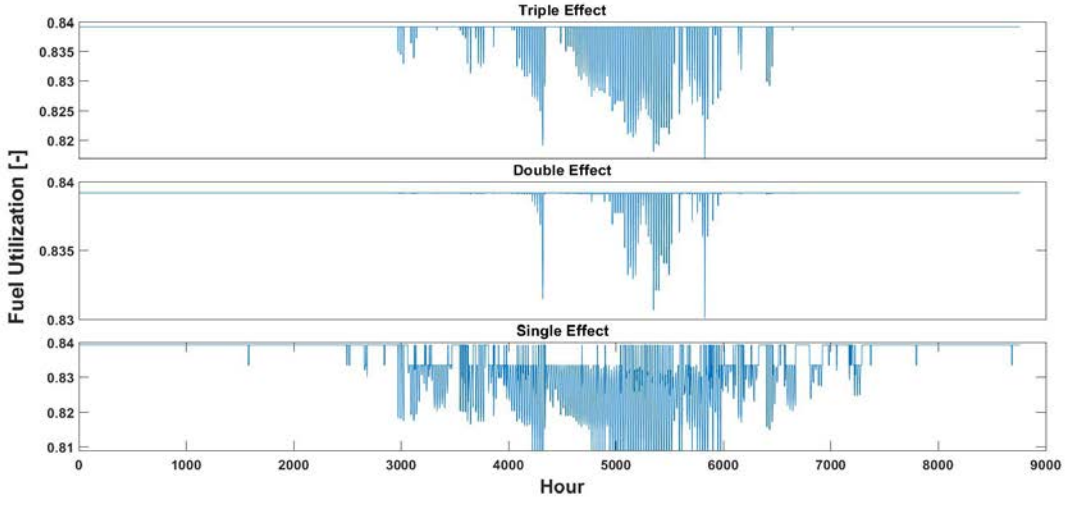
Triple Effect
Double Effect
Single Effect
Fuel Utilization [-]
Hour

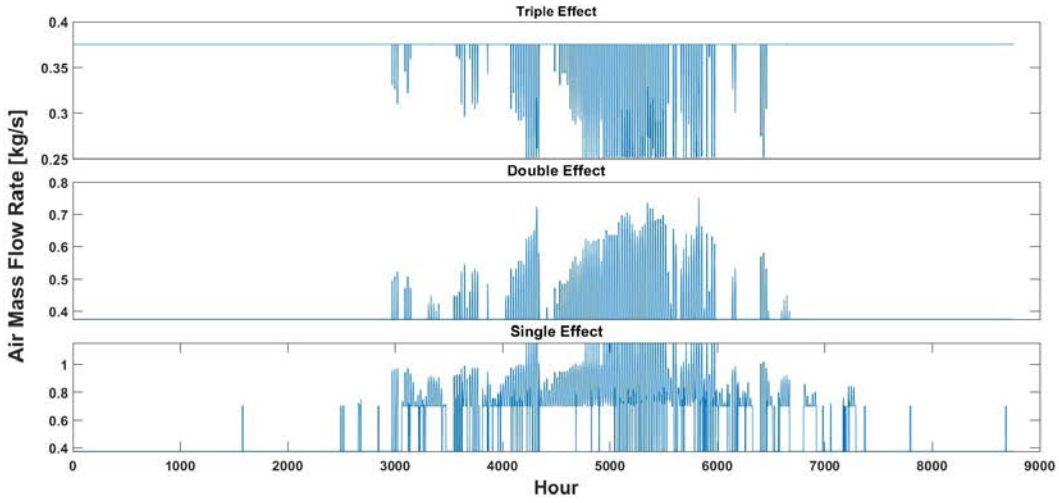
Triple Effect
Double Effect
Single Effect
Air Mass Flow Rate [kg/s]
Hour

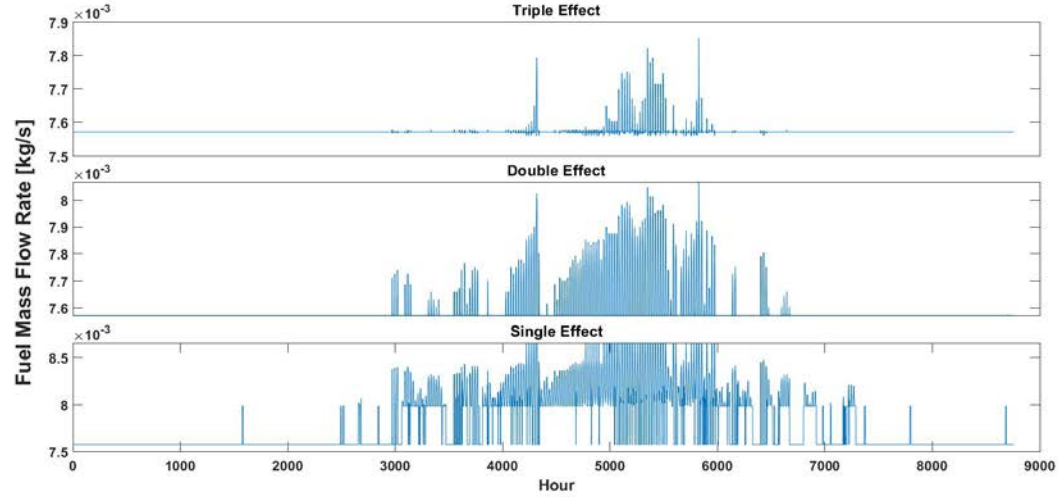
Triple Effect
Double Effect
Single Effect
Fuel Mass Flow Rate [kg/s]
Hour

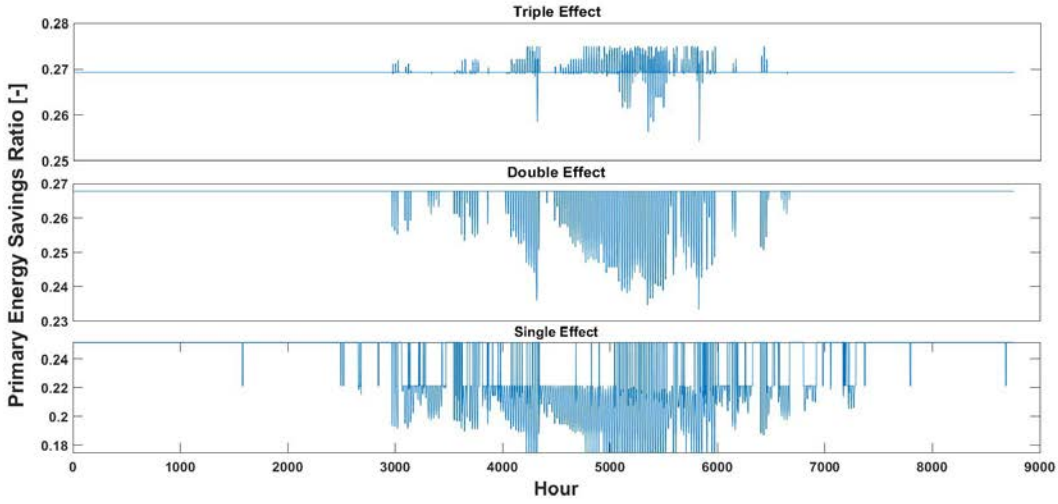
Triple Effect
Double Effect
Single Effect
Primary Energy Savings Ratio [-]
Hour

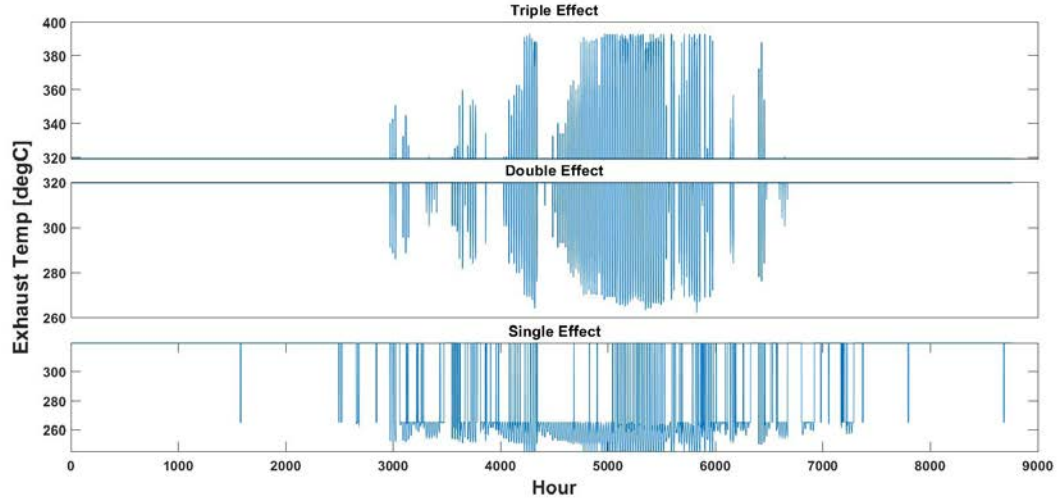
Triple Effect
Double Effect
Single Effect
Exhaust Temp [degC]
Hour

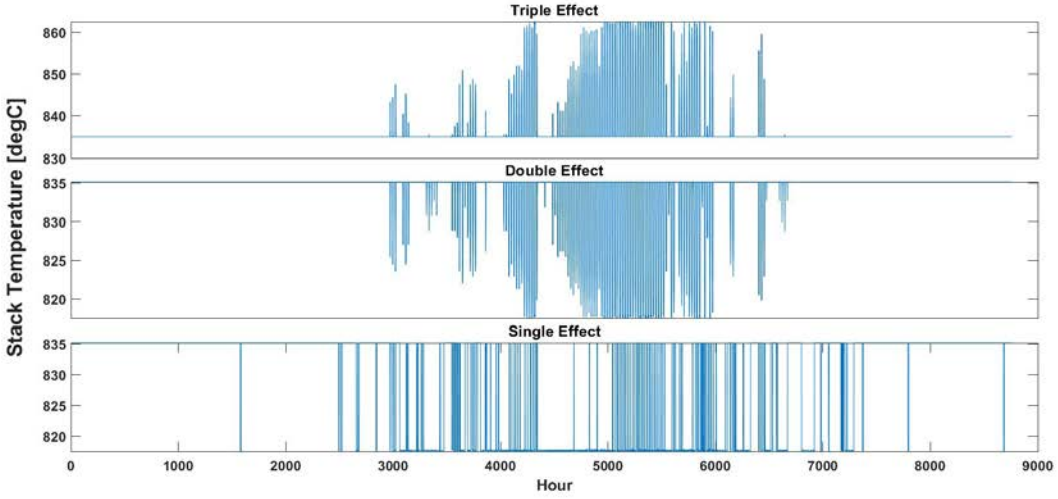
Triple Effect
Double Effect
Single Effect
Stack Temperature [degC]
Hour

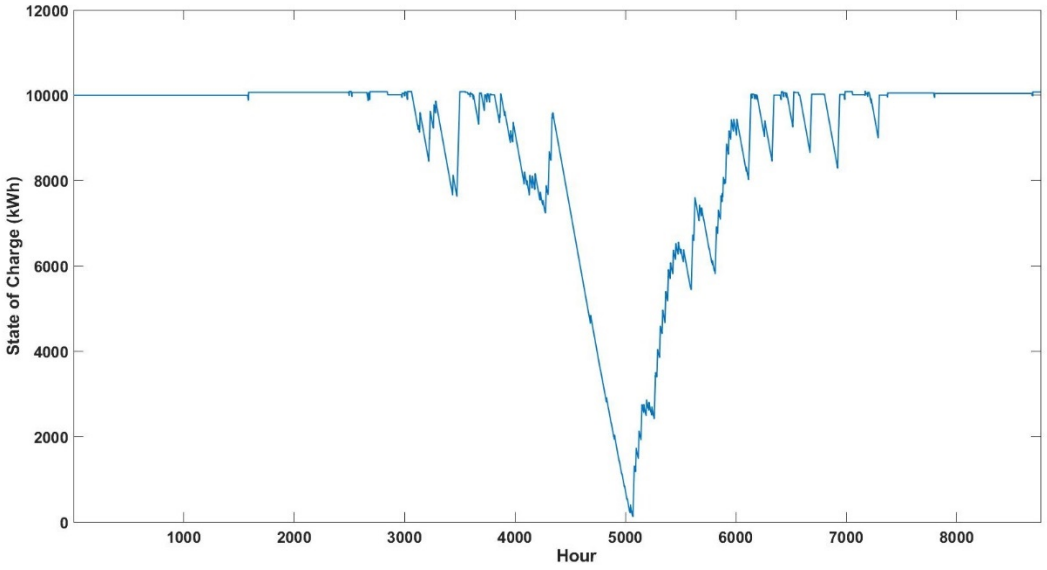
State of Charge (kWh)
Hour
0
2000
4000
6000
8000
10000
12000
1000
2000
3000
4000
5000
6000
7000
8000

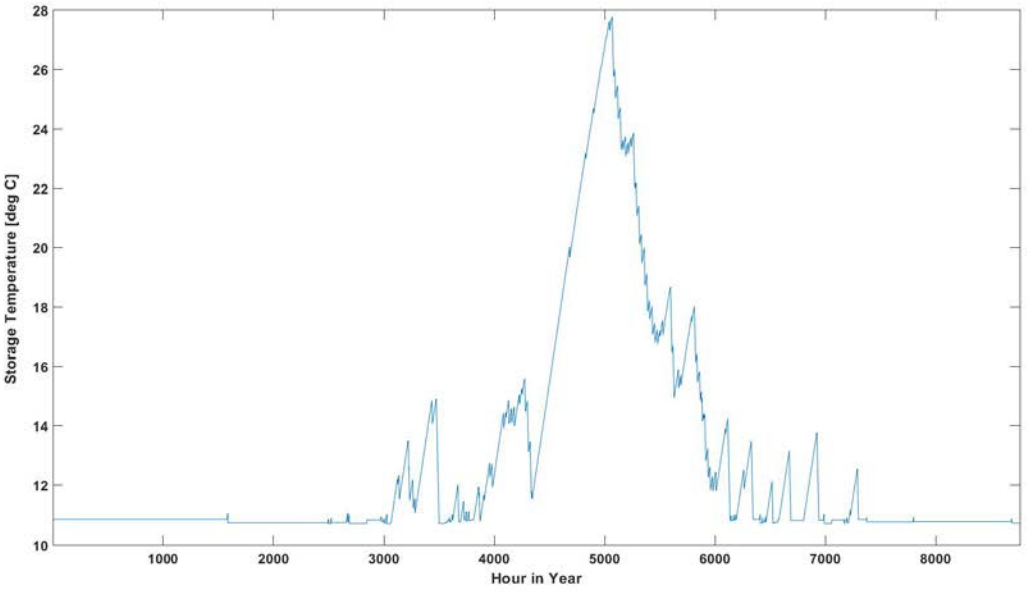
Storage Temperature [deg C]
Hour in Year
10
12
14
16
18
20
22
24
26
28
1000
2000
3000
4000
5000
6000
7000
8000